Dissertation
submitted to the
Combined Faculties for the Natural Sciences and for Mathematics
of the Ruperto-Carola University of Heidelberg, Germany
for the degree of
Doctor of Natural Sciences

presented by
Diplom-Physiker Sven Kühl
born in Cloppenburg

Oral examination: July, 7, 2005

Quantifying Stratospheric Chlorine Chemistry

by the Satellite Spectrometers GOME and SCIAMACHY

Referees: Prof. Dr. Ulrich Platt

Prof. Dr. Bernhard Jähne

Zusammenfassung

Seit Mitte der achtziger Jahre des vorigen Jahrhunderts ist bekannt, dass über dem Südpol im dortigen Frühling (und im geringeren Ausmaß auch über dem Nordpol) ein fast vollständiger Abbau der Ozonschicht stattfindet, welcher bedingt ist durch die Freisetzung von atomarem Chlor und Brom aus anthropogenen Halogenverbindungen. Durch den schnellen Ausstieg aus der Produktion der FCKWs konnte der Anstieg des stratosphärischen Chlorgehalts gebremst werden, und es wird erwartet, dass sich die Ozonschicht um das Jahr 2050 erholen wird. Dennoch sind die Auswirkungen für die Chemie der Atmosphäre, das Klima sowie das Leben auf der Erde beträchtlich.
Mit der differentiellen optischen Absorptionsspektroskopie (DOAS) können gleichzeitig verschiedene Moleküle mit charakteristischem Absorptionsspektrum in der Atmosphäre nachgewiesen werden, darunter auch viele Halogenverbindungen. In dieser Arbeit wurden Messungen der Satelliten-Spektrometer GOME und SCIAMACHY hinsichtlich des atmosphärischen Spurengases Chlordioxid (OClO) ausgewertet und bezüglich ihrer Relevanz für die polare stratosphärische Ozonchemie analysiert. OClO ist ein wichtiger Indikator für die stratosphärische Chloraktivierung, die Umsetzung des zum größten Teil anthropogenen Chlors aus seinen gegenüber Ozon inerten Reservoirverbindungen in ozonzerstörende (aktive) Verbindungen. Diese Chloraktivierung erfolgt durch heterogene Reaktionen an polaren stratosphärischen Wolken, welche bei den während der Polarnacht vorherrschenden, extrem kalten stratosphärischen Temperaturen gebildet werden können.
In dieser Arbeit werden die Messungen der OClO-Säulendichte in den polaren Wintern 1995-2005 durch GOME und SCIAMACHY quantitativ in Bezug gesetzt zu den meteorologischen Bedingungen, dem Effekt auf die Ozonsäule und das Zusammenwirken mit anderen stratosphärischen Spurengasen. Die Messungen von SCIAMACHY in Limb-Geometrie können unter Berechnung des Strahlungstransportes zu vertikalen Profilen invertiert werden, was den Informationsgehalt gegenüber einer Messung der Säulendichte wesentlich erhöht. In dieser Arbeit wurden Algorithmen zur Bestimmung von Vertikal-Profilen von OClO, Ozon, BrO und NO_2 entwickelt und erste Ergebnisse hierzu werden vorgestellt.

Abstract

Since the mid eighties of the past century, an almost complete destruction of the ozone layer above the Antarctic in springtime (and to a lesser extent also above the Arctic) is observed, which is caused by the release of atomic chlorine and bromine from anthropogenic halogen compounds. Due to the fast phase out of the production of CFCs, the increase of the stratospheric chlorine loading could be slowed down, and the recovery of the ozone layer is expected around the year 2050. However, the impacts on atmospheric chemistry, the climate and the biosphere are considerable.
By differential optical absorption spectroscopy (DOAS) various molecules with characteristic absorption spectra can be detected simultaneously in the atmosphere, among them also many halogen compounds. In this thesis, measurements of the satellite spectrometers GOME and SCIAMACHY were evaluated for the atmospheric trace gas chlorine dioxide (OClO) and analysed with respect to their relevance for the polar stratospheric ozone chemistry. OClO is an important indicator for stratospheric chlorine activation, the conversion of the mainly anthropogenic chlorine from its ozone-inert reservoir compounds into ozone destroying (active) species. This activation of chlorine takes place by heterogeneous reactions on polar stratospheric clouds, which may be formed under the extremely cold stratospheric temperatures prevailing in polar nights.
In this thesis, measurements of the OClO column density by GOME and SCIAMACHY during the polar winters 1995-2005 are quantitatively related to the meteorological conditions, the effect on the ozone column and the interaction with other stratospheric trace gases. The measurements by SCIAMACHY in the limb geometry can be inverted to vertical profiles by calculation of the radiative transfer, which increases the information content with respect to a measurement of the column density essentially. In this thesis, algorithms for the retrieval of vertical profiles of OClO, ozone, BrO and NO_2 were developed and first results are presented.

Table of Contents

Introduction **1- 3**

1 Relevant Background of Atmospheric Sciences 5 - 21

1.1 The vertical structure of Earth's Atmosphere……..6

1.2 Interaction of light and matter……..8
1.2.1 Absorption
1.2.2 Scattering
1.2.3 Atmospheric radiative transfer

1.3 Atmospheric ozone chemistry (homogeneous)…….14
1.3.1 Chapman cycle
1.3.2 Catalytic ozone destruction by trace gases
1.3.3 Null cycles, holding cycles and reservoir compounds

1.4 The influence of atmospheric circulation on the ozone layer……...17

1.5 Perturbations of stratospheric ozone by human activities……..…19
1.5.1 The Ozone hole

2 Stratospheric ozone loss 23 - 36

2.1 Heterogeneous chemistry…….24

2.2 Meteorology and chemistry of the polar stratosphere…….25
2.2.1 The Polar vortex
2.2.2 Polar Stratospheric Clouds
2.2.3 Polar Stratospheric ozone loss

2.3 Global ozone depletion……..……32

2.4 Consequences of ozone loss……..33

2.5 Future of the ozone layer……..35

3 Retrieval: Methodology and Instruments 37 - 60

3.1 Differential Optical Absorption spectroscopy (DOAS) ……38
3.1.1 Principle of DOAS
3.1.2 The air mass factor
3.1.3 Corrections for scattered light DOAS

3.2 Measurement geometries……43

3.3 Profile retrieval by optimal estimation……..45

3.4 The Global Ozone Monitoring Experiment (GOME) ……..47

3.5 The Scanning Imaging Absorption Spectrometer for Atmospheric Chartography (SCIAMACHY) ……48

3.6 OClO Retrieval from GOME nadir spectra……..…52

3.7 OClO Retrieval from SCIAMACHY nadir spectra……54

3.8 OClO Retrieval from SCIAMACHY limb spectra……..…56

3.9 Retrieval of O_3, NO_2, BrO from SCIAMACHY limb spectra……..…57

4 OClO as Indicator of Stratospheric Chlorine activation 61 - 67

4.1 Problems in calculating OClO VCDs ……62

4.2 Photochemistry of OClO……63

4.3 Relation to ClO……..…66

4.4 Relation to NO_2……..…67

4.5 Relation to BrO……..…67

5 GOME Results 69 - 98

5.1 Monitoring of chlorine activation……...70
5.1.1 Overview of GOME OClO measurements 1995-2004
5.1.2 Comparison between northern and southern hemisphere
5.1.3 The Arctic winter 1996/97
5.1.4 The Arctic winter 1998/99
5.1.5 The Arctic winter 1999/2000
5.1.6 The Arctic winter 2002/03

5.2 Comparison with other measurements of chlorine activation……79
5.2.1 Comparison to ground-based OClO measurements
5.2.2 Comparison to MLS ClO
5.2.3 Comparison to ODIN ClO

5.3 Comparison with model results……..84
5.3.1 Comparison to Slimcat ClOx
5.3.2 Comparison to Slimcat OClO

5.4 Case Studies……90
5.4.1 Dependence of chlorine activation on stratospheric temperatures
5.4.2 Relation to PSC formation
5.4.3 Relation to ozone depletion
5.4.4 Deactivation: Relation to Denitrification

6 SCIAMACHY Results 99 - 130

6.1 SCIAMACHY measurements of OClO in nadir mode……..……100
6.1.1 First results
6.1.2 Comparison to GOME

6.2 SCIAMACHY measurements of O_3, NO_2 and BrO in limb mode……108
6.2.1 Retrieval of vertical O_3 profiles
6.2.2 Retrieval of vertical NO_2 profiles
6.2.3 Retrieval of vertical BrO profiles

6.3 SCIAMACHY measurements of OClO in limb mode……124

7 Mountain wave-induced chlorine activation 131- 150

7.1 Mountain Waves……132

7.2 The event of 20-22 January 1997……...133
7.2.1 Meteorological situation
7.2.2 OClO Measurements
7.2.3 Quantifying the increase in chlorine activation
7.2.4 Estimation of the measurement errors and uncertainties of the calculation

7.3 The event of 20-27 January 2000……..…146

7.4 The event of 18-20 December 2002……..…148

7.5 Implications for Arctic stratospheric chemistry……...150

Conclusions 153

References 157

Introduction

Since the ancient times, humans have had an impact on their environment, leading in some cases also to large scale and irreversible changes (e.g. deforestation of Italy by the Romans). With the growth of industry, economy and technology the impact of mankind on the environment largely increased. The last four to five decades have shown that mankind is able to affect equilibria in nature in an irreversible manner and on a global scale, also when this is not intended. It became evident that the extent to which mankind harms the system Earth is often underestimated, and that its impact on some parts of this system is not or only poorly understood.

One part of the Earth system that was found to be very sensitive to perturbations caused by human activities is the atmosphere. Despite its negligible mass compared to the Earth ($M_A = 1.5*10^{18}$ kg, $M_E = 5.98*10^{24}$ kg) it is of major importance for the biosphere. Crucial changes in the atmosphere were recognized not until their hurtful impact on the vegetation or on human health: so the London smog episode in 1952, when about 4000 people died. At the same time the summer-smog of Los Angeles was build up with amplified concentration of ozone, PAN and further photo-oxidants and led to grave affection of mucous membrane and respiratory tracts. The problem of acid rain has been identified in the seventieth of the last century when the European forest died over vast areas and many lakes were found to be acidificated.

Besides of such rather local encroachments into the atmosphere, also global changes due to human activities affect our life on earth. The discovery of the stratospheric ozone hole in the eighties of the last century revealed a big and dangerous source to enhance the disease of skin cancer due to intensified UV-radiation on earth. Furthermore, the increase of greenhouse gases (e.g. CO_2, CH_4) was observed which leads to global warming. The chemical and physical processes of stratospheric ozone destruction and the consequences of global warming are not yet understood in each detail. But we know that such shifts in the atmospheric balances cause global changes of our climate and have the potential to endanger the survival of mankind. Thus, it is of utter importance to observe trends of meteorological parameters and of atmospheric trace gases to investigate the processes and to assess the future evolution.

This thesis is focusing on studies which concern the ozone chemistry in the stratosphere. The ozone layer is of major importance for the biosphere since it absorbs all UV-B radiation of the sunlight, that means just the part of the UV-radiation range which causes skin cancer. However, anthropogenic halocarbon emissions have led to detectable depletions in the stratospheric ozone layer both at mid and high latitudes. Despite from ozone losses directly above the poles, a negative trend of about 1.5 to 3 % per decade is observed also in the abundance of ozone at mid latitudes.

Although the main processes which effect the polar ozone loss are now well understood [*WMO, 2003*], there are still unexplained features like the following:

- The future development of polar ozone loss is difficult to predict, especially for the Arctic [Austin et al. 2003]
- The mechanisms that lead to formation of PSCs are still not fully understood [*Peter 1997, WMO, 1999*]
- In the northern hemisphere, temperature disturbances on the mesoscale by mountain waves are thought to contribute significantly to the ozone depleting processes [*Carslaw et al. 1998*]. However, the extent to which active chlorine levels are increased by mountain wave activity remains an open issue [*WMO 1999, EUR 2001*]
- In the Arctic, the observed chemical depletion of ozone is higher than calculated by chemical transport models, especially in January [*Rex et al., 2003*]
- In September 2002, a major warming, which by definition should occur only in the Arctic stratosphere, took place above the Antarctic. The reason for this is not identified.
- There is a discrepancy in the OClO and NO_2 night time abundances between model simulations and observations, implying that the understanding of the coupling between chlorine and nitrogen is not complete
- The effect of denitrification on ozone loss in polar spring is not accounted for correctly by current model simulations
- The growing greenhouse effect, the cooling of the stratosphere and the increase in the abundance of water vapor in the stratosphere have significant effects on the future development of the ozone layer that can not be quantified

Among other aspects, the existent gaps of knowledge concern the relation of the chlorine chemistry to the ozone chemistry. This thesis presents investigations of the chlorine chemistry to obtain a deeper understanding of the nonlinear processes in the ozone distributions. The investigations are performed on the base of satellite measurements. Satellite observations have the advantage to observe the whole globe with the same instrument on a long time scale. Thus, it is possible to gain important details of long-term temporal evolutions and global variability of the atmospheric state.

The satellite instruments GOME and SCIAMACHY are measuring since about 10 years now. Their concept contains the technique of Differential Optical Absorption Spectroscopy (DOAS). By this they are able to observe many trace gases which are related to chlorine and ozone chemistry like O_3, BrO or OClO simultaneously.
GOME measurements of OClO are available from 1995 to 2005. These data enable us to intercompare the chlorine activation in different years under several meteorological situations occurring in both hemispheres and are therefore valuable to investigate several of the above mentioned open questions.

In this thesis monitoring data of OClO will be discussed, interhemispheric differences are assessed. The relation between stratospheric temperatures, formation of Polar Stratospheric Clouds (PSCs), the volume of possible PSC formation, the chemical ozone depletion and the chlorine activation will be investigated. Of special interest above the Arctic is the influence of mesoscale processes on the chlorine activation. We consider case studies of mountain wave events to see in which intensity mountain waves are able to enhance chlorine activation locally. One further important aspect is the coupling of chlorine chemistry to nitrogen chemistry. Denitrification processes are correlated to both chlorine and ozone distributions.

The higher resolved SCIAMACHY OClO data, available since 2002, will be compared to GOME OClO measurements. One very important advancement of SCIAMACHY is the possibility to do limb measurements, i.e. to resolve the vertical direction of distributions and to provide vertical profiles of trace gases. First results of limb retrievals of ozone, nitrogen dioxide, bromine monoxide and chlorine dioxide will be presented.

1 Relevant Background of Atmospheric Sciences

The increasing impact of man's activities on environment, leading to the undesired consequences described above, was resulting from a growth of economy, industry and population, which in turn based on a progress in technology and science. However, the science that magnified the impact of human beings on their environment, at the same time also developed the knowledge, methods, and instruments to detect this impact. The growing awareness of anthropogenic perturbations to natural equilibria in the environment (and the consequences of this for mankind) led to the development of a new scientific branch: The environmental sciences, which are studying the interactions of the different spheres of the Earth by chemical and physical methods.
For the atmosphere, observations by in situ and remote sensing methods gave evidence of the responsibility of human activities for smog episodes, acid rain, the ozone hole, global ozone depletion, and the global warming by the increasing abundance of greenhouse gases. Thereby, the knowledge of the atmosphere and its interaction with the other spheres immensely increased.
In particular, the vulnerability of the ozone layer and its importance for the biosphere was demonstrated.

This chapter shall give an overview of the theoretical basis of atmospheric physics, chemistry and meteorology, which are relevant for the topic of this thesis. As well, it shall provide a more detailed background on certain topics that are necessary for the interpretation and discussion of the presented measurements and results:

- First the structure of the atmosphere, its composition, and the importance of trace gases in atmospheric chemistry, especially of ozone, is summarized.

- Then, the interaction of light and atmospheric constituents, which is the basis of the spectroscopic methods applied for remote sensing of atmospheric trace gases, is reviewed (section 1.2.). The remote sensing method DOAS applied in this thesis is described in chapter 3.

- The chapter continues with an overview of the knowledge about stratospheric ozone and its chemistry before the discovery of the ozone hole: The atmospheric dynamics related to ozone abundances, the Chapman cycle, and the catalytic ozone destruction cycles by trace gases (sections 1.3 to 1.4).

- The last section then describes the possible impact of anthropogenic emissions and the spotting of the Antarctic ozone hole, which could not be predicted by the prevalent knowledge about stratospheric ozone and related compounds at that time and therefore gave rise to explore the underlying mechanisms.

1.1 The vertical structure of Earth's Atmosphere

The mixture of gases, called atmosphere or air, that surrounds the Earth is hindered from escaping into free space by Earth's gravity. Since gases are compressible, the density of air molecules is increasing towards the ground, resulting via Daltons law in an exponential decrease of **pressure** with altitude [*Roedel, 2000*]:

$$p(h) = p_0 * \exp\left(-\frac{mg}{kTh}\right) = p_0 * \exp\left(-\frac{h}{h_0}\right) \qquad (1.1)$$

where m is the average mass of an air molecule, g the gravitational acceleration, k the Boltzmann constant, T the temperature (the assumption of an isothermal atmosphere is made), $p_0 \approx 1000$ hPa the pressure at ground level, and $h_0 = kT/mg \approx 7.6$ km is the **scale height**. The scale height is equivalent to the height of the atmosphere if it had constant pressure. Due to eq. (1.1), about 99 % of the mass of the atmosphere ($M \approx 5*10^{18}$ kg) is situated within the lowest 30 km.

The **composition** of air is dominated by molecular nitrogen ($m(N_2) = 28{,}013$ g/mol) and oxygen ($m(O_2) = 31{,}999$ g/mol), which make up 99 % of the dry air, compare table 1. Another 0.93 % is made up by Argon ($m(Ar) = 39{,}948$ g/mol) resulting in an average molecular air mass of 28,965 g/mol ≈ 29 g/mol. The remainder is formed by trace gases like CO_2, N_2O, CH_4, and O_3, which occur in highly variable abundances.

Although the scale height is different for each atmospheric component due to different molecular weight, a de-mixing of the air components is observed only for altitudes above 100 km in the **Heterosphere**, where molecular diffusion determines the distribution. Below, from ground to 100 km height, in the **Homosphere**, turbulence provides a constant mixing ratio. Exceptions to this constant composition are the trace gases, which are naturally and anthropogenically emitted, and also have (photo-) chemical sources and sinks that are strongly dependent on altitude, temperature, pressure and solar intensity.

For example, the ozone maximum in the stratosphere is generated by photolysis of oxygen which requires radiation in the UV region. The ozone layer also demonstrates that, despite their almost vanishing abundance, trace gases can be of great importance for the atmosphere and its relation to the biosphere.

Besides molecules, also particles like e.g. the sulfate aerosols in the Junge layer, which is located at altitudes around 20 km (close to the ozone layer), play an important role in atmospheric chemistry as well as in radiation transport. They provide the surface for heterogeneous reactions (see section 2.1), and remove atmospheric compounds by wet deposition.

Gas	**Volume mixing ratio**		**Molecular mass**
	percent	**ppmv**	**10^{-3} kg / mol**
Nitrogen (N_2)	78.08	780,0	28,013
Oxygen (O_2)	20.95	209,5	31,999
Argon (Ar)	0.93	9,3	39,948
Neon (Ne)	0.0015	15	20,183
Water vapor (H_2O)	0.00001 – 4.0	0.1 – 40	18,016
Carbon dioxide (CO_2)	0.0360	360	44,010
Methane (CH_4)	0.00017	1.7	16,043
Ozone (O_3)	0.000003 – 0.001	0.03 – 10	47,995

Table 1A: Average composition of the lowest 100 km in the Earth's atmosphere [*Jacobson, 2000*].

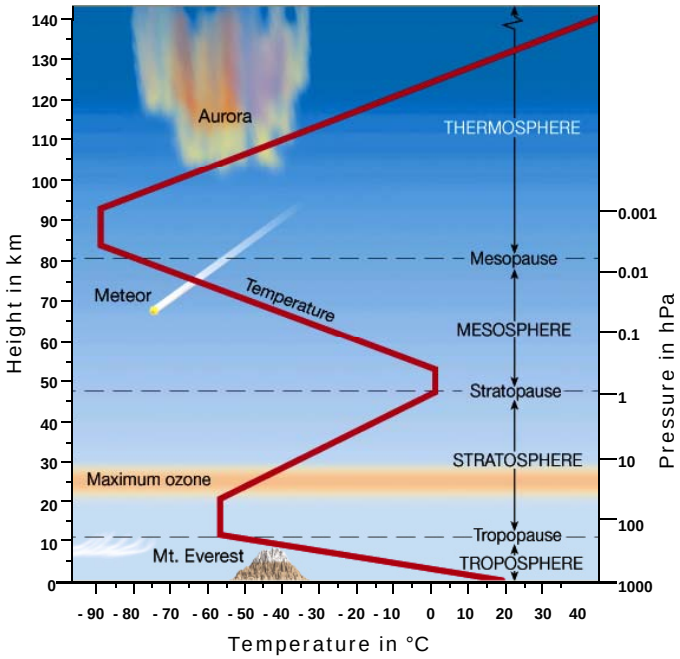

Figure 1.1: Temperature as a function of altitude and pressure for the different atmospheric layers, modified from [*http://www.ux1.eiu.edu/~cfjps/1400/*].

The most common criterion to subdivide the atmosphere is the **temperature gradient**, which due to radiative heating and cooling changes its sign depending on the altitude of the air mass (see Fig 1.1). In the **Troposphere**, the absorption of solar radiation by the ground and the consequent expansion of the ascending warm air masses results, in equilibrium, in an adiabatic decrease of the temperature [*Roedel, 2000; Kraus, 2001*] :

$$-dT/dh = g/c_p = \Gamma_d = 9.81\ K/m \qquad \text{dry adiabatic}$$
$$-dT/dh = \alpha\, g/c_p = \Gamma_w = \alpha\, \Gamma_d \quad (\text{with } 0 < \alpha < 1) \qquad \text{wet adiabatic}$$

The first value Γ_d is calculated for dry air. Water vapour, which constitutes up to 4% of the wet air, contains latent heat which is set free by condensation in an ascending air parcel. Therefore, the wet adiabatic lapse rate Γ_w is smaller (its value depends on temperature and pressure). The actual lapse rate of a given air layer is resulting from a combination of different water vapour contents, pressure and temperature history and also of vertical transport, and has a mean value of: $\gamma = -dT/dh = 0{,}0065\ K/m = 0.65\ K / 100\ m$ in the troposphere.

If the actual lapse rate is larger than the adiabatic ($\gamma > \Gamma$), ascending air masses remain warmer and lighter than the surrounding air and therefore can ascend. Such a stacking of air masses is therefore called unstable layered. On the other hand, a temperature profile where $\gamma < \Gamma$, and ascending air gets colder and heavier than the surrounding air and thus is hindered to ascend, is called stable layered. This situation is given in the **Tropopause**, the temperature minimum of approx. -60° C, which in equatorial regions is located at 18 km and in polar regions at 8 km height.

Since the tropopause is determined by the temperature gradients of both the troposphere and stratosphere, which strongly depend on solar illumination, its height is a function not only of latitude but also of season. A common approach to define the tropopause is by **potential temperature**. This is the temperature that an air mass would acquire if it was adiabatically compressed to standard pressure. It is defined by [*Kraus, 2001*] :

$$\Theta = T\left(\frac{p_0}{p}\right)^{\kappa} \qquad \text{where} \quad \kappa = R/c_p = 0.286 \qquad (1.2)$$

and, unlike temperature and pressure, stays constant during adiabatic processes. Approximately, the tropopause is located at Θ = 380 K for equatorial regions and at Θ = 320 K for high latitudes.
The stable layered tropopause prevents vertical mixing of air with the **Stratosphere** above. There, pressure ranges approximately from 300 to 1 hPa and temperature increases with altitude. This temperature **inversion**, which is caused by radiative heating due to absorption of solar radiation by the ozone layer (compare Fig. 1.1), makes vertical mixing with the troposphere even more improbable. As a result, the stratosphere has a long circulation time (≈ 5 years, see section 1.4), making it extremely vulnerable to perturbations by anthropogenic emissions. On the timescale of days, diabatic processes can be neglected in the stratosphere, and thus the potential temperature Θ can be taken as a conserved value and is often used as altitude coordinate. Surfaces of constant potential temperature are called **isentropes**.
The temperature maximum of approx. 0° C near 50 km (≈ 1 hPa) is called **Stratopause**. The **Mesosphere** above shows a negative temperature gradient, caused by radiative cooling due to IR emission mainly by CO_2, while the positive temperature gradient in the **Thermosphere** is due to absorption of short-wave radiation (λ < 200 nm) by N_2 and O_2.

1.2 Interaction of Light and Matter

The vertical temperature gradient and thus the atmospheric layers, which in turn determine the distribution of trace gases, result from **radiative cooling** and **heating**, which require emission and absorption of electromagnetic radiation. Furthermore, many of the special features of trace gases arise from the ability to absorb the energy of the incident sunlight. This energy may lead to excited states (see Appendix A) and thereby enables chemical reactions that are thermodynamically not possible for the ground state species. Also, **photo-dissociation** of the excited molecule is possible, thereby forming species with different effect on atmospheric chemistry and physics.
Maxwell's equations describe electromagnetic radiation as consisting of fields which accelerate charged particles. Thus, sunlight traversing the Earth's atmosphere may interact with the dipoles of atmospheric molecules. Depending on the energy of the radiation and the kind of interacting species, the incident sunlight may either be absorbed, scattered, or transmitted. That is, the probability of a molecule to interact with a photon and the kind of interaction is determined by the wavelength of the incident light beam.

1.2.1 Absorption

In quantum mechanics, atoms and molecules can be described by wave functions with Eigenstates that possess not continuous but discrete energy values. Similarly, electromagnetic radiation interacts with matter as light quanta (photons) that carry energy of the radiation field as a multiple of the Planck constant: E = hν = hc/λ. As a result of time dependent perturbation theory, absorption of a photon may occur only if its energy is equal to the difference of two Eigenstates of the molecule (**resonance criterion**: ΔE = E_n – E_m = hν). The probability of this process is determined by the transition moment:

$$R_{nm} = \int \Psi_n^* \vec{\mu} \Psi_m d\tau \qquad \text{with} \quad \vec{\mu} = \sum q_i \vec{r}_i$$

where Ψ_n and Ψ_m are the wave functions describing the initial and final state of the molecule and $\vec{\mu}$ is the dipole operator. Transitions are possible only for $R_{nm} \neq 0$, which leads to selection rules like conservation

of angular momentum, spin, etc. The energies of the stationary states are related to the wave functions via the Hamilton operator: $H\Psi = E\Psi$.

In the Born-Oppenheimer approximation, the wave function of a molecule can be written as a product of three wave functions that describe the electronic, vibrational and rotational state of the molecule:

$$\Psi = \Psi_{el}\Psi_{vib}\Psi_{rot}$$

Accordingly, the energy of the molecule separates in an electronic, a vibrational and a rotational part. Electronic transitions are of the order of 1 eV and thus require absorption of radiation with wavelengths of below 1100 nm. Transitions between vibrational states afford energies approx. one order of magnitude smaller and occur approximately in the range 2.5 μm < λ < 50 μm, while rotational transitions appear in the microwave region and far infrared, see Figure 1.2.

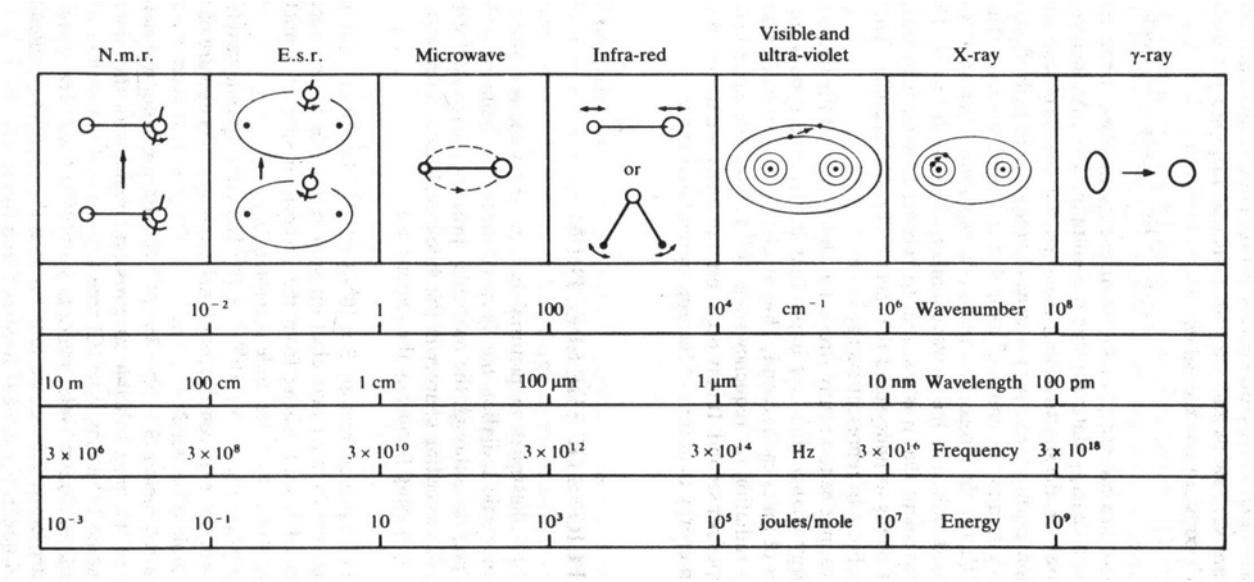

FIGURE 1.2: Electromagnetic spectrum, adapted from [*Banwell, 1994*].

The property of a molecule to absorb only photons of specific energy is quantitatively described by Fermi´s golden rule:

$$\sigma_a(\omega) = \frac{\pi}{h\varepsilon_0 c}\omega_{nm}\delta(\varpi_{nm} - \varpi)\left\|R_{nm}\right\|^2 \qquad (1.3)$$

where σ_a is the **absorption cross section** for the wave number ω, ω_{nm} the wave number corresponding to the energy difference of the states described by Ψ_n and Ψ_m, and δ the delta function.
Equation (1.3) connects the stationary states of a molecule with its absorption cross section at a certain wavelength. Since the electronic, vibrational and rotational stationary states differ much for every molecule, eq. (1.3) leads to characteristic absorption spectra. Fig. 1.3 shows the absorption cross sections of the species most important for this thesis.

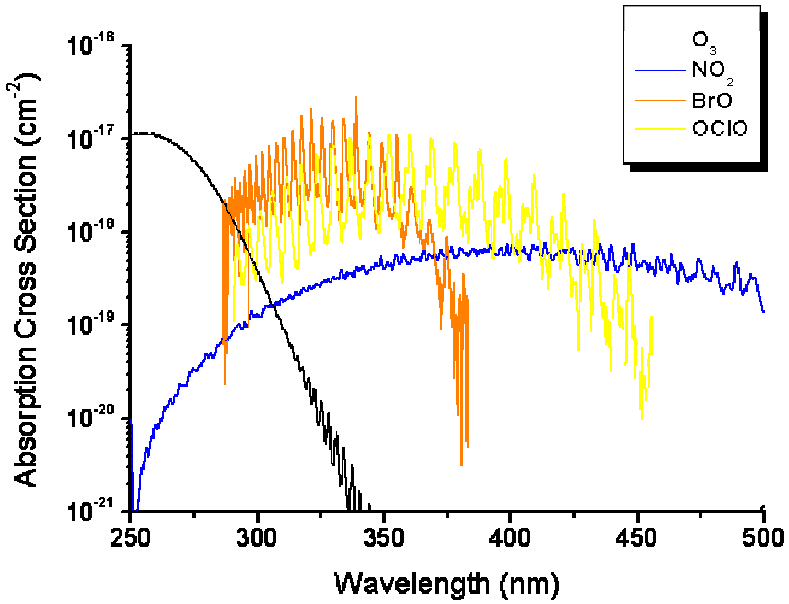

FIGURE 1.3: Absorption Spectra of ozone, nitrogen dioxide, bromine monoxide and chlorine dioxide in the wavelength range from 250 to 500 nm.

Besides from calculation, the absorption cross section is usually determined experimentally via the Lambert-Beer law: For an absorber with concentration c and absorption cross section σ_a, the intensity at the wavelength λ decreases exponentially with the length L of the traversed light path:

$$I(\lambda) = I_0(\lambda) \cdot exp\ (-\ L\ c\ \sigma_a\ (\lambda)) \qquad (1.4)$$

The exponent in Eq. (1.4) is called **optical density** D, and the product of c and σ is called absorption coefficient ε_a:

$$D = \ln\left(\frac{I_0(\lambda)}{I(\lambda)}\right) = Lc\sigma_a(\lambda) = L\varepsilon_a(\lambda) \qquad (1.5)$$

For a given concentration the cross section can be determined by measuring the attenuation of the light intensity. Vice versa, for known cross section, inversion of the measured quantities I_0 and I yields the concentration of the absorber, a method widely used in absorption spectroscopy.

1.2.2 Scattering

Besides inducing transitions between stationary states, electromagnetic radiation may cause the dipoles of molecules to oscillate, which in turn reemit radiation with a change in phase and direction. Contrary to the absorption of photons, which is only possible for discrete energy quanta, this scattering is a continuum process. In the Earth's atmosphere, scattering of sunlight is caused by molecules, aerosol and cloud particles. Since scattering is accompanied by a change in direction, the initial light intensity gets attenuated. Analogous to eq. (1.4), the Lambert Beer law can be written, replacing σ_a with the **scattering cross section** σ_s.
Depending on the size of the scattering particle compared to the wavelength of the incident light, different scattering processes are treated. For particles, which are small compared to the wavelength of the incident light ($R << \lambda$), a single dipole is excited to reemit radiation. This **Rayleigh scattering** (or molecule

scattering) occurs for air molecules (mostly N_2 and O_2) and small aerosol particles. The Rayleigh scattering cross section can be calculated by:

$$\sigma_s = \frac{8\pi^3 (n_{a,\lambda}^2 - 1)^2}{3\lambda^4 N_{a,0}^2} f(\delta_*)$$

where $n_{a,\lambda}$ is the refraction index of air, $N_{a,0}$ the number concentration of air molecules at standard temperature and pressure, and $f(\delta_*)$ the anisotropic correction term, which varies from 1.08 at λ=200 nm to 1.047 at λ=1 μm. σ_s is inversely proportional to the fourth power of wavelength, thereby causing the blue light of the air during daytime and the red sunset. Since the air density is increasing exponentially towards low altitudes, so does the extinction coefficient ε_R for Rayleigh scattering.
Apart from the elastic Rayleigh scattering, the photon may also be scattered in an inelastic process, meaning that a part of the photons energy may be used for a change of the rotational or vibrational state of the molecule. Consequently, the scattered radiation shows a shift in wavelength. This **Raman scattering** is approx. three orders of magnitude less intensive than elastic Rayleigh scattering.
For molecules present in vibrationally or rotationally excited states, it is also possible that a part of the internal energy is transferred to the scattering process and the emitted photon is of higher energy (shorter wavelength) than the incident one. The scattering leading to lower energy photons is termed Stokes, while the one to higher frequency photons is termed Anti-Stokes. Raman scattering by air molecules is the most probable explanation for the Ring Effect (see section 3.1.3).

If the scattering particle has a diameter approximately equal to or larger than the wavelength of the incident radiation, several dipoles may reemit electromagnetic waves, which then have the possibility of interference, making this **Mie Scattering** a process that can only be described by complex mathematics [*Mie, 1908; Bohren and Hufmann, 1998*]. For visible light, Mie scattering occurs for medium and large aerosol particles (λ > 0.1 μm), cloud droplets, ice particles, fog drops and haze. The Mie scattering cross section is only slightly wavelength dependent ($\sigma_s \sim \lambda^{-1..3}$), for larger particles also independent: $\sigma_s \sim \lambda^0$, which is the reason why clouds are white. While the probability for Rayleigh scattering is the same in forward and backward direction, most of the Mie scattering processes leave the direction of the incident radiation almost unchanged, meaning that the intensity is largest in forward direction.

1.2.3 Atmospheric Radiative Transfer

Any photon not absorbed or scattered in the Earths atmosphere reaches the surface, which partially absorbs the downwelling radiation. The remaining part is reflected back into the atmosphere, depending on the **albedo** (= ratio of the fluxes of reflected and incident radiation), which is a function of wavelength and the type of the surface (land, water, vegetation).
Thus, the intensity for all wavelengths remains conserved : $I = I_t + I_a + I_r + I_s$
However, scattering and reflection may also cause **polarisation** of the radiation.
For the Earth's atmosphere, two sources of electromagnetic radiation are important: The Sun and the Earth, which can be regarded as black bodies with temperatures of 5780 and 255 K respectively, see Fig. 1.4a. These sources of spectral radiances, together with the various possibilities for electromagnetic radiation of interacting with molecules and particles, and the altitude dependent abundance of trace gases leads to the attenuation of the downwelling and upwelling radiation as function of altitude, see Fig. 1.4 b and c.
Due to the strong absorption features of H_2O in the infrared, it is evident that clouds, which also cause multiple scattering, have an important effect on the radiation transport, especially in the lower troposphere.

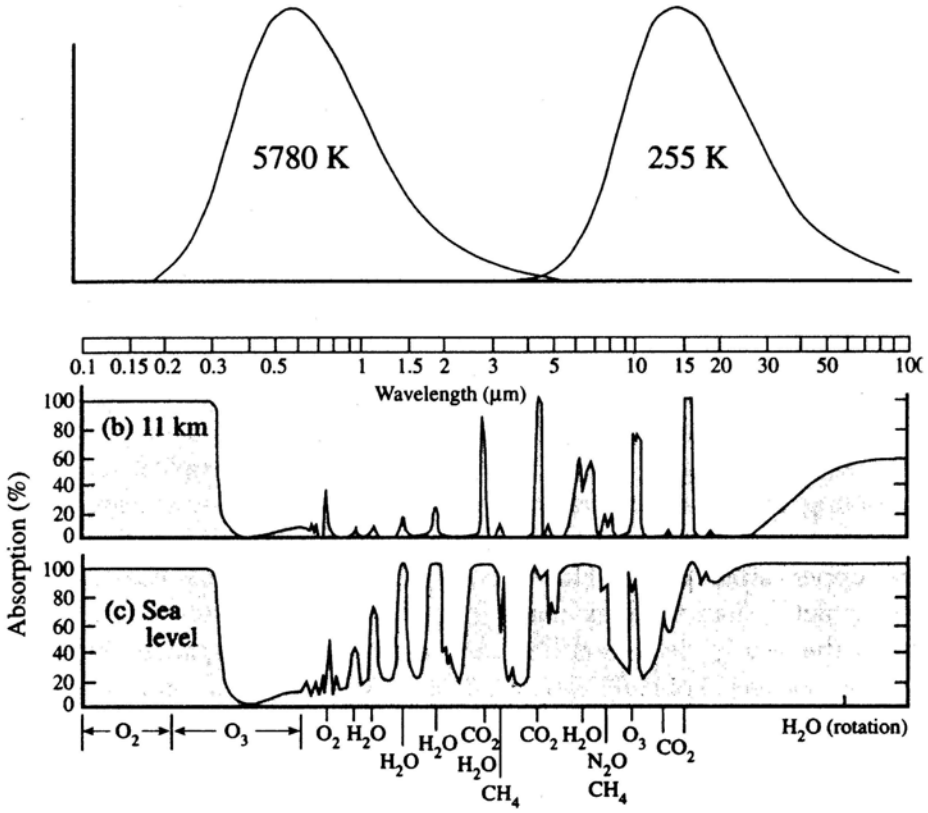

FIGURE 1.4: a) Planck radiation of black bodies with temperatures corresponding to the surface of the sun and earth and the absorption of their radiation in the atmosphere: b) at 11 km and c) at sea level, taken from [*Goody and Yung, 1999*].

Figs 1.4 b and c also show that there exist wavelength regions for which there occurs almost no absorption of the incident sunlight, so called **optical windows** (for example at 4 and 8 μm and around 10 to 12 μm). Therefore, these wavelength regions can be utilized for measurements by absorption spectroscopy. Also, the effect of an increase in trace gas concentrations on the radiative equilibrium is very pronounced in these windows. The figures also demonstrate the effect of ozone as a shield against UV radiation: For wavelengths smaller than 315 nm the intensity is drastically reduced (compare with Fig. 1.3), so that practically no UV-B radiation reaches altitudes below 20 km.

An important quantity in atmospheric radiative transfer is the **actinic flux**, which is the spectral radiance integrated over all angles around a sphere:

$$F_\lambda = \int_{\Omega_a} I_\lambda d\Omega_a = \int_0^{2\pi}\int_0^{\pi} I_\lambda \sin\theta d\theta d\phi$$

The Actinic flux in the wavelength region from 150 to 400 nm, based on calculations from radiative transfer simulations, is shown in Fig. 1.5, which also reveals very nicely the strong impact of the ozone layer on the height dependent spectral radiance.

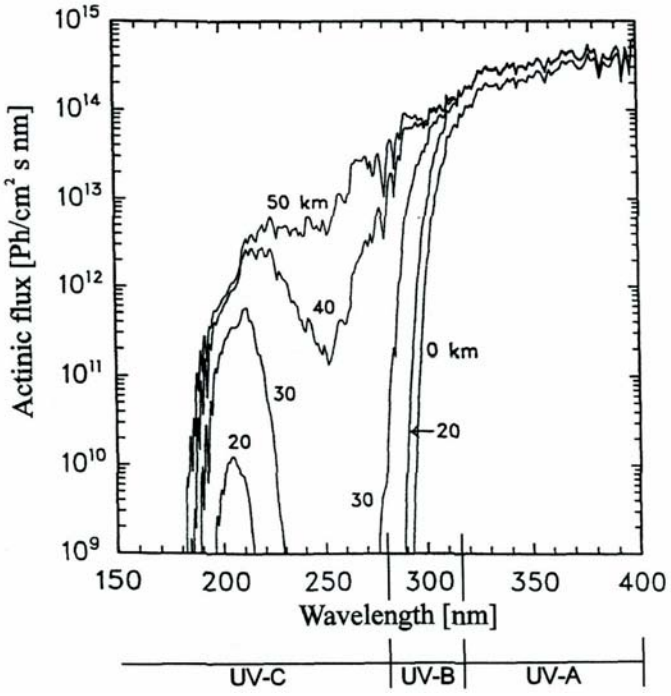

FIGURE 1.5: Actinic flux as a function of altitude, adapted from [*Sanders, 1997*].

As comparison, radiances from the space borne spectrometer SCIAMACHY, measured at different viewing angles in limb geometry, are shown in Figure 1.6. The difference in the lapse of the curves arises from the different nature of the presented quantity: While the actinic flux is integrated over all angles, the measured limb spectra result from scattering in direction of the spectrometer only (see also different units at the y-axis). Fig. 1.6 also reveals the prominent Fraunhofer lines arising from the absorption by elements in the photo-sphere of the sun (for example the Ca-II line at 393 and 397 nm), see also section 3.1.

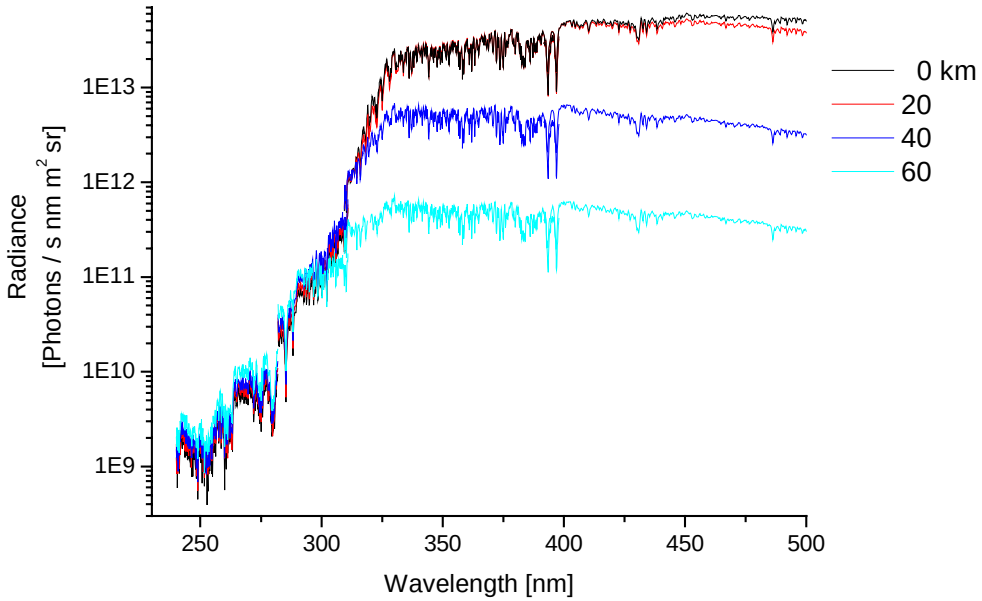

FIGURE 1.6: SCIAMACHY Limb radiances at different viewing angles, corresponding approximately to the altitudes stated.

1.3 Atmospheric Ozone Chemistry (homogeneous)

Ozone is a trace gas of utterly importance for atmospheric chemistry and life on Earth. In the troposphere, photolysis of ozone by UV-B radiation leads to formation of excited oxygen atoms and in turn to the production of the hydroxyl radical:

$$O_3 + h\nu \rightarrow O_2 + O(^1D) \qquad (\lambda < 310\ nm)$$
$$O(^1D) + H_2O \rightarrow 2\ OH \qquad (R\ 1.1)$$

Due to its high reactivity, OH is the primary oxidizing agent and determines the lifetime of almost all trace gases. It thereby also reduces the concentrations of hazardous species like CH_4, NO_2, CH_3Cl.
In the stratosphere, absorption of sunlight by the Hartley band (see Fig 1.3) protects the biosphere from UV-B radiation, which is harmful for all life forms (see section 2.4). By this absorption of the Sun's energy, radiative heating takes place, which determines the thermal structure of the stratosphere.

1.3.1 The Chapman cycle

The first theory regarding stratospheric ozone was developed by *Chapman* [1930] and based on the photochemistry of oxygen:

$$O_2 + h\nu \rightarrow 2\ O \qquad (\lambda < 242\ nm) \qquad (R\ 1.2)$$
$$O + O_2 + M \rightarrow O_3 + M \qquad (R\ 1.3)$$
$$O_3 + h\nu \rightarrow O_2 + O \qquad (\lambda < 1180\ nm) \qquad (R\ 1.4)$$
$$O_3 + O \rightarrow 2\ O_2 \qquad (R\ 1.5)$$

The formation of ozone takes place by reaction of molecular oxygen with oxygen atoms (R 1.3). The main source for odd oxygen ($O_x = O + O_3$) is the photolysis of O_2 (R 1.2), which requires radiation with wavelengths below 240 nm, whose intensity is reduced for altitudes below 40 km (see Fig. 1.5). On the other hand, the concentration of molecular oxygen decreases with altitude due to the lower pressure. Both factors together result in the maximum production rate of ozone at altitudes between 35 and 50 km (see also Figure 1.9).
The Chapman cycle is able to describe the vertical position of the maximum ozone concentration, but laboratory studies of the rate of reaction (R 1.5) performed in the 1960s yielded very low values, leading to steady state concentrations of ozone much higher than actually measured in the atmosphere [*Benson et al., 1965*]. Thus, other atmospheric constituents with an important effect on the ozone budget have to exist in the atmosphere. Since there are no substances occurring in such large abundances that the observed discrepancy can be explained by simple removal reactions, these constituents must be trace gases which deplete ozone in catalytic cycles.

1.3.2 Catalytic ozone destruction by trace gases

Already in the year 1950 (years before the experiment of *Benson et al.* [1965]), *Bates and Nicolet [1950]* postulated an influence of the HO_x cycle on the ozone budget. *Crutzen [1970]* described a similar catalytic cycle for the nitrogen oxides, *Stolarski and Cicerone [1974]* for atomic chlorine and *Wofsy et al. [1975]* for bromine. Generally, these tracegas-induced ozone destruction reactions can be described by the same catalytic scheme:

$$X + O_3 \rightarrow XO + O_2 \qquad \text{where } X = HO, NO, Cl, Br$$
$$XO + O \rightarrow X + O_2$$
$$\text{netto}: O_3 + O \rightarrow 2\ O_2$$

The effect of the different catalytic species strongly varies with altitude, see Fig. 1.7a. Including the NO_x, HO_x, ClO_x and BrO_x cycle in model simulations leads to a good agreement of the calculated vertical ozone profile with observations, see Fig. 1.7b.

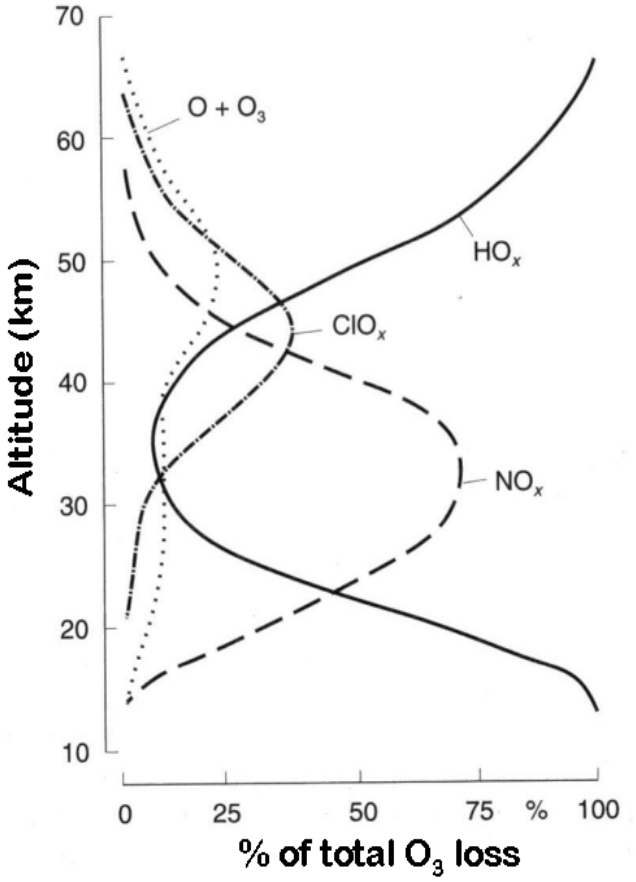

FIGURE 1.7a: Contribution of the different catalytic cycles to the overall chemical ozone depletion, latitudinal and seasonal averaged [*Bliefert, 2002*].

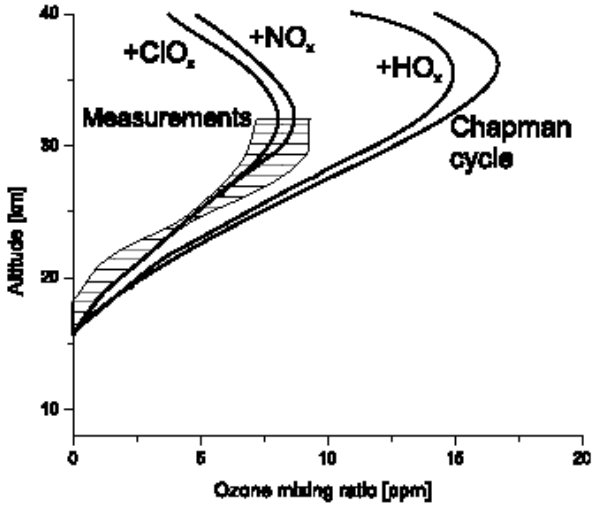

FIGURE 1.7b: Calculated ozone mixing ratios as function of altitude for the Chapman cycle, and including in turn the HO_x, NO_x and ClO_x cycle, in comparison to measured values [*Röth, 1994*].

1.3.3 Null cycles, holding cycles and reservoir compounds

The NO_x, HO_x, ClO_x and BrO_x cycle would destroy all ozone much faster than it is re-supplied by (R 1.3). Thus, besides the ozone depleting cycles, there must exist also other reactions of the catalytic agents that have either no effect on ozone (e.g. by forming atomic oxygen), so called **null cycles**, or that (temporarily) reduce their abundance (**holding cycles**). For example, instead of reacting with atomic oxygen, the nitrogen dioxide formed by reaction of NO and O_3 may also be photolysed:

$$NO_2 + hv \rightarrow NO + O \qquad (R\ 1.6)$$

The oxygen atom may then react via (R 1.3) to form ozone, leaving this cycle without effect on the abundance of ozone. Also, reactions take place, which lead to the formation of **reservoir gases** that are inert regarding ozone and have a much longer lifetime than the active species.

For example, NO_2 may react with the nitrate radical to form the reservoir dinitrogen pentoxide:

$$NO_2 + NO_3 \rightarrow N_2O_5$$

Furthermore, the different catalytic species may also react amongst one another, thereby reducing their ozone depletion capability. For example, the reaction between OH and NO_2 may form the reservoir nitric acid:

$$OH + NO_2 + M \rightarrow HNO_3 + M$$
$$HNO_3 + h\nu \rightarrow OH + NO_2$$

which can be photolysed back to the educts only with a slow rate, thereby constituting an effective holding cycle for NO and OH.
Similarly, reaction of chlorine monoxide with nitrogen dioxide forms chlorine nitrate, an important reservoir gas for chlorine and nitrogen, which also has a long lifetime:

$$ClO + NO_2 + M \rightarrow ClONO_2 + M \qquad (R\ 1.7)$$
$$ClONO_2 + h\nu \rightarrow ClO + NO_2$$

The main reservoir of chlorine, hydrogen chloride, which constitutes about 70-95 % of the total chlorine loading, is formed by the reaction:

$$Cl + CH_4 \rightarrow HCl + CH_3 \qquad (R\ 1.8)$$

Due to the dependence of the governing reactions on temperature, pressure and intensity of solar light, the partitioning of chlorine is a function of altitude, see Fig. 1.8.

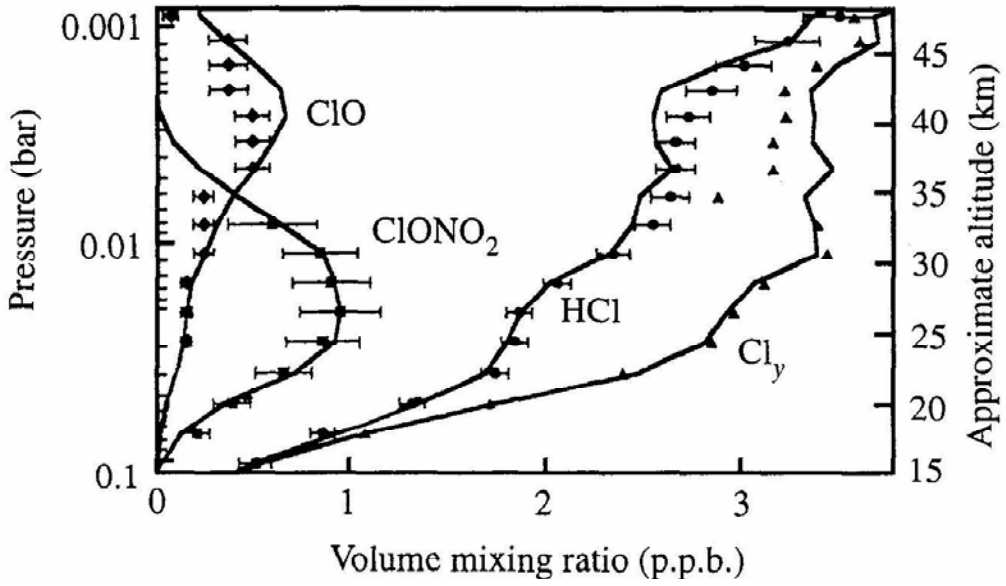

FIGURE 1.8: Partitioning of chlorine species as a function of altitude, measured by shuttle borne instruments [*Michelsen et al., 1996*].

Between the ozone destroying catalytic agents and their reservoirs, an equilibrium is acquired, which results in the natural ozone concentration that the biosphere is accustomed to. Any change in the partitioning of the active species and its reservoirs can lead to drastic results for the ozone layer, see section 1.5.

1.4 Influence of Atmospheric circulation on the ozone layer

The Chapman cycle and the catalytic depletion cycles lead to a lifetime for ozone of ≈ 2 days at an altitude of 40 km and of ≈ 3 years at an altitude of 15 km [*Wayne, 2002*]. Therefore, the global distribution of ozone abundance is not solely determined by (photo-)chemical reactions but also by transport processes. Figures 1.9 and 1.10 show the ozone production rate and the total ozone column. Due to the intensity of the solar radiation, the highest O_3 production is found at the equator at altitudes around 40 km. However, the regions with largest ozone columns appear close to the polar regions, in particular at times when there is no sunlight.

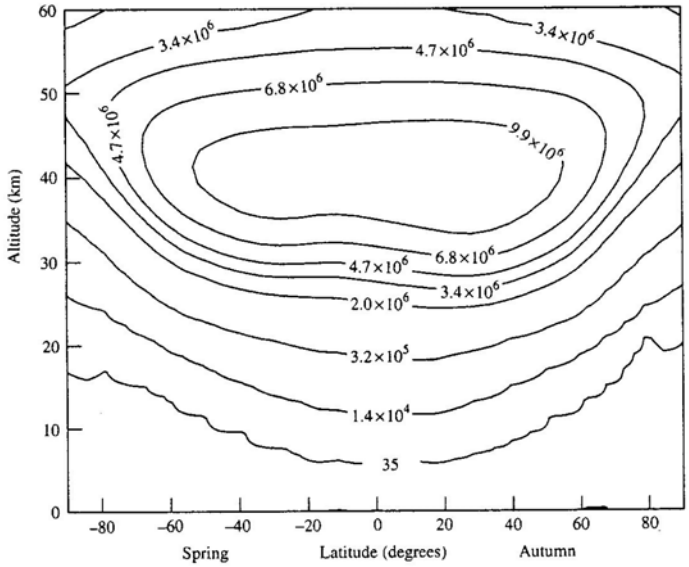

FIGURE 1.9: Vertical profile of the zonally averaged rate of ozone formation from the photolysis of O_2 in units of molecule cm^{-3} s^{-1}, adapted from [*Wayne, 2002*].

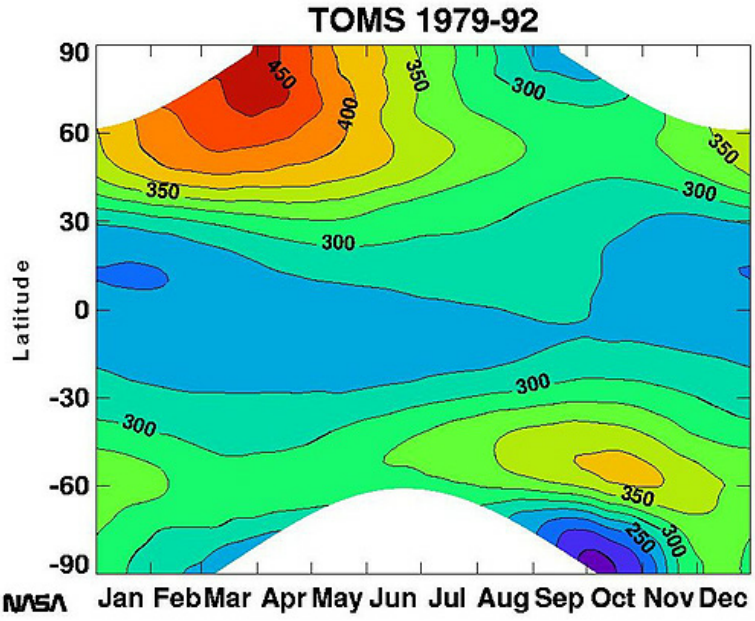

FIGURE 1.10: Annual cycle of the zonally averaged ozone distribution, as measured by TOMS. Provided by *http://toms.gsfc.nasa.gov.*

This demonstrates, that effective transport of ozone rich air from the equatorial regions to high latitudes takes place. From this latitudinal gradient of ozone, *Dobson* [1930] inferred large scale circulation cells, a theory which was later confirmed by observations of hydrogen by *Brewer* [1949]. This **Brewer-Dobson circulation** provides the mechanism for large scale transport in the troposphere and stratosphere, see Figs. 1.11 and Fig. 1.12.

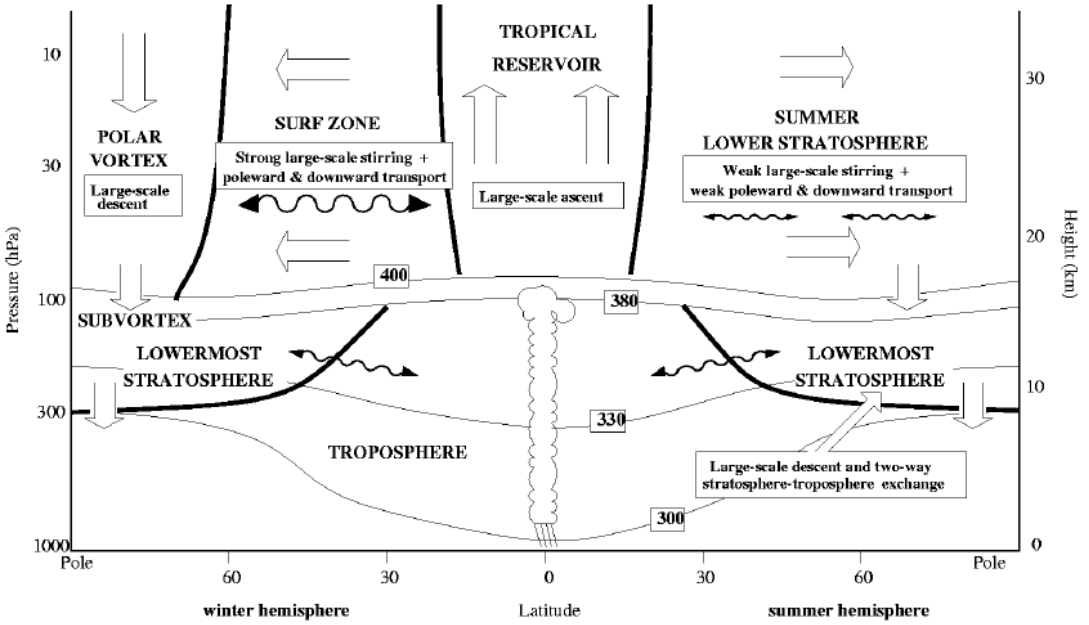

FIGURE 1.11: Scheme of the global transport processes in vertical and horizontal direction and troposphere-stratosphere exchange through the tropopause. Adapted from [*WMO, 1999*].

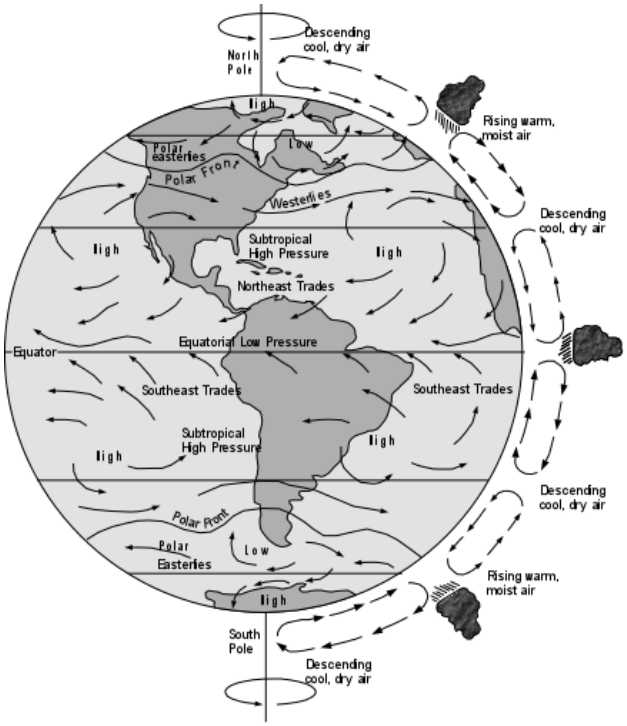

FIGURE 1.12: Global circulation for the three-cell circulation model of a rotating earth, adapted from [*Murck et al., 1998*].

1.5 Perturbations of stratospheric ozone by human activities

The catalytic agents of the ozone depletion cycles sketched in section 1.3 have natural sources, but are also anthropogenically emitted, either directly or as products of photo-chemical reactions. Therefore, the possibility arises that the equilibrium between ozone, the catalysts and their reservoirs (see section 1.3.3) is disturbed by anthropogenic emissions.

Johnston [1971] indicated that the injection of large quantities of NO_x into the stratosphere by exhaust of supersonic stratospheric transport (SST) may increase depletion of ozone due to the NO_x cycle. However, the effect on ozone is strongly dependent on the altitude where the additional NO_x is emitted: For low altitudes, an increase in NO_x leads to reduction of ozone loss by the ClO_x cycle, because active chlorine is faster removed to $ClONO_2$ (R 1.7). Although the fleet of 500 SSTs, anticipated at that time, has not been built, the flight altitude of commercial subsonic aircrafts has since moved up to the lower stratosphere. Thus, aircraft emissions may increase the depletion of ozone due to the NO_x cycle and the net effect of aircraft NO_x emissions on the ozone layer depends much on the future flight altitudes.

The largest anthropogenic change concerning ozone depleting substances was brought about with the production of CFCs: In 1945, the global average chlorine level in the atmosphere was about 1 ppb, of which about 25 % was man made; by 1995 the total chlorine loading had increased to 3.5 ppb, 85 % of which was of anthropogenic origin [*Russell et al., 1996; Seinfeld and Pandis, 1998*]. CFCs are used as propellants, solvents and cooling elements in refrigeration. The most abundant are $CFCl_3$, CF_2Cl_2, CH_3CCl_3 and CCl_4. CFCs are chemically inert, insoluble, non flammable and thus have long lifetimes, see table 1B.

Compound	**Mixing ratio (ppt)**	**Lifetime (yr)**	**Sources**	**Sinks**
$CFCl_3$	262	50 ± 5	Anthropogenic	Strat.: hν
CF_2Cl_2	535	102	Anthropogenic	Strat.: hν
$CF_2ClCFCl_2$	82	85	Anthropogenic	Strat.: hν
CCl_4	99	42	Anthropogenic	Strat.: hν
CH_3CCl_3	46	5.4 ± 0.6	Anthropogenic	Trop.: OH
CH_3Cl	536	1.5	Natural: Ocean	Trop.: OH
CF_2HCl	142	13.3	Anthropogenic	Trop.: OH

Table 1B: Mixing ratio (at surface in the year 2000), lifetime, sources and sinks of halogen-containing compounds [*Seinfeld and Pandis, 1998; WMO, 2003*].

Molina and Rowland [1974] pointed out, that the photolysis of CFCs may be a significant source of atomic chlorine in the upper stratosphere. Due to their insolubility and inertness they are not removed by dry or wet deposition in the troposphere. Thus, practically all CFCs produced reach into the stratosphere, where they are dissociated by short wave UV radiation:

$$CFCl_3 + h\nu \rightarrow Cl + CFCl_2 \qquad (\lambda < 250\ nm)$$
$$CF_2Cl_2 + h\nu \rightarrow Cl + CF_2Cl \qquad (\lambda < 230\ nm)$$

The free chlorine radicals then destroy ozone in a catalytic cycle like those sketched in section 1.3.2:

$$Cl + O_3 \rightarrow ClO + O_2 \qquad (R\ 1.9)$$
$$ClO + O \rightarrow Cl + O_2 \qquad (R\ 1.10)$$
$$\text{netto: } O_3 + O \rightarrow 2\ O_2$$

For this ClO_x cycle, a sufficient concentration of atomic oxygen is required, see reaction (R 1.10) (photolysis of ClO would induce a null cycle like (R 1.6) for NO_2).The only significant sources of atomic oxygen in the stratosphere are the photolysis of either molecular oxygen (R 1.2) or ozone (R 1.4). Both processes require radiation of wavelengths below 240 nm and 310 nm respectively and therefore are important only at altitudes above 40 km (compare Fig. 1.5). Thus, the ClO_x-cycle can efficiently destroy ozone only in the upper stratosphere.
On the other hand, the major part of the ozone column is situated at altitudes between 15 and 25 km. Also, the additional chlorine does not remain as active chlorine, but is quickly bound in the reservoir compounds by reactions (R 1.7) and (R 1.8). Therefore, the increase in stratospheric chlorine concentrations due to emissions of CFCs was expected to have only a small effect on the total ozone column. An increase of the UV radiation in the lower stratosphere would even enhance ozone production there, resulting in a net reduction of the total ozone column of around 1-2% [*WMO, 1982; Brasseur and Solomon 1984*].

1.5.1 The Ozone Hole

However, since the mid 80s a dramatic decline in the total ozone column has been observed above the south pole every austral spring [*Chubachi 1984, Farman et al., 1985*]: Ground based measurements at Halley Bay (75 °S / 26 °W) in October dropped from 300 DU in 1970 to 200 DU in 1984 and below 150 in the 1990s, see Figure 1.13 a. Satellite measurements confirmed the dramatic ozone loss and revealed that the spatial extent of the anomalously low ozone columns (below 220 DU) exceeded the area of the Antarctic continent [*Stolarski, 1986*], see Figure 1.13 b.

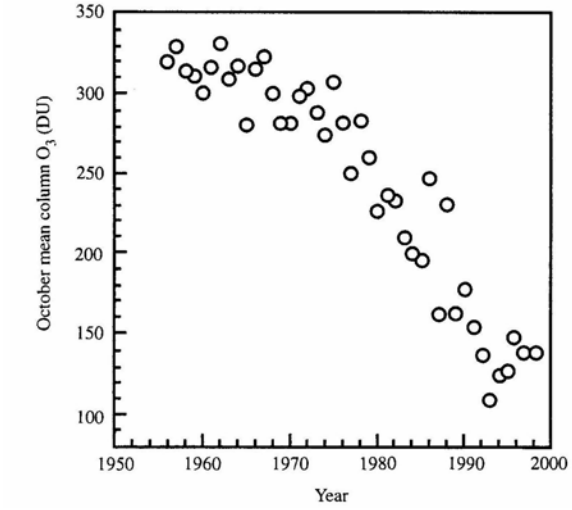

FIGURE 1.13 a:
Decline in mean October ozone levels over Halley Bay during the period 1957-1998, adapted from [*Wayne 2000*].

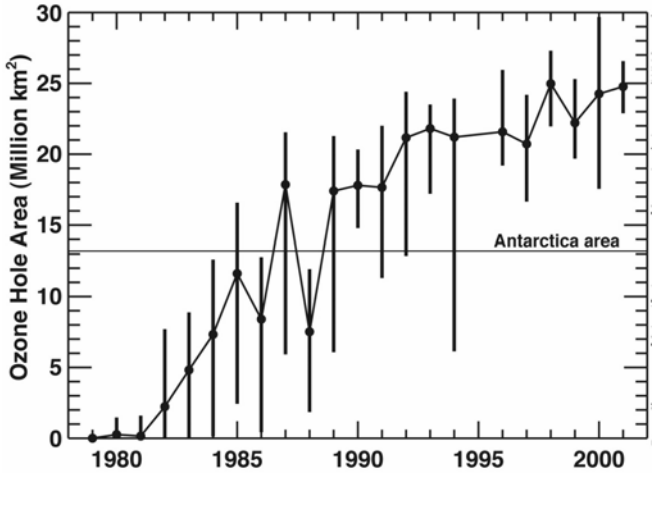

FIGURE 1.13 b:
Area of total ozone values below 220 DU between 7 September and 13 October (points: average of daily values; vertical lines: range of values) from 1979 to 2001 based on TOMS satellite data, adapted from [WMO 2003].

Since the loss of the total ozone column is more than 50 %, it must occur at the bulk of the ozone layer. Vertical profiles obtained from balloon measurements (see Fig. 1.14a) confirmed, that the depletion of ozone is largest between 10 and 20 km altitude.

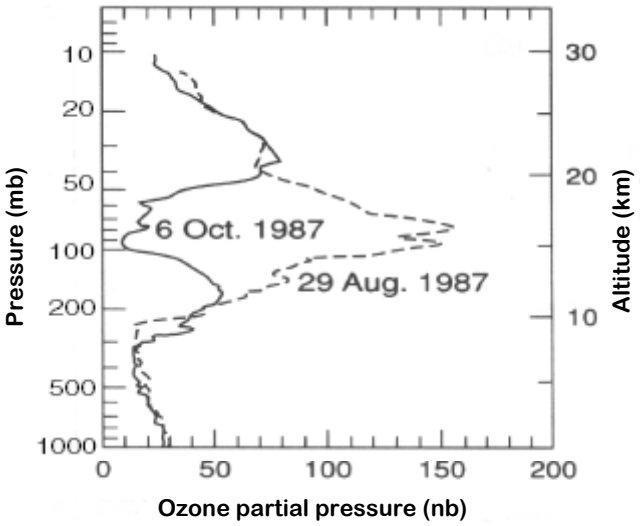

FIGURE 1.14 a:
Balloon measurements of the ozone partial pressure as function of the altitude before and after the formation of the polar vortex above the Antarctic (77° S) [*Hofmann et al., 1989*].

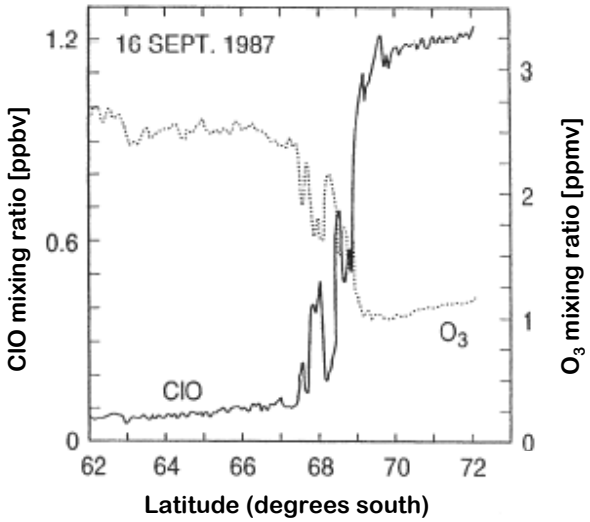

FIGURE 1.14 b:
Aircraft measurements of the mixing ratios of O_3 and ClO above the Antarctic at an altitude of approx. 18 km [*Anderson et al., 1989*].

It was soon assumed that the ozone loss is related to the increase of the chlorine loading [*Farman et al., 1985*]. This assumption was supported by measurements of large abundances of chlorine monoxide [*de Zafra et al., 1987, 1989*] and chlorine dioxide (OClO) [*Solomon et al., 1987a*], implying that active chlorine causes the ozone depletion.
However, this explanation is in contradiction to the observations that the ozone depletion took place at an altitude where no atomic oxygen is available, which would be necessary for the ClO_x cycle. Finally, airborne measurements revealed that the mixing ratio of chlorine monoxide (ClO) is anti-correlated to the mixing ratio of ozone (see Fig. 1.14b), which strongly supports that the ozone depletion is taking place by chlorine radical catalysis. Thus, in the polar stratosphere one or more chlorine catalyzed ozone destruction cycles other than the ClO_x cycle have to exist, which can proceed without participation of atomic oxygen.

2 Stratospheric Ozone Loss

The state of atmospheric science around 1985, sketched in sections 1.4 to 1.6, was unable to explain the massive depletion of ozone occurring in the Antarctic stratosphere during spring since the late 1970s. This meant that the understanding of at least the polar stratospheric ozone chemistry was by far incomplete and, due to the importance of the ozone layer for all living organisms, gave rise to an intensive research program on the causes and mechanisms.
Observations revealed that before the massive ozone destruction, nearly all of the chlorine is converted to active chlorine. Because of the coupling of nitrogen and chlorine species in the formation of reservoirs, such an increase in active chlorine needs to be accompanied by very low levels of nitrogen oxides, which were indeed also observed.
Two prerequisites for the drastic ozone loss observed in the lower polar stratosphere are therefore mechanisms that significantly reduce the concentrations of nitrogen dioxide and convert the chlorine reservoirs to ozone destroying species. Furthermore, a catalytic cycle needed to be found that is based on active chlorine species and could destroy ozone in the lower stratosphere, i.e. without the participation of atomic oxygen. Since the ozone depletion occurred in the spring- and wintertime polar stratosphere, it was reasonable to assume that these mechanisms had to depend on the meteorological conditions occurring solely in this region during that season.
The study of stratospheric ozone loss has been topic of intensive research for the last two to three decades. This chapter gives a short overview of the most important findings and puts an emphasize on those topics that are most relevant for this thesis:

- Sections 2.1 to 2.3 sketch the findings made by field campaigns, model simulations and laboratory experiments that explained the mechanisms for the development of the ozone hole within two years after its discovery.

- Besides from the polar ozone loss, a negative ozone trend of 3-6 % per decade is observed at mid latitudes. Possible explanations for this trend include transport of ozone poor air from the polar regions, heterogeneous reactions in the upper troposphere/lower stratosphere region or further, still unknown mechanisms (section 2.4).

- Section 2.5 reviews the implications for the atmosphere and biosphere that are associated with polar and global ozone depletion.

- Although the production of CFCs has been stopped and the global atmospheric chlorine loading is declining, the further fate of the ozone layer is uncertain, due to complicated interactions with stratospheric temperature trends and greenhouse gas abundances. Section 2.6 gives an overview of the topical findings regarding the future development of the ozone layer.

2.1 Heterogeneous Chemistry

As mentioned in section 1.1, the atmosphere contains not only gaseous components, but also liquid and solid particles (soot, sea-salt, water droplets and ice crystals) like e.g. the sulfate aerosols in the Junge layer. Thus, besides homogeneous reactions between gas phase species, also heterogeneous chemistry takes place. In addition, the solid or liquid particles may promote reactions between gas phase partners by surface catalysis. Heterogeneous reactions in the atmosphere were known to exist, but their importance for atmospheric chemistry was largely underestimated before the detection of the ozone hole. *Cadle et al.* [1975] investigated the importance of various heterogeneous reactions for the stratosphere by model simulations and came to the conclusion, that the hydrolysis of dinitrogen pentoxide, proceeding with water molecules dissolved in H_2SO_4 aerosols,

$$N_2O_5\ (g) + H_2O\ (s,l) \rightarrow 2\ HNO_3 \quad (g=gaseous,\ l=liquid,\ s=solid) \qquad (R\ 2.1)$$

might have a significant impact on the nitrogen partitioning, especially in the lower stratosphere.
However, it was recognized only ten years later [*Evans, 1985*] that (R 2.1) is the reason for the so called **Noxon-Cliff**, the abrupt decline of NO_2 observed in the high latitude winter stratosphere [*Noxon, 1973*]: While N_2O_5 has a photolysis rate of $5*10^{-5}$ s^{-1} and a lifetime of few days, the photolysis rate of HNO_3 is much lower ($3*10^{-6}$ s^{-1}), leading to a lifetime of few weeks. Thus, in the presence of stratospheric aerosols, up to 50 % of NO_x may be stored in HNO_3, thereby efficiently changing the NO_y to NO_x partitioning and extensively reducing the NO_2 concentration: At aerosol concentrations typical to the Junge layer at 24 km, the NO_2/HNO_3 ratio is a factor of five lower compared to gas phase chemistry only [*Webster et al., 1994*]. With an earlier insight into this relation, and including reaction (R 2.1) in model calculations, the ozone hole might have been predicted before it was observed [*Solomon, 1999*].
In particular, the importance of the low nitrogen oxide abundance for the partitioning of chlorine in the wintertime polar stratosphere was not recognized. Still a few months before the report of the severe springtime ozone depletion above the Antarctic, *Molina et al.* [1985] implied from laboratory measurements, that the heterogeneous reaction between HCl and $ClONO_2$, which was later shown to be central for the development of the ozone hole (see section 2.2.2), would be of no significance for the stratosphere. *Rowland et al.* [1986] found that the rate for hydrolysis of $ClONO_2$ is significantly increased on laboratory surfaces. They concluded that this reaction (and other heterogeneous reactions involving chlorine species) may also be promoted by stratospheric aerosols and therefore could explain the anomalous ozone loss in the Antarctic stratosphere, an assumption that was later confirmed by model studies [*Solomon et al., 1986*] and following laboratory studies of heterogeneous reactions on ice crystals [*Molina et al., 1986*].
Nowadays, it is clear, that the massive ozone destruction in the polar stratosphere can only be explained by heterogeneous processing of chlorine species on liquid and solid particles, which - as a consequence of the increased chlorine loading due to production of CFCs - act as catalysts for ozone depletion. Moreover, also the negative ozone trend in mid latitudes (see section 2.3) can only be reproduced by model calculations when including heterogeneous reaction schemes.
Fig. 2.1 shows the **uptake coefficient** of the most important heterogeneous reactions for the stratosphere as a function of temperature. The uptake coefficient γ is the ratio of molecules lost to a surface to the number of gas-surface collisions that occur and thus proportional to the heterogeneous reaction rate. Fig. 2.1 reveals that the rate for reaction (R 2.1) is not depending on temperature, while the heterogeneous hydrolysis of $BrONO_2$ is gradually enhanced towards lower temperatures. In contrast, the rate for heterogeneous processing of chlorine reservoirs rapidly increases for temperatures that occur in the wintertime polar stratosphere: Between 210 and 190 K, the uptake coefficient for the reaction between HCl and $ClONO_2$ rises by five orders of magnitude.

In the following section it is reviewed that this temperature dependence is the crucial factor why the ozone hole appeared above the south pole, the region most far away from the sources of CFCs.

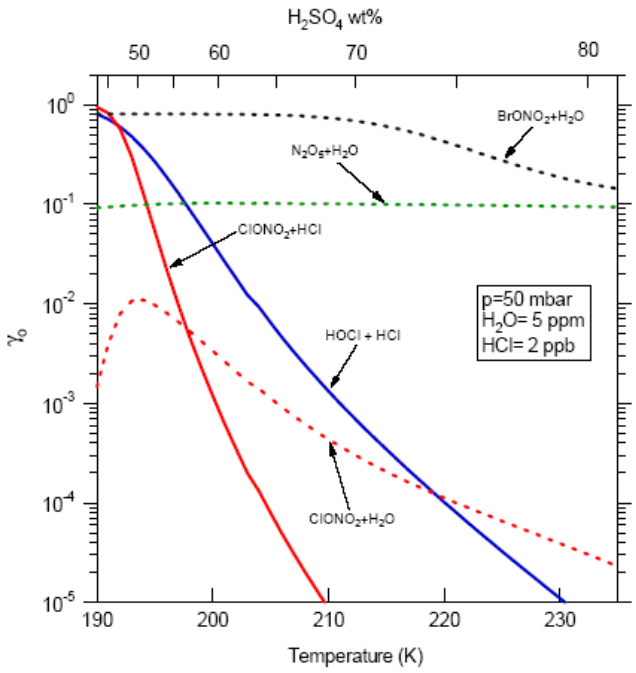

FIGURE 2.1: Uptake coefficients as a function of temperature for key stratospheric heterogeneous reactions on sulfuric acid aerosols. Adapted from *Sander et al.* [2000].

2.2 Meteorology and Chemistry of the Polar Stratosphere

2.2.1 The Polar Vortex

The lack of solar illumination during the polar night leads to extreme radiative cooling of the atmosphere, starting at the air masses near ground. Due to the lower temperatures, the air density increases and the consequent volume loss is compensated by a descent of air masses from higher altitudes. The resulting low pressure system in the wintertime polar stratosphere is in turn replenished by a stream of air from lower latitudes (compare Fig. 1.11). This stream is deflected by the coriolis force (which is particularly strong at polar latitudes), leading to a stable vortex above the winter pole (compare Fig. 1.12).
Since the Antarctic continent is concentrically located around the geographic south pole, minimum stratospheric temperatures are located close to the center of the polar vortex, which itself is centered above the south-pole. For the Arctic, the distribution of land and water is much more inhomogeneous, and the polar vortex is deformed and asymmetric (often placed over northern Scandinavia). Moreover, the Arctic stratosphere is frequently disturbed by planetary wave activity, which also have their origin in the variable topography.
Thus, long-lasting cold stratospheric temperatures occur regularly inside the stable polar vortex above the Antarctic, while for the Arctic, the intensity, size, shape and lifetime of the polar vortex vary significantly during one winter and from year to year [*Pawson et al., 1995; Labitzke, 1999*], see also Fig. 2.2.
The difference in the strength, extension, stability and duration of the vortex is the main cause for the much more intensive ozone depletion above the southern pole compared to its northern counterpart: Strong gradients in the **potential vorticity** at the edge of the polar vortex act as a dynamical barrier and inhibit mixing of polar and midlatitude air. Therefore the polar vortex can be regarded as an isolated air mass whose composition is virtually independent of the one outside. Any change in the partitioning of ozone destroying catalytic agents and their reservoir compounds that might occur during the polar night will not be compensated by air flow from outside, and thus may accumulate and persist until the vortex breaks up in polar spring. In fact, such a change in the partitioning of chlorine species takes place inside

the vortex and is promoted by the cold temperatures occurring in the wintertime polar stratosphere, as will be described in the next section.

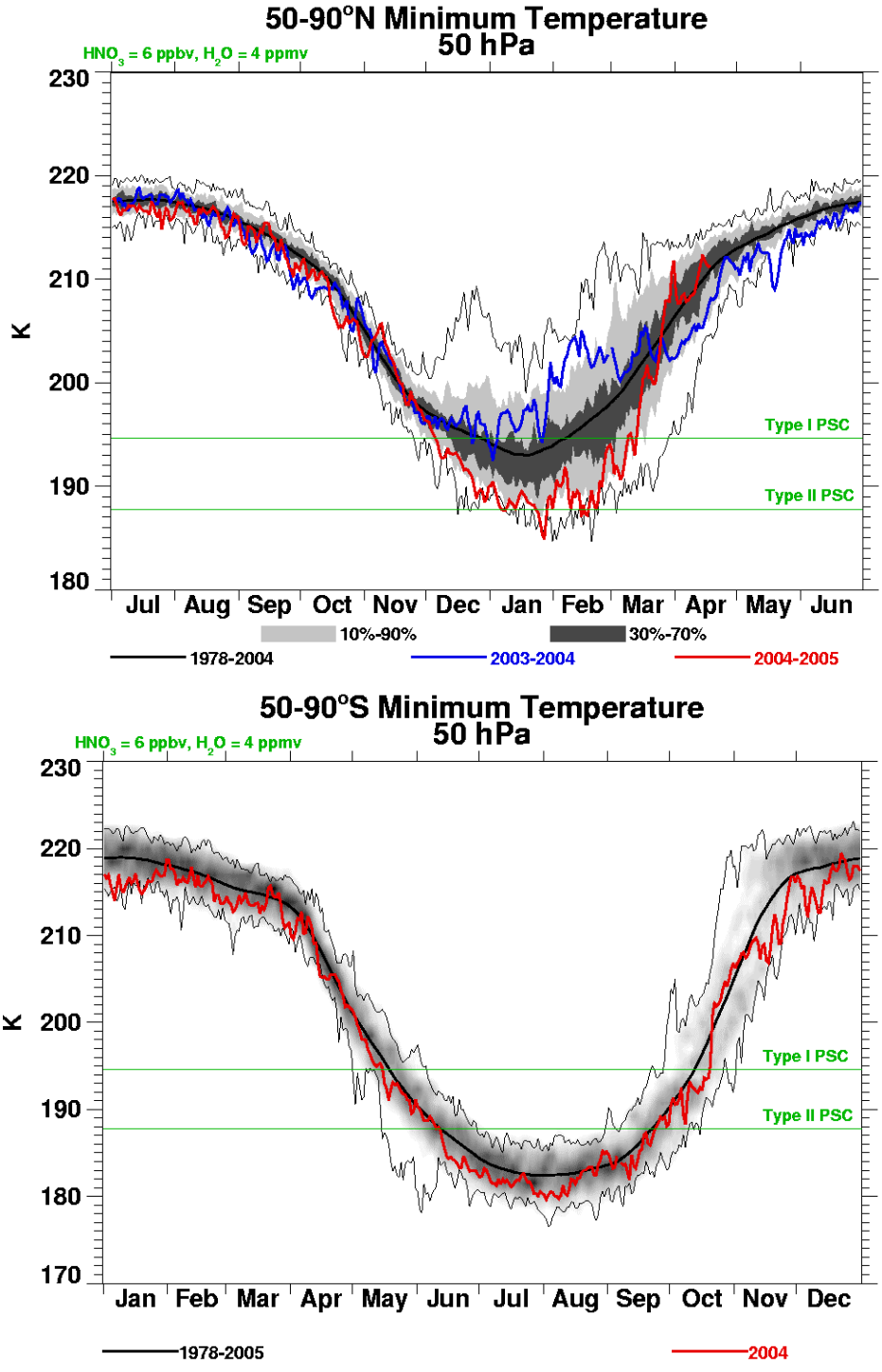

FIGURE 2.2: Time series of minimum polar temperatures at 50 hPa (approx. 19 km height). The black line shows the mean value during the years 1978 – 2005, the shading the density of observations, and the red line the values of 2004/05 for the northern (top panel), and of 2004 for the southern hemisphere (bottom panel). Also shown are the threshold temperatures for the formation of polar stratospheric clouds (see section 2.2.2). Figures provided by: http://hyperion.gsfc.nasa.gov/Data_services/met/ann_data.html.

2.2.2 Polar Stratospheric Clouds

When temperatures inside the polar vortex drop below a certain height dependent threshold (see Fig. 2.3), condensation of mixtures of nitric acid and water leads to the formation of Polar Stratospheric Clouds (PSCs). By satellite measurements [*McCormick et al., 1982; Poole and McCormick, 1988*] two types of PSCs were identified, forming respectively above (type 1) and below (type 2) the ice frost point temperature (T_{ice}). While type 2 PSCs are composed of water ice crystals, type 1 PSCs were suggested to be composed of nitric acid trihydrate (NAT) [*Toon et al., 1986*; *Crutzen and Arnold, 1986*], which was shown to be stable at stratospheric conditions [*Hanson and Mauersberger, 1988*].

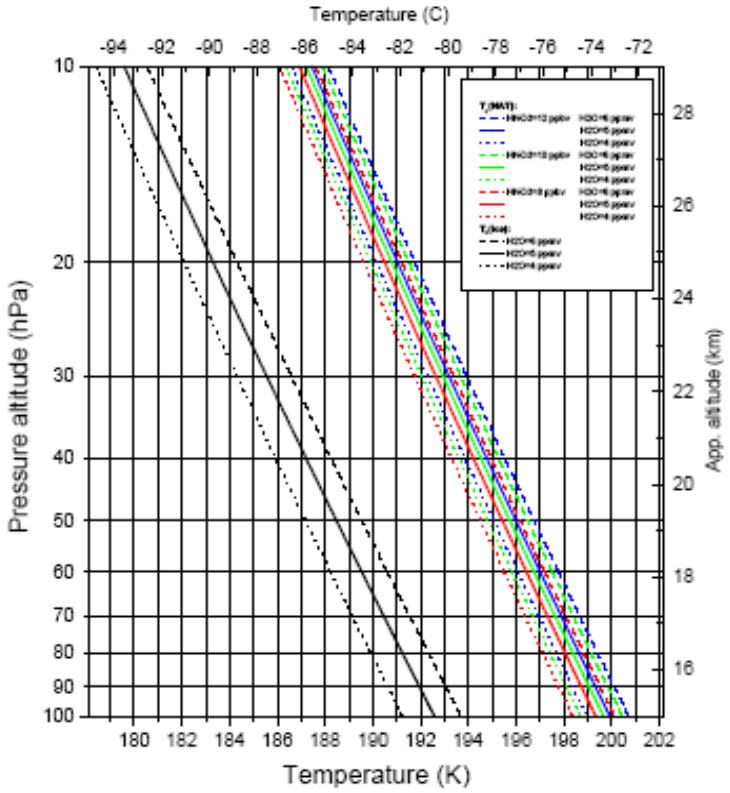

FIGURE 2.3: Condensation temperatures of NAT (T_{NAT}) and ice (T_{ICE}) plotted as function of pressure altitude for different HNO_3 and H_2O gas phase mixing ratios. Dotted, solid and dashed curves correspond to H_2O = 4, 5 and 6 ppmv. Red, green and blue curves to HNO_3 = 8, 10 and 12 ppbv. The right hand ordinate gives the approximate geometric altitude. Adapted from [*Larsen*, *2000*].

From lidar measurements the type 1 PSCs were later subdivided into lidar depolarizing (solid) type 1a and non-depolarizing (liquid) type 1b PSCs. Observations, laboratory experiments and model studies are consistent with the assumption that type 1b are supercooled ternary solutions (STS) of HNO_3, H_2SO_4 and H_2O [*Tabazadeh et al., 1994; Carslaw et al., 1994*]. The type 1a are supposed to be NAT particles, and PSCs consisting of NAT were in fact measured in situ in the Arctic stratosphere [*Schreiner et al., 1999; Voigt et al., 2000, 2003*]. But there are also findings contradicting this assumption [*Toon and Tolbert, 1995*; *Koop et al., 1997; Pagan et al., 2004*] and the composition of type 1a PSCs, and the question how these particles form is still a topic of research [*Tolbert and Toon, 2001; WMO, 2003*].
On the PSC particles, heterogeneous reactions take place through which chlorine is converted from the reservoir species HCl and $ClONO_2$ into compounds that can rapidly destroy ozone (so called active chlorine: Cl, ClO, HOCl) [*Solomon et al., 1986; Toon and Turco, 1991; Solomon et al., 1999*].

The most important **chlorine activation** reactions on the surfaces of PSCs are:

$$ClONO_2 + HCl \rightarrow Cl_2 + HNO_3 \quad (R\ 2.2)$$
$$ClONO_2 + H_2O \rightarrow HOCl + HNO_3 \quad (R\ 2.3)$$
$$HOCl + HCl \rightarrow Cl_2 + H_2O \quad (R\ 2.4)$$

During the polar winter, these reactions cause a dramatic build up of Cl_2 and HOCl. With the return of sunlight in polar spring, both species are rapidly photolysed:

$$Cl_2 + h\nu \rightarrow 2\ Cl \quad (R\ 2.5)$$
$$HOCl + h\nu \rightarrow Cl + OH \quad (R\ 2.6)$$

By reaction of the atomic chlorine with ozone (R 1.9), ClO is formed, which then takes part in the ClO dimer or ClO-BrO ozone depletion cycle, see section 2.3.
The growth of PSC-particles and their potential to activate chlorine species increases with lower temperatures [*Ravishankara and Hanson, 1996; Borrmann et al., 1997; Peter, 1997*], see also Fig. 2.4. In addition, the various types of PSCs form at different threshold temperatures and have heterogeneous reaction rates, which differ by orders of magnitude. However, for a given temperature history during a polar winter, the level of chlorine activation is mostly insensitive to assumptions about the PSC composition [*Drdla, 2003*].

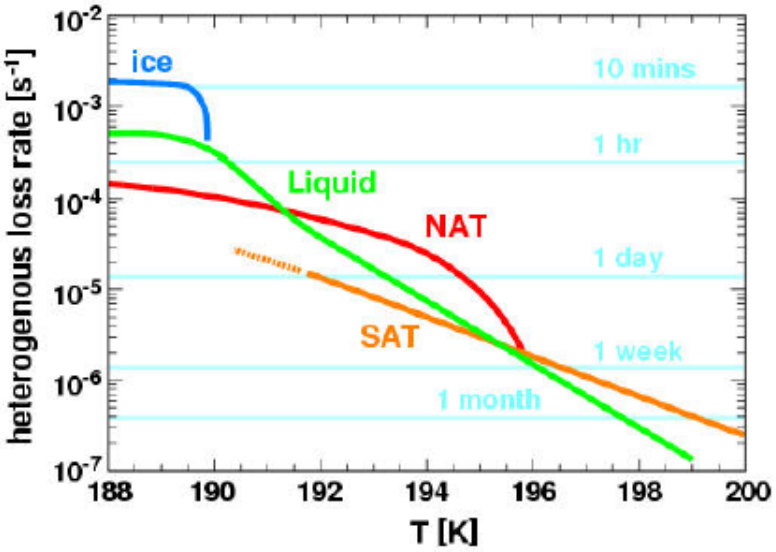

FIGURE 2.4: Rate of the reaction $ClONO_2 + HCl \rightarrow Cl_2 + HNO_3$ for different PSC particles as function of temperature for 50 hPa and 1 ppb HCl. The horizontal lines indicate the lifetime of the reaction partners. Adapted from [*Carslaw et al.*, *1999*].

Figure 2.5 summarizes the change in the partitioning of the chlorine species that is brought about by the formation of PSCs: The CFCs entering the stratosphere are dissociated by short-wave solar radiation, producing chlorine radicals which, after destroying a few ozone molecules in the ClO_x cycle, are bound in the reservoir compounds HCl and $ClONO_2$. In the polar winter, both chlorine reservoirs are heterogeneously processed to active chlorine on the surface of PSCs. With the photolysis of HOCl, Cl_2 (and also $ClONO_2$) chlorine radicals are produced, that effectively destroy ozone in the ClO dimer and ClO-BrO cycle. The reaction of ClO with BrO also leads to the formation of OClO, which therefore is used as an indicator for stratospheric chlorine activation, see chapter 4.

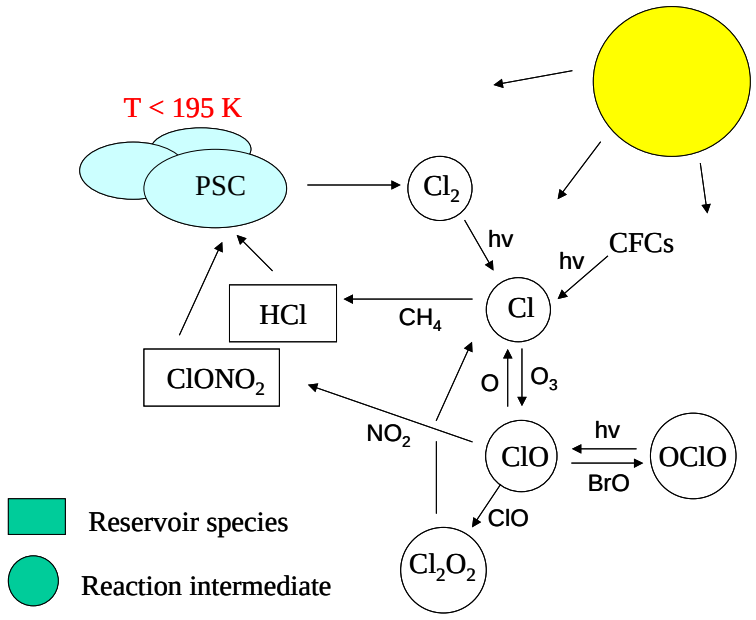

FIGURE 2.5: Scheme of the stratospheric chlorine chemistry during polar winter.

PSCs also maintain the medium for the heterogeneous removal of nitrogen from the gaseous phase: First, the nitric acid formed by (R 2.2) or (R 2.3) remains in the PSC particles in the solid phase. Furthermore, PSCs also catalyse the depletion of the nitrogen reservoir N_2O_5, either by hydrolysis (R 2.1) or by reaction with HCl:

$$N_2O_5 + HCl \rightarrow ClNO_2 + HNO_3 \qquad (R\ 2.7)$$

These processes change the partitioning of nitrogen from the nitrogen oxides (NO_x = NO + NO_2) and its reservoir N_2O_5 towards the long living reservoir HNO_3 and are therefore termed **denoxification**. Since the abundance of NO_2 is decisive for the deactivation of ClO by reaction (R 1.7), the net removal of NO_2 from the polar stratosphere leads to drastically increasing concentrations of ClO inside the polar vortex.
Furthermore, the "raining out" of the HNO_3 by sedimentation of PSC particles leads to permanent removal of nitrogen from the lower stratosphere that can only be replenished by mixing with air masses from outside the polar vortex. This **denitrification** prolongs the time for the conversion of the active chlorine into the reservoir chlorine nitrate, and thus substantially enhances ozone depletion in polar spring [*Waibel et al., 1999; Tabazadeh et al., 2000*].
Due to the more stable and persistent vortex, denitrification in the southern polar vortex is much stronger than in its northern counterpart, and also the area of the vortex where denitrification occurs is larger in the southern hemisphere. However, also temperatures in the southern spring remain low enough to cause low NO_x abundances already by denoxification. Thus, regarding the springtime loss of ozone in the southern hemisphere, the effect of denitrification is not essential [*Portmann et al., 1996*]. On the other hand, the degree of denitrification can be determining for ozone loss in the Arctic stratosphere [*Chipperfield and Pyle, 1998*].
Also, since stratospheric temperatures in the Arctic winters are often near the threshold for PSC-formation, adiabatic cooling due to stratospheric **mountain waves**, which can shift the temperatures by up to ΔT = 10 K, promotes the formation of PSCs [*Deshler et al., 1994; Voigt et al., 2000*]. Therefore, mesoscale PSCs induced by mountain wave activity not only lead to activation of chlorine and enhanced ozone depletion [*Carslaw et al., 1998, 1999*], but also can cause substantial denitrification [*Flentje et al., 2002; Mann et al., 2005*].

2.2.3 Polar Stratospheric Ozone loss

With the PSCs being identified as the medium by which extensive chlorine activation and denoxification occurs, two of the necessary mechanisms to explain the drastic ozone destruction in the polar stratosphere were found. However, still a catalytic ozone depletion cycle is needed that proceeds without atomic oxygen. Laboratory studies revealed that, for the cold temperatures existing in the spring/wintertime polar stratosphere, such cycles do exist.
Denoxification and denitrification leads to an increase of the ClO concentration by the factor of 100 [*Schoeberl et al., 1996*]. For such high ClO concentrations, and for temperatures as low as 195 K, the combination of two ClO molecules to the ClO dimer, chlorine peroxide (ClOOCl), is favorized. This molecule possesses a strong absorption cross section also in the near UV (λ > 300 nm) and can be photolysed to yield atomic chlorine [*Molina and Molina, 1987*]:

$ClO + ClO + M$	→	$Cl_2O_2 + M$	
$Cl_2O_2 + h\nu$	→	$ClOO + Cl$	($\lambda < 450$ nm)
$ClOO + M$	→	$Cl + O_2 + M$	
$2\,(Cl + O_3$	→	$ClO + O_2)$	
netto: $2\,O_3 + h\nu$	→	$3\,O_2$	

This ClO-Dimer cycle does not require atomic oxygen. While in earlier studies this cycle accounted for 70 to 80 % of the ozone depletion in Antarctic spring [*Brune et al., 1991; Solomon et al., 1999*], in current model calculations 40 to 50 % is due to this cycle [*Daniel et al., 1999; Lee et al., 2002; Millard et al., 2003*]. For the Arctic stratosphere, the ClO dimer cycle is less important: Due to the higher temperatures there, the rate constant for the ClO dimer formation is smaller. Consequently, total depletion of the ozone column is smaller and the role of the ClO-BrO-cycle [*Mc Elroy et al., 1986*] for stratospheric ozone loss is increased.

$ClO + BrO$	→	$ClOO + Br$
$ClOO + M$	→	$Cl + O_2 + M$
$Cl + O_3$	→	$ClO + O_2$
$Br + O_3$	→	$BrO + O_2$
netto: $2\,O_3$	→	$3\,O_2$

This cycle contributes around 40 % to the Antarctic springtime ozone depletion, and 40-60 % to the Arctic ozone loss, depending on the coldness of the respective winter [*Daniel et al., 1999;Lee et al., 2002*].
The ClO dimer cycle needs sunlight to proceed, and the ClO-BrO cycle is also most effective during daytime: In darkness, two other pathways of the reaction between BrO and ClO become important, which form the nighttime reservoirs BrCl and OClO (see also chapter 4).
Therefore, the depletion of ozone is most intensive when, after the return of sunlight to the poles in spring, large sunlit areas of the vortex match with high levels of chlorine activation. Due to the dependence of chlorine activation on the formation of PSCs, this is the case, when temperatures below T_{NAT} persist until late in spring and/or the time for deactivation of chlorine species is long. While in the Arctic, PSCs usually occur only one month longer after the end of polar night, in the Antarctic, formation of PSCs still happens three months after return of sunlight [*WMO, 2003; Drdla et al., 2003*]. This is the main reason why, although the levels of chlorine activation are comparable, much more chemical destruction of ozone takes place in the southern hemisphere.
Due to different meteorology and chemical processing during the winter, also the recovery of the chlorine reservoirs in late spring is different for the two hemispheres. Since the Antarctic spring time stratosphere contains much less gaseous nitrogen due to denoxification and denitrification, reformation of $ClONO_2$ by (R 1.7) takes place much slower. In addition, there is less ozone, which favors the recovery of HCl [*Groos*

et al., 1997]. For the Arctic stratosphere in late spring, the situation is different: Due to the earlier break up of the vortex, NO_2 rich air mixes with the chlorine activated air masses, causing a fast deactivation by the reaction of ClO with NO_2 to chlorine nitrate (R 1.7) [*Douglass et al., 1995*].
As mentioned in section 2.2.1, the Arctic stratosphere is frequently disturbed by planetary wave activity, causing the polar vortex to weaken and thereby initiating a major or final warming [*Labitzke, 1999*].
Figures 2.6 and 2.7 give an overview of the temporal evolution of stratospheric temperature, the occurrence of PSCs and the abundance of stratospheric ozone and related species for the southern hemisphere.

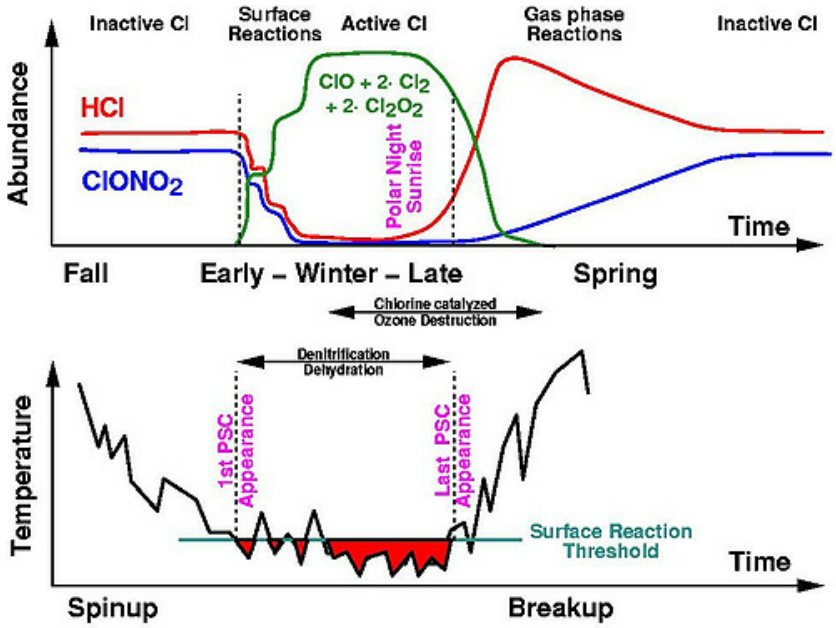

FIGURE 2.6: Scheme of the southern hemisphere polar stratospheric temperatures, PSC appearances and chlorine partitioning from fall to spring, adapted from [*Webster et al., 1993*].

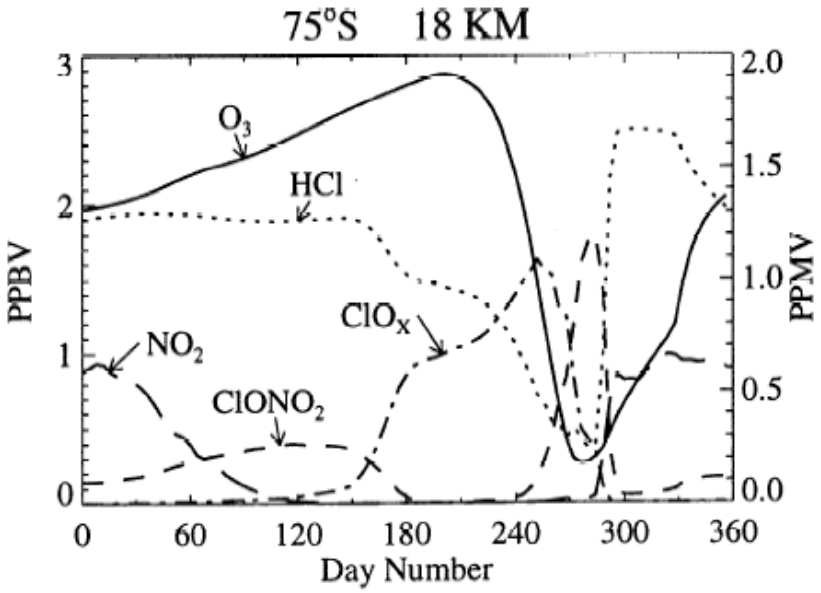

FIGURE 2.7: Annual cycle of ozone and related chlorine nitrogen species in the Antarctic lower stratosphere, adapted from [*Portmann et al.,1996*] .

2.3 Global Ozone Depletion

After the end of the polar night and the break up of the vortex, the ozone loss is replenished by mixing with ozone rich air masses from outside the vortex. In fact, ozone that was transported from lower latitudes by the Brewer Dobson circulation, has accumulated during the winter at the edge of the polar vortex (see also Fig. 1.10). However, this replenishment does not fully compensate the chemical destruction in spring, leading to a negative trend in the ozone abundances at high latitudes: The total ozone column decreases by 1.04 ± 0.39 % per year for the Arctic in March and by 2.51 ± 0.62 % per year for the Antarctic in October [*Bodeker et al., 2001; WMO, 2003*].
Besides from the ozone depletion in the polar regions, a negative trend in the total ozone column is observed also for mid latitudes [*Logan et al. 1999; Fioletov et al., 2002; Wang et al., 2002*], see Fig. 2.8. The total column ozone, averaged over the years 1997-2001, was 3 % lower for the northern and 6 % lower for the southern midlatitudes (35-60°) relative to average values before 1980 [*WMO, 2003*].
This ozone depletion at midlatitudes is probably a combination of many effects and results from transport of ozone poor air masses from the polar regions [*Millard et al., 2003*], heterogeneous reactions on background aerosols and cirrus clouds [*Solomon et al., 1996, 1997; Bormann et al., 1996*], bromine chemistry [*Salawitch et al., 2005*] or further unknown mechanisms.

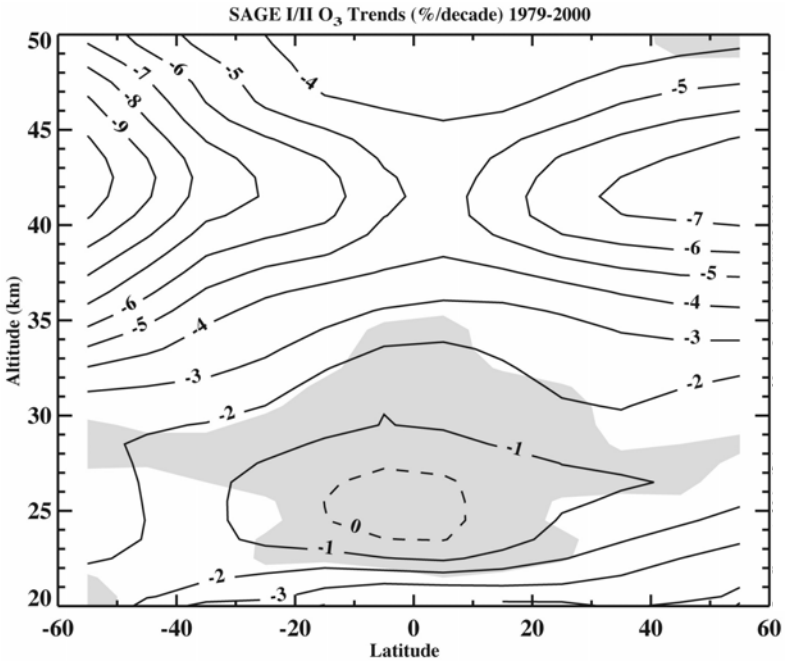

FIGURE 2.8: Meridional cross section of ozone profile trends derived from the combined SAGE I and SAGE II datasets. Trends were calculated in percent per decade, relative to the overall time average. Shading indicates that the trends are insignificant at the 2σ level, adapted from [*Wang et al., 2002*].

Fig 2.9 shows the trend of the total column as a function of latitude derived from measurements and from model calculations. It reveals that none of the eight models is able to reproduce the observed trends, especially the constant values near the equator. This possibly indicates that stratospheric ozone chemistry is still not fully understood and that other effects, which are not represented by the dynamic and chemistry schemes implemented in current model simulations, have an important impact on the ozone column.

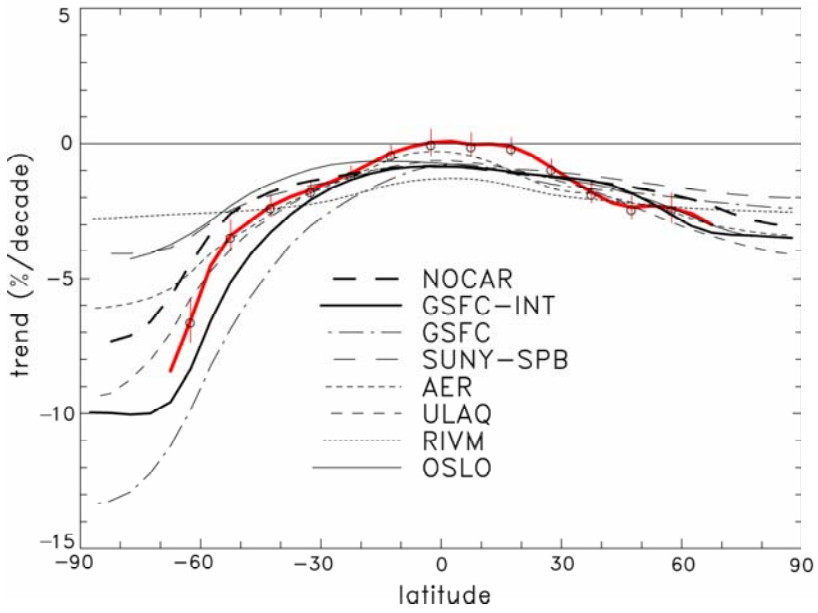

FIGURE 2.9: Latitudinal profile of annual mean column ozone trends from TOMS and SBUV2 dataset (red line) in comparison with results from eight 2-D models for 1980 - 2000, adapted from [*WMO, 2003*].

2.4 Consequences of ozone loss

The chemical depletion of stratospheric ozone has three major effects: First, it causes an increase in UV-B radiation at the surface, which is harmful for all life forms. Second, it changes the radiative equilibrium of the atmosphere, which mainly leads to a decrease of stratospheric temperatures and thereby also has consequences on stratospheric dynamics (see section 2.5). And third, a reduced ozone shield lets more higher energy photons reach the ground, thereby altering the photochemistry of the troposphere.

The effect of increasing UV-B radiation for the biosphere depends on the response of the organism as function of the wavelength, the **action spectrum**. While bacteria and viruses are instantaneously destroyed at high UV-B doses (a technique used in modern food industry), the short term effect for multi cell organisms is restricted to the regions where the radiation is absorbed. Therefore, damage due to increased UV-B radiation occurs in those parts of the body most exposed to sunlight like the skin or the eyes. However, UV-B radiation also has a substantial long term effect.

It is able to change the strands of the DNA by chemically linking neighbouring pyrimidine bases to form pyrimidine dimers. Transcription and replication of this change leads to damage of the DNA, thereby contributing to the formation of skin cancer. As a rule of thumb, for every 1 % decrease in stratospheric ozone, the amount of UV-B radiation reaching the ground increases by 2 %, raising the risk of skin cancer by around 4 % [*Van der Leun, 1998*]. In addition, increased UV-B exposure may be harmful to the immune system, possibly leading to a growth in infectious and other diseases [*de Gruijl et al., 2003*].

For plants, the growth is reduced for larger UV-B doses, possibly causing a decrease of harvest. Components that are very sensitive to increases in UV-B radiation are the parts functioning as centers for photosynthesis: The enzymes and proteins responsible for the electron transport chain are destroyed, thus reducing the efficiency of the conversion of the sun energy. In particular, micro organisms and algae which are important producers of oxygen, are vulnerable to UV-B radiation. Phytoplankton, which resides in the uppermost regions of the oceans, is the base of the marine food chain, and also an important sink for CO_2. Thus, a reduction of the amount of phytoplankton in the world's oceans due to increased UV-B doses may lead to an enhancement of the greenhouse effect.

Figure 2.10 shows the increase in UV-B radiation (erythemal UV) for different scenarios. Only due to the international agreements on the production stop for CFCs, the UV change could be pushed to below 5 % and will reach values of before the ozone hole in 2040.

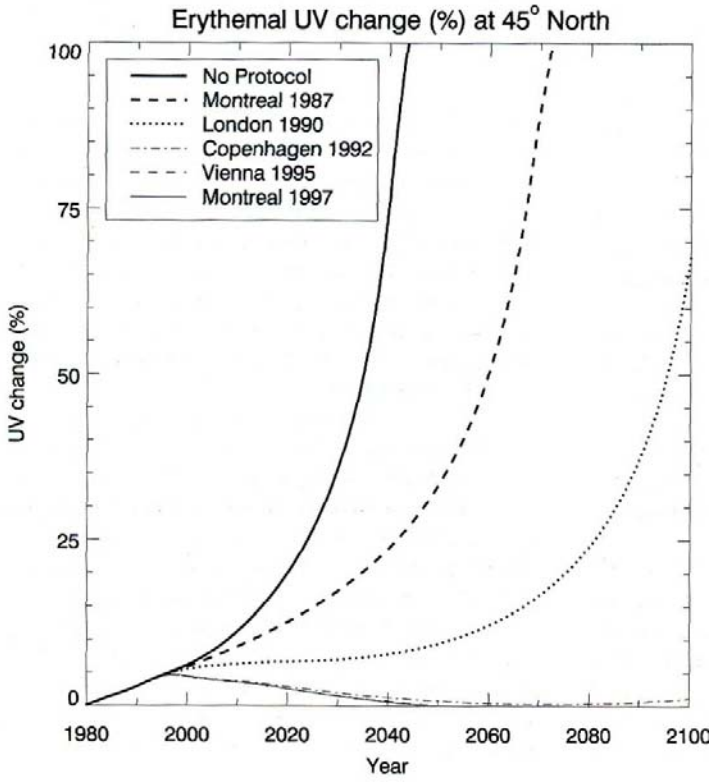

Figure 2.10: Estimated increase in surface erythemal UV radiation at 45° N for the amendments and adjustments of the Montreal Protocol, as well as a scenario with no international agreement on ozone-depleting substances, adapted from *Slaper et al. [1996]*.

Of major concern are also the effects of stratospheric ozone loss on radiative transport. As described in section 1.1, the thermal structure of the stratosphere is mainly determined by the UV absorption of ozone. Less ozone in the stratosphere leads to decrease in the absorption of solar UV and terrestrial infra red radiation at these altitudes (see Fig. 1.4). One consequence is the cooling of the stratosphere, which in turn increases the occurrence of PSCs and thereby further enhances ozone depletion in a positive feedback [*Rex et al., 2004*], see also section 2.5. Temperatures in the lower stratosphere reveal a trend of - 0.5 to -1 K per decade, which is partly caused by the depletion of ozone in the last two decades [*Hare et al., 2004; WMO, 2003*].

Another contribution to the observed trend of stratospheric temperatures arises from the anthropogenic greenhouse effect, which causes the troposphere to warm and the stratosphere to cool [*Santer et al., 2003; Fu et al., 2004*]. Vice versa, increased UV-B radiation enforces the warming of the troposphere, thereby further increasing the greenhouse effect.

A further consequence of increased UV-B radiation is enhancing the chemical activity in the troposphere [*Tang et al., 1998*].Model studies suggest that additional UV-B radiation reduces tropospheric ozone in clean environments (low NO_x) and increases tropospheric ozone in polluted areas (high NO_x) [*Van der Leun, 1998*]. Maybe the only positive expected effect of reduced stratospheric ozone is larger concentrations of OH due to more efficient photolysis of tropospheric O_3, which will result in a faster removal of pollutants.

2.5 Future of the ozone layer

As a consequence of the international agreements on the phasing out of production of CFCs, tropospheric concentrations of most CFCs have peaked and started to decline [*Montzka et al., 1996; Anderson et al., 2000*]. In the stratosphere, the chlorine loading is expected to reach values of before the ozone hole around 2050. Fig. 2.11 shows the expected decline of the stratospheric chlorine loading .

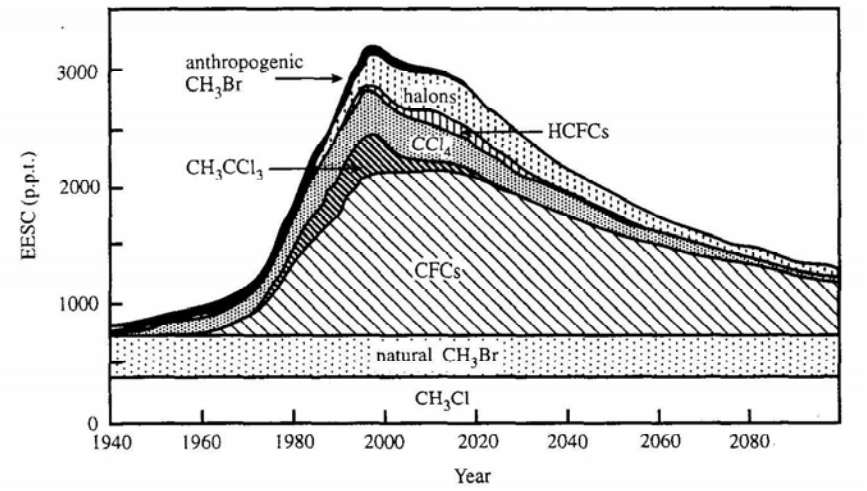

FIGURE 2.11: Contributions of different halogen containing substances to the Equivalent Effective Stratospheric Chlorine (EESC) based on a future emission control scenario incorporating the 1997 Montreal amendments, adapted from [*WMO, 1998*].

In turn, the ozone layer is expected to gradually recover and pre-1980 values are expected for 2040 in the southern, and around 2050 in the northern hemisphere [*Rosenfield et al., 2002; WMO, 2003*]. However, the prediction of future ozone levels and the time for recovery of the ozone layer is complicated by dynamical effects, especially in the northern hemisphere [*Austin et al., 2002*].
Also, other parameters have changed meanwhile that are expected to enhance ozone depletion and thus prolong the time for recovery: Stratospheric temperatures have fallen by around 0.5 K per decade since the 1950s, causing more PSCs to form and increasing the rate at which ozone is destroyed, see also Fig. 2.12.

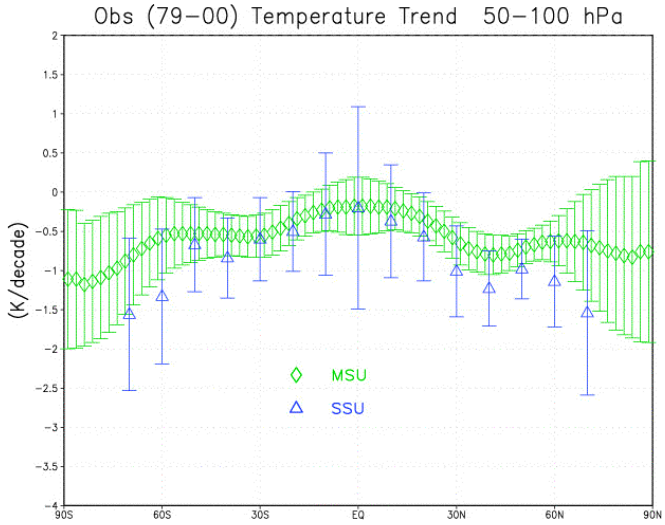

FIGURE 2.12: Zonal annual mean temperature trends in the 50-100 hPa region for 1979-2000, as derived from the MSU and SSU 15x satellite observations, taken from [*SPARC, 2000*].

The decrease of stratospheric temperatures is a result of twenty five years of stratospheric ozone depletion [*Rosier and Shine, 2000; Hare et al. 2004*] and, with growing evidence, also a consequence of the climate change due to the anthropogenic greenhouse effect. The increase of CO_2 is expected to delay the ozone recovery especially for the Arctic stratosphere, where maximum ozone losses are predicted to occur between 2010 and 2015 [*Austin et al., 1992; Shindell et al., 1998; WMO, 2003*].
Furthermore, water vapor concentrations in the atmosphere have significantly increased over the period 1964 to 2000 [*Oltmans et al., 2000; Rosenlof et al., 2001*] with a trend of 1% per year in the lower stratosphere [*WMO, 2003*]. While the causes for the increase in the stratosphere are still uncertain, it will lead to enhanced ozone reduction in the lower stratosphere by homogeneous chemistry, prolonging the time for ozone recovery by about 10 to 20 years. Furthermore it magnifies ozone destruction due to heterogeneous chemistry twofold: First, the probability for PSC formation increases for larger water vapor content (compare Fig. 2.3) and second, it causes radiative cooling, thereby again leading to formation of more PSCs.

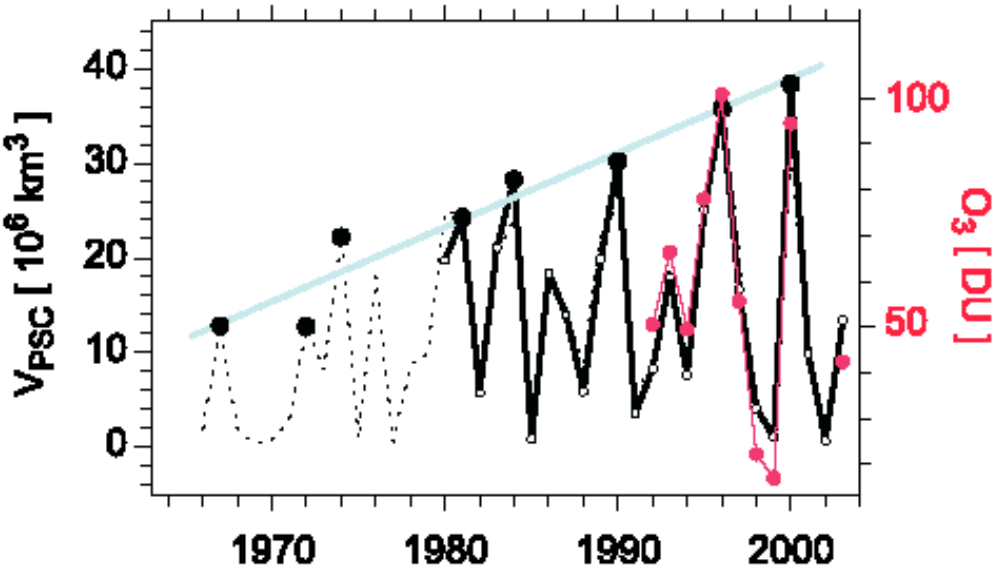

FIGURE 2.13: Evolution of V_{PSC} from 1966 to 2003 composed from ECMWF data (solid black line) and data from the FU-Berlin (dashed line), scaled to the chemical ozone loss from 1992 to 2003 (red line). Adapted from [*Rex et al., 2004*].

For the Arctic stratosphere, *Rex et al.* [2004] found an increase of the volume with possible PSC formation and the chemical ozone loss over the last 30 years, see Fig. 2.13. Since the formation of PSCs is determined by stratospheric temperatures, this is a strong evidence for the impact of climate change on the ozone layer. For the Antarctic, there is a tendency of the polar vortex to persist longer in spring: While it broke up in late November during the 1970 to 1980 period, it remained until early December in the last decade [*WMO, 2003*]. Probably a further indication for a change in global circulation patterns is the major warming, which occurred in the Antarctic stratosphere in September 2002. Per definition, a major warming does not occur above the south pole and accordingly was not observed before.
Concluding it can be said that, although the ozone layer is expected to recover to values of 1980 in the years 2040-2060, it is not at all sure that it will actually do so. The cooling of the stratosphere, enforced by the increasing abundances of green house gases, could lead to unexpected interactions like the occurrence of the ozone hole was itself. It will therefore be necessary to monitor ozone as well as the related compounds, and to improve our understanding of the complex relations regarding stratospheric ozone. It is evident that satellite observations are essential for this long-term monitoring of stratospheric chemistry on a global scale.

3 Retrieval: Methodology and Instruments

The fast exploration of the mechanisms responsible for the ozone hole was possible only by an intensive research program, which combined field measurements, model simulations and laboratory experiments. Besides in situ measurements by aircrafts, balloons and ozone sondes, remote sensing methods have largely contributed to increase the knowledge of atmospheric chemistry:
While the ozone hole was discovered by ground based measurements, satellite observations have revealed its spatial extension. As well, the dependence of PSCs on stratospheric meteorology and their different compositions were exposed by space borne infrared and ground based Lidar measurements. Finally, also the increase of active chlorine in the perturbed wintertime polar stratosphere and its relation to the ozone loss was discovered by ground based, aircraft and balloon remote sensing.
Nowadays, spectroscopic measurements are a well established method to derive abundances of trace gases in the troposphere up to the mesosphere in the ultraviolet, visible, infrared and microwave regions of the electromagnetic spectrum. One technique that is widely applied in the retrieval of trace gases abundances from atmospheric spectra is the DOAS method. It has proven to be especially valuable for the retrieval of reactive trace gases like the halogen oxides in the stratosphere and also in the troposphere.
GOME was the first spectrometer built to retrieve atmospheric trace gases by DOAS from space. It has not only successfully monitored global ozone for almost ten years now, but was the first satellite instrument to provide also global maps of weak absorbers like BrO and OClO. In addition, GOME could determine also abundances of trace gases like NO_2 and BrO in the troposphere.
SCIAMACHY, launched with ENVISAT in February 2002, is one of very few space borne instruments that performs the UV/VIS-spectroscopy from backscattered sunlight in nadir and also in limb geometry. With these measurements, concentration profiles of the considered absorbers can be retrieved by inversion of the column densities measured at different viewing angles.

This chapter describes the method applied for the retrieval, its caveats and necessary corrections, and the further computing of the measurements by combination with radiative transfer simulations and inversion techniques. As well, a description of the utilized space borne spectrometers is given, and the retrieval of the absorbers discussed in this thesis is described exemplarily:

- First, the DOAS method, its application in satellite measurements and the concept of air mass factor is reviewed.

- The different measurement geometries applied in satellite remote sensing are illustrated in section 3.2. One main part of this thesis, the inversion of the measured column densities in limb geometry to derive vertical concentration profiles, is described in detail in section 3.3.

- In sections 3.4 and 3.5, the instruments GOME and SCIAMACHY are introduced.

- At last, the OClO retrieval from GOME and SCIAMACHY nadir spectra and the retrieval of O_3, NO_2, BrO and OClO from SCIAMACHY limb spectra is described in detail (sections 3.6 to 3.9).

3.1 Differential Optical Absorption Spectroscopy (DOAS)

Like most absorption spectroscopy measurements, the DOAS method is based on the Lambert-Beer law (see section 1.2.1), which enables to determine the concentration of a single absorber in a gaseous or liquid probe. In the atmosphere however, the absorptions of several species add together and the light passing through a distance L is attenuated by the sum of the optical densities of all present absorbers relevant for the respective wavelength:

$$I_A(\lambda) = I_0(\lambda)\exp(-\int_0^L \sum_i \sigma_i c_i dl) \qquad (3.1)$$

Rayleigh and Mie-Scattering as well as absorption due to aerosols result in further reduction of the light intensity (see section 1.2.2):

$$I_{A,S}(\lambda) = I_A(\lambda)\exp(-\int_0^L (\varepsilon_R(\lambda) + \varepsilon_M(\lambda) + \sigma_A(\lambda)c_A)dl)$$

3.1.1 The principle of DOAS

The main idea of the DOAS method is to account for these difficulties by measuring the absorption over a spectrum instead at a single wavelength, and utilizing the characteristic ("narrow") absorption structures of the molecules by parting their optical densities from the broadband absorption and scattering. With a high pass filter each molecular absorption spectrum $\sigma(\lambda)$ is separated into a component that varies only slowly with wavelength ($\sigma_C(\lambda)$), and one that contains the characteristic high frequent structures ($\sigma'(\lambda)$, the **differential absorption spectrum**) [*Platt, 1994*], see also Fig. 3.1:

$$\sigma(\lambda) = \sigma_c(\lambda) + \sigma'(\lambda) \qquad (3.2)$$

Similarly, the extinction due to scattering processes and absorption by aerosol are only slowly varying with wavelength and therefore can also be described by a broadband polynomial. The degree of the polynomial depends on the wavelength range applied for the retrieval and also on the spectral resolution of the instrument. *Platt et al.* [1979] suggest a degree of five as typical value for the UV/VIS region.
DOAS measurements are performed either by using an artificial light source like e.g. a Xenon lamp (active DOAS), or natural light sources like the sun, moon or stars (passive DOAS). For the artificial light source, the intensity usually shows no or only broadband spectral structures. In that case, the polynomial describes all attenuation due to scattering and broadband absorption, and the knowledge of I_0 becomes obsolete for the determination of the trace gas absorptions, see Fig. 3.2.
For ground based or air borne atmospheric measurements using scattered sunlight, the intensity of the sunlight contains the high frequent structures arising from absorptions in the sun's photosphere, the **Fraunhofer lines**, which were first analyzed in detail by J. Fraunhofer (1787-1826), see also Fig. 1.6. Thus, I_0 cannot be determined by a low order polynomial. Instead, the trace gas absorptions in the measurement spectrum are determined relative to a reference spectrum that is measured under similar conditions, the so called **Fraunhofer Reference**. The measured spectra are then divided by this Fraunhofer reference, thereby removing the Fraunhofer lines. The Fraunhofer reference usually also contains absorption structures of the considered trace gas. However, by measuring spectra at different solar zenith angles, it is possible to determine the absorption in the Fraunhofer reference and thus to correct the measurements by this offset (Langley Plot).
In this work, satellite measurements of scattered sunlight are analysed. In that case, I_0 is determined by measuring a direct sunlight spectrum, which therefore contains no absorptions from atmospheric trace gases. By using this spectrum as Fraunhofer reference, the retrieved trace gas absorptions are not relative but absolute. In some cases, like e.g. for the DOAS analysis of OClO, an earth shine spectrum that does not reveal significant absorption structures of the investigated trace gas (due to a strong diurnal cycle or latitudinal dependence), is used as Fraunhofer reference (see section 3.6).

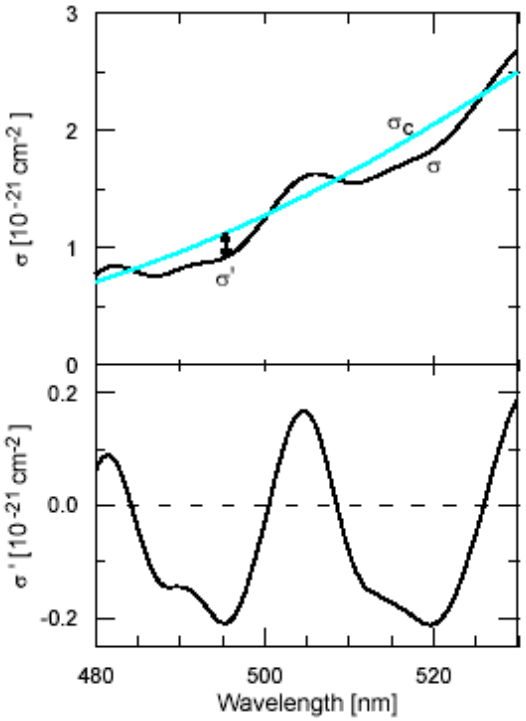

FIGURE 3.1: Splitting of the absorption cross section into parts varying slowly (σ_C) and rapidly (σ') with wavelength, adapted from *[Wagner 1999]*.

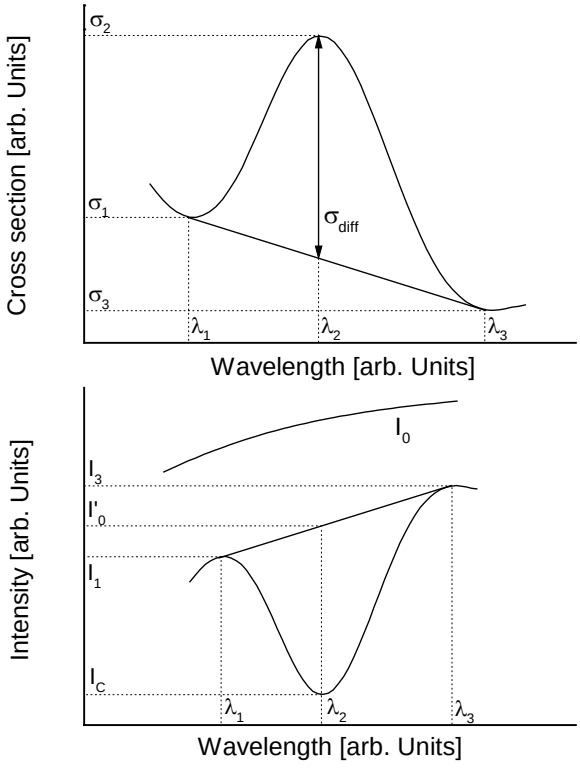

FIGURE 3.2: Approximation of the broadband absorption and scattering by the polynomial (bottom), and determination of the trace gas absorption by the differential absorption cross section (top).

To determine the trace gas absorptions, the spectra are evaluated by a least squares algorithm based on the **Levenberg-Marquard method** [*Levenberg, 1944; Marquard, 1963; Ottoy and Vansteenkiste, 1981; Press, 1995; Kraus, 2004*]. It simultaneously fits the optical densities of several absorbers with known absorption cross sections $\sigma_j(\lambda)$ together with the broadband polynomial to the difference of the logarithm of the measured spectrum $I(\lambda)$ and the Fraunhofer reference $I_0(\lambda)$, and minimizes the difference for all wavelengths that have been chosen for the retrieval:

$$\sum_{\lambda} \left| \ln I(\lambda) - \left(\ln I_0(\lambda) - \sum_j S_j \sigma_j - \sum_p a_p \lambda^p \right) \right|^2 \rightarrow 0 \qquad (3.3)$$

The quantity derived from this analysis is the integrated concentration of the absorber along the light path, the **slant column density** (SCD) S, which has the unit of molec/cm^2:

$$S_i = \int_0^L c_i \, dl \qquad (3.4)$$

In principle, every molecule for which the absorption spectrum is known from laboratory measurements (or calculations) can be retrieved, if its concentration and differential absorption cross section is sufficiently large compared to the measurement errors [*Stutz and Platt, 1996*]. For the various trace gases, specific "fitting windows" have been found, where the species of interest can be retrieved most accurately and the interference with other absorbers is small.

3.1.2 The air mass factor

Due to the slant viewing geometry, the derived SCD depends on the solar zenith angle (SZA) ϑ, see Fig. 3.3. Apart from this geometrical extension, the probability of scattering increases for longer light paths, which needs to be accounted for by radiative transfer simulations: An **air mass factor** (AMF) can be calculated, which describes the relation between the SCD and the vertical column density (VCD), the vertically integrated concentration [*Solomon et al., 1987b; Marquard et al., 2000*] :

$$VCD = \frac{SCD}{AMF(\vartheta)} \qquad (3.5)$$

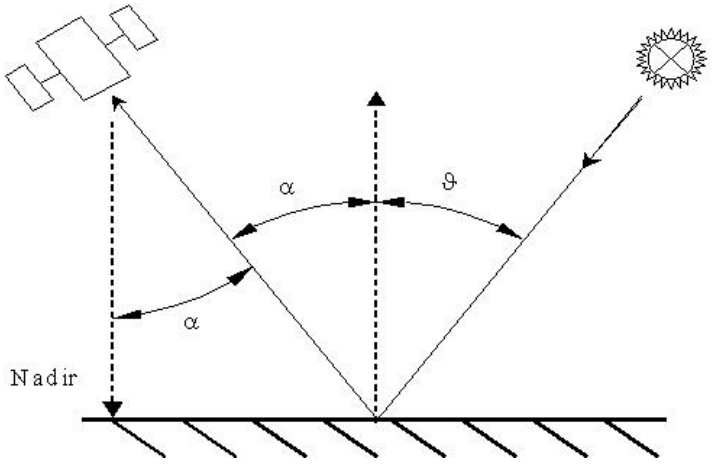

FIGURE 3.3: Scheme of a satellite measurement in nadir view, illustrating the SZA, the SCD and the VCD. Adapted from [*Platt, 2004*].

For medium and small SZAs, i.e. $\vartheta < 70°$, the AMF can be approximated by the geometrical relation between the SCD and the VCD: $AMF \approx 1/\cos(\vartheta)$. For larger SZAs, the effective AMF is increasingly impacted by scattering processes. Also, its value depends on the vertical profile of the considered absorber. Generally, the approximation by the geometrical AMF is valid for stratospheric absorbers, while for tropospheric ones the AMF is more impacted by scattering processes, the albedo, and also less photons reach the troposphere for larger SZA. Fig. 3.4 shows the AMF at a wavelength of 340 nm for box profiles located in the troposphere and stratosphere.

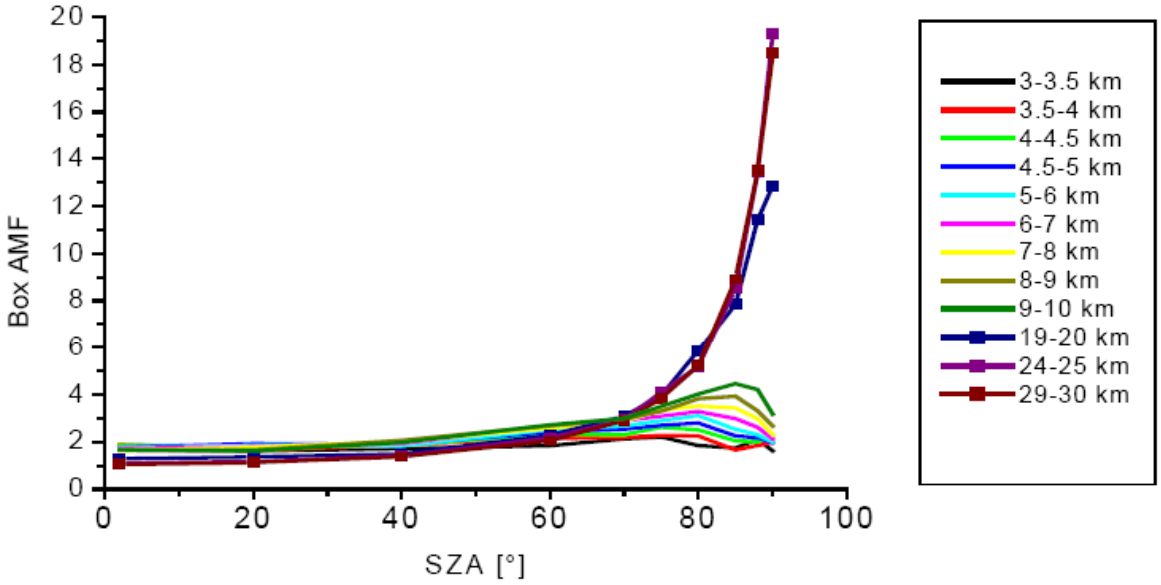

FIGURE 3.4: AMF for box profiles situated at the altitudes given in the legend [*v. Friedeburg, 2003*].

Since for satellite measurements the light passes the probed atmospheric layers at least twice, namely from the sun to the scattering point and from there to the satellite, the convergence value of the AMF for low SZAs is nearly two. The radiative transfer simulations also account for modifications of the light path due to albedo, clouds and aerosol. For the calculation of AMFs applied in this thesis, the radiative transfer models AMFTRAN [*Marquardt, 1998*] and TRACY [*von Friedeburg, 2003*] were used.

3.1.3 Corrections for scattered light DOAS

Eq. (3.3) is a generalization in so far as it neglects caveats that arise from atmospheric contributions not accounted for (Raman scattering, unknown absorbers), shortcomings of the instrument (like its resolution, degradation, stray light), uncertainties and temperature dependence of the applied absorption cross sections, etc. In practice, further corrections [*Platt et al., 1997*] are necessary to derive the trace gas absorption accurately. The most important ones for the retrieval of trace gas abundances from spectra measured by satellite instruments shall be briefly discussed in the following.

Shift and Squeeze

Since the absorption reference spectra are generally not measured with the instrument that measures the atmospheric spectra, there might be discrepancies in the wavelength calibration. Also, the calibration of the instrument might change due to temperature dependence or degradation when measuring over a long time period. To account for these effects, the analysis allows a shift and also a stretch or squeeze of the spectra. The adjusted cross section is calculated by $f(i) = a + b*i$, where i is the original value, and a and b are the shift and squeeze parameters, for which the value is determined in a non linear modification of Eq. (3.3), see *Stutz and Platt* [1996].

Ring Effect

By comparing spectra from direct and scattered sunlight, *Grainger and Ring* [1962] discovered that the optical depth of the Fraunhofer lines for scattered sunlight is reduced. The most probable explanation for this effect is inelastic rotational Raman scattering, mainly by the air molecules N_2 and O_2 [*Fish and Jones, 1995*]. For a detailed description of the history of the Ring effect and its correction in the DOAS retrieval of trace gases, see [*Wagner, 2001b*]. Fig 3.5 illustrates the "filling up" of the Fraunhofer Lines by rotational Raman scattering.

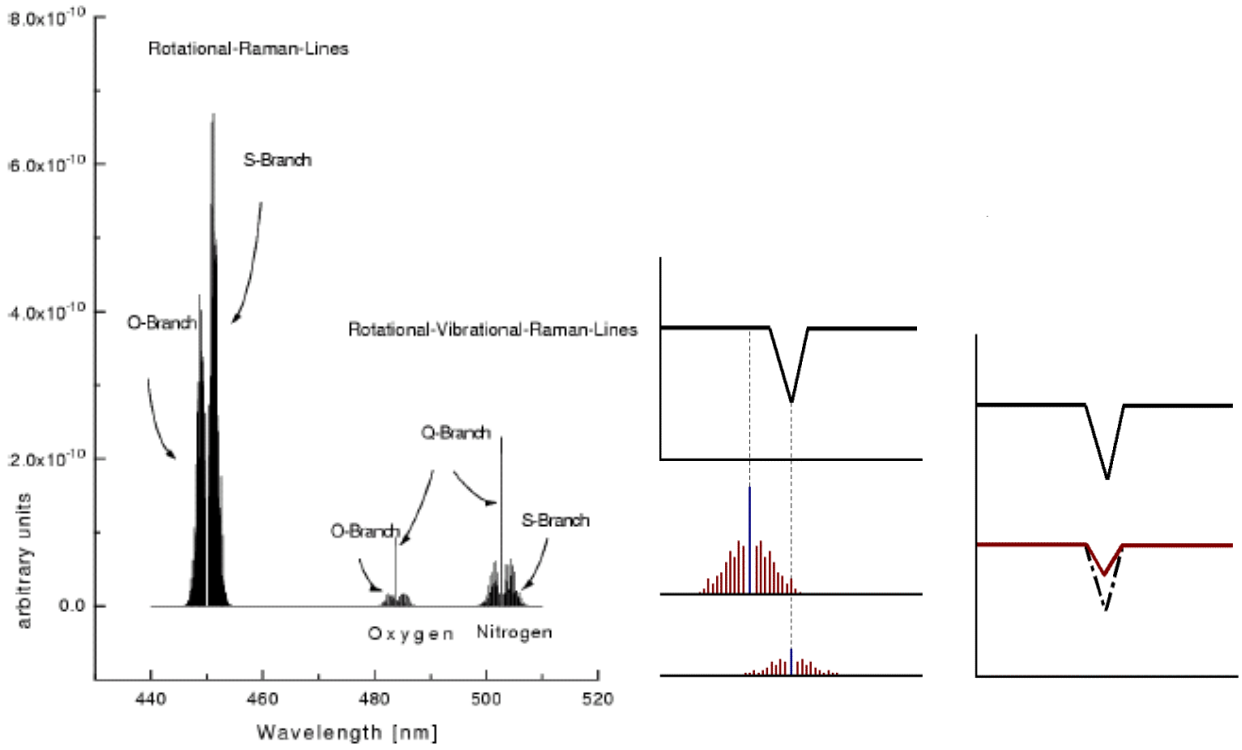

FIGURE 3.5: Ring Effect a) Rotational-vibrational Raman lines for oxygen and nitrogen b) Raman scattering from outside and inside of the Fraunhofer lines leads to a reduction of the intensities in the line centers.

Due to the large abundance of molecular nitrogen and oxygen in the atmosphere, the Ring effect can cause spectral structures of up a few percent optical thickness (especially in the UV region), which can become (except for ozone) one or two magnitudes larger than the optical densities of the trace gases retrieved by DOAS. Thus, for an accurate retrieval, an optimal correction of the Ring Effect is important, especially for weak absorbers like BrO and OClO.

Usually this correction is done by including a Ring Spectrum in the DOAS analysis [*Solomon, 1987a*]. The Ring spectrum is obtained either from polarization measurements [*Solomon, 1987a; Fish, 1994*] – in contrast to Rayleigh scattering, the Raman scattering is largely unpolarized – or calculated from the rotational states of N_2 and O_2 [*Bussemer, 1993; Fish and Jones, 1995; Vountas, 1998*]. An approximate correction is achieved by including the reciprocal of the Fraunhofer reference [*Noxon, 1975*].

The correction of the Ring effect is especially important for satellite measurements, where the direct sunlight, which contains the original unattanuated Fraunhofer lines, is used as Fraunhofer reference spectrum [*Wagner, 2001b*].

I_0-Effect

The trace gas absorption cross sections and also the Fraunhofer lines are generally not resolved by the typical resolution (from a few tenths to several nanometers) of a spectrometer used for DOAS measurements. Instead, the spectra are convoluted by the instrumental slit function:

$$I^*(\lambda) = f * I(\lambda) = f * I_0(\lambda)\exp(-\sigma(\lambda)S))$$

On the other hand, in the analysis of the spectra, the convolution of the trace gas absorption cross sections is accounted for by folding with the instrumental slit function, which assumes constant intensity as function of the wavelength:

$$\sigma^*(\lambda) = f * \sigma(\lambda)$$

Because of the Fraunhofer lines, the intensities of the I_0-spectrum varies significantly with wavelength. Therefore, the optical densities resulting from convolution of the intensities by the instrument may differ considerably from the ones resulting from the convolution of the cross sections:

$$\tau(\lambda) = -\ln\left(\frac{f * I_0\exp(-\sigma(\lambda)S)}{f * I_0(\lambda)}\right) \neq f * -\ln\left(\frac{I_0\exp(-\sigma(\lambda)S}{I_0(\lambda)}\right) = f * \sigma(\lambda)S$$

Although this leads only to negligible effects for the atmospheric absorbers themselves, the I_0 effect of strong absorbers (like O_3 and NO_2) can be important for the retrieval of weak absorbers like BrO or OClO [*Huppert, 2000*]. For the retrieval of BrO in near UV, the I_0 effect of NO_2 is of the same order of magnitude as the optical density of BrO [*Aliwell, 1998*].
The solar I_0 effect can be accounted for by using "I_0 corrected"-spectra [*Wagner, 2001b, Aliwell et al., 2002*]. For the BrO and OClO analysis from GOME spectra, the I_0 effect was found to be of the order of only a few percent, which is by far smaller than the errors introduced by other effects [*Wagner, 1999 and references therein*]. Thus, the cross sections applied in the retrieval for this thesis are not I_0 corrected.

3.2 Measurement Geometries

The DOAS technique is widely used in laboratory-, ground based-, balloon-, aircraft- and also satellite-remote sensing of trace gases. In these fields, various measurement geometries are applied; in this work satellite measurements of scattered sunlight in nadir and limb geometries are analyzed.
In **Nadir** geometry, the spectrometer measures radiances of the light that is backscattered or reflected from the Earth's atmosphere and the ground in vertical direction, Fig. 3.6.

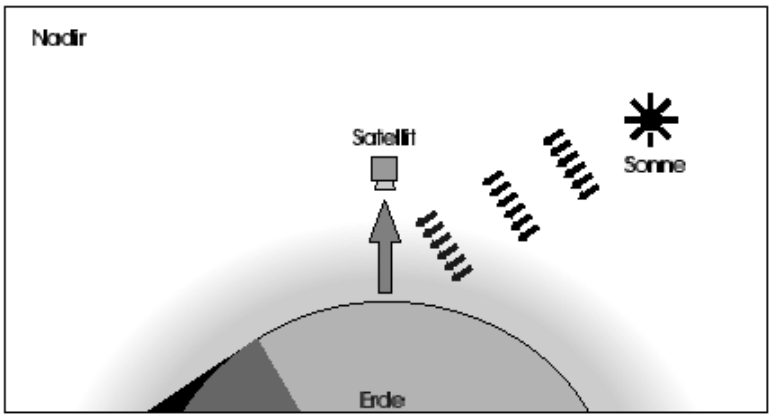

FIGURE 3.6: Scheme of the Nadir geometry.

In many cases the AMF can be calculated by radiative transfer simulation, and by Eq. (3.5) the SCDs can be converted to VCDs. However, one is often interested not only in the total column, but in the concentration of the absorber at a certain altitude. An average concentration could be calculated by dividing the VCD with the light path, but according to the specific vertical profile of the considered absorber, the concentration along the light path may show large variations, and thus determining the concentration is generally not possible.
To overcome this shortcoming, various approaches can be applied. For some cases the altitude range of the absorber can be constrained to certain regions of the atmosphere, for example the boundary layer. However, these constraints rely on assumptions about sources, sinks and atmospheric chemistry of the considered trace gas. Another approach that has been applied in the ground based measurements of scattered sunlight, is to probe the atmosphere under various viewing angles (Multi-Axis, see [*Hönninger, 2002; Sinnreich, 2003*]), which provide more information about the location of the absorbers.
A similar information is obtained by satellite measurements in **Limb** geometry, where the spectrometer measures radiances of light that is backscattered or reflected from the Earth's atmosphere in horizontal direction (see Fig. 3.7) under a variable viewing angle.

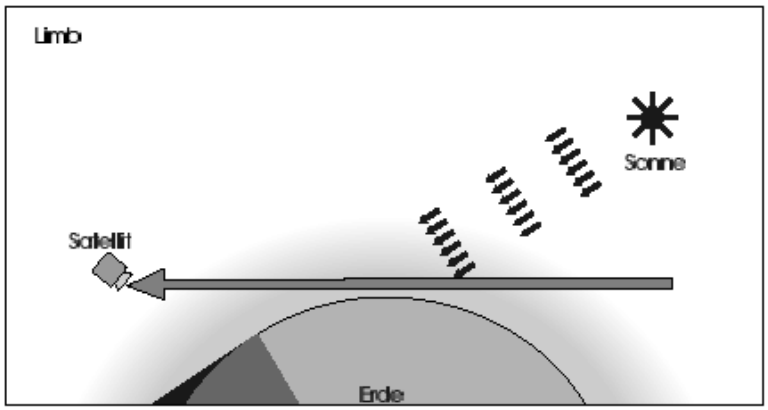

FIGURE 3.7: Scheme of the Limb geometry.

Consequently, the measurement is representative not for the total column, but most sensitive for the trace gas abundance at that specific altitude range probed by the respective viewing angle, the so called **tangent height**. By changing the viewing angle sequentially, the whole atmosphere is probed, thereby enabling the vertical profile of the absorber to be retrieved.
However, the measured radiance at a certain tangent height is determined not only by the absorbers and scattering particles at this height, but due to radiative transfer processes, also molecules at other altitudes contribute to the signal. In expression, the light that is scattered at an altitude of 20 km must have passed the atmosphere above and therefore is attenuated by absorbers and scatters present there. Vice versa, backward scattering may also lead to contributions from altitudes below. Thus, to obtain the vertical profile of the considered absorber, an inversion algorithm is necessary, that accounts for the impacts of an absorber concentration at a certain altitude on each SCD measured at the different tangent heights. For this purpose, various methods exist.
In the **Onion peeling** method, the inversion starts with the uppermost tangent height of the considered altitude range, disregarding the contributions of the spheres below. The inversion process continues downwards into the atmosphere, using the results for the tangent heights above in the respective next step [*Connor et al., 1988*]. In this thesis, the method of **optimal estimation** is applied. It inverts the measured SCDs to a vertical profile by combining the measurements for all tangent heights simultaneously and is described in detail in the following section.

3.3 Profile Retrieval by Optimal Estimation

Any inversion approach assumes that there is some relation between the measured and the desired quantity that is, at least partly, understood and can be described by a function:

$$\boldsymbol{y} = F(\boldsymbol{x}, \boldsymbol{b}) + \varepsilon = \boldsymbol{K}\boldsymbol{x} + \varepsilon \qquad (3.6)$$

where **y** is a measurement vector containing m measurements and **x** a state vector with n states, F is the **forward function** that describes the relation, **b** parameters that are known to influence the measurement but are not intended to be retrieved, and ε the error of the measurement. If the function F is linear or can be linearly approximated, then F may be written as a **weighting function matrix**: $\mathbf{K}_{ij} = \partial F_i(x) / \partial x_j$.
For the retrieval of the desired quantity - the state vector **x** - from the measured vector **y**, the matrix **K** needs to be inverted, a calculation that is possible only if the matrix has full rank, i.e. if m = n. For over determined matrices **K** (m > n), the inverse can be found with a least square approach. If n > m, the matrix **K** is underdetermined and it is necessary to constrain the inversion of the matrix by knowledge about the state **x** that existed before the measurement (a priori).
The combined solution should refer to the a priori for components of **x**, for which there is no information from the measurement vector (or the measurement error is large), but should depend on the measurements for those components of **x** that can be deduced from **y** with only small error.
This is achieved by the **Bayes theorem**, which connects the probability density function (*pdf)* of the measurement to the *pdf* of the state [*Rodgers, 2000*]:

$$P(x/y) = \frac{P(y/x)P(x)}{P(y)} \qquad (3.7)$$

P(x) describes the knowledge about the state **x** before the measurement is made: It is the probability that **x** lies in the multidimensional volume (**x**, **x**+d**x**). P(y/x) describes the mapping of the state space into measurement space by the forward model. It is the probability that **y** lies in (**y**, **y**+d**y**) when **x** has a given value. And P(y) is the *pdf* of the measurement before it is made. It is a normalizing factor which is often not needed and can be obtained by integrating P(y/x)P(x) over all **x**.
The quantity on the left side of Eq. (3.7), P(x/y), is the one of interest in the inverse problem. It is the probability that the state vector **x** lies in (**x**, **x**+d**x**) when the measurement vector **y** has a given value.

It can be shown [*Rodgers, 2000*] that the **x** at the maximum of the posterior *pdf* - the maximum a posteriori (MAP) solution: $x = \max_x P(x/y)$ can be obtained by:

$$\hat{x} = x_a + S_a K^T \left[K S_a K^T + S_y \right]^{-1} \left(y - K x_a \right) \qquad (3.8)$$

where x_a is the a priori of the state, S_a the covariance of the a priori and S_y the measurement covariance.
With the generalized inverse of **K**, the gain matrix $\mathbf{G} = \mathbf{S_a K^T [K S_a K^T + S_y]^{-1}}$, Eq. (3.8) can be written as

$$\hat{x} - x_a = G(y - K x_a) = G\left[K\left(x - x_a\right) + \varepsilon\right] \qquad (3.9)$$

A very useful quantity is the matrix **A=GK**. It relates the expected state $\hat{x}$ to the true state x through

$$\hat{x} - x_a = G\left[K\left(x - x_a\right) + \varepsilon\right] = A\left(x - x_a\right) + G\varepsilon \quad \text{or} \quad \hat{x} = x_a + A\left(x - x_a\right) + G\varepsilon \qquad (3.10)$$

It is called the **Averaging kernel** matrix [*Backus and Gilbert, 1970*], the model resolution matrix [*Menke, 1999*] or resolving kernel. For an ideal observing system the matrix would be a unity matrix; in reality, the values of A are close to 1 if the impact of the measurement vector on the retrieved state is large, i.e. if the measurement error and the deviation to the *pdf* of the a priori is small.

In our case, i.e. the limb measurements from SCIAMACHY, **y** in Eq. (3.6) are the measured SCDs as function of the tangent height and **x** the vertical concentration profile of the respective absorber, that shall be calculated from **y**. We know that due to radiative transfer, the SCD at a certain tangent height is a function not only of the absorbers in the probed height interval, but is also influenced by trace gas concentrations from altitudes below and above (see section 3.2). That is what our forward model needs to account for. We also know from nadir geometry that the relation between the SCD and the VCD is described by the air mass factor. Hence, the weighting function matrix **K** is in our case a matrix of air mass factors: **SCD = AMF * VCD** or

$$\begin{pmatrix} SCD_1 \\ \dots \\ \dots \\ SCD_{m-1} \\ SCD_m \end{pmatrix} = \begin{pmatrix} AMF_{1,1} & \dots & \dots & \dots & AMF_{1,n-1} & AMF_{1,n} \\ \dots & & \dots & & \dots & \dots \\ \dots & & & \dots & \dots & \dots \\ AMF_{m-1,1} & \dots & \dots & \dots & AMF_{m-1,n-1} & AMF_{m-1,n} \\ AMF_{m,1} & \dots & \dots & \dots & AMF_{m,n-1} & AMF_{m,n} \end{pmatrix} * \begin{pmatrix} VCD \\ \dots \\ \dots \\ VCD_{n-1} \\ VCD_n \end{pmatrix} \qquad (3.11)$$

Fig. 3.8 shows air mass factors for boxes of constant concentration with 3 km vertical extension as function of the tangent height for two different wavelengths.

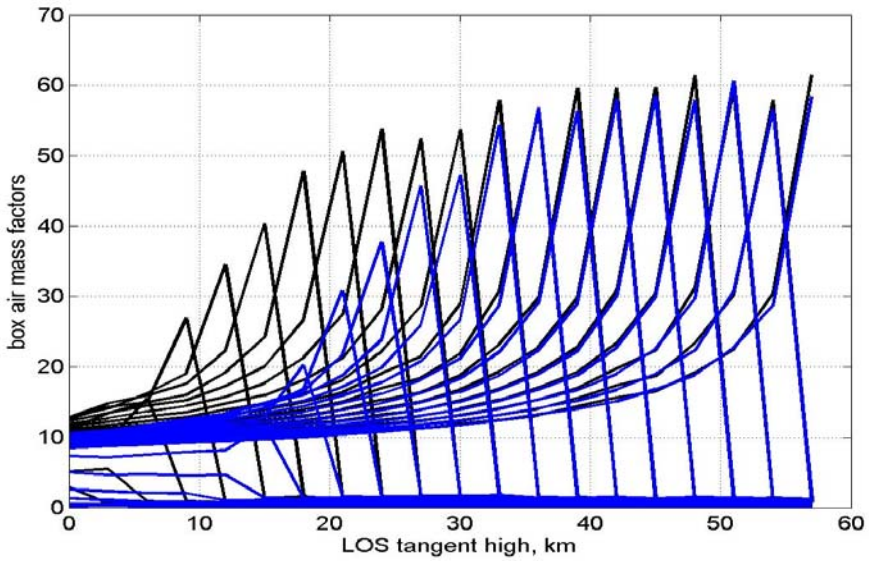

FIGURE 3.8: Box air mass factors for wavelengths of 340 nm (blue line) and 500 nm (black line), calculated by the radiative transfer model TRACY [*J. Pukite, personal communication, 2005*].

The retrieved profile is always a combination of the measured SCDs, the measurement error, the applied AMFs, and the a priori. Therefore, the retrieved SCDs and the calculated AMFs should be of little uncertainty. Also, the a priori has to be carefully chosen and should describe the mean value and the variance of the state to be retrieved as good as possible. In the optimal case, the a priori is a climatology that reflects the mean and variability of the trace gas profile at the season and daytime similar to the measurement. The last point is especially important for species with a strong annual or diurnal cycle, like e.g. OClO.

3.4 The Global Ozone Monitoring Experiment (GOME)

The GOME instrument on board the **E**uropean **R**emote **S**ensing Satellite-2 (ERS-2) consists of a set of four spectrometers covering the wavelength range between 240 and 790 nm. It measures the intensities of the direct sunlight and of the light scattered back to the satellite from the earth and its atmosphere in nadir view (see e.g. *Burrows et al. [1999]*). By means of DOAS, these spectra can be analyzed for various trace gases. Developed mainly for monitoring of ozone, GOME is able to detect a range of atmospheric absorbers, among them NO_2, BrO, OClO, SO_2, HCHO, H_2O, O_2 and its dimer O_4 [*Burrows et al., 1999; Wagner et al., 2002b*].

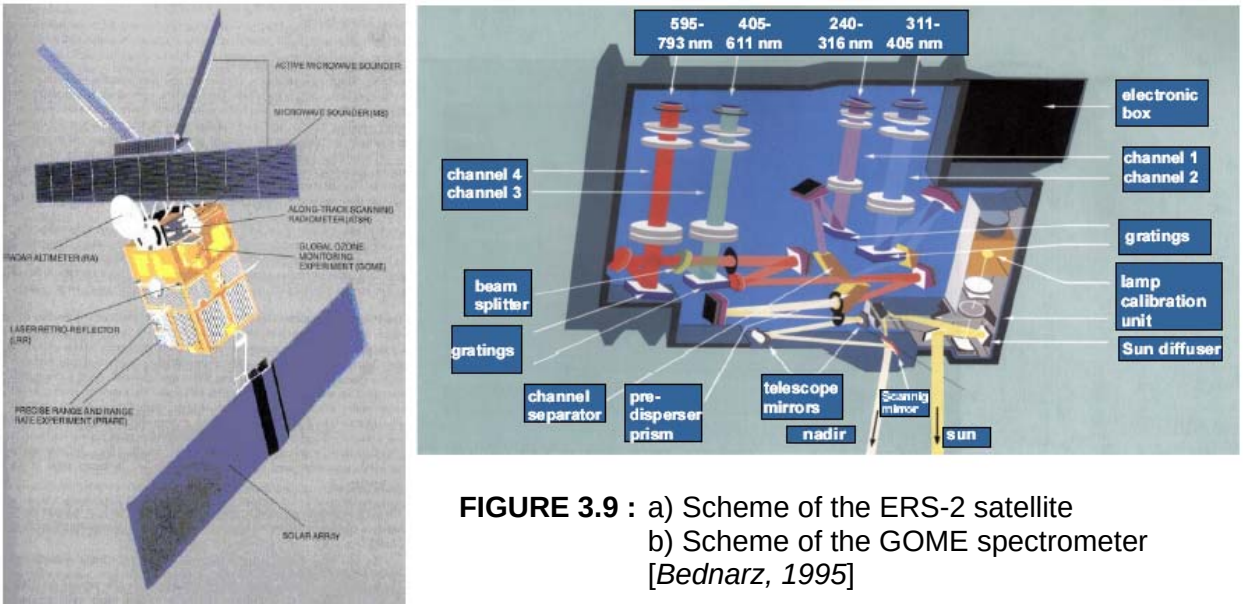

FIGURE 3.9 : a) Scheme of the ERS-2 satellite
b) Scheme of the GOME spectrometer
[*Bednarz, 1995*]

The ERS-2 satellite operates at an altitude of about 780 km in a sun-synchronous, nearly polar orbit (inclination: 98.5 degrees), with a local equator crossing time of 10:30 am. While the satellite travels in an almost north-south direction on the daylight half of each orbit, the GOME instrument scans the surface in the perpendicular east-west direction. During one scan, three individual spectra are recorded, each corresponding to one of the three adjacent ground pixels, see Fig. 3.10. With a ground pixel size of 320 km (east-west) by 40 km (north-south) and up to 15 orbits per day, the whole global surface is covered in three days. For polar regions (latitude $\phi > 70°$), a daily coverage is achieved (excluding the polar night region).

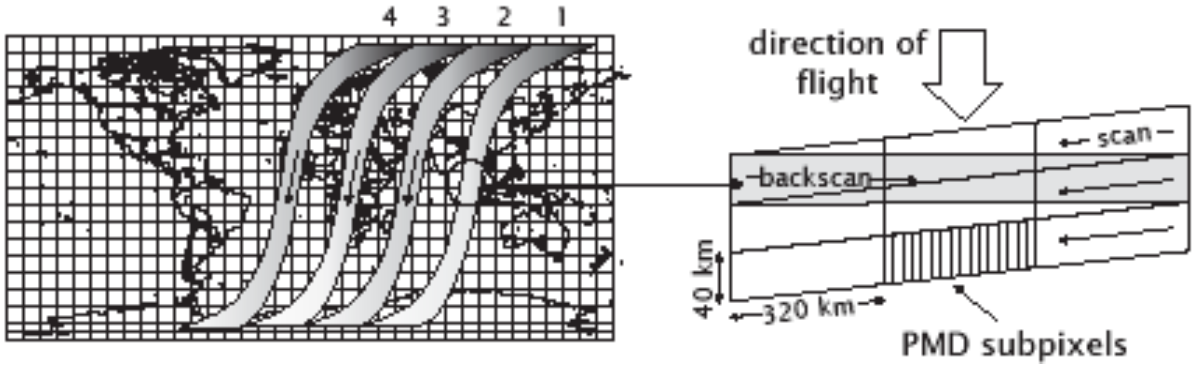

FIGURE 3.10: Scan Modus and pixel size of GOME.

3.5 The Scanning Imaging Absorption Spectrometer for Atmospheric Chartography (SCIAMACHY)

On 1st of March 2002, ENVISAT-1, the first satellite designed exclusively for the monitoring of environmental and climatic changes, was launched in a sun-synchronous, nearly polar orbit. Besides various instruments for probing land, ice and ocean surfaces by radar and imaging techniques, it carries three instruments for the observation of atmospheric trace gas abundances: The Michelson Interferometer for passive atmospheric sounding (MIPAS), The Global Ozone Monitoring by occultation of stars (GOMOS), and the Scanning Imaging Absorption Spectrometer for Atmospheric Chartography (SCIAMACHY).

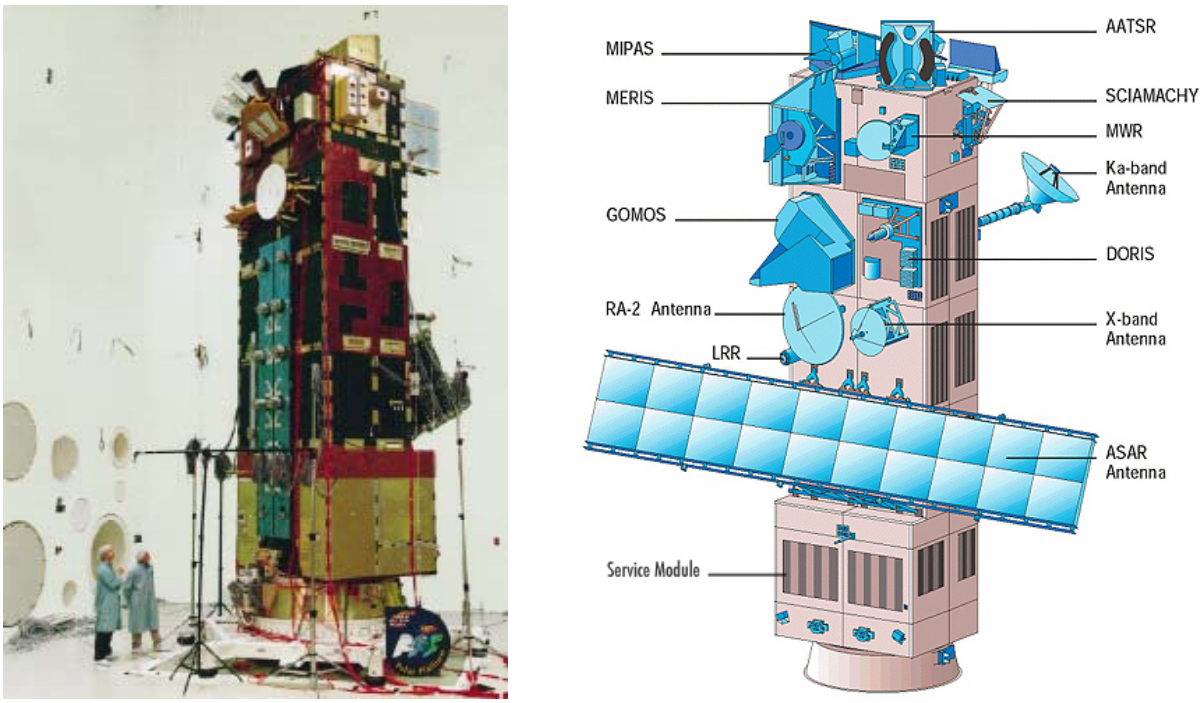

FIGURE 3.11: ENVISAT-1 a) picture taken before launch
b) instrumentation, adapted from http://envisat.esa.int

SCIAMACHY is a medium-resolution UV-VIS-NIR spectrometer, which measures solar light back scattered and reflected by the Earths atmosphere or surface simultaneously in eight spectral channels. Channels 1-6 provide continuous spectral coverage of the wavelengths between 240-1750 nm with a resolution between 0.2 nm (at 240 nm) and 1.5 nm (at 1750 nm). Channels 7 and 8 provide 0.4 nm resolution in bands around 2.0 and 2.3 μm (see table 3A).

During the majority of an orbit, SCIAMACHY is measuring the earthshine radiance in alternating nadir and limb viewing geometries. In addition, the solar or lunar light transmitted through the atmosphere is regularly observed in occultation measurements. The extra-terrestrial solar irradiance and lunar radiance are determined from observations of the sun and the moon above the atmosphere. Figure 3.12 details the measurement mode procedure for a typical SCIAMACHY orbit.

Ch.	Spectral range [nm]	Spectral resolution FWHM [nm]	Species retrievable by DOAS
1	240 - 314	0.24	O_3, ClO, NO
2	309 - 405	0.26	HCHO, SO_2, BrO, **OClO**, O_4, NO_2
3	394 - 620	0.44	O_3, O_4, NO_2, H_2O
4	604 - 805	0.48	O_2, O_4, NO_3, H_2O
5	785 - 1050	0.54	H_2O
6	1000 - 1750	1.48	H_2O, CO_2, CH_4
7	1940 - 2040	0.22	H_2O, CO_2
8	2265 - 2380	0.26	H_2O, CO, CH_4, N_2O

Table 3A: Spectral channels of SCIAMACHY with wavelength range, spectral resolution, and the atmospheric trace gases that can be retrieved by DOAS.

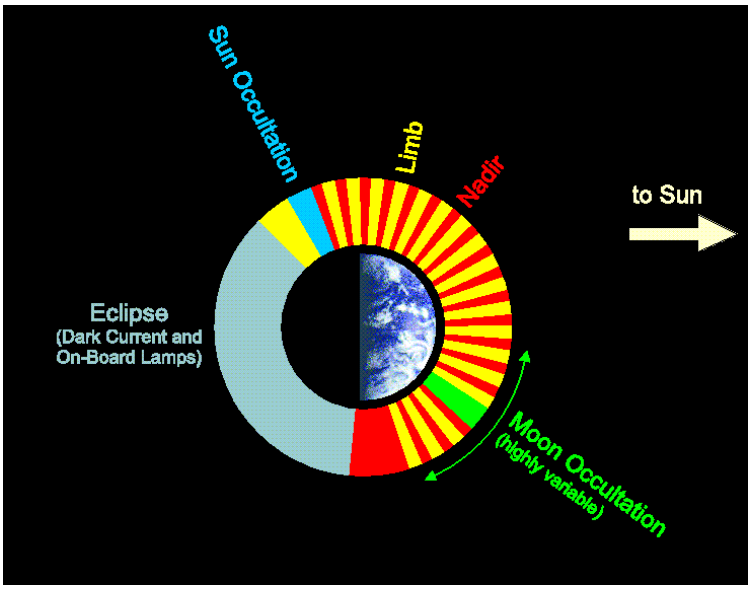

FIGURE 3.12: Typical sequence of measurements performed by SCIAMACHY during one orbit.

Inversion of the SCIAMACHY measurements enables the derivation of amounts and distribution of the atmospheric constituents O_3, O_2, O_4, BrO, OClO, ClO, SO_2, H_2CO, NO, NO_2, NO_3, CO, CO_2, CH_4, H_2O, N_2O, and aerosol, as well as providing knowledge about the parameters pressure p, temperature T, radiation field, cloud cover, cloud top height and surface spectral reflectance. A special feature of SCIAMACHY is the combined limb-nadir measurement mode. The inversion of the combination of limb and nadir measurements enables tropospheric column amounts to be determined [*Sierk et al., 2004*], see Figs. 3.13 to 3.15.

The variable measurement geometries are possible, because SCIAMACHY has two mirrors to direct the light path: the Elevation scanning mirror (ESM), which scans in vertical, and the Azimuth scanning mirror (ASM) which scans in horizontal direction, see Fig. 3.16.

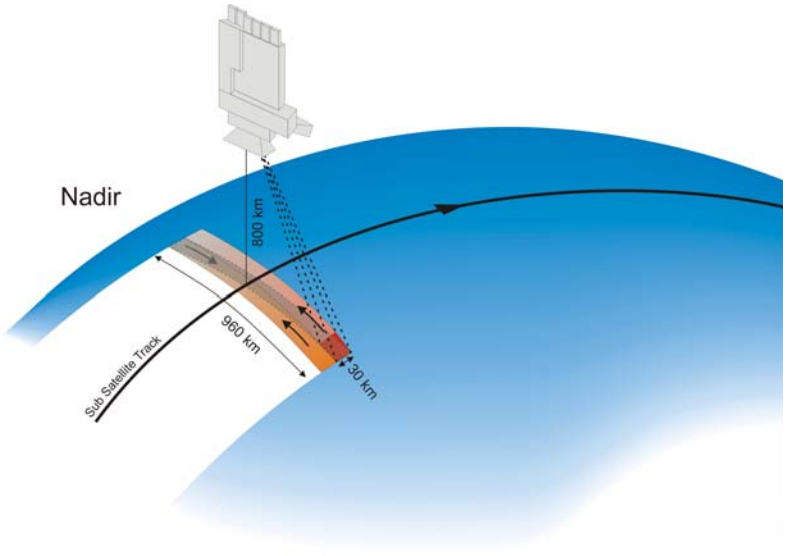

FIGURE 3.13: Geometry, pixel size and scan modus for SCIAMACHY nadir measurements, adapted from [*Noel, 2000*].

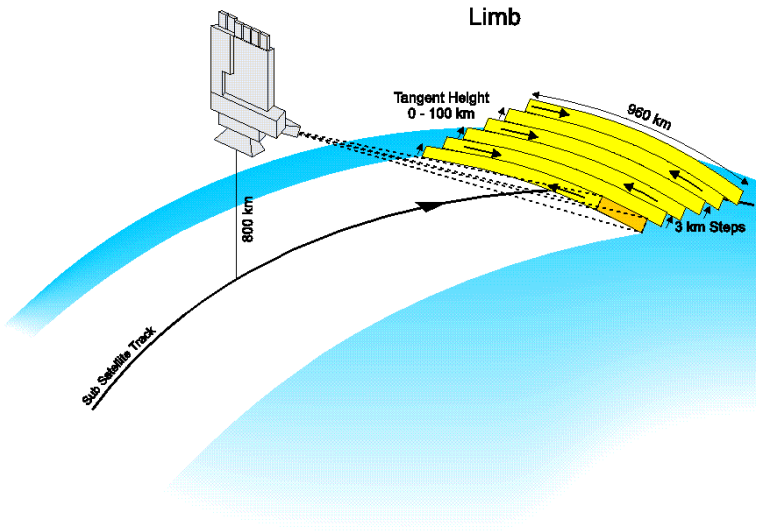

FIGURE 3.14: Geometry, pixel size and scan modus for SCIAMACHY limb measurements, adapted from [*Noel, 2000*].

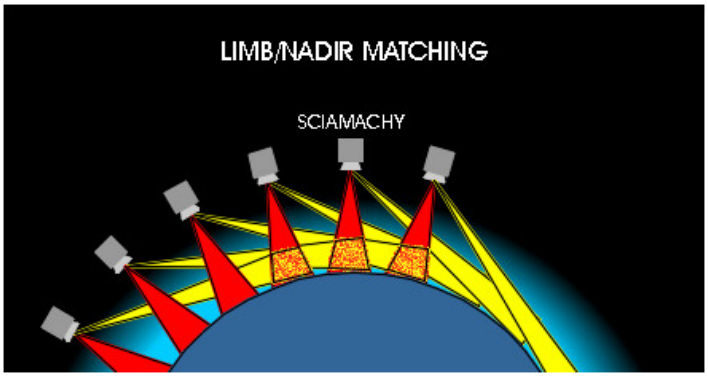

FIGURE 3.15: Alternate probing of the same air mass by SCIAMACHY limb and nadir measurements.

These two nearly-orthogonal scan mirrors enable across-track scanning in Nadir and in Limb, as well as sideways viewing for occultation and calibration measurements of Sun and Moon. The incoming radiation enters the instrument via one of three ports:

(i) for nadir measurements the radiation from the Earth's scene is directed by the elevation mirror into a telescope (off axis parabolic mirror) which focuses the beam onto the entrance slit of the spectrometer,

(ii) for limb and solar/lunar occultation measurements the radiation is reflected by the azimuth mirror to the elevation mirror and then into the telescope which focuses the beam onto the entrance slit of the spectrometer,

(iii) for internal and sub-solar calibration measurements the radiation of internal calibration light sources or the solar radiation is directed by the elevation mirror into the telescope.

The optical layout of the instrument is schematically shown in Fig. 3.16.

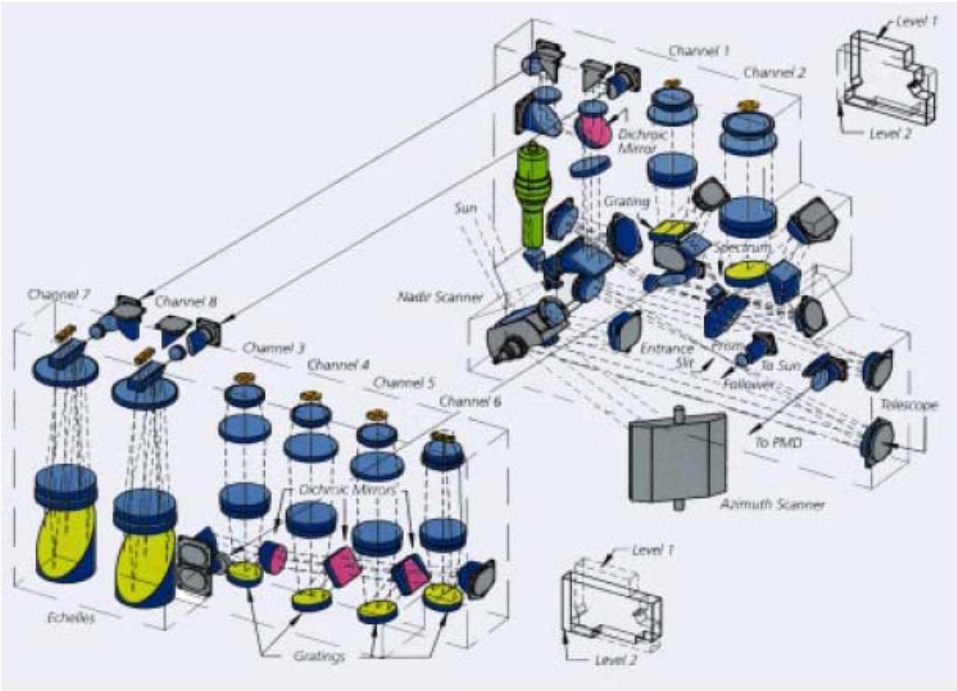

FIGURE 3.16: Optical layout of SCIAMACHY.

3.6 OClO Retrieval from GOME NADIR Spectra

The OClO analysis of GOME spectra has been developed by Thomas Wagner and is described in detail in [*Wagner, 1999; Wagner et al., 2001*]. The wavelengths utilized for the analysis range from 363 to 391 nm and cover three bands of OClO (see Fig. 1.3 and Fig. 3.17). The included reference spectra are listed in table 3B. The chosen fit window excludes the strong Ca II Fraunhofer lines at 393 and 397 nm (see Fig. 1.6), the broadband absorption of O_4 around 360 nm, and prevents also interference with the stronger O_3 absorption for smaller wavelengths.

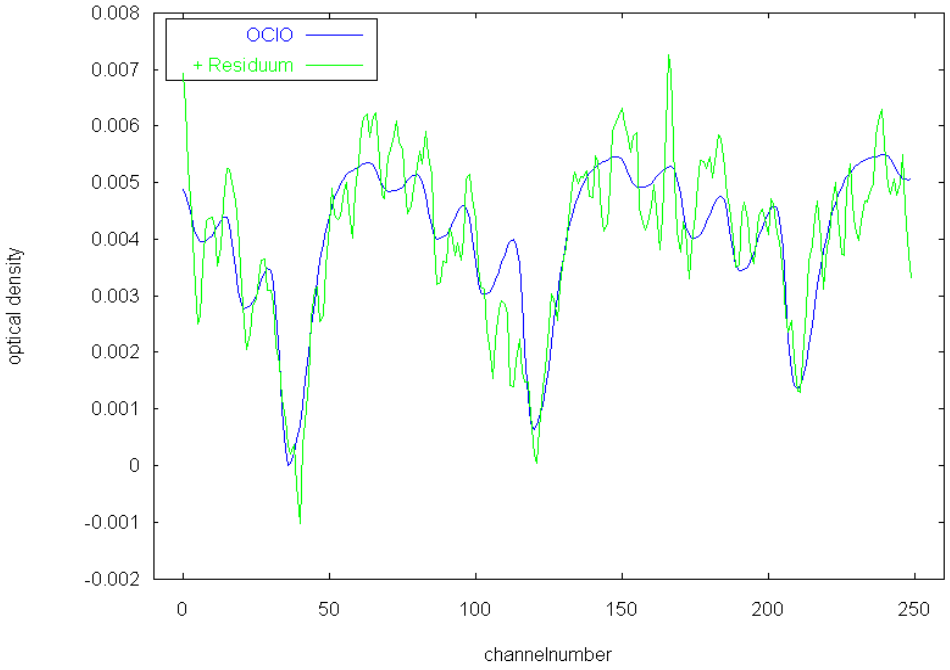

FIGURE 3.17: Example for an OClO analysis of GOME spectra. Pixel Number 2183 from orbit 60918082.

Reference Spectrum	Temperature	Source
NO_2	227 K	[*Burrows et al., 1998*]
OClO	203 K	[*Wahner et al., 1987*]
O_4	296 K	[*Greenblatt et al., 1991*]
Calculated Ring spectrum	250 K	MFC, [*Bussemer, 1993*]
Fraunhofer spectrum	-	Average of 10 GOME earth shine spectra around SZA = 70°

Table 3B: Reference spectra included in the GOME OClO analysis, adapted from [*Wagner, 1999*].

However, the diffuser plate problem of GOME [*Richter and Wagner, 2001; Martin et al., 2002; Wenig et al., 2003*] leads to artificial spectral structures, which vary with season and cause seasonal dependent offsets for all absorbers retrieved from GOME spectra. Due to this effect, the OClO retrieval with the direct sun spectrum depends largely on the chosen sun reference: For sun spectra from different days the magnitude of the retrieved OClO SCDs is offset by values as large as the SCD itself (see [*Wagner, 1999*]).

In order to avoid this effect, and also to reduce the impact of GOME's "undersampling problem" [*Roscoe et al.,* 1996; *Platt et al.,* 1997; *Chance,* 1998; *Van Roozendael et al.,* 1999; *Wagner,* 1999], an atmospheric spectrum taken at midlatitudes was chosen as Fraunhofer reference spectrum. This Fraunhofer reference is taken from a mean of ten earth shine spectra around a SZA of 70° for every orbit, see Fig. 3.18. Due to the rapid photolysis of OClO (see chapter 4), spectra in this SZA region can be expected to contain no absorption signals of OClO.

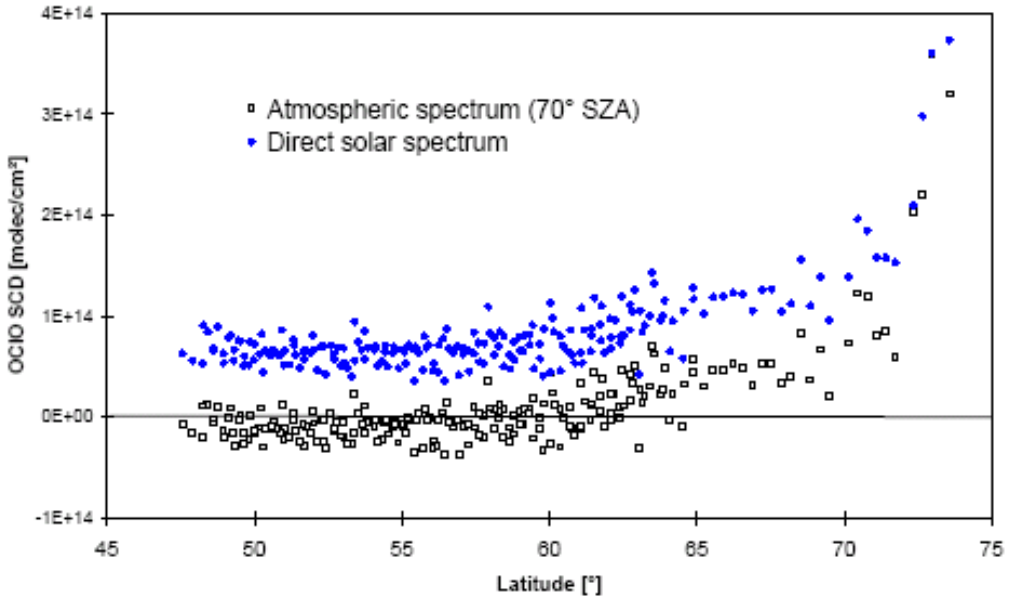

FIGURE 3.18: OClO SCDs as function of latitude for the GOME orbit 70118075 from 18.01.1997. Retrieval performed by using as Fraunhofer Reference either the direct solar spectrum (blue dots) or an atmospheric spectrum at SZA of 70 degrees (black squares). Adapted from [*Wagner, 1999*].

During this thesis, a few modifications to the original OClO analysis described in [*Wagner, 1999*] have been implemented:

1) Along with the update to the 'New Fit', programmed by Stefan Kraus [*Kraus, 2004*], the Fraunhofer Fit coefficient is now set to 1. Before, in the fit programmed by Carsten Leue [*Leue, 1999*], the coefficient of the Fraunhofer reference spectrum was determined by the least squares analysis (Eq. 3.3), and usually values between 0.995 and 1.002 were derived.

2) An 'additional polynomial' of degree 1 is now included in the OClO analysis. It is fitted in the intensity space:

$$\ln(I(\lambda) - P_{add}) = \ln(I_0(\lambda)) - \sum S_i \sigma_i - P$$

The purpose of the additional polynomial P_{add} is to correct for a possible intensity offset due to stray light, insufficient correction of polarisation features, dark current, etc.
The analysis including the additional polynomial results in slightly lower OClO SCDs (≈ 5 %), see Fig. 3.19; also, the error of the fit is reduced by 5 to 50 %

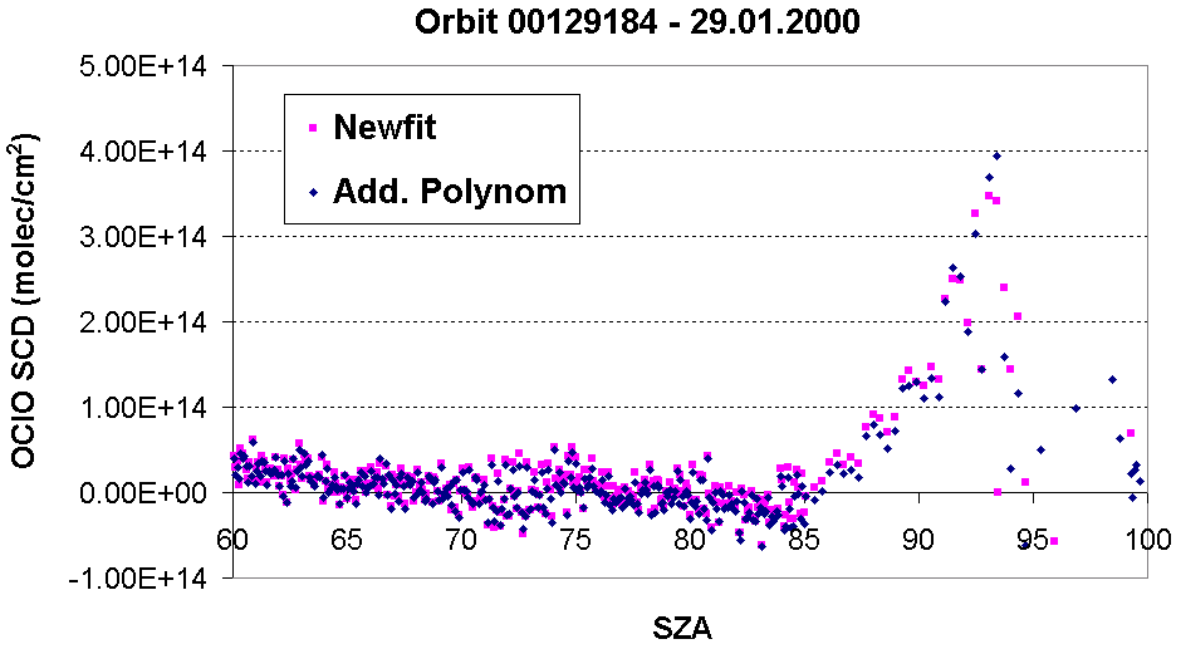

FIGURE 3.19: OClO SCDs as function of the SZA for an analysis without (purple squares) and with (blue diamonds) the additional polynomial.

3) A pre-shift of the Fraunhofer reference spectrum is allowed. This accounts for a possible degradation of the instrument, that might cause a shift relative to the spectrum used for the wavelength calibration of the absorption cross sections.

4) The software, which is applied for the calibration of the measured earth shine spectra, and also accounts for the degradation of the GOME spectrometer, has been updated from ESA 13 to ESA 22.

5) An ozone absorption spectrum was included in the analysis for sensitivity studies. Since the ozone absorption in the utilized wavelength interval is small, this has no significant effect on the magnitude of the retrieved OClO SCDs.

While the last three modifications have been tested for a few orbits to check for consistency, the other modifications have been applied to the whole GOME dataset. Thus, the OClO results presented in this thesis are obtained by the analysis with the 'new fit', setting the Fraunhofer fit coefficient to 1 and also including the additional polynomial.

3.7 OClO Retrieval from SCIAMACHY NADIR Spectra

Due to the strong effect of polarisation features on the SCIAMACHY spectra [*Krijger, et al., 2003; Tilstra et al., 2003*], especially in the near UV, the retrieval of absorbers in this wavelength range, like BrO and OClO is complicated. For the OClO DOAS analysis of SCIAMACHY spectra various wavelength ranges were tested. For the first spectra obtained from ESA, a fit window consisting of two bands (363 – 382 nm) was found to provide the best results in terms of reasonable column densities and fit error. For later, newly calibrated spectra also a third band could be included, so that for the SCIAMACHY OClO results presented in this thesis, we used the wavelength range from 363 to 391 nm, the same as for GOME (see Fig. 3.20). Included reference spectra are: OClO, NO_2, O_3, O_4, Ring, and the Eta and Zeta Spectrum (from key data) for the correction of polarisation features, see Table 3C.

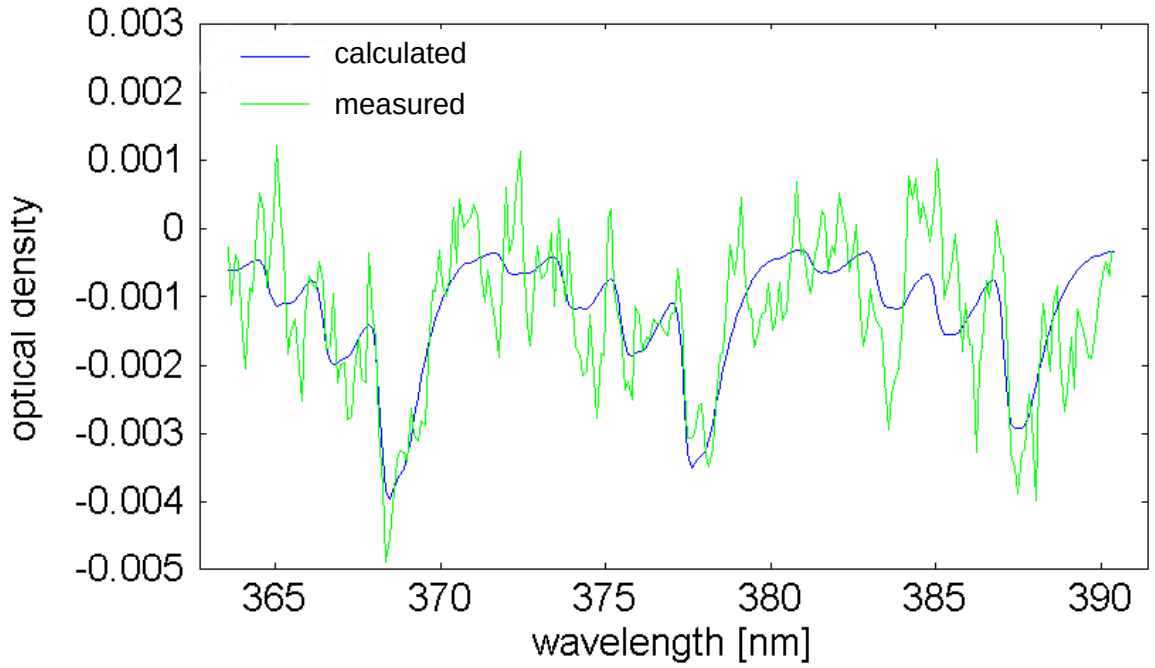

FIGURE 3.20: Example for an OClO analysis of SCIAMACHY nadir spectra. Orbit No. 4426 from 4th of January, 2003. SZA = 89.2°, OClO SCD = 3.5 * 10^{14} molec/cm^2.

Spectrum	Remark
OClO	213 K, [*Krominga et al., 2003*]
O_3	223 K, [*Bogumil et al., 2003*]
O_4	298 K [*Greenblatt et al., 1990*]
NO_2	220 K, [*Vandaele et al., 1997*]
Ring	Calculated, [*Bussemer, 1993*]
Offset	$1/I_o$ included in Fit
Polarisation 1	Eta from key data
Polarisation 2	Zeta from key data
Fraunhofer 1	Atmospheric spectrum, SZA 70°
Fraunhofer 2	Direct solar spectrum, ESM
Fraunhofer 3	Direct solar spectrum, ASM

Table 3C: Reference spectra included in the OClO analysis of SCIAMACHY nadir spectra.

As stated in table 3C, various alternatives for the Fraunhofer reference spectra were tested for the analysis: The spectrum measured after the diffuser of the elevation scanning mirror (ESM, compare Fig. 3.16), a spectrum recorded from the azimuth scanning mirror (ASM), and a mean of earth shine spectra at a solar zenith angle of 70°, like in the GOME OClO analysis (see section 3.6).
The results obtained for the OClO SCDs by applying these different Fraunhofer references are discussed in section 6.1.1.

3.8 OClO Retrieval from SCIAMACHY LIMB Spectra

For the OClO analysis of SCIAMACHY spectra measured in the limb geometry, the same wavelength range as for the SCIAMACHY nadir analysis is used. Also, the included reference spectra are similar (see table 3D), the only exception is the Fraunhofer reference.

Spectrum	Remark
OClO	213 K, [*Krominga et al., 2003*]
O_3	223 K, [*Bogumil et al., 2003*]
O_4	298 K [*Greenblatt et al., 1990*]
NO_2	220 K, [*Vandaele et al., 1997*]
Ring	Calculated, [*Bussemer, 1993*]
Offset	$1/I_o$ included in Fit
Polarisation 1	Eta from key data
Polarisation 2	Zeta from key data
Fraunhofer 1	Atmospheric spectrum, Tangent Height of 27 km
Fraunhofer 2	Direct solar spectrum, ASM

Table 3D: Reference spectra included in the OClO analysis of SCIAMACHY limb spectra

While the analysis was tested with various Fraunhofer reference spectra, the best results in terms of consistency with expectations from atmospheric chemistry and smallest fit errors are obtained for the reference consisting of a mean of spectra measured at a tangent height of 27 km. An example for the OClO retrieval is shown in Fig. 3.21. The fit with the ASM spectrum provides similar OClO SCDs, but the error of the fit is considerably larger. This causes the averaging kernels of the optimal estimation to be reduced, resulting in the retrieved profiles to be stronger influenced by the a priori (see section 3.3).

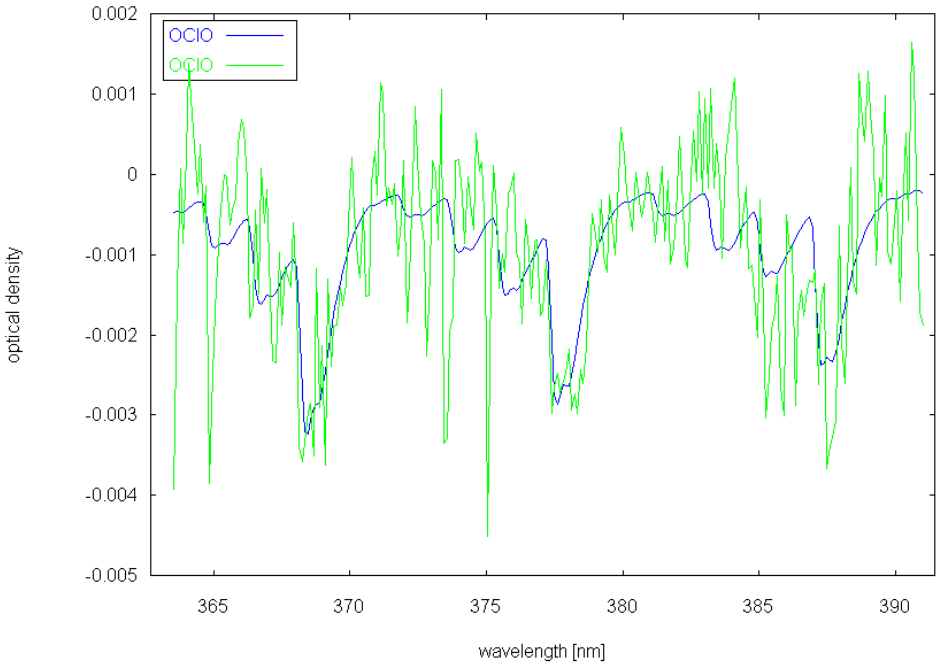

FIGURE 3.21: Example for an OClO analysis of SCIAMACHY limb spectra, Fraunhofer reference consisting of the mean of the four limb scan pixels at a tangent height of 27 km.

3.9 Retrieval of O_3, NO_2 and BrO from SCIAMACHY Limb Spectra

Limb Retrieval of O_3

For the O_3 analysis of SCIAMACHY limb spectra we utilize the wavelength range from 337 to 358 nm. Included reference spectra are: O_3, BrO, NO_2, Ring, and the Eta and Zeta Spectrum (from key data) for the correction of polarisation features, see Table 3E. The absorption spectrum of ozone shows a significant temperature dependence: For colder temperatures (corresponding to the stratosphere) the cross section at the peaks of the spectrum increases (and thereby the differential absorption spectrum), which needs to be considered in the DOAS analysis. Therefore, we use ozone absorption cross sections, measured by the SCIAMACHY spectrometer, at two different temperatures. To avoid interference, these spectra were orthogonalized.

Spectrum	Remark
O_3	243 K, [*Bogumil et al., 2003*]
O_3	223 K, [*Bogumil et al., 2003*]
BrO	228 K, [*Wilmouth et al., 2002*]
NO_2	220 K, [*Vandaele et al., 1997*]
Ring	Calculated, [*Bussemer, 1993*]
Offset	$1/I_o$ included in Fit
Polarisation 1	Eta from key data
Polarisation 2	Zeta from key data
Fraunhofer	Direct solar spectrum, ESM

Table 3E: Reference spectra included in the ozone analysis of SCIAMACHY limb spectra

Due to less intensity of the scattered sunlight measured for tangent heights corresponding to higher altitudes (see Fig. 1.6.) the signal to noise ratio decreases, thereby increasing the error of the retrieved SCD, see Fig. 3.22.

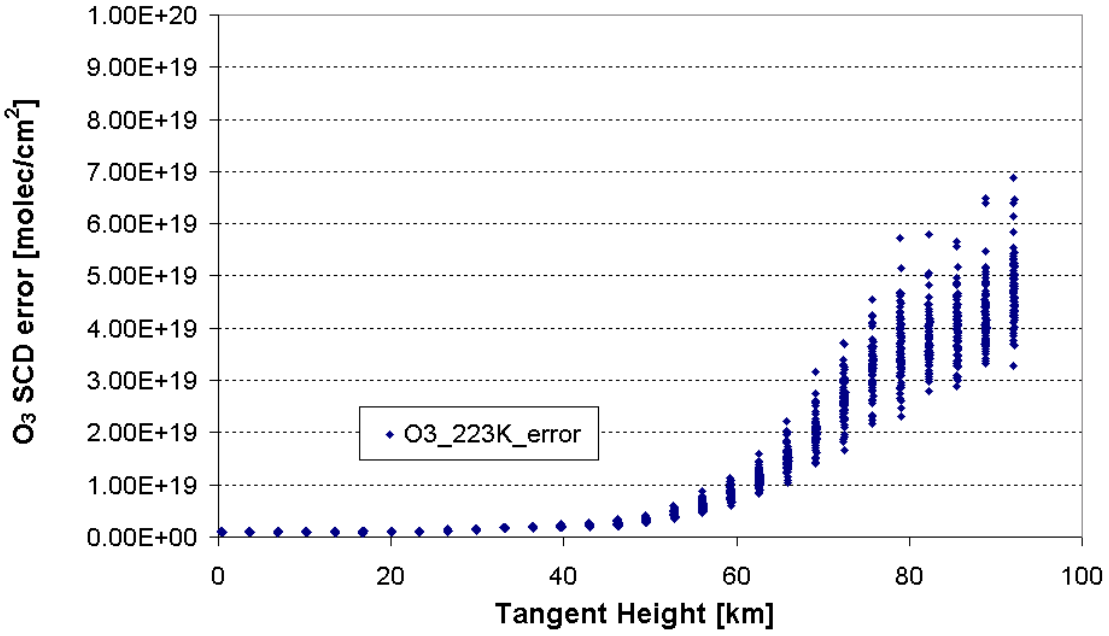

FIGURE 3.22: Typical error of SCIAMACHY O_3 SCDs, determined by the DOAS analysis.

Also, the ozone absorption is significantly smaller for tangent heights above the ozone layer, thereby again decreasing the signal to noise ratio, as can be seen in the examples for ozone retrievals at tangent heights of 20 and 40 km, shown in Fig. 3.23.

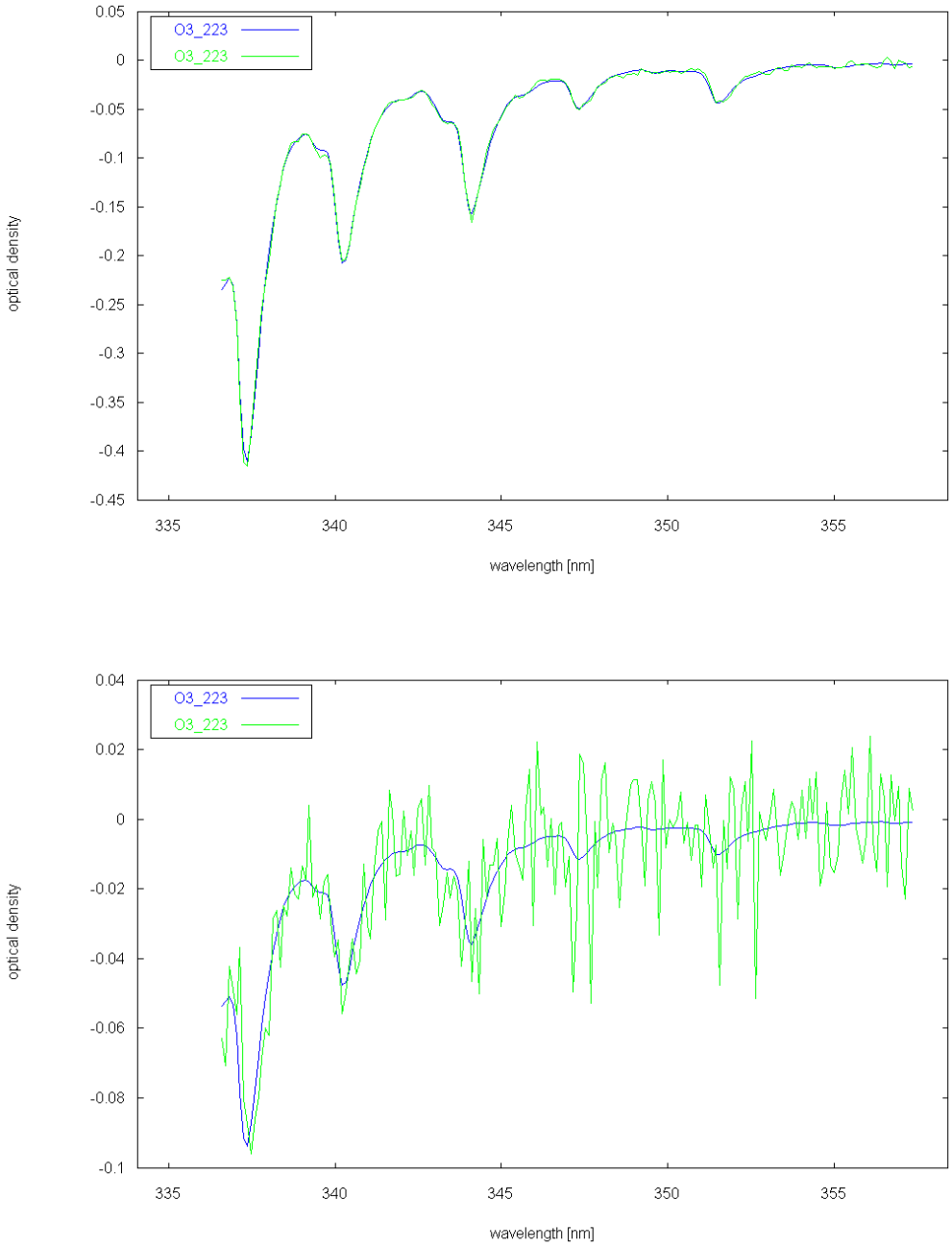

FIGURE 3.23: Example for an O_3 analysis of limb spectra. Shown is the optical density of the fitted ozone cross section (blue line) and the same including also the residual of the fit (green line). Top: for a measurement spectrum at a tangent height 20 km, bottom: for a measurement spectrum at a tangent height of 40 km.

Limb Retrieval of NO_2

The NO_2 analysis of SCIAMACHY limb spectra is performed in the wavelength range from 420 to 450 nm, see Fig 3.24. Included trace gas absorption cross sections are: NO_2, O_3 H_2O and O_4, see table 3F.

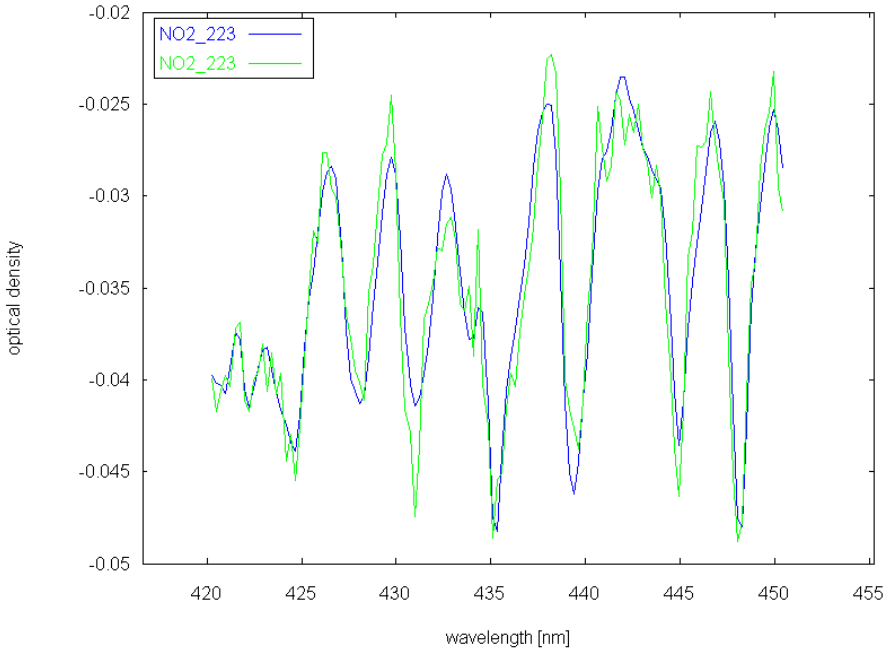

FIGURE 3.24: Example for an NO_2 analysis of limb spectra. Shown is the optical density of the fitted NO_2 cross section (blue line) and the same including also the residual of the fit (green line).

Spectrum	Remark
NO_2	223 K, [Bogumil et al., 2003]
O_3	241 K, [Bogumil et al., 2003]
H_2O	273 K, [HITRAN]
O_4	298 K [*Greenblatt et al., 1990*]
Ring	Calculated, [*Bussemer, 1993*]
Offset	$1/I_o$ included in Fit
Fraunhofer	Atmospheric spectrum, Tangent Height of 37 km

Table 3F: Reference spectra included in the NO_2 analysis of SCIAMACHY limb spectra.

During this thesis it turned out that the NO_2 SCDs, which are fitted also in the OClO analysis (see section 3.8, table 3C) are of similar magnitude like the ones from the actual NO_2 fit window. Also the fit error is comparable, in some cases even smaller. Thus, in order to minimize the calculations for box air mass factors, which are very time consuming, the results of the vertical NO_2 profiles presented in this thesis are obtained by the analysis in the OClO fit window. However, this is only a preliminary solution, to save time and work. Once the retrieval and the calculation of box AMFs is working on a routinely basis, we will derive the NO_2 profiles from the traditional NO_2 fit window from 420 to 450 nm, which will also increase the sensitivity for lower altitudes.

Limb Retrieval of BrO

The BrO analysis of SCIAMACHY limb spectra is performed in the wavelength range from 337 to 358 nm (see Fig 3.25), the same as for the limb retrieval of ozone. Included reference spectra are also the same as for ozone (see table 3E) except for the spectrum used as Fraunhofer reference. While for the ozone retrieval, the ESM spectrum is used, for BrO we use a spectrum measured at a tangent height of 37 km as Fraunhofer reference. This results in considerable smaller fit errors, which is essential to assure that the retrieved profile results mainly from the measurement and not from the a priori (see section 3.3).

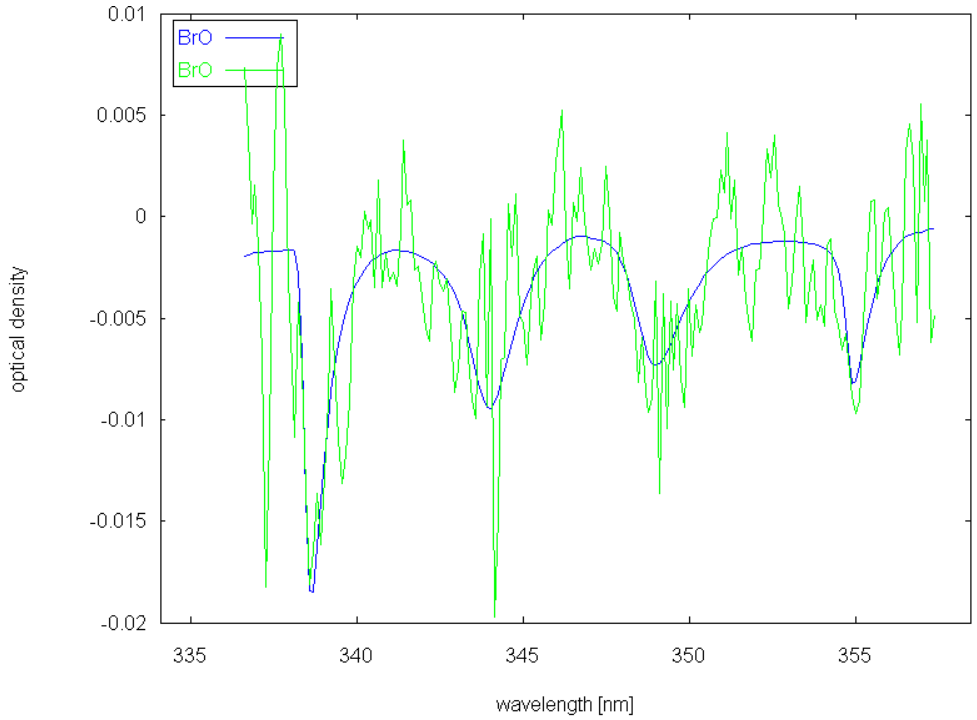

FIGURE 3.25: Example for an BrO analysis of limb spectra. Shown is the optical density of the fitted BrO cross section (blue line) and the same including also the residual of the fit (green line).

First results on the retrieval of vertical BrO profiles and a comparison to other BrO analyses of SCIAMACHY limb spectra are presented in section 6.2.3.

4 OClO as Indicator of Stratospheric Chlorine Activation

While ClO can be measured in the stratosphere by established in situ methods and microwave spectroscopy, Cl_2O_2 could be measured only recently in situ. Thus, of the active chlorine species in the stratosphere, none can be measured by UV/VIS absorption spectroscopy. However, OClO, which is formed by reaction of ClO and BrO and possesses a large differential cross section in the near UV, can be detected by DOAS. This makes OClO an important molecule to observe for studying stratospheric chemistry.
In particular, satellite measurements, which provide global and long time monitoring of active chlorine are very sparse. Therefore the GOME and SCIAMACHY measurements of OClO are an important contribution to increase the knowledge of stratospheric ozone chemistry. However, these observations also have considerable caveats.
First, the SCDs of a nadir measurement are inherently amplified for larger solar zenith angles due to the increase of the air mass factor. This is especially important for OClO measurements which are usually analysed for large SZAs. The dependency of the AMF on the vertical profile, which is not known a priori for OClO, also increases for larger SZAs. Therefore, OClO vertical column densities are usually not determined.
Second, also if converted to VCDs, the OClO observations can not be interpreted as a measurement of the chlorine activation level, since they still depend on the photolysis rate of OClO, which in turn strongly depends on the intensity of solar illumination and thereby also on the SZA. I.e., because of the short lifetime due to rapid photochemical depletion, the same concentrations (or column densities) of OClO, measured at different SZAs, correspond to different abundances of ClO.

This chapter investigates the aforementioned points in detail in order to assess how measurements of OClO can (qualitatively and quantitatively) be interpreted as indication of active chlorine species:

- First, the uncertainty in calculation of air mass factors due to the unknown vertical profile, and the related problems in converting the OClO SCDs to VCDs is described.

- Then, the photochemistry of OClO and its impact on the presented GOME observations is studied.

- Finally, the relation of OClO to its educts, ClO and BrO, and to NO_2, which together with ClO forms the important chlorine reservoir $ClONO_2$, is investigated.

4.1 Problems in calculating OClO VCDs

As described in section 3.1, the quantity derived from the DOAS analysis is the slant column density (SCD). To convert the SCDs into vertical column densities, they need to be divided by the air mass factor (AMF), see Eq. (3.5).
Fig. 4.1 shows AMFs for OClO calculated by the radiative transfer model AMFTRAN [*Marquard et al., 2000*] for different vertical profiles of OClO. At large SZA ($\vartheta > 88°$), for which OClO measurements are typically analysed, the AMF depends strongly on the profile shape. Thus, the calculation of OClO AMFs for SZAs larger than 88° is only possible if the profile is known (or can be estimated) from an independent measurement. However, this is generally not the case.
Due to the formation by the ClO-BrO reaction, the vertical OClO profile is determined by the abundance of ClO (and also BrO), which in turn depends very much on the occurrence of PSCs. PSCs form when the temperatures drop below T_{NAT} or T_{ICE} respectively, (see section 2.2) and may occur at altitude ranges from 15 to 25 km [*Poole and Pitts, 1988*]. Of course also vertical transport can shift the OClO enriched air masses. However, especially in the activation phase in early winter, the height of the maximum in OClO concentration will be largely determined by the height at which PSC formation is possible. Thus, just like the PSCs, the maximum OClO concentration can be situated at very different heights. As can be seen in Fig. 4.1, a difference in the height of the OClO maximum of 3 km makes already an uncertainty of factor 2 in the AMF calculation.

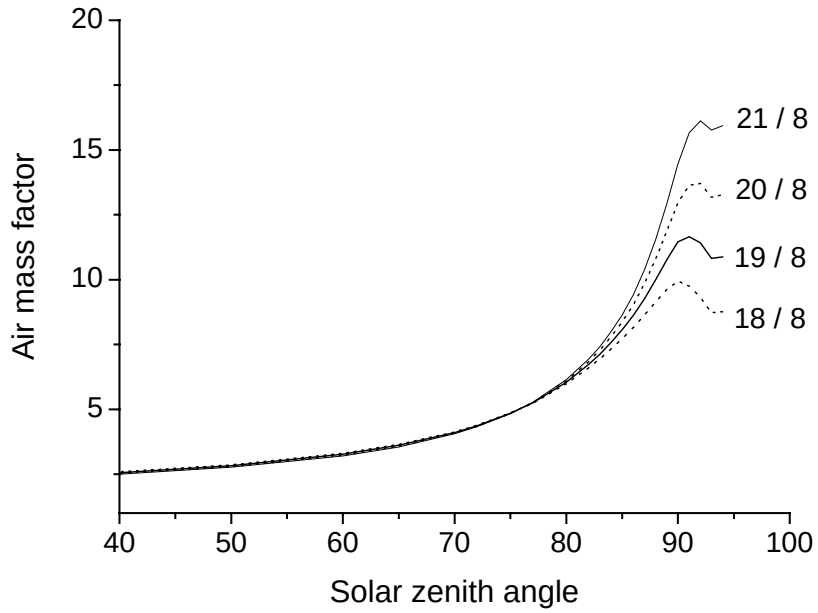

FIGURE 4.1: Air mass factors for OClO as a function of the solar zenith angle calculated by the radiative transfer model AMFTRAN for different gaussian vertical profiles of the OClO mixing ratio (Height of maximum and full width at half maximum in km as stated).

Therefore, most of the GOME and SCIAMACHY OClO observations in this thesis are presented as SCDs. An exception is the chlorine activation induced by mountain waves, which takes place at regions corresponding to relatively low SZAs (85°). For these SZAs, the AMF of OClO shows only a slight dependence on the vertical profile and thus the SCDs can be converted to VCDs with only little uncertainty (see section 7.2).

4.2 Photochemistry of OClO

OClO is almost entirely formed by one product channel of the reaction between ClO and BrO [*Sander and Friedl, 1989; Toumi, 1994*], which forms a null-cycle regarding ozone destruction:

$$ClO + BrO \rightarrow OClO + Br \qquad (R\ 4.1)$$

Other channels of the ClO-BrO reaction lead to the formation of BrCl and ClOO (which rapidly decays to Cl and O_2), see also section 2.2.3.

$$ClO + BrO \rightarrow ClOO + Br \qquad (R\ 4.2)$$

$$ClO + BrO \rightarrow BrCl + O_2 \qquad (R\ 4.3)$$

Since the reaction constants for these path ways show a different dependency on temperature, also the branching ratio of the ClO-BrO reaction varies with temperature: For lower temperatures, like the ones occurring in the polar stratosphere, the path forming OClO is favorized, see Fig. 4.2.

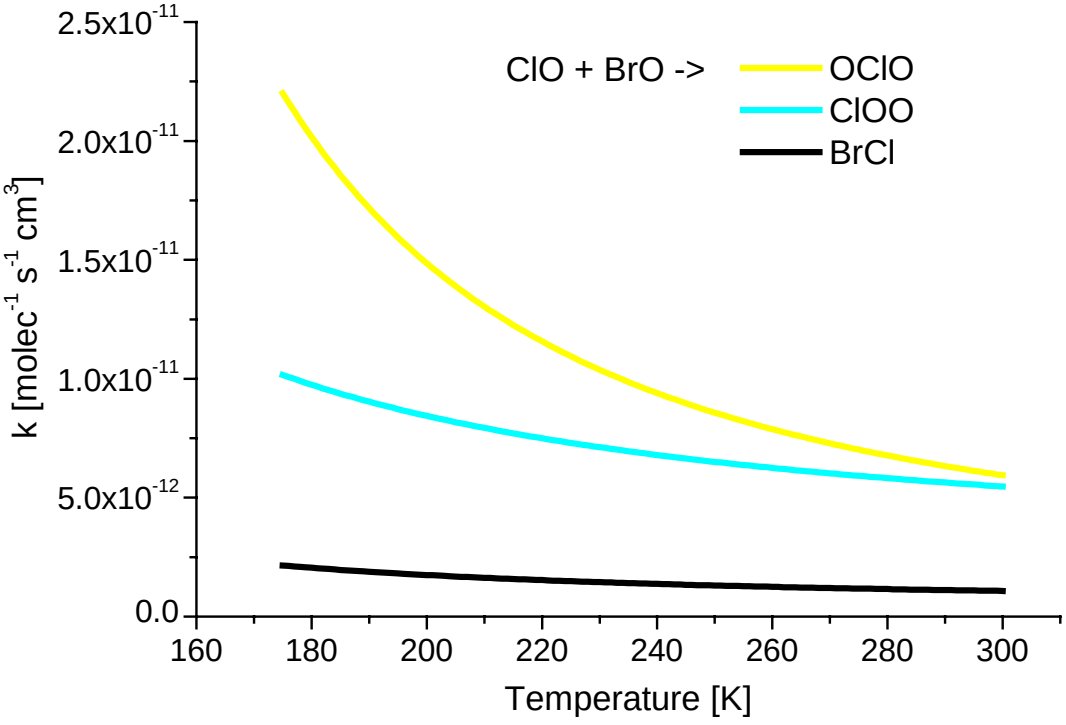

FIGURE 4.2: Temperature dependence of the rate coefficients for the three paths of the bimolecular reaction ClO + BrO in the range from 175 to 300 K. Reaction rates are taken from [*JPL, 2003*].

The major loss mechanism for stratospheric OClO is its rapid photolysis:

$$OClO + h\nu \rightarrow ClO + O \quad (\lambda < 480\ nm) \qquad (R\ 4.4)$$

The formation reaction (R 4.1) and the photolysis of OClO (R 4.4) lead to a quickly attained balance between ClO and OClO. Assuming a steady state, the concentration of OClO at daytime is given by [*Solomon et al., 1990; Schiller and Wahner, 1996*]:

$$[OClO] \approx \frac{k[ClO][BrO]}{J(OClO)} \qquad (4.1)$$

In the above equation, the square brackets represent the concentration of the molecules, k is the rate constant for the formation reaction (R 4.1), and J(OClO) the photolysis frequency of OClO.
This steady state assumption and therefore the linearity between the concentrations of ClO and OClO is valid only for small SZAs ($\vartheta < 90°$). For larger SZAs (especially above 92°) bromine chloride (BrCl), formed in (R 4.3), becomes an important reservoir and the production of OClO via (R 4.1) is limited by the availability of BrO [*Sessler et al., 1995; Schiller and Wahner, 1996*]. Although OClO is not a good quantitative indicator of chlorine activation for large solar zenith angles ($\vartheta > 92°$) [*Sessler et al. 1995*], there is general agreement that the concentration of OClO depends nearly linearly on the concentration of ClO and BrO for $\vartheta < 90°$ [*Schiller and Wahner, 1996; Sessler et al., 1996; Tornkvist et al., 2002*].

The photolysis frequency J (OClO) can be calculated by multiplying the actinic flux (see section 1.3) with the absorption cross section:

$$J(OClO) = F * \sigma(OClO)$$

For this study, photolysis frequencies of OClO were calculated by the photolysis model as used in the SLIMCAT chemical transport model [*Chipperfield, 1999*], which is based on *Lary and Pyle* [*1991*]. The model takes into account spherical geometry and multiple scattering. OClO absorption cross sections are taken from *Wahner et al.* [*1987*]. Our standard calculations assumed an albedo of 0.3. Sensitivity calculations with albedos of 0.9 and 0.1 led to a variation of the OClO photolysis frequency of only about +/- 5% at a solar zenith angle of 83 degrees. As the maximum of the OClO absorption cross section is around 350 nm, there is little impact of the overhead ozone column on the OClO photolysis frequency.
Figure 4.3 shows photolysis frequencies of OClO (J(OClO)) as a function of the solar zenith angle (SZA) for 5 pressure levels between 210 and 8 hPa.

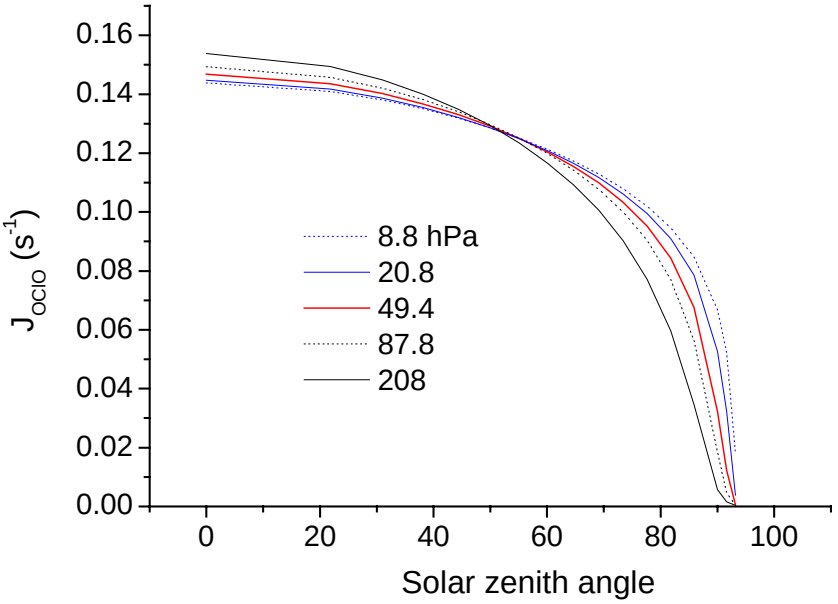

FIGURE 4.3: Photolysis frequency of OClO (J(OClO)) for different pressure levels calculated by a photolysis model based on *Lary and Pyle [1991]*. J(OClO) is plotted as a function of the solar zenith angle for 5 pressure levels between 210 and 8 hPa.

Especially for SZAs above 90°, J(OClO) drops rapidly, reaching values close to zero around SZA=95°. Thus, OClO features a strong diurnal cycle, see Fig. 4.4.

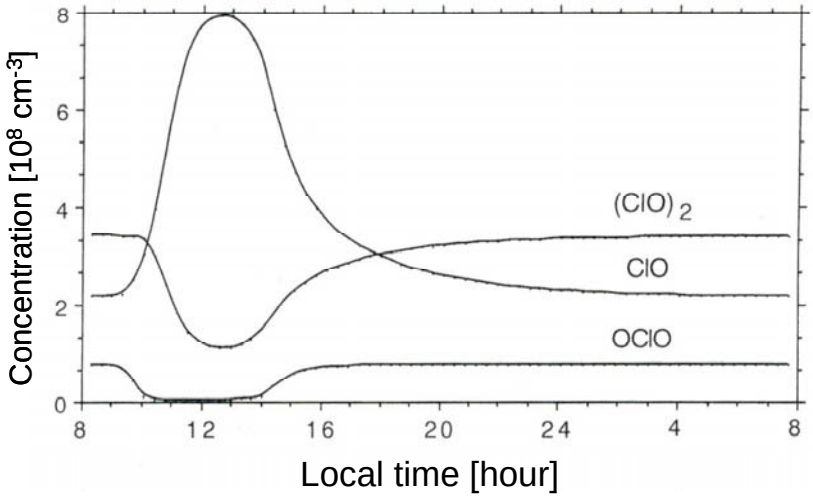

FIGURE 4.4: Diurnal cycle of OClO, ClO and the ClO dimer. Adapted from [*Schiller, 1990*].

The dependence of the OClO SCDs on the air mass factor (see section 4.1) and the photolysis frequency of OClO both lead to larger OClO SCDs for high SZAs. For a quantitative comparison of OClO measurements at different SZAs, these effects have to be taken into account. Another difficulty in interpreting the OClO SCDs arises from the strong diurnal cycle of OClO and the fact that measurements of OClO are usually made at large SZAs. Due to the slant viewing geometry (compare Fig. 3.3) the measurement is an average of air masses with a horizontal extent of several 100 km. For example, a measurement made at a SZA of 90° contains contributions from locations with SZAs in the range from 86° to 90° [*Platt et al., 1997*] and thus with lower OClO concentration. One possibility to account for this chemical enhancement [*Solomon et al., 1987; Platt et al., 1997*] is to apply a chemical air mass factor to the measurement, see Fig. 4.5

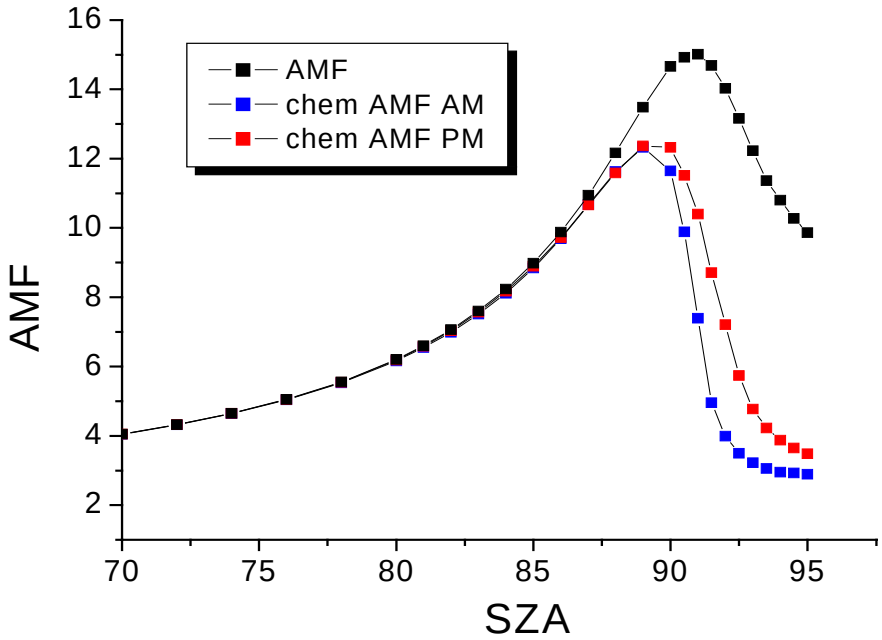

FIGURE 4.5: Chemical air mass factor for OClO for sunrise (blue dots) and sunset (red dots) as function of the SZA. In comparison, the black line shows the standard AMF for OClO [*Hendrick and van Roozendael, personal communication, 2004*].

4.3 Relation to ClO

As described above OClO is a good quantitative indicator for SZAs below 90 degrees. If the OClO SCD can be converted to a vertical column density and the concentration of OClO can be determined, the concentration of ClO can be calculated according to (Eq. 4.1):

$$[ClO] \approx \frac{[OClO] * J(OClO)}{k[BrO]} \qquad (4.2)$$

Thus, to estimate the concentration of ClO from the one of OClO, the following parameters need to be known:

- The concentration of OClO
- The temperature, to calculate the reaction rate constant k - (see Fig. 4.2)
- The SZA to calculate the photolysis rate J(OClO) – (see Fig. 4.3)
- The concentration of BrO – see section 4.4

Fig. 4.6 illustrates the relation between the vertical column density of OClO as a function of the ClO mixing ratio for different mixing ratios of BrO.

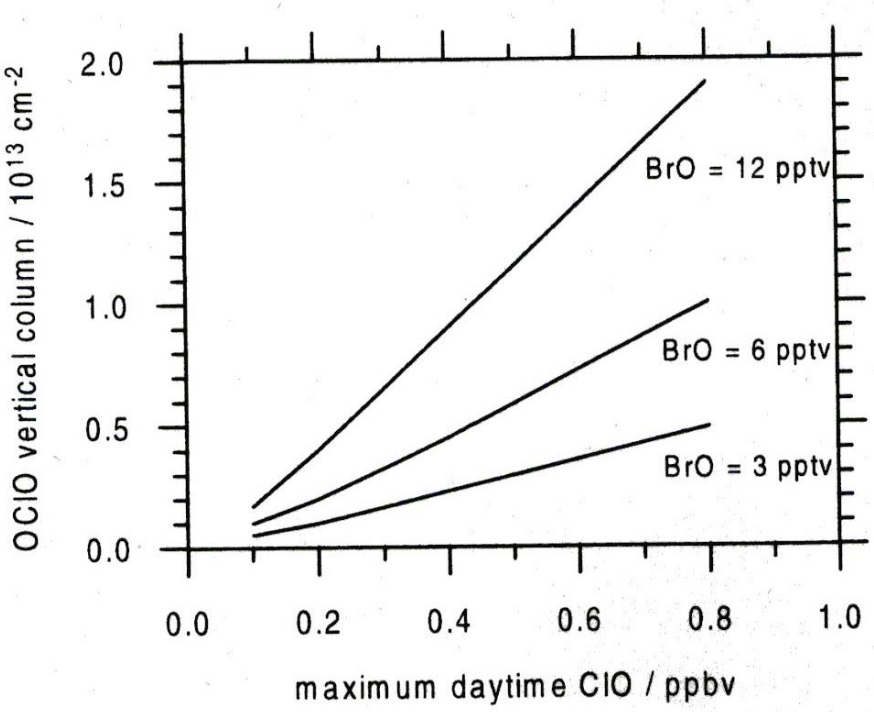

FIGURE 4.6: Dependence of OClO column abundances at SZA=88° on the mixing ratio of ClO and BrO. Adapted from [*Schiller and Wahner, 1996*]

4.4 Relation to BrO

According to (Eq. 4.1), the concentration of OClO is linear to both of its educts, ClO and BrO. Thus, to quantify the level of chlorine activation from the OClO observations, the abundance of BrO needs to be accounted for. Fig. 4.7 shows measurements and calculations of the BrO mixing ratio for the altitude range from 6 to 40 km. For the altitude range where peak mixing ratios of ClO and OClO are expected (17 to 24 km), the mixing ratio of BrO varies between 10 and 15 pptv for the polar regions.

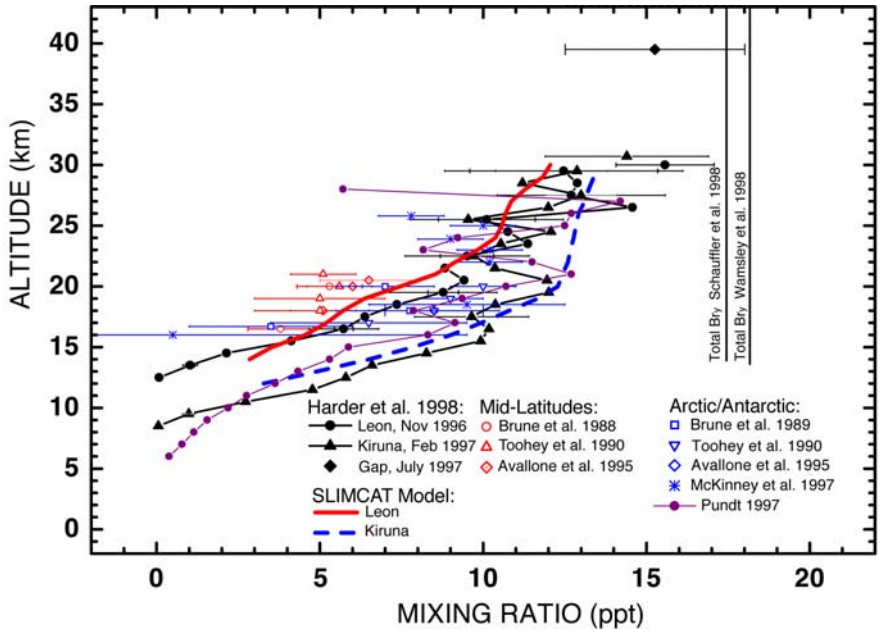

FIGURE 4.7: BrO profiles measured for midlatitudes and polar region between 1989 and 1998, compared to results from the chemical transport model for midlatitude (red) and polar conditions (blue). Also shown is the total Br_y. Adapted from [WMO, 2003]

4.5 Relation to NO_2

Stratospheric chlorine and nitrogen chemistry is coupled by formation of the reservoir compound chlorine nitrate, $ClONO_2$, through reaction of ClO and NO_2, see also section 1.3.3.
The partitioning between $ClONO_2$ and its educts has been studied by simultaneous satellite measurements of ClO, NO_2 and $ClONO_2$ [*Dessler et al., 1996*]. For the investigated latitude range (60° S to 60° N) the observations were found to be consistent with photochemical calculations for SZAs below 80°.
On the other side, nighttime measurements of OClO and NO_2 in the Arctic polar vortex revealed considerable discrepancies between modeled and observed abundances of both species [*Riviere et al., 2003; Canty et al., 2005*], indicating that there are uncertainties in the interaction of chlorine and nitrogen species. However this discrepancy does not concern measurements of OClO for SZAs below 92°.

5 GOME Results

The GOME observations of global atmospheric trace gas column densities for now almost ten years provide a unique dataset to study various aspects of stratospheric and tropospheric chemistry.
This chapter focuses on the monitoring of chlorine activation by the GOME OClO measurements, the intercomparison of the magnitude, duration and spatial extent of chlorine activation for the two hemispheres, and the question how well these observations agree with other measurements and model studies. In addition, in case studies we investigated the dependence of heterogeneous processing of chlorine species on meteorological conditions, and the relation of chlorine activation to stratospheric ozone and related compounds like nitrogen dioxide also observed by GOME.

The chapter is structured as follows:

- The first section gives an overview of the GOME OClO observations in Arctic winters in comparison to the ones in Antarctic winters. For certain interesting winters, the evolution of chlorine activation is investigated in detail.

- The GOME OClO observations are then compared to other measurements of chlorine activation, like ground-based OClO and space borne ClO observations (section 5.2), as well as to results from model simulations (5.3).

- The chapter concludes with some case studies: The dependence of chlorine activation (as derived from the GOME OClO measurements) on stratospheric temperatures and the occurrence of PSCs is investigated. This is related to the observations of chlorine activation due to adiabatic cooling in mountain waves, which are discussed in detail in chapter 7. Then the relation to other trace gases observed by GOME is investigated: GOME measurements of ozone and OClO in polar spring reveal the relation between chlorine activation and ozone depletion. As well, the dependence of the time for chlorine deactivation on the degree of denitrification inside the polar vortex is studied.

5.1 Monitoring of chlorine activation

The observation of the activation of chlorine species on a global scale and for a long time period is an important issue in atmospheric chemistry: First, the degree of chlorine activation during polar winter and spring is directly related to the amount of chemical ozone loss in polar spring. Second, the decrease of the chlorine loading as consequence of the Montreal protocol will cause also the amount of active chlorine to be gradually reduced. Global long time measurements will allow to track this decrease and to study if it is declining as expected or if the increase of the abundances of greenhouse gases and the decrease in stratospheric temperatures will cause unexpected magnifications in the activation of chlorine species.
Ground based measurements of ClO and OClO serve this need only partially, since they can provide just a regional overview of the active chlorine abundance at the location of the measurement site. Thus, the advantage of satellite instruments, to provide global and long time measurements, is in particular valuable for the monitoring of chlorine activation.
The dependence of active chlorine on the formation of PSCs and thus on stratospheric temperatures makes its measurement essential to forecast polar ozone depletion. Especially for the northern hemisphere, the large variability of stratospheric temperatures and the strength of the polar vortex is determining the magnitude of the ozone loss in spring.
Satellite measurements of ClO [*Santee et al., 1995; Santee et al., 2003*] and OClO [*Wagner et al., 2001*] have displayed this dependency of stratospheric chlorine activation on meteorological conditions: The intensity, the beginning and duration, and the spatial extent of chlorine activation derived from GOME OClO measurements correlates well with the evolution of the stratospheric temperatures and the location of the polar vortex [*Wagner et al., 2001; Wagner et al., 2002a; Kühl et al., 2002; Richter et al., 2004*]. Therefore, OClO column densities measured by GOME in the Arctic stratosphere show a strong annual variability [*Wagner et al., 2001; Wilms-Grabe et al., 2002; Kühl et al., 2004*]. In contrast, OClO column densities above the Antarctic show the same magnitude and temporal evolution each year [*Wagner et al., 2001*], with the exception of the winter 2002, where a major warming in September caused a rapid decrease of the observed OClO values [*Richter et al., 2004*]. In both hemispheres, a strong anti-correlation exists between the GOME OClO column densities and the winter eddy heat flux [*Weber et al., 2003*].

5.1.1 Overview of GOME OClO Measurements 1995-2004

During this thesis, the monitoring of stratospheric chlorine activation by GOME OClO measurements, begun with the studies of Thomas Wagner [*Wagner et al., 2001; Wagner et al., 2002a*], has been continued and thus, all northern and southern hemisphere winters observed by GOME were analysed for OClO absorptions. However, due to a tape record failure of ERS-2, the GOME measurements since June 2003 are transferred only for some small orbit parts when the satellite is in contact with the ESA ground station in Kiruna, providing only very small coverage of the polar regions. Therefore, the actual time period investigated ranges from 1995 to 2003.
As discussed in chapter 4, OClO shows a strong diurnal cycle, which has to be taken into account when studying measurements for different times and locations. To compare the magnitude of the chlorine activation for different days and regions, the OClO measurements are analysed at a fixed SZA of 90°. For this SZA, the concentration of OClO is almost linear to the one of ClO. However, the retrieved SCD is impacted by the vertical profile of OClO. Also, one has to consider that the latitude corresponding to a SZA of 90° changes during the winter.
Figure 5.1 shows the OClO SCDs at SZA=90° for all Arctic and Antarctic winters observed by GOME. It reflects the difference in the meteorological conditions (compare section 2.2 and Fig. 2.2): While the SCDs measured over the Antarctic show the same evolution for all winters (corresponding to the constant strength of the polar vortex), the large variability of stratospheric meteorology above the Arctic results in winters with large OClO SCDs (like 1995/96, 1996/97, 1999/2000) and winters with weak or almost no chlorine activation (like 1997/98, 1998/99, 2000/01, 2001/02).

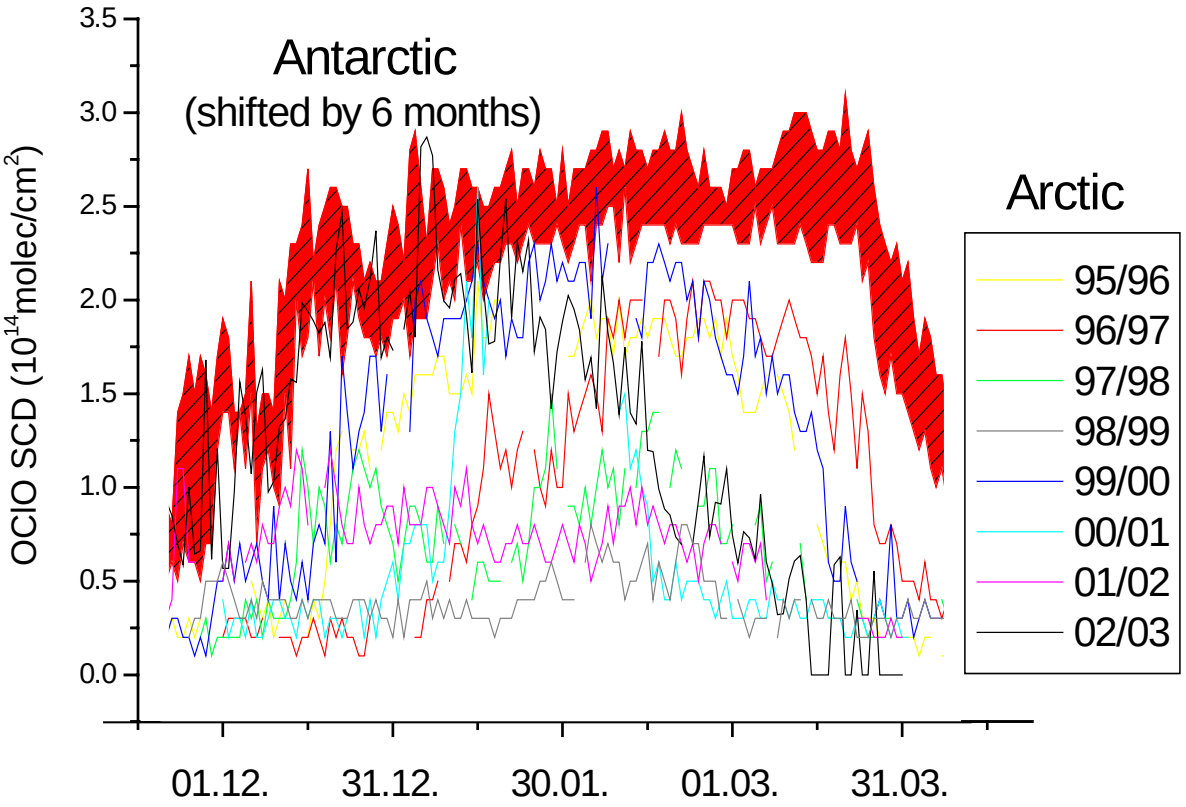

FIGURE 5.1: Daily maximum OClO SCD at an SZA of 90° for the Arctic winters 1995/96 to 2002/03. As comparison the values for the Antarctic winters, shown as envelope of the maximum and minimum values from 1996 to 2001, are shifted by 6 months.

Of course this relation is expected, since the formation of PSCs and the heterogeneous reactions converting the reservoir compounds into active species is strongly depending on temperatures (see Figs. 2.1 and 2.4). Figure 5.2 reveals this dependence of chlorine activation on stratospheric temperatures for all Arctic winters observed by GOME. Displayed is again the OClO SCD at a SZA of 90°. Also shown is the minimum temperature at the T_{pot} = 475 K level. The dotted line marks the threshold temperature for formation of PSC type I. One can see very nicely that these two values are strongly anti-correlated: As soon as the temperature falls below the threshold for PSC formation (T_{NAT}) the column densities of OClO increase. Vice versa, when the minimum temperature rises above this value (195 K for the altitude of ≈ 19.5 km, corresponding to the Θ = 475 K level) the SCDs of OClO gradually decline.
The relation of the OClO SCDs to stratospheric temperatures is further investigated in section 5.4.1.

Some of the winters are especially interesting due to their extraordinary low or high temperatures or OClO SCDs:

- The winter 1996/97 with large OClO SCDs (> 1.5 * 10^{14} molec/cm^2) observed up to mid of march.
- The winter 1998/99, which was the warmest of all GOME winters and thus only sporadic activation of chlorine was observed.
- In 1999/2000 the coldest synoptic scale temperatures so far were observed, resulting in large OClO SCDs from end of December until beginning of March
- And in the winter 2002/2003, OClO SCDs in December were extremely large, resulting from temperatures below T_{NAT} over a wide altitude range already in the early winter.

These winters are investigated in detail in sections 5.1.3 to 5.1.6

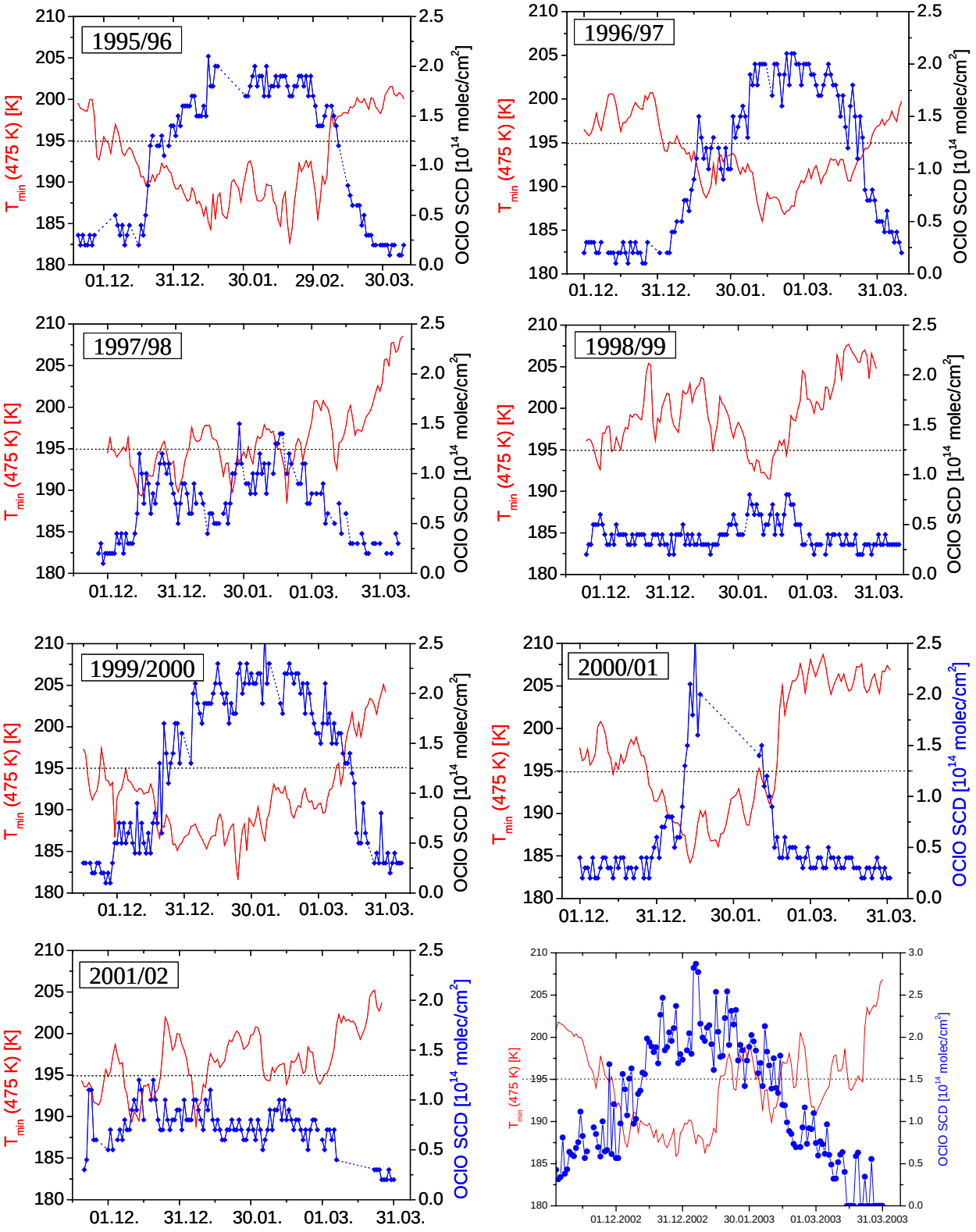

FIGURE 5.2: Daily maximum OClO SCDs at a SZA of 90° and minimum temperature at the Θ=475 K level (according to ECMWF data obtained from the NILU data server) for the Arctic winters 1995/96 to 2002/03.

5.1.2 Comparison between northern and southern hemisphere

The analysis of the OClO SCDs at a SZA of 90° revealed the differences in magnitude, duration and variability of chlorine activation in the austral and boreal winters (see Fig. 5.1). To study these and possible further interhemispheric differences in more detail, we consider the temporal evolution of the spatial extent of air masses showing enhanced chlorine activation during typical Arctic and Antarctic winters. As described in section 2.2 the larger variability in topography of the northern hemisphere causes the Arctic polar vortex to be displaced from the pole, while the southern counterpart is concentrically located around the pole. Fig 5.3 shows that, as consequence, minimum temperatures inside the Arctic vortex are usually found above Northern Scandinavia. Since low temperatures favor the formation of PSCs, this displacement of the vortex should also lead to larger mean values of the OClO SCDs above Northern Scandinavia compared to the remainder of the Arctic region.
To investigate this issue, we studied the evolution of air masses with enhanced OClO SCDs for characteristic Arctic and Antarctic winters. Fig. 5.4 shows monthly mean maps of GOME OClO SCDs for selected polar winters. For the Arctic, monthly mean OClO maps for the warmest winter 1998/99 and the coldest winter 1999/2000 are displayed, for the Antarctic we chose the winters of the year 2000 and the year 2002, when a major warming caused a rapid decrease of the OClO SCDs at the end of September [*Richter et al., 2004*]. Therefore, the chosen winters represent the largest variability in the extent of chlorine activation during the time of GOME observations for the respective hemisphere.
The monthly means reveal very nicely the much larger year to year variability in the degree of chlorine activation for the northern hemisphere; as well the spatial extent of activated air masses is much larger for the Antarctic. The difference in the duration of stratospheric chlorine activation can also be seen in the mean maps: For the Antarctic, the period with elevated OClO SCDs lasts much longer into spring, the time when the catalytic ozone depletion cycles are most effective. Even in the winter 1999/2000, which inhibited the largest OClO SCDs measured over a long time period for the North pole, almost no active chlorine remained until March, the month with most sunlight in polar spring and thus largest ozone depletion potential (compare section 2.2.3). Contrary, large OClO SCDs are observed in the Antarctic stratosphere until end of September, thereby causing much more depletion of ozone, see also section 5.4.2. One can also see that above the Antarctic, the chlorine activated air masses are concentrically located around the pole, while for the Arctic, they are displaced and shifted towards Northern Scandinavia, in good agreement with the location of the polar vortex and the minimum temperature, see Fig 5.3.

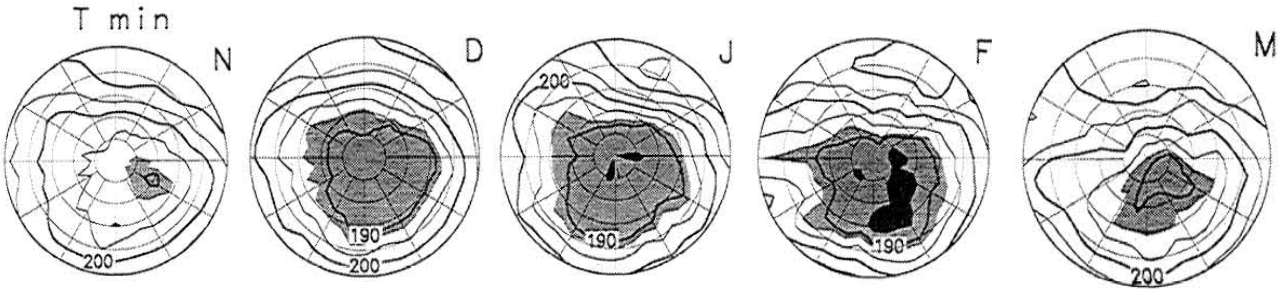

FIGURE 5.3: Average minimum temperatures at 30 hPa poleward of 40° N for the winter months of the years 1965/66 to 1993/94. Contour interval 5 K, light shading for T_{min} < 192 K, dark shading for T_{min} < 185 K, adapted from [*Pawson et al., 1995*].

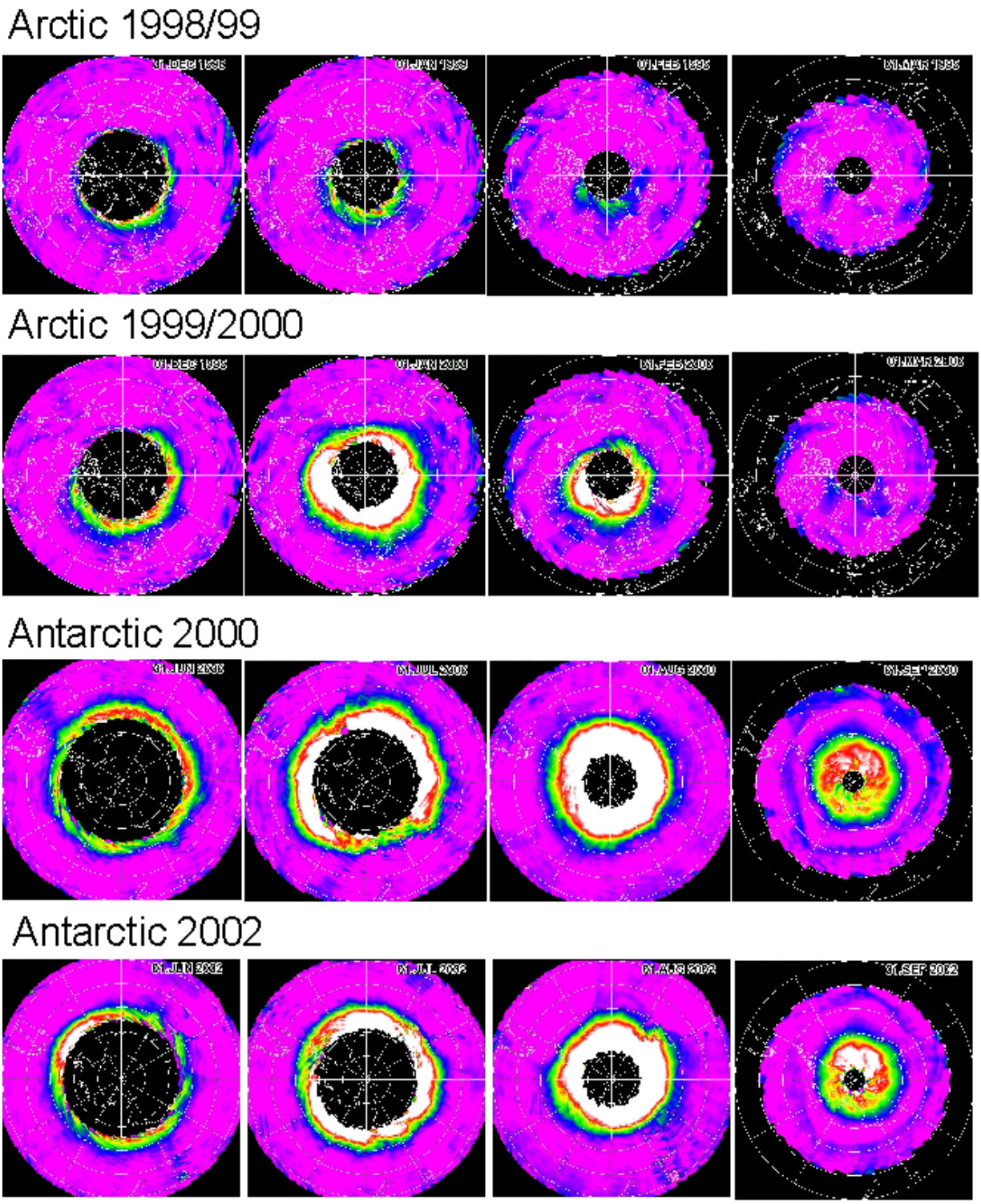

FIGURE 5.4: Monthly mean OClO maps for the Arctic winters 1998/99 and 1999/2000 and the Antarctic winters 2000 and 2002. Pole at center of the map, values are displayed for 66<SZA<92.

5.1.3 The Arctic winter 1996/97

Although GOME OClO SCDs for this winter were not unusually large, the total ozone column in March were the lowest in the time of the GOME observations, see also section 5.4.2. The reason for this was the extraordinarily late break up of the Arctic vortex, which enabled PSC formation until end of March, see Fig. 5.2. During the late winter and spring 1996/97 the polar vortex was very strong, cold and symmetric [*Coy et al., 1997*]. GOME measurements of OClO reveal that chlorine activation started in early January and lasted until end of March [*Wagner et al., 2001*], in consistency with observations from MLS and HALOE [*Santee et al., 1997; Müller et al., 1997*]. This persistence of high active chlorine levels until the end of the polar night resulted in substantial ozone loss [*Newman et al., 1997; Manney et al., 1997; Lefèvre et al., 1998; Terao et al., 2002; Tilmes et al., 2003*], stressing the increased efficiency of the ozone destruction cycles for days with more hours of sunlight.
In January 1997, there were diverse episodes of mountain wave activity above Northern Scandinavia (on the 11th, 16th, and from 20-22), the one on 21 January resulting in record low stratospheric temperatures for the northern polar region [*Dörnbrack et al., 1999*]. This strong mountain wave event caused formation of mesoscale PSCs type 2 (Ice) leading to a rapid increase in chlorine activation over a widespread region, as can be seen very clearly in the GOME OClO measurements [*Kühl et al., 2004*], see section 7.2.

5.1.4 The Arctic winter 1998/99

This winter was the warmest during the time of GOME observations, resulting in the smallest area for possible PSC formation since 1984/85. Accordingly, GOME observed only a brief period with enhanced OClO SCDs from end of January until end of February, see Fig. 5.2.
The meteorology and stratospheric chemistry during this winter has been intensively studied by the THESEO campaign and the results agree nicely with the GOME observations, demonstrating that OClO is also a good indicator for winters with only weak chlorine activation. There were mountain wave activities above Northern Scandinavia on January 22 and 26 [*Voigt et al., 2000*], which lead to local enhancements of the GOME OClO SCDs, see section 7.5.

5.1.5 The Arctic winter 1999/2000

In this winter, extremely cold stratospheric temperatures occurred inside the Arctic vortex from mid of December until beginning of March, resulting in the largest OClO SCDs observed for a long time period so far in the Arctic stratosphere [*Wagner et al., 2001*]. Again, these observations agree very well with results from the THESEO 2000 campaign. Single day OClO maps of this winter are shown in section 5.3.1, where the temporal evolution of the magnitude and spatial extent of chlorine activation is compared to results from the chemical transport model SLIMCAT.
From 25 to 27 January 2000, a large amplitude mountain wave event took place above Northern Scandinavia. This event has been intensively studied by model simulations [*Dörnbrack et al., 2002; Larsen et al., 2003*], and in situ [*Voigt et al., 2003*] and remote sensing observations [*Bevilacqua et al., 2002*]. Again, GOME OClO measurements during these days show a strong increase at the location of the mountain wave activity, see section 7.3.

5.1.6 The Arctic winter 2002/03

This winter is characterized by extraordinarily cold temperatures already in December, causing formation of PSCs over a large altitude range and the largest calculated area of possible PSC formation at the T_{pot} = 550 K level (≈ 21 km altitude) for all Arctic winters so far, see Fig. 5.5. The temporal evolution of the OClO SCDs observed by GOME is shown as the daily maximum value at a SZA of 90 degrees in Fig. 5.6 and as daily maps in a 15 day interval in Fig. 5.7. In comparison, the corresponding maps of stratospheric temperatures and the shape and strength of the polar vortex are also shown.

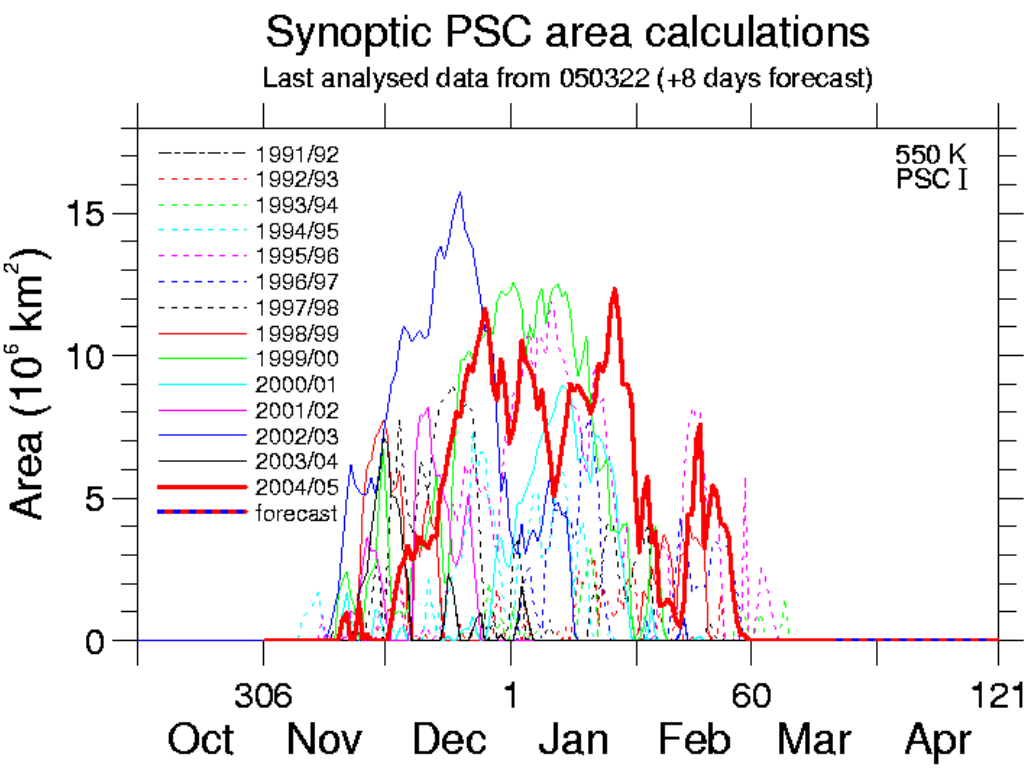

FIGURE 5.5: Daily areas of possible PSC type 1 (NAT) formation at the 550 K level for all Arctic winter since 1991/92, based on ECMWF temperatures and on the NAT existence hypothesis. Threshold temperatures are calculated according to [*Hanson and Mauersberger, 1988*]. Adapted from: http://www.awi-potsdam.de/www-pot/atmo/met/psc1.html

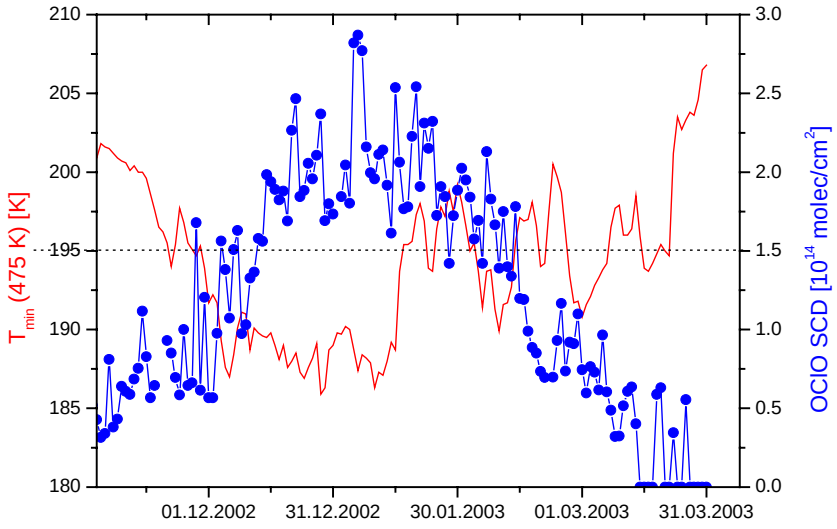

FIGURE 5.6: Daily maximum OClO SCDs at a SZA of 90° and minimum temperature at the Θ=475 K level (according to ECMWF data obtained from the NILU data server) for the Arctic winter 2002/03. Abscissa (date) scaled to match with Fig. 5.5.

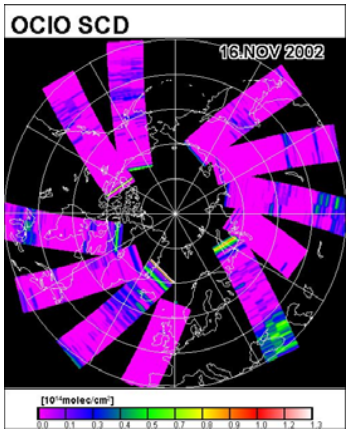
OCIO SCD
16.NOV 2002

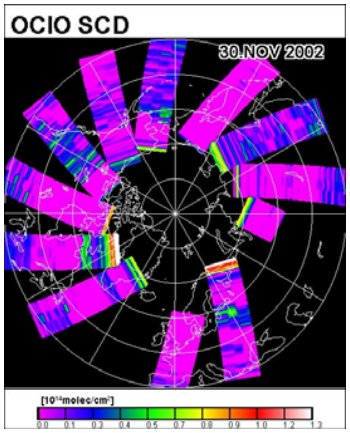
OCIO SCD
30.NOV 2002

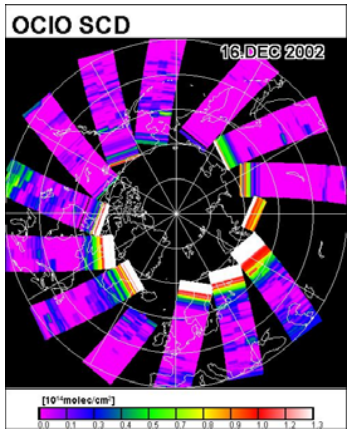
OCIO SCD
16.DEC 2002

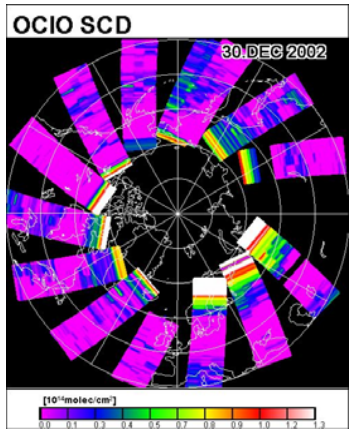
OCIO SCD
30.DEC 2002

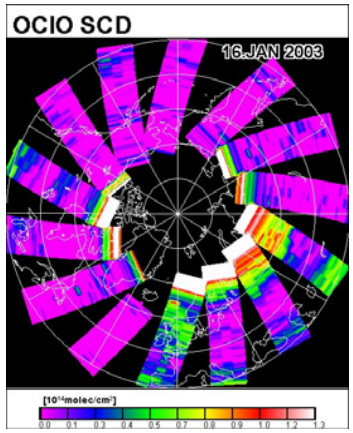
OCIO SCD
16.JAN 2003

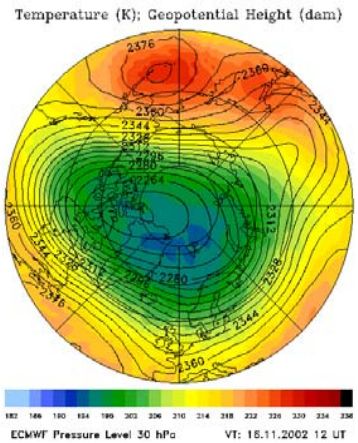
Temperature (K); Geopotential Height (dam)
ECMWF Pressure Level 30 hPa
VT: 16.11.2002 12 UT

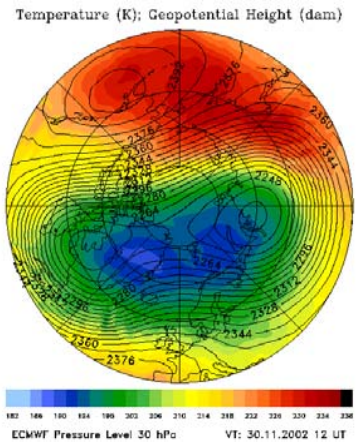
Temperature (K); Geopotential Height (dam)
ECMWF Pressure Level 30 hPa
VT: 30.11.2002 12 UT

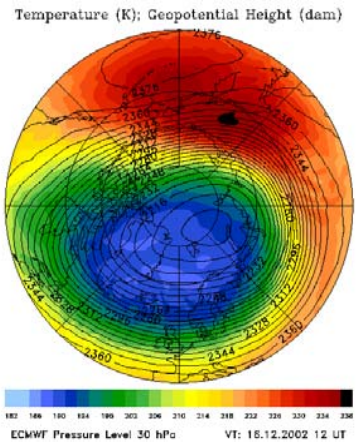
Temperature (K); Geopotential Height (dam)
ECMWF Pressure Level 30 hPa
VT: 16.12.2002 12 UT

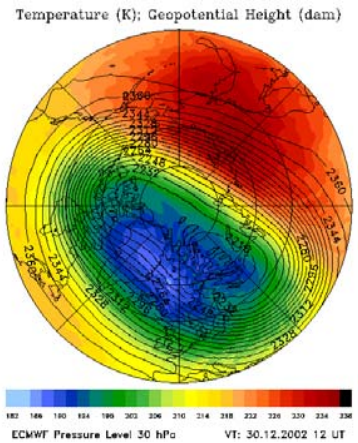
Temperature (K); Geopotential Height (dam)
ECMWF Pressure Level 30 hPa
VT: 30.12.2002 12 UT

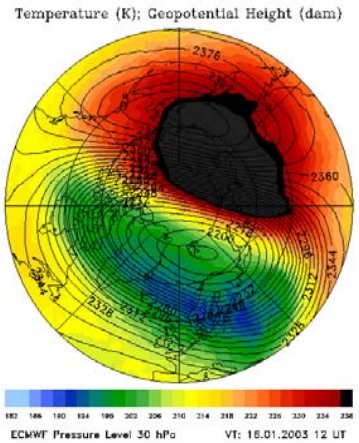
Temperature (K); Geopotential Height (dam)
ECMWF Pressure Level 30 hPa
VT: 16.01.2003 12 UT

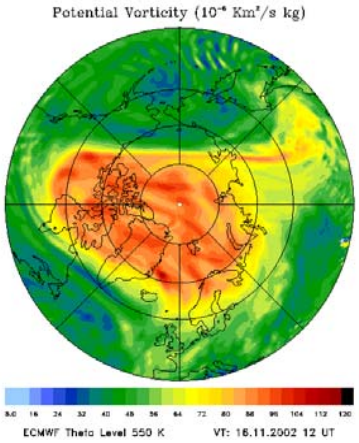
Potential Vorticity (10⁻⁶ Km²/s kg)
ECMWF Theta Level 550 K
VT: 16.11.2002 12 UT

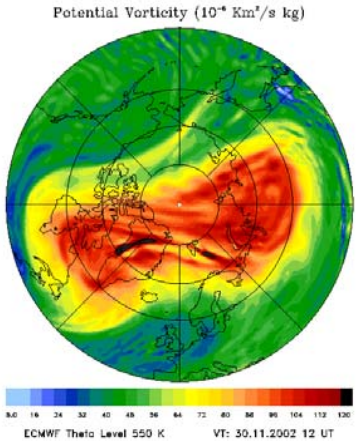
Potential Vorticity (10⁻⁶ Km²/s kg)
ECMWF Theta Level 550 K
VT: 30.11.2002 12 UT

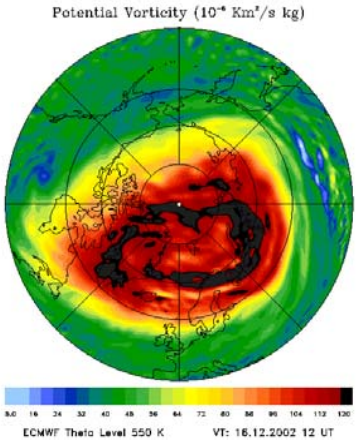
Potential Vorticity (10⁻⁶ Km²/s kg)
ECMWF Theta Level 550 K
VT: 16.12.2002 12 UT

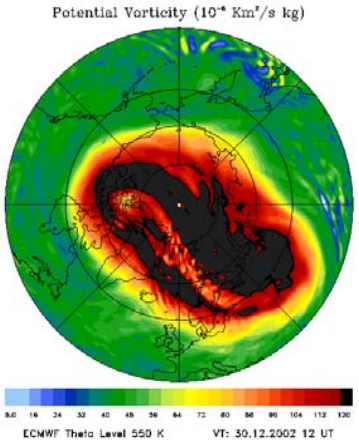
Potential Vorticity (10⁻⁶ Km²/s kg)
ECMWF Theta Level 550 K
VT: 30.12.2002 12 UT

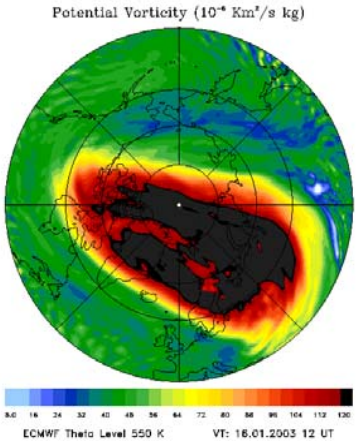
Potential Vorticity (10⁻⁶ Km²/s kg)
ECMWF Theta Level 550 K
VT: 16.01.2003 12 UT

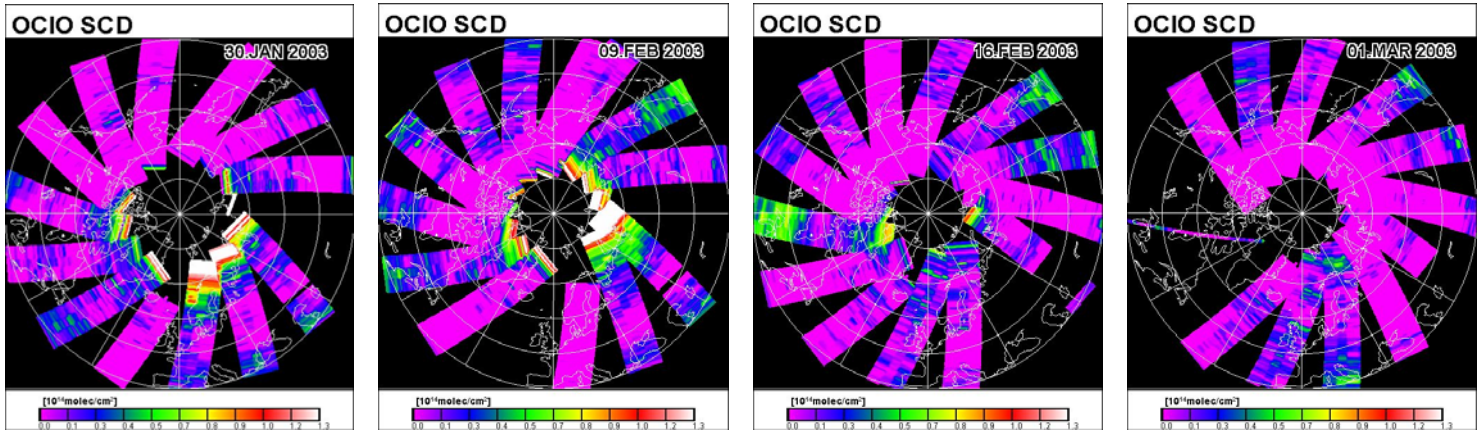
OCIO SCD
30.JAN 2003
OCIO SCD
09.FEB 2003
OCIO SCD
16.FEB 2003
OCIO SCD
01.MAR 2003
[10¹³molec/cm²]

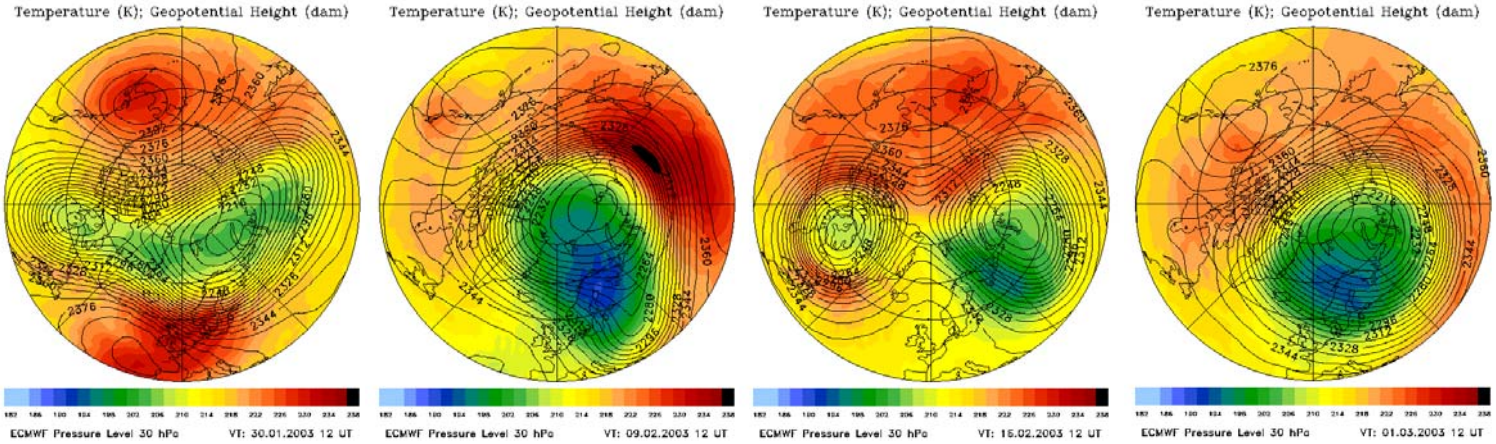
Temperature (K); Geopotential Height (dam)
ECMWF Pressure Level 30 hPa
VT: 30.01.2003 12 UT
VT: 09.02.2003 12 UT
VT: 16.02.2003 12 UT
VT: 01.03.2003 12 UT

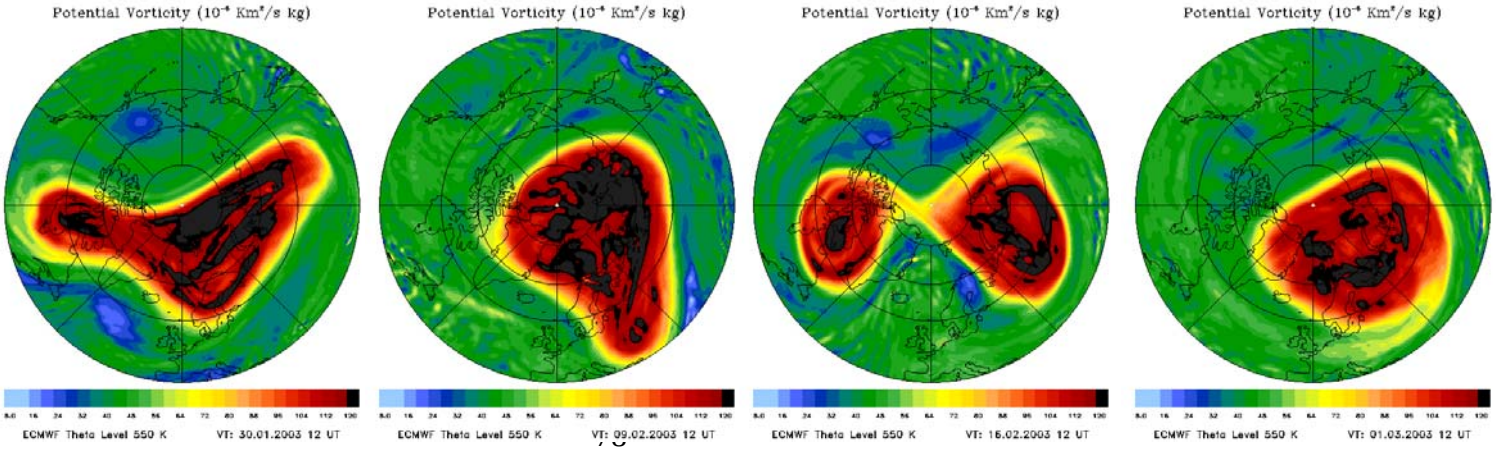
Potential Vorticity (10⁻⁴ Km²/s kg)
ECMWF Theta Level 550 K
VT: 30.01.2003 12 UT
VT: 09.02.2003 12 UT
VT: 16.02.2003 12 UT
VT: 01.03.2003 12 UT

FIGURE 5.7 (last two pages): Temporal evolution of active chlorine, stratospheric temperatures and the polar vortex during the winter 2002/03. Shown are single day maps of GOME OClO SCDs, temperatures at the 30 hPa level and potential vorticity at the 550 K level (both vertical coordinates correspond to an altitude of approx. 21 km) in a 15 day interval.

In the following we investigate how well the GOME OClO observations during this time agree with the respective meteorological conditions.

The polar vortex was formed in the middle of November. Stratospheric temperatures were extremely low already in November and December, dropping below T_{NAT} and leading to formation of PSC and consequently to production of OClO, as can be seen in Fig. 5.7.
At the beginning of December, minimum temperatures at the 475 K level even fell below the threshold for formation of PSC type II (T_{ICE} = 188 K). This resulted in enhanced PSC formation and caused strong chlorine activation inside a broad polar vortex. The distributions of PV, temperature and OClO at 16 December and 30 December point up the intensity of the polar vortex, combined with very low temperatures and intensified chlorine activation over a vast area. This is in accord with ground measurements at Harestua (62.2°N / 10.8°E), which show extraordinarily large OClO SCDs for the middle of December (see section 5.2).
For the time of the GOME observations, the OClO SCD are the largest measured in all Arctic winters in December so far, see Fig. 5.1. During 18-20 December, mountain wave activity above Northern Scandinavia occurred, inducing additional local cooling of the synoptic scale temperature and allowing the formation of ice PSCs. The strong and rapid increase of mountain wave induced PSCs and its correlation to additionally enhanced OClO can clearly be seen in the MIPAS PSC and GOME OClO measurements, presented in section 7.4.
After the cold early winter, a major stratospheric warming around the 20th of January basically changed the dynamical and chemical conditions in the polar stratosphere. The polar vortex was deformed and split into two fragments, the weaker one above northern Europe, the stronger one above Canada [*EUR, 2003*]. The stronger fragment remained existent until end of January. The PV-, temperature- and OClO-distributions in Fig. 5.7. still hint the two centers of the split vortex with higher temperatures and a reduced area of chlorine activation.
At the beginning of February, the vortex was re-established due to a colder period again. The temperatures restarted dropping below T_{NAT} and OClO SCDs reveal a slight increase (see 9 February in Fig. 5.7). The incidence of another minor warming around 16 February, affecting the altitude around 30 hPa, led to a new break of the vortex until 23 February. Consequently, the PV- and temperature-distributions of 16 February in Fig. 5.7 show two centers of the vortex with relative high temperatures. OClO has significantly decreased. Around 1st of March, the vortex reformed, correlated with a moderate decrease of temperature above Northern Scandinavia. In this case, GOME OClO measurements do not show significantly enhanced chlorine activation. At the end of March and in April, the final warming finished the existence of the polar vortex and by this the conditions for stratospheric chlorine activation.

5.2 Comparison with other measurements of chlorine activation

Of the active chlorine species (Cl_x = Cl, ClO, Cl_2O_2, OClO), ClO, OClO and Cl_2O_2 have been measured, either in situ [*Anderson et al., 1989; Vogel et al., 2002; Thornton et al., 2003; Stimpfle et al., 2004*] or by remote sensing [*Waters et al.,1993; Wagner et al., 2001; Santee et al., 2003; Urban et al., 2004*]. In addition, the degree of chlorine activation can also be derived by measuring the reservoir compounds HCl and $ClONO_2$ [*Müller et al., 1997*]. While OClO can be retrieved by means of DOAS in the near UV, unambiguous detection of ClO by remote sensing (and with less accuracy also Cl_2O_2) is possible only by microwave spectroscopy.

This section investigates how well the GOME OClO measurements agree with other observations of active chlorine species. We compare the GOME observations to ground based OClO and space borne ClO measurements and discuss the occurring discrepancies and similarities. For the comparison with the ground based measurements we assume that the local measurement is representative for the level of chlorine activation inside the polar vortex. This assumption is more valid for the southern than for the northern hemisphere where vortex is often deformed. Due to the strong diurnal cycle of OClO and ClO, the time and the SZA of the measurement needs to be considered in the comparison.

5.2.1 Comparison to ground based measurements of OClO

Validation studies of GOME OClO measurements have been reported by *Wittrock et al.* [1999] and *Richter et al.* [1999]. These studies showed a good qualitative and quantitative agreement with ground based zenith-sky measurements of OClO. *Miller et al.* [2000] analysed ground based measurements of OClO at two polar sites and obtained similar results regarding the interhemispheric differences as the ones derived from GOME OClO measurements [*Wagner et al., 2001*], see also section 5.1.2.
Fig. 5.8 displays OClO measurements at the Neumayer station (70° S / 8° W) during the years 1999 to 2001. Also shown is the potential vorticity at the 475 K level (approx. 19 km altitude), which indicates if the polar vortex was located above the measurement site. The onset, duration and ending (enhanced OClO from beginning of May until middle of September) is in good agreement with the GOME OClO observations (compare Fig. 5.1). For the SZA of 90 degrees, also the magnitude of the OClO SCD (2.5 to $3.0*10^{14}$ molec/cm^2) during the time of maximum chlorine activation (July and August) agrees quite good. Note that the larger scatter of the ground based measurements mainly results from the fact that they are local, while the GOME SCDs displayed in Fig. 5.1 are the maximum values found for the whole southern hemisphere.

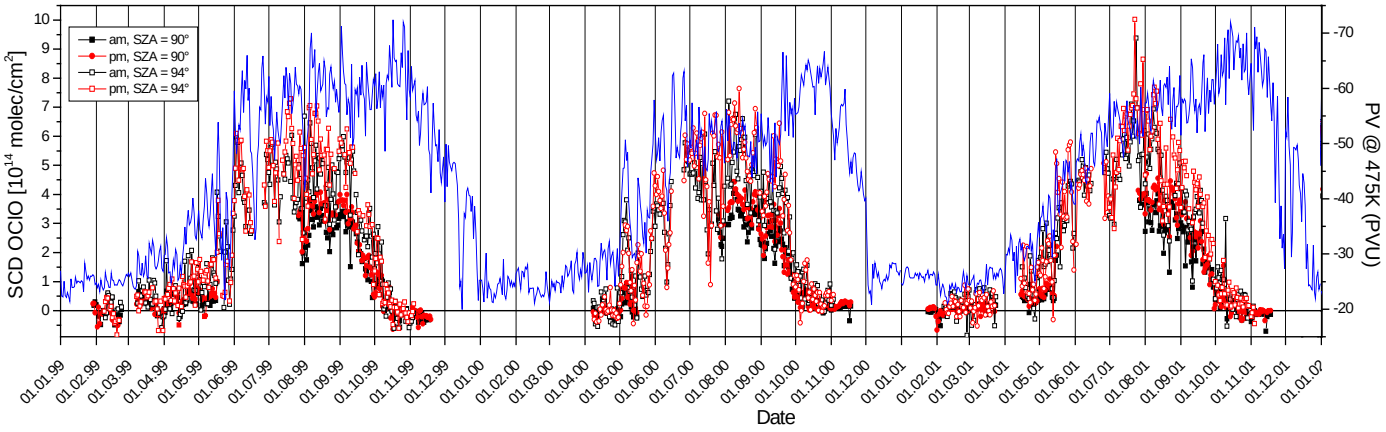

FIGURE 5.8: OClO SCDs measured at the Neumayer station [*Friess, 2001*] for the SZA of 90° (filled points) and 94° (open points) at sunrise (black) and sunset (red) during the years 1999 to 2001. The potential vorticity above Neumayer at the 475 K level is indicated by the blue line.

Tornkvist et al. [2002] reported ground based measurements of OClO over Ny-Alesund (79° N / 11° E) and Andoya (69.3° N / 16° E) during the winters 1995/96, 1996/97 and 1998/99. For 1996, the OClO SCDs observed over Ny-Alesund decline from $2.5*10^{14}$ at the end of February to $1.3*10^{14}$ in the beginning of March, and reach values close to zero around middle of March, which is in very good agreement with the GOME measurements for the Arctic stratosphere during this time. In spring 1997, for which GOME observed enhanced OClO SCDs until middle of March, the measurements at Ny-Alesund also show this extraordinarily long duration of chlorine activation for the northern hemisphere. In the warm winter 1998/99 the OClO SCDs are around $1.0*10^{14}$ molec/cm^2, which is also of the same magnitude as the GOME OClO observations for that winter.

Measurements of OClO SCDs at Harestua for the same winter reveal a short period of chlorine activation between 6th and 11th of February, see Fig. 5.9. Also GOME measurements noticed an increase of the OClO SCDs only during this time (see Fig. 5.1). For the winter 2002/03 the OClO measurements at Harestua observe the early, extraordinarily strong onset of activation in mid of December that is also seen in the GOME measurements, as has been described in section 5.1.6.

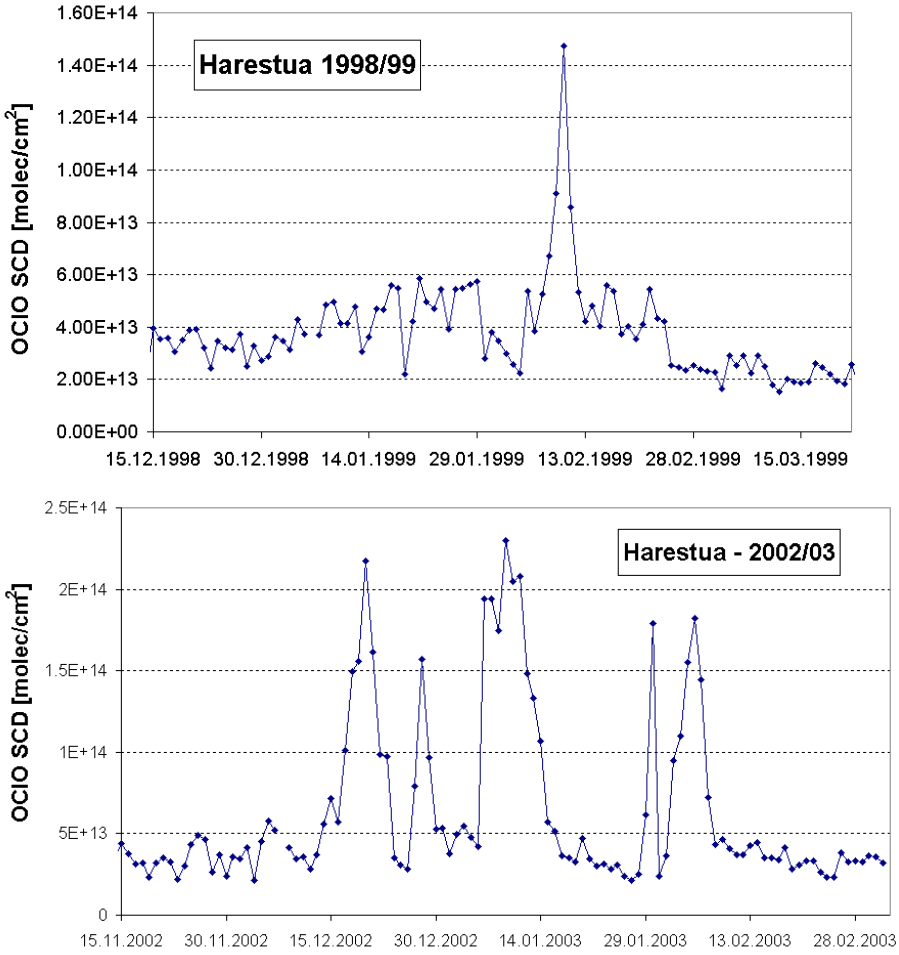

FIGURE 5.9: OClO SCDs measured at Harestua in the winter 1998/99 and 2002/03 [*M. van Roozendael, personal communication, 2005*].

5.2.2 Comparison to MLS ClO

Also, space borne measurements of ClO by the Microwave Limb Sounder (MLS) aboard the Upper Atmosphere Research Satellite (UARS) during the years 1991/92 to 1996/97 and 1999/2000 reveal the same interhemispheric differences in magnitude and duration of chlorine activation as the ones derived from GOME OClO observations, see Fig. 5.10.
While the ClO mixing ratio over the Antarctic is of the same magnitude for every winter (maximum of 2.5 ppbv at the 520 K level, 1.7 ppbv at the 465 K level and 1.2 ppbv at the 420 K level), it shows a strong year to year variability in the Arctic stratosphere. There, the largest levels of chlorine activation are observed for the winters 1995/96 and 1999/2000, in good agreement with the GOME OClO observations (see Figs. 5.1 and 5.2). Also the duration of the period with enhanced active chlorine are equal. For the Arctic, it starts mid December and ends in mid March, and large ClO mixing ratios and OClO SCDs are observed above the Antarctic from beginning of May until middle of September.

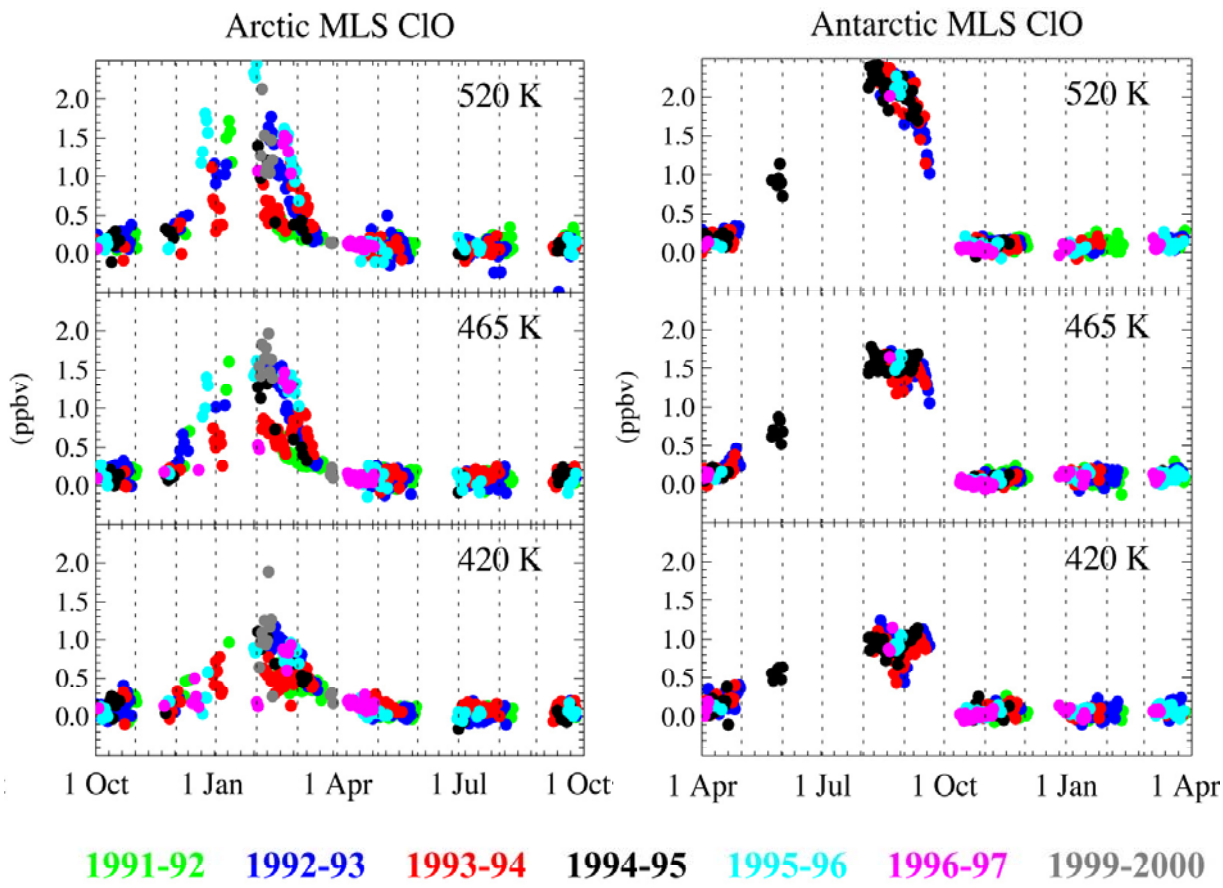

FIGURE 5.10: ClO mixing ratio at three different potential temperature levels (θ=520 K, 465 K and 420 K corresponding to approx. 20.5, 18.5 and 17 km altitude), derived from MLS measurements for the Arctic and Antarctic winters of the years 1991 to 1997 and 1999-2000. Adapted from [*WMO, 2003*].

5.2.3 Comparison to ODIN ClO measurements for the winter 2002/03

While the MLS ClO measurements cover most of the polar winters observed by GOME, they do not measure the same hemisphere for a whole winter, and also provide only a poor spatial coverage. However, since February 2001, there are measurements of ClO by the Sub-Millimeter Radiometer aboard the ODIN satellite. Fig. 5.11 shows GOME OClO and ODIN (SMR) ClO measurements as polar projection maps for selected days from the beginning of November until end of February.

It reveals that throughout the winter, the location of the activated air masses agree very good: No significant activation is observed for the beginning of November, in good agreement with the stratospheric temperatures, which were well above T_{NAT} at that time (see Fig. 5.6). In the beginning of December, both measurements reveal moderate chlorine activation above East Canada and Northern Siberia. In the middle of January, the level of activation increases and is located above the main part of Siberia and the eastern part of Northern Scandinavia, in good agreement with the location of the polar vortex.

Also, the observed degree of chlorine activation is in good accord: For both datasets, the maximum in spatial extent of chlorine activated air masses occurs around 13/14.01. From then on, a gradual decrease is observed, and after the vortex split on 16th February, 2003 (see also section 5.1.6), active chlorine rapidly disappears in both datasets.

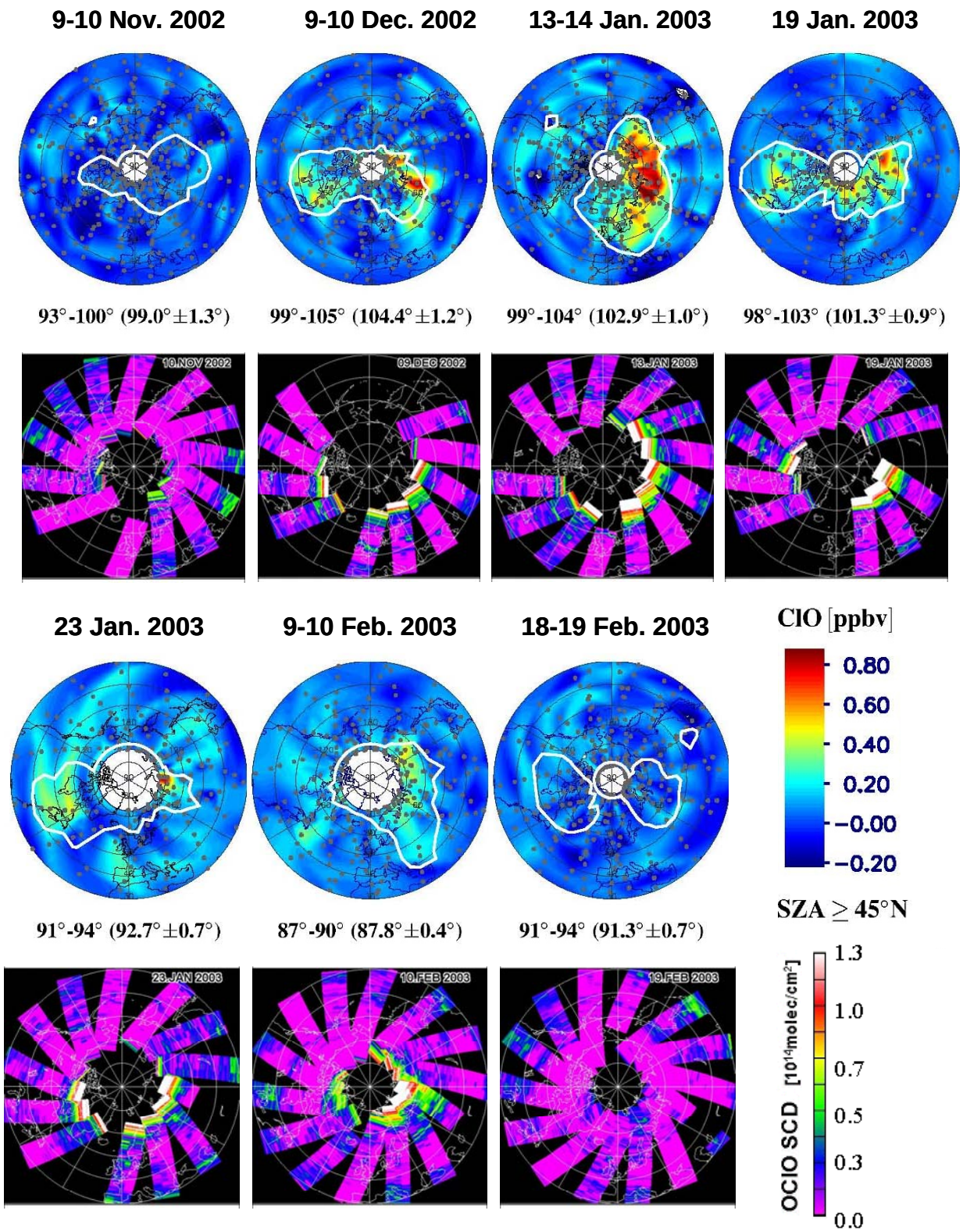

FIGURE 5.11: Maps of the ODIN ClO mixing ratio at the 525 K level and corresponding GOME OClO SCDs for selected days of the Arctic winter 2002/03. For the ODIN measurements the SZA range is given below the maps (range for all measurements, and in brackets mean value plus standard deviation). The white line is the 125 ppbv contour of N_2O which roughly indicates the edge of the polar vortex [*Urban et al., 2004*]. Note that the SZA of the OClO and ClO measurements differ and also change during the winter.

5.3 Comparison with model results

An important test for the understanding of atmospheric chemistry is to study how well the results of model simulations, which incorporate the prevailing knowledge about atmospheric dynamics, radiative processes, chemical mechanisms and kinetics agree with observations. For that purpose, we compared the mixing ratios of ClO_x (= ClO + 2*Cl_2O_2) and OClO, calculated by the chemical transport model SLIMCAT, to the GOME OClO measurements.
The SLIMCAT data has been provided by Martyn Chipperfield, University of Leeds. For details on the SLIMCAT model, see [*Chipperfield, 1998*]. It is a well established model of stratospheric chemistry, which has been intensively compared with observations, also of active chlorine species [*Solomon et al., 1998, 2002*]. Also, ground based OClO measurements at Kiruna have been compared to SLIMCAT OClO data [*Otten, 1997*]. However, as far as we know, GOME OClO observations have not been compared to SLIMCAT ClO_x or OClO results before.

5.3.1 Comparison to Slimcat ClOx

To get a first impression of the overall agreement, we investigated the relation between observations and simulation for the cold Arctic winter 1999/2000. Fig. 5.12 displays daily maximum ClO_x mixing ratios in comparison to the maximum OClO SCD at SZA=90 for the same day and shows a good correlation of the observed and calculated values, especially in the late winter and spring. In the early winter, GOME cannot observe regions with chlorine activation close to the pole due to the polar night, which is the main reason for the discrepancy during this time.

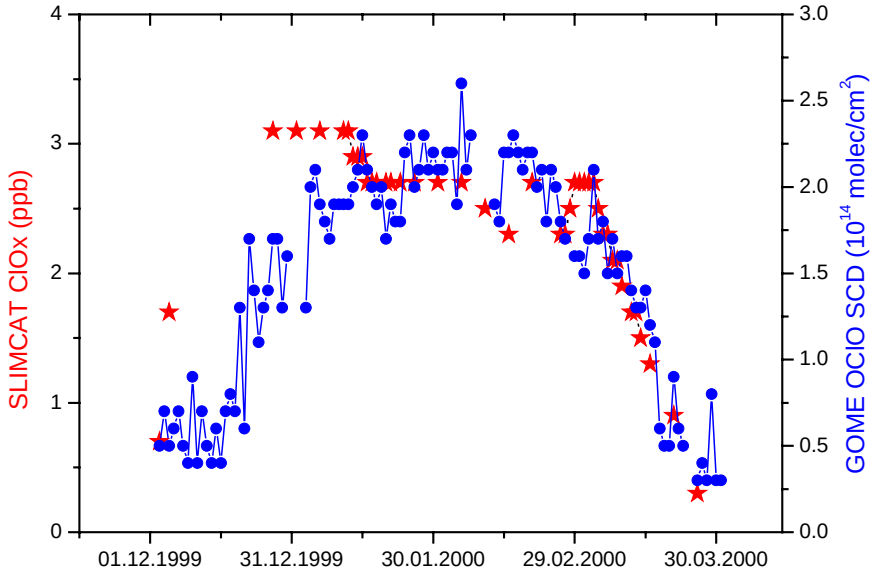

FIGURE 5.12: Maximum SCDs of OClO measured by GOME at a solar zenith angle of 90° (blue circles) compared to the maximum concentration of ClO_x at the 475 K level calculated by SLIMCAT (red stars) for the Arctic winter 1999/2000.

Although Fig. 5.12 demonstrates that the relative evolution of the degree of chlorine activation in the model and observations agree, the question arises if the calculated areas with enhanced chlorine activation are also situated at the same locations where it is observed and if the magnitude of chlorine activation also agrees. The following figure and the next section are related to these two aspects.
Fig. 5.13 shows maps of the ClO mixing ratio in comparison to maps of GOME OClO SCDs for selected days of the winter 1999/2000.

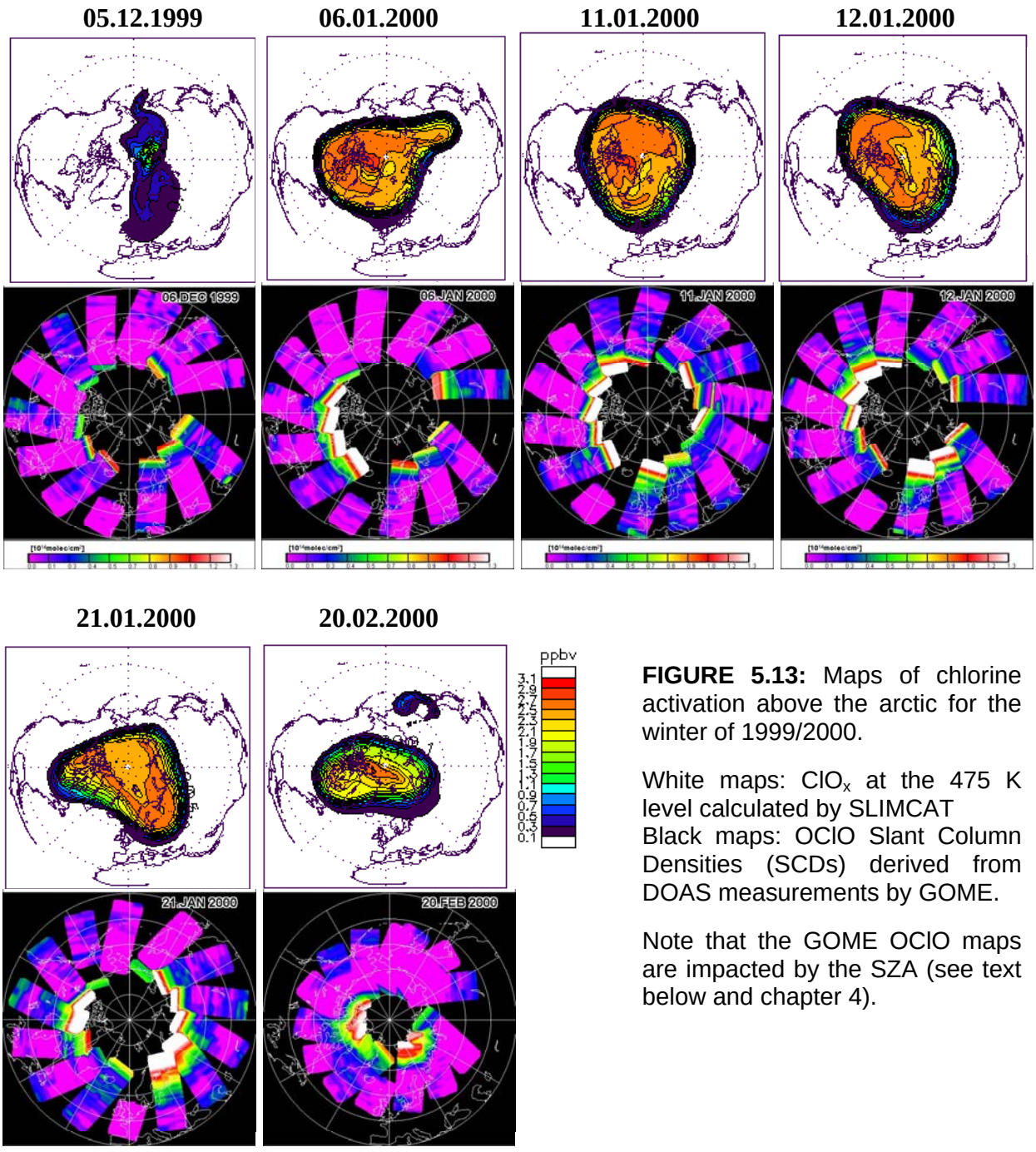

FIGURE 5.13: Maps of chlorine activation above the arctic for the winter of 1999/2000.

White maps: ClO_x at the 475 K level calculated by SLIMCAT
Black maps: OClO Slant Column Densities (SCDs) derived from DOAS measurements by GOME.

Note that the GOME OClO maps are impacted by the SZA (see text below and chapter 4).

The GOME maps of OClO show the activated air masses in the same region in a comparable intensity (note for example, the activation above East-Siberia on the 6th of January and the evolution of the shape of the region with enhanced ClO_x and OClO levels on the 11th, 12th and 21st of January). In the early winter (5th of December), the activation close to the pole is not visible for GOME due to the polar night. Also, there are discrepancies in the spatial extension, which arise from the fact that the SLIMCAT data is given as concentration at a defined altitude while the OClO SCD is impacted by a large altitude range. In addition, the AMF increases for large SZAs while the photolysis rate of OClO decreases. Both factors result in an enhancement of the OClO SCDs for larger latitudes, see chapter 4. Therefore, the GOME OClO maps tend to undervalue the chlorine activation for smaller latitudes.

Since the SLIMCAT model is intensively validated (especially for the investigated winter 1999/2000), the agreement to the calculated ClO mixing ratio demonstrates that the GOME OClO observations do give a good representation of the spatial extent and also of the degree of chlorine activation inside the polar vortex, at least for the cold Arctic winter 1999/2000.

5.3.2 Comparison to Slimcat OClO

Since the comparison to the SLIMCAT results for ClO was quite promising, we decided to compare also the simulated values for OClO with the GOME observations. Because of the rapid decay by photolysis, OClO has a strong diurnal cycle. Therefore, any comparison of OClO abundances needs to be performed for the same time of the day.
For that purpose, the SLIMCAT data set version MPC 320 was calculated [*M. Chipperfield, personal communication, 2003*]. While the usual output of the SLIMCAT model is for 12 UT, the version MPC 320 is especially calculated to match the time of GOME measurement: The model output is at 10.00 am local time, close to the equator crossing time of GOME of 10:30 am local time. However, for higher latitudes in the northern hemisphere the time difference is around 15 minutes, which might still cause discrepancies for OClO due to its strong diurnal cycle.
Another complication arises from the different nature of the model and measurement data: While the SLIMCAT data are given in mixing ratios, which were then integrated to vertical column densities (VCDs), GOME measures SCDs. Due to the problems in calculating an AMF for OClO (see section 4.1) converting the SCDs to VCDs might introduce significant errors, making the comparison difficult.
Therefore, the first comparison is performed with SCDs for GOME and VCDs for SLIMCAT. Fig. 5.14 shows this qualitative comparison of the respective column densities as the daily mean value in two latitude bands (zonal means at 67.3 ± 2.5 and 72.3 ± 2.5 degrees North, corresponding to the SLIMCAT grid points) for the Arctic winter 1999/2000.
While the OClO column densities of both datasets show a good qualitative agreement, there are also some discrepancies: At 67° N the increase in the observed column densities at the beginning of the winter appears about two weeks later. However, the time of the maximum in chlorine activation around end of December as well as the decrease from mid January to end of March is very similar.
At 72° N, the time for maximum chlorine activation is the same in the model and in the observations, but the time of the activation and especially of the deactivation period do not agree. The observations reveal that chlorine activated air masses are found about three weeks longer than in the simulation. Also, the observed OClO column densities decrease smoothly from January to February, while the simulated OClO shows an abrupt decline from the 8th to the 20th of January. In general, the agreement seems better for the latitude band around 67° N.
To investigate the agreement also in a quantitative manner it is necessary to convert the SCDs measured by GOME to VCDs. Also, it needs to be considered that due to the large SZAs, the measurement is impacted by air masses of wide horizontal extent [*Solomon et al., 1987; Platt et al., 1997*], which causes the GOME OClO SCDs to be decreased (see section 4.2). To correct for this chemical enhancement, we applied a chemical AMF (see Fig. 4.5) to the measurement.
Figs. 5.15 and 5.16 show the OClO VCDs for the Arctic winters 1999/2000 and 2002/03, respectively. In comparison, also the VCDs resulting from applying the standard AMF are shown. For the calculation of the standard AMF, we assumed a gaussian shape for the vertical profile of OClO with the maximum located at 19 km and a full width at half maximum (FWHM) of 8 km.
As expected, the GOME OClO VCDs derived with the chemical AMF are significantly larger. While for 65° N, the VCDs derived by the standard AMF agree surprisingly good to the modeled VCDs (nearly the same magnitude (around 30 % difference) for the whole time period of both investigated winters), applying the chemical AMF reveals the disagreement between model and observation between beginning of December and middle of January. For the latitude of 72°, the magnitude of the SLIMCAT OClO VCDs agrees much better with the GOME observations when applying the chemical AMF. However, the time period for which maximum OClO VCDs occur, differs substantially.

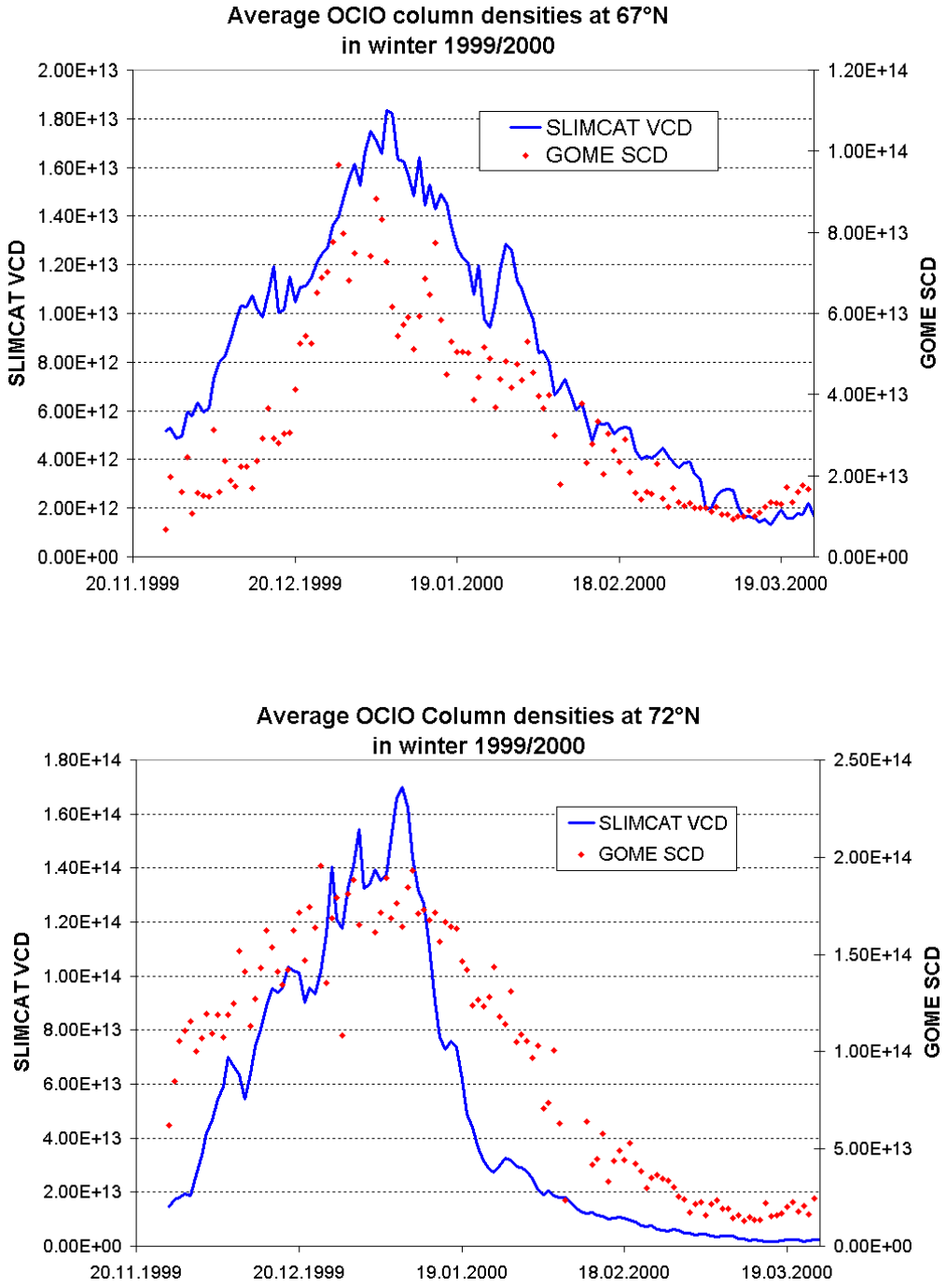

FIGURE 5.14: Zonal average of the daily mean values for the SLIMCAT OClO VCDs (blue line) and GOME OClO SCDs (red diamonds) for two latitude bands at the north pole. Top: Zonal average for 67.3 ±2.5 °N. Bottom: Zonal average for 72.3 ±2.5 °N.

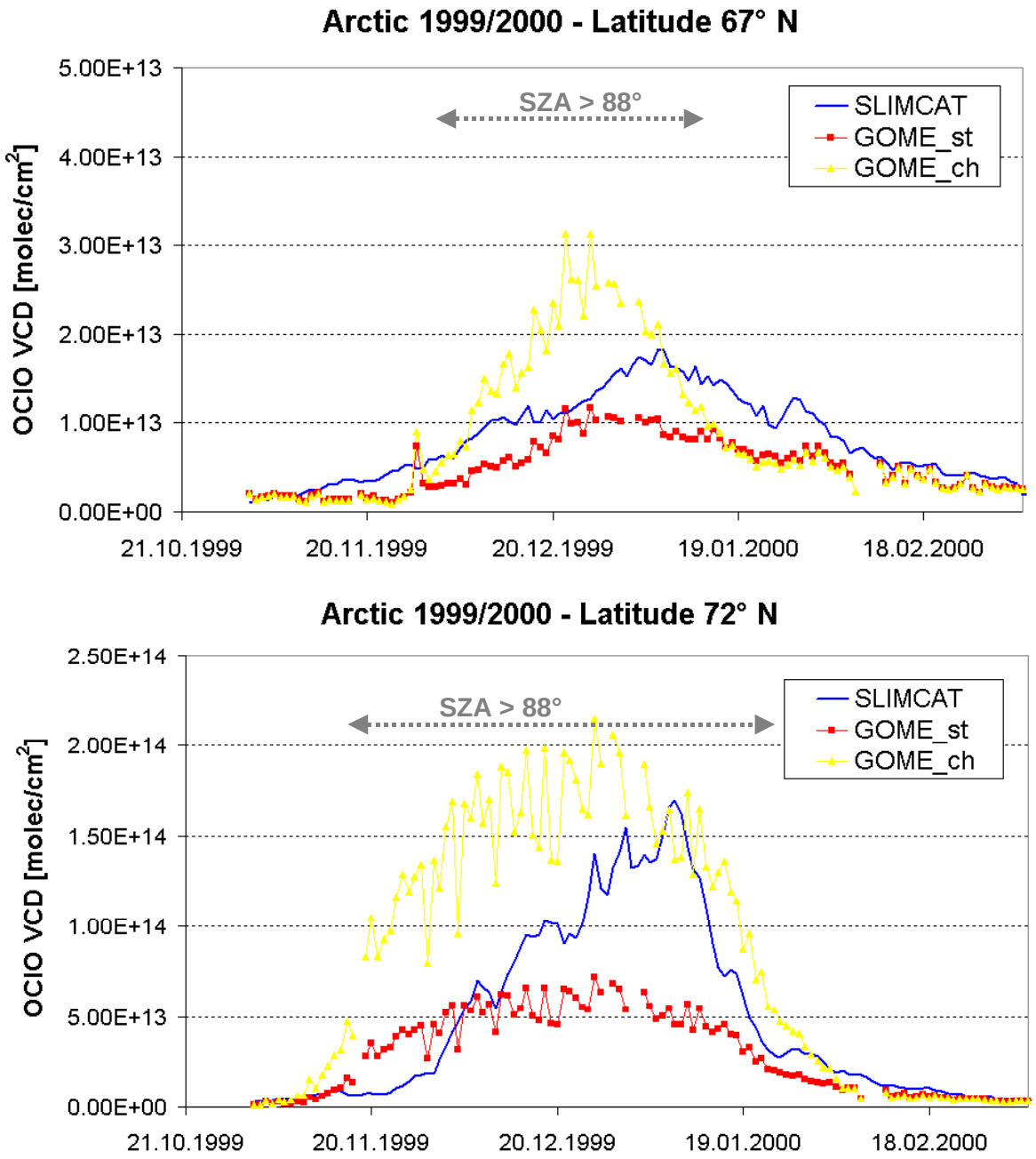

FIGURE 5.15: GOME OClO VCDs for "chemical" AMF (yellow line) and "standard" AMF (red line) in comparison to the VCD calculated by SLIMCAT. Top panel: for the latitude band around 67° N. Bottom panel: For the latitude band around 72 °N.

As mentioned above, there is a time difference of approx. 15 minutes at high latitudes between the output of the SLIMCAT MPC 320 data and the time of the GOME measurement. Due to the strong diurnal cycle of OClO, this will impact the comparison in a way that the modeled VCDs, which are calculated 15 minutes before the measurement, are larger than the observed. This is seen for the latitude of 67° N where GOME OClO VCDs are around 30 % smaller from mid-January until mid-February. Also, this impact is expected to vary with the SZA of the considered region and thus might create also a seasonal dependent offset. However, it can not explain the large discrepancy between modeled and observed VCDs found for both investigated winters from end of November until end of December for 72° N (see Fig. 5.15 and 5.16, lower panel) and from middle of December until middle of January for 67° N.

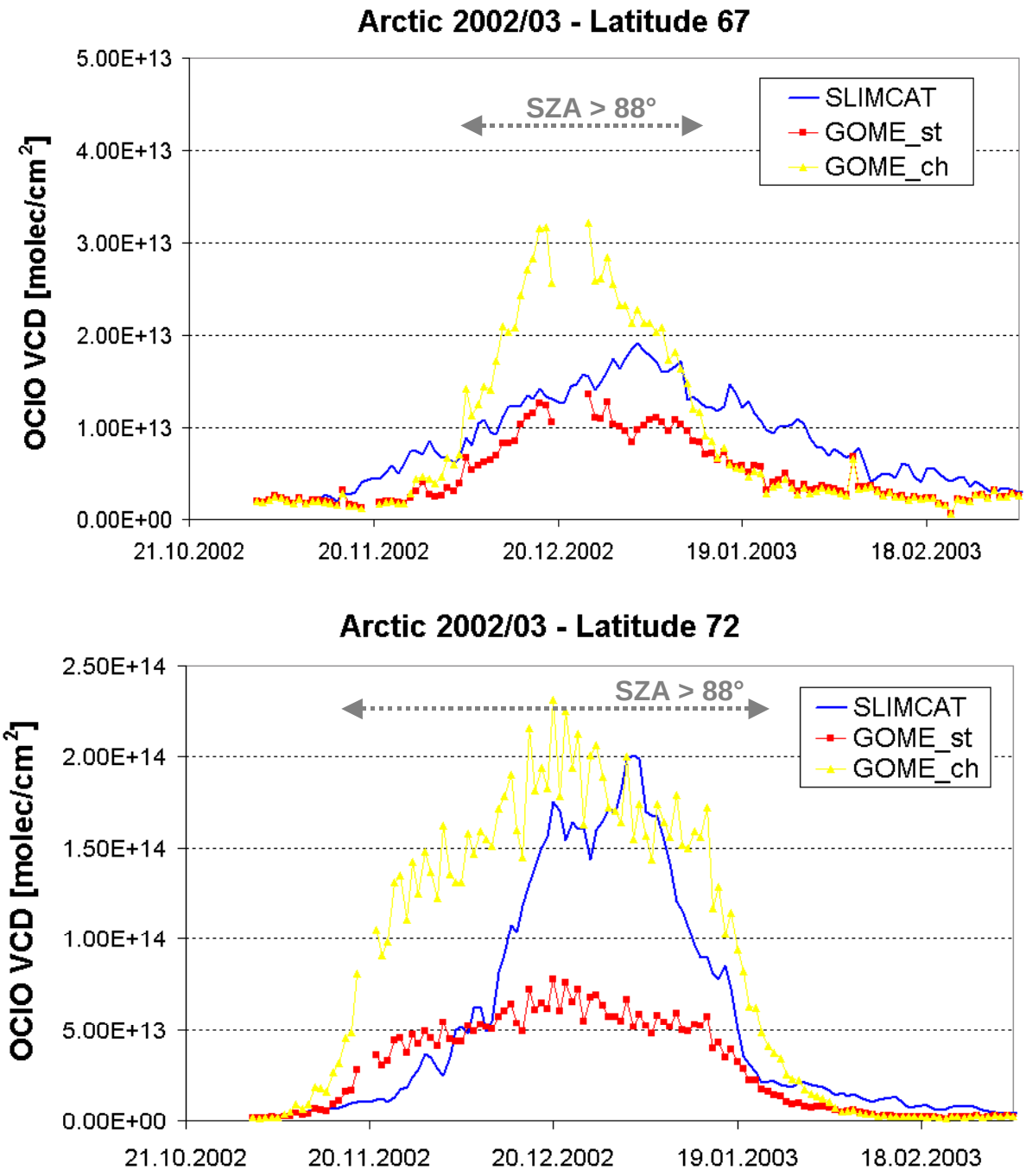

FIGURE 5.16: same as Fig. 5.15, but for the Arctic winter 2002/03

Likely, this substantial discrepancy indicates the known problems of current chemistry transport models in describing the stratospheric chemistry in polar winters, like underestimation of chlorine activation and subsequent ozone depletion [*Becker et al., 2000; Solomon et al., 2000; WMO, 2003*]. Thus, this study may be useful to identify the causes for this discrepancy and thereby to improve the above mentioned shortcomings of the model simulations.

However, the results are also very promising. In some cases, the temporal evolution and also the magnitude of the OClO VCDs agree astonishingly good, considering the described difficulties in modeling the OClO abundances and comparing them to observations.

5.4 Case Studies

The long time series of GOME OClO observations (section 5.1) as well as the comparison to other measurements and simulations of active chlorine (section 5.2 and 5.3) demonstrated that satellite measurements of OClO are a valuable quantity for determining the degree of chlorine activation. In addition, they may also be useful to study still open questions in stratospheric chlorine chemistry.
In the following, we further investigate the relation of the GOME OClO observations to stratospheric meteorology and other trace gases observed by GOME.

5.4.1 Dependence of chlorine activation on stratospheric temperatures

The graphs shown in Fig. 5.2 revealed the anti-correlation of the OClO SCDs observed by GOME to the temperature at the altitude where PSC formation occurs. Fig. 5.17 shows the same relation visualized in an alternative way. Displayed is the maximum OClO SCD observed by GOME at a SZA of 90 degrees as function of the minimum temperature for all cold Arctic winters.

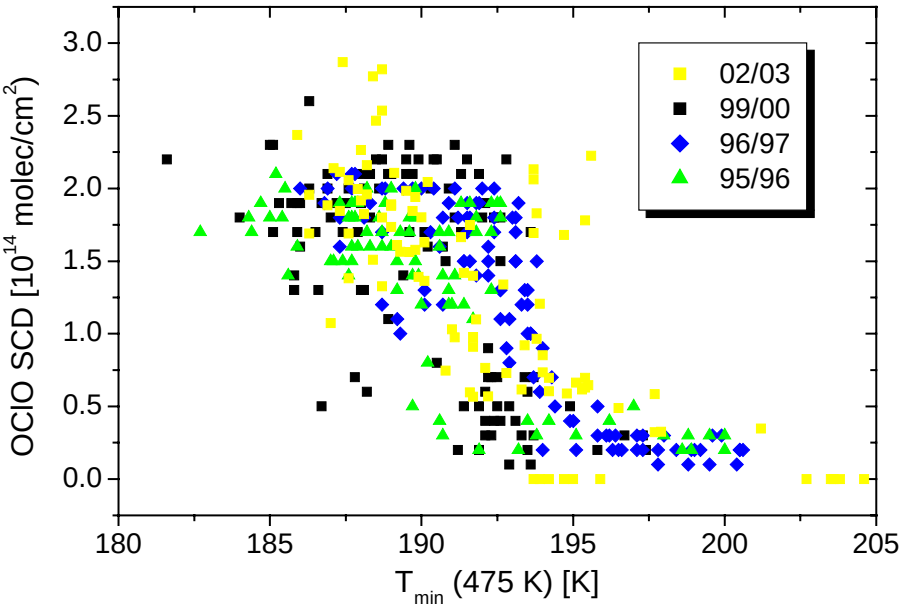

FIGURE. 5.17: Maximum OClO SCDs measured by GOME at a SZA of 90 degree, as function of the minimum temperature in the northern hemisphere at the Θ = 475 K level.

It can be easily seen that when temperatures drop below T_{NAT}, the OClO SCDs rapidly increase. Above this threshold, no significant enhancements of the OClO SCDs are observed. This relation indirectly proves the heterogeneous processing of chlorine species on PSCs. In the following we further study the effect of formation of PSCs on the OClO SCDs.

5.4.2 Relation to PSC formation

For the Arctic winters 1995/96 to 2002/03, *Rex et al.* [2004]calculated the volume of the air masses where formation of PSCs was possible (V_{PSC}) by using the NAT equilibrium temperature an standard profiles for HNO_3 and H_2O. This definition for V_{PSC} has been shown to accord well with observations [*Rex et al., 2002*]. Fig.5.18 displays V_{PSC} for the winters 1995/96 to 2002/03 in comparison to the sum of the OClO SCDs observed from February to March by GOME. The graph reveals the expected correlation between the two quantities: The sum of the OClO SCDs observed in Arctic springs increases almost linearly with the size of the volume where formation of PSCs is expected.

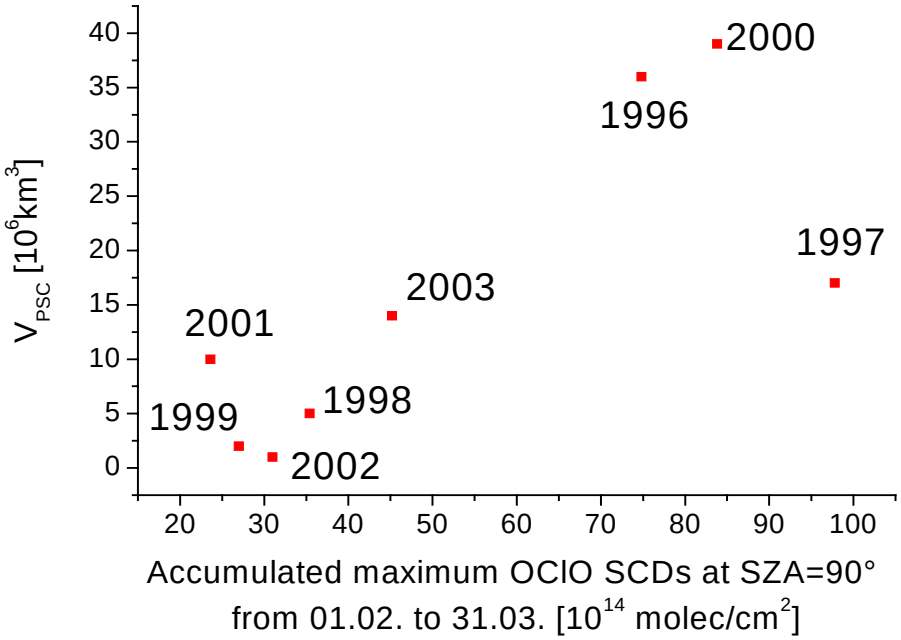

FIGURE 5.18: Volume of the polar vortex where meteorological conditions were cold enough for the formation of PSCs [*Rex et al., 2004*] in comparison to the OClO SCDs observed by GOME in the corresponding winter.

5.4.3 Relation to Ozone depletion

Since polar stratospheric ozone loss in springtime is dominated by chlorine catalysed reaction cycles (see section 2.2.3), the extent of chlorine activation in polar spring largely impacts the ozone column during this time. In fact, the chemical ozone loss due to the ClO-BrO cycle for a given time interval is related to the OClO column density observed during this time [*Solomon et al., 1990*]:

$$\frac{dO_{3col}}{dt} = -2\left(\frac{k_2 + k_3}{k_1}\right) * J(OClO)_{col} \qquad (5.1)$$

However, to estimate the chemical ozone loss with this relation requires measurements of the OClO columns for the whole time of possible ozone destruction. In the case of GOME, where only one measurement per day is available for a give location, the extrapolation of the measured OClO column to the whole daytime would result in large uncertainties.
Also, the chemical ozone depletion by the ClO dimer cycle, which, depending on the temperature contributes 20-50 % to the overall ozone loss in Arctic winters, is not accounted for by Eq. 5.1.
Therefore, the relation between the GOME OClO observations and springtime polar ozone loss is investigated in a qualitative manner in the following. Figure 5.19 shows the OClO SCD map for a selected day in middle of February for the years 1996 to 2003, representative for the level of chlorine activation in the spring of the respective year.
Also shown is the monthly mean of total ozone columns measured by GOME above the Northern Hemisphere in March of the same year. One can see very clearly that for the cold Arctic winters 1995/96, 1996/97, 1999/2000, the ozone column in March is considerably reduced compared to the remaining winters. Vice versa, the warm and moderately cold Arctic winters 1997/98, 1998/99, 2000/01, and 2001/02 with only weak chlorine activation result in large ozone columns in March.

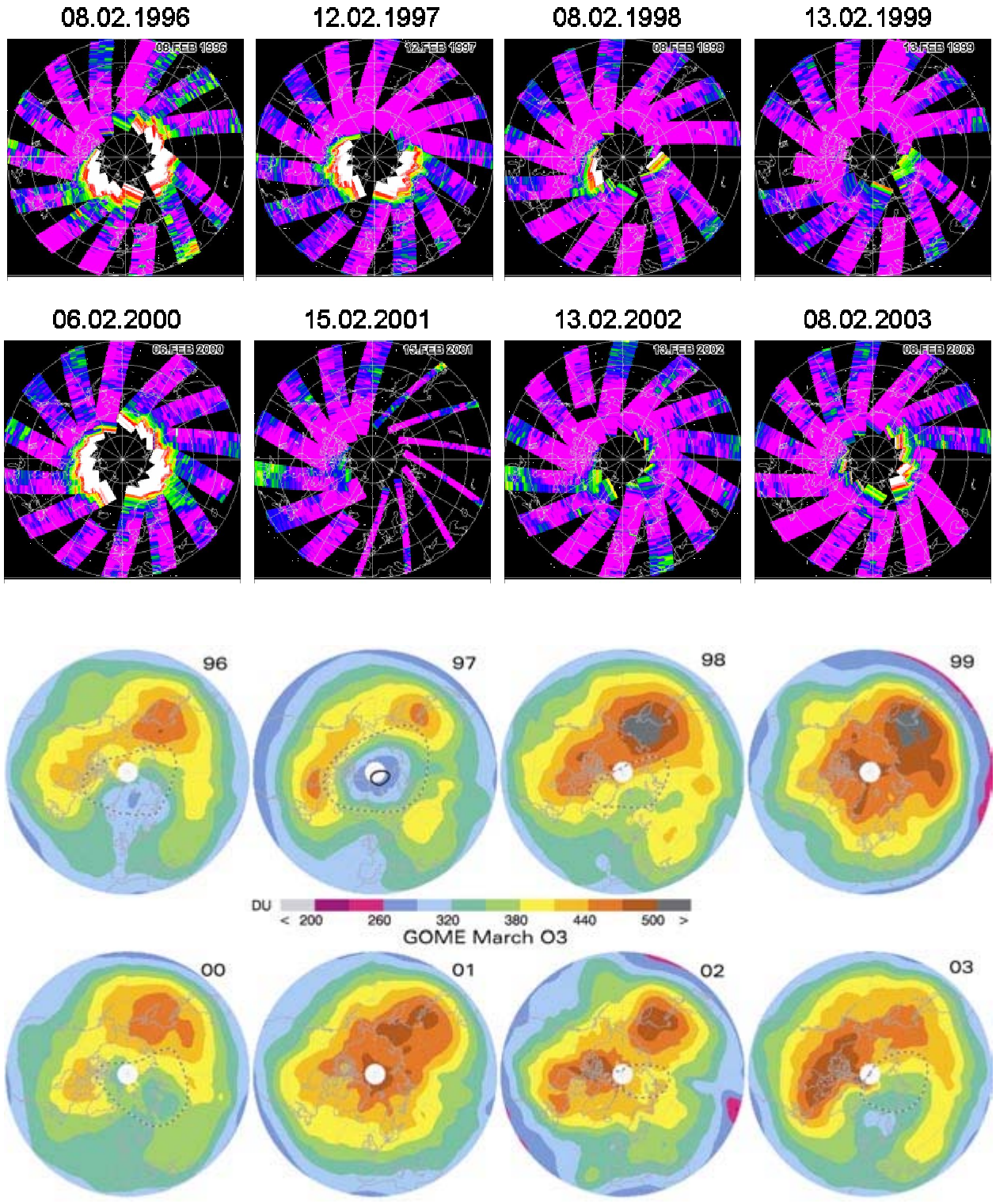

FIGURE 5.19: GOME measurements of OClO SCDs in February (selected, typical daily map) and ozone total columns (in DU) in March (monthly mean map) for the Arctic winters 1995/96 to 2002/03. GOME ozone maps adapted from [*EORCU, 2003*].

To further investigate this relation, we co-added the SCDs of OClO measured between February and March and plotted them against the mean of the total ozone column in March as observed by GOME, see Fig. 5.20.

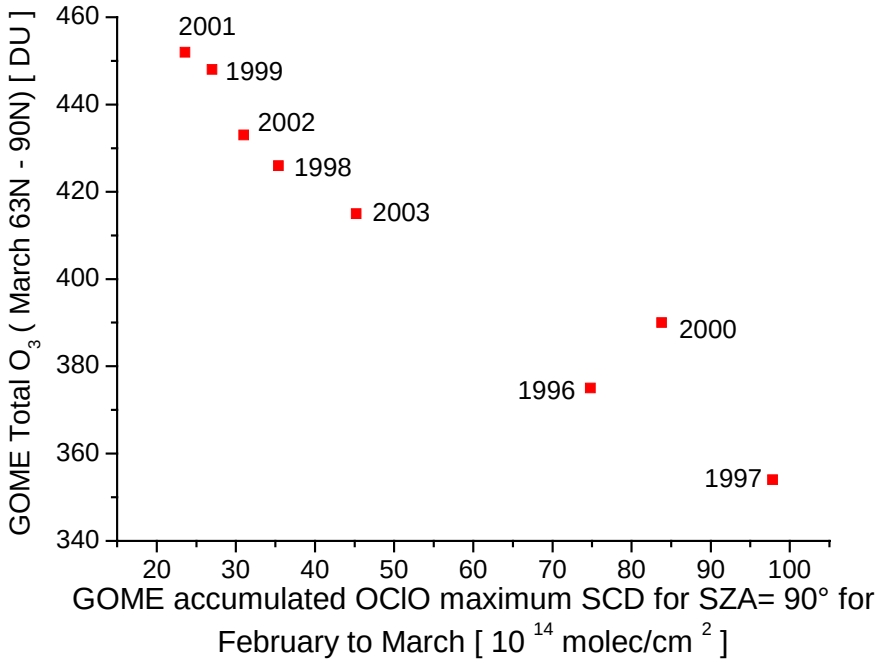

FIGURE 5.20: GOME Total O_3 in March (63° N –90° N) in Dobson Units, taken from the official DLR level 2 data, plotted against the sum of the daily OClO maximum SCDs at SZA = 90° from February to March, for all Arctic winters observed by GOME. In spring 2000, the peak of the vertical OClO (and ClO) profile was located at lower altitudes, leading to smaller O_3 loss than expected [*Wagner et al.*, 2002a, and references therein].

The graph reveals that the O_3 column decreases almost linearly for larger sums of the OClO SCDs. The (anti-)correlation appears rather strong, raising the question if the amount of chlorine activation solely determines the springtime ozone columns, and dynamics play only a negligible role. However, this strong correlation might not (only) be due to the impact of chlorine chemistry: By GOME observations, *Weber et al.* [2003] showed that there exists a strong correlation between ozone and the eddy heat flux on one side, and a strong anti-correlation between OClO and the eddy heat flux on the other side for the Arctic and Antarctic winters 1995-2002.
Therefore, the strong correlation in Fig. 5.20 might not (only) be due to increased chemical ozone loss for years with stronger activation of chlorine, but may also arise from the impact of dynamics on both species. In particular, diabatic descent in the polar region is responsible for the steady increase of lower stratospheric ozone during the winter, especially in the Arctic [*Chipperfield and Jones, 1999*].
To further investigate this issue, we compared the OClO measurements in Arctic springs to the chemical ozone loss derived from the match analysis and from chemical transport models. Fig. 5.21 shows the ozone loss for the Arctic winters of the GOME observation period, determined by different methods (ozone sondes, chemical transport models). In Fig. 5.22 and 5.23 we plotted the OClO SCDs in comparison to the chemical ozone loss derived from the SAOZ ozone sondes and the match analysis, respectively. Although there is a correlation, it is much weaker than the one between the OClO SCDs and the total ozone column, shown in Fig. 5.20. This implies that there is also a considerable impact of stratospheric dynamics (like e.g. heat flux and diabatic descent) on both trace gases. This impact is probably also the main reason for the imperfect correlation of V_{PSC} and the OClO SCDs, shown in Fig. 5.18.

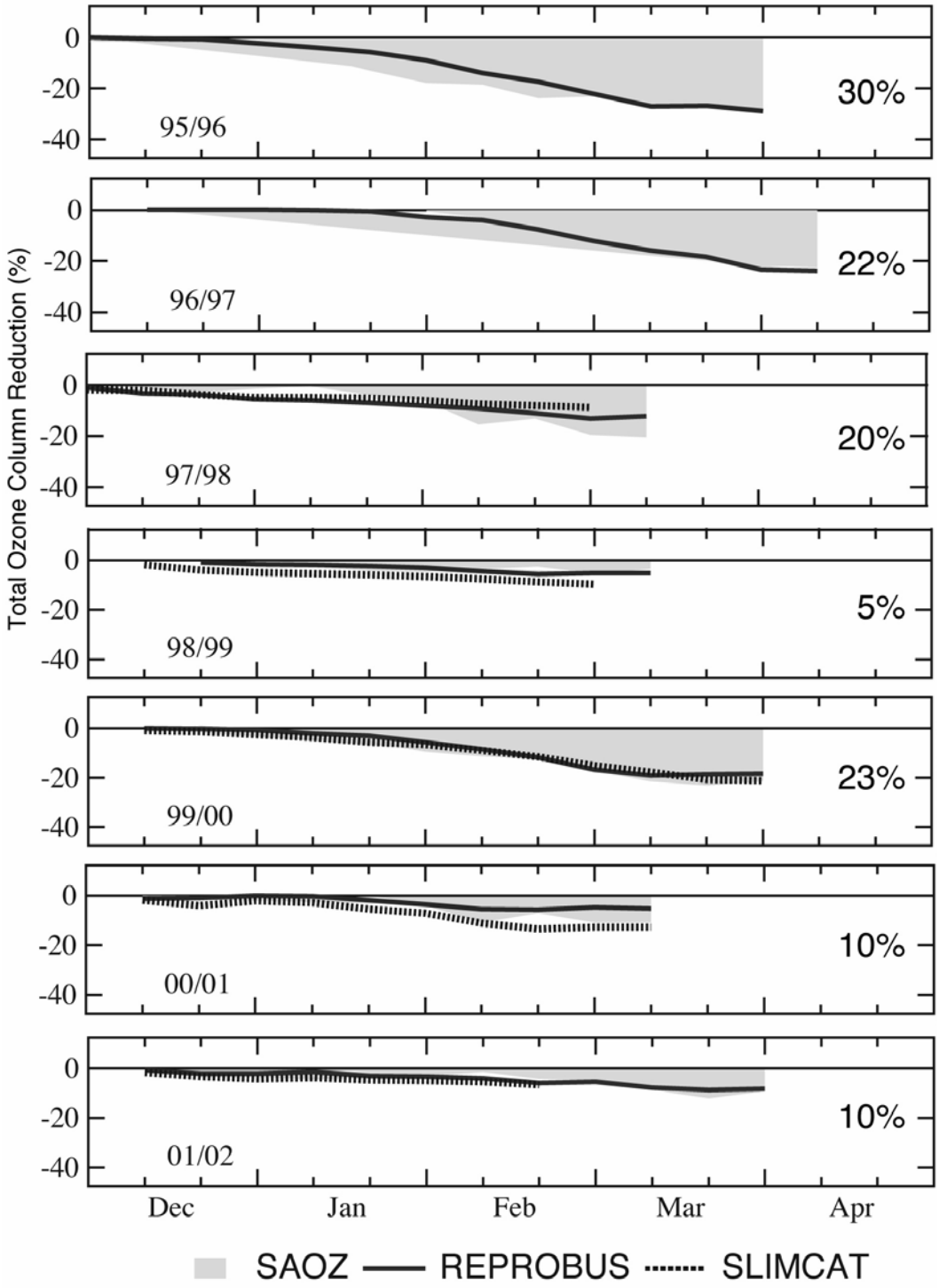

FIGURE 5.21: Total ozone reduction in the Arctic derived by comparing the SAOZ observations with passive ozone in REPROBUS (gray shaded area) and comparison to the ozone loss calculated by the chemical transport models REPROBUS (solid line) and SLIMCAT (dotted line). The percentages on the right side are the cumulative ozone losses derived by observations from the SAOZ network. Adapted from [*WMO,2003*].

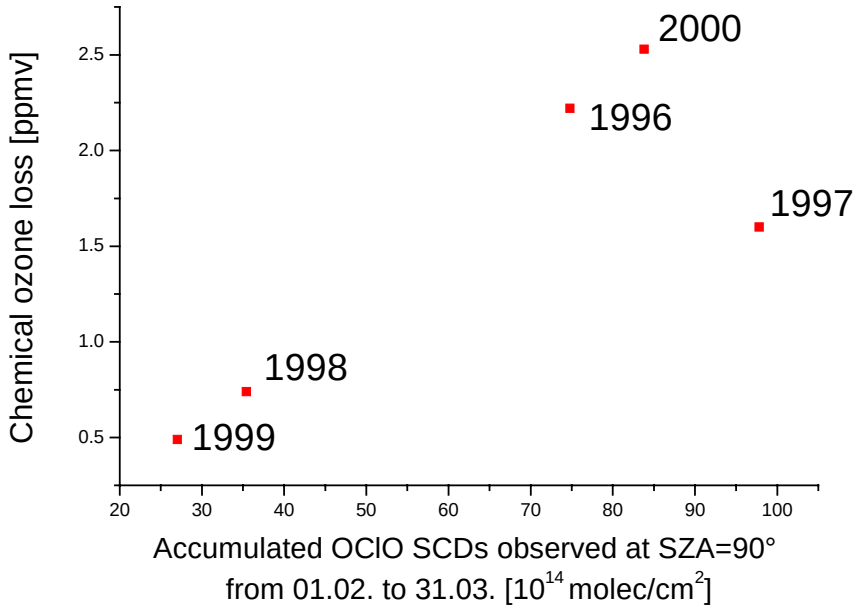

FIGURE 5.22: OClO SCDs observed by GOME in comparison to the chemical ozone loss in ppmv derived by analysis of the SAOZ ozone sondes, [*Braathen, personal communication, 2005*].

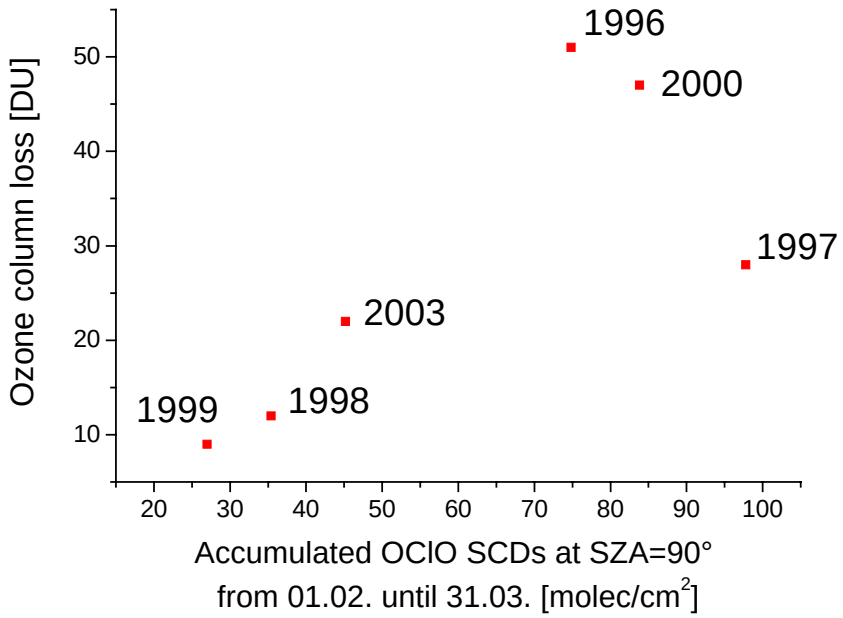

FIGURE 5.23: OClO SCDs observed by GOME in comparison to the ozone column loss derived by the match analysis for the respective winter. For the winter 2000/01 and 2001/02, the match analysis could not be applied [*Rex et al., 2004*].

5.4.4 Deactivation: Relation to Denitrification

In the polar spring, when sunlight returns and temperatures rise above T_{NAT}, the repartitioning of chlorine from its active species to the reservoir compound begins. Of course, deactivation of chlorine also takes place before, but due to the much faster processing of the chlorine reservoir compounds by heterogeneous reactions for cold temperatures, the equilibrium is far on the side of the active chlorine species. This situation changes rapidly when temperatures remain above the threshold for PSC formation.
Since in the Arctic, deactivation of chlorine takes place mainly be the reaction of ClO with NO_2 (see section 2.2.3), the time for deactivation of chlorine is largely determined by the nitrogen dioxide available. Measurements of HNO_3, the polar night time reservoir of NO_x, by the MLS instrument reveal the large variability in the degree of denitrification for the Arctic winters, see Fig. 5.24: HNO_3 abundances at the 520 and 465 K level observed between the months of February and March for the winters 1993/94 and 1999/2000 differ by factor of up to three. The lowest mixing ratios of HNO_3 are measured for the cold winters 1995/96 and 1999/2000 (around 5 and 8 ppbv respectively). On the other hand, HNO_3 abundances in the Antarctic stratosphere are very similar for every winter and reach values close to O ppbv from July until September.

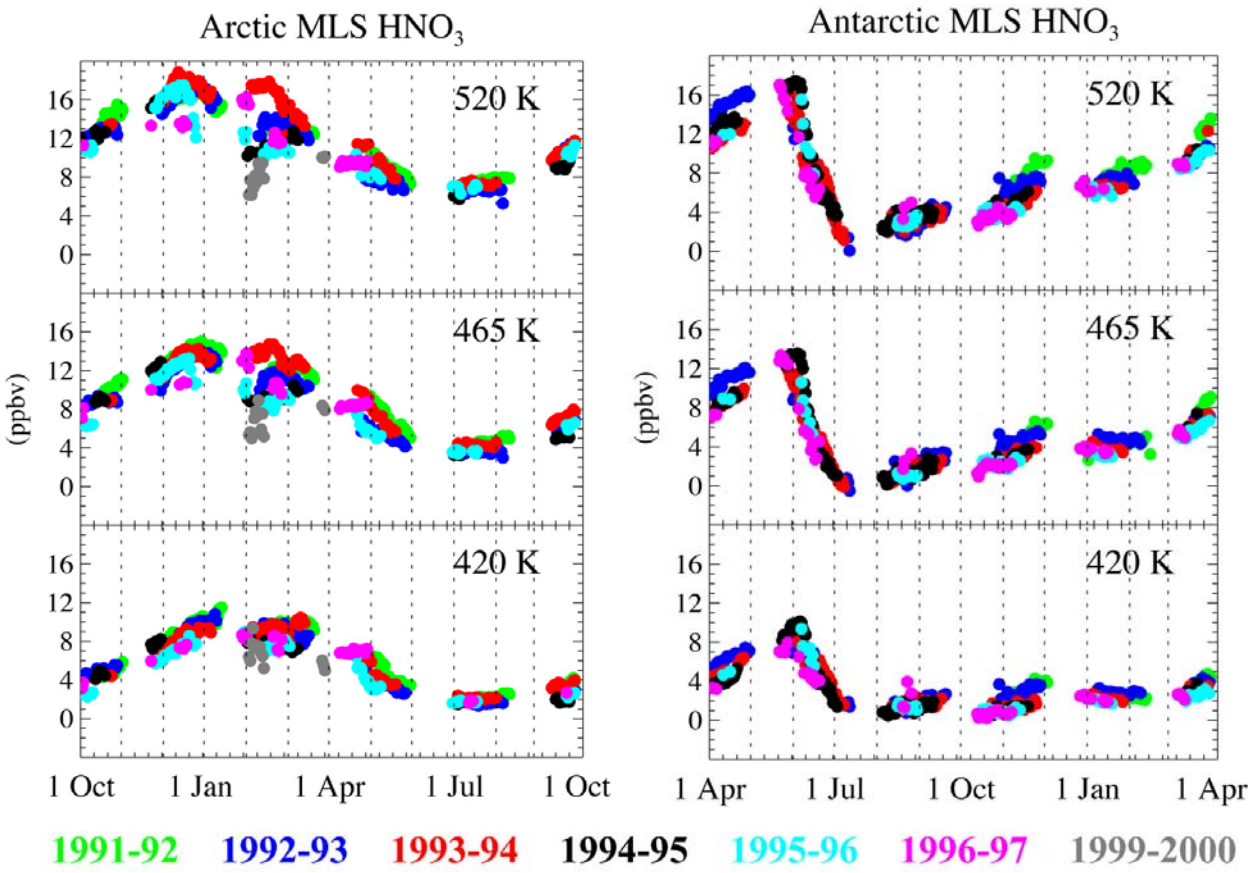

FIGURE 5.24: HNO_3 mixing ratio at three different potential temperature levels derived from MLS measurements for the Arctic and Antarctic winters 1991 to 1997 and 1999-2000.

The degree of denitrification determines the abundance of NO_2 in polar spring and therefore also the speed by which chlorine is deactivated by formation of $ClONO_2$ (R 1.7). To study if there is a measurable relation between deactivation of chlorine and the degree of denitrification, we investigated the column densities of OClO observed by GOME in different Arctic springs and derived a time needed for the deactivation of chlorine species by fitting an exponential decay curve to the OClO SCDs (see Fig. 5.25).

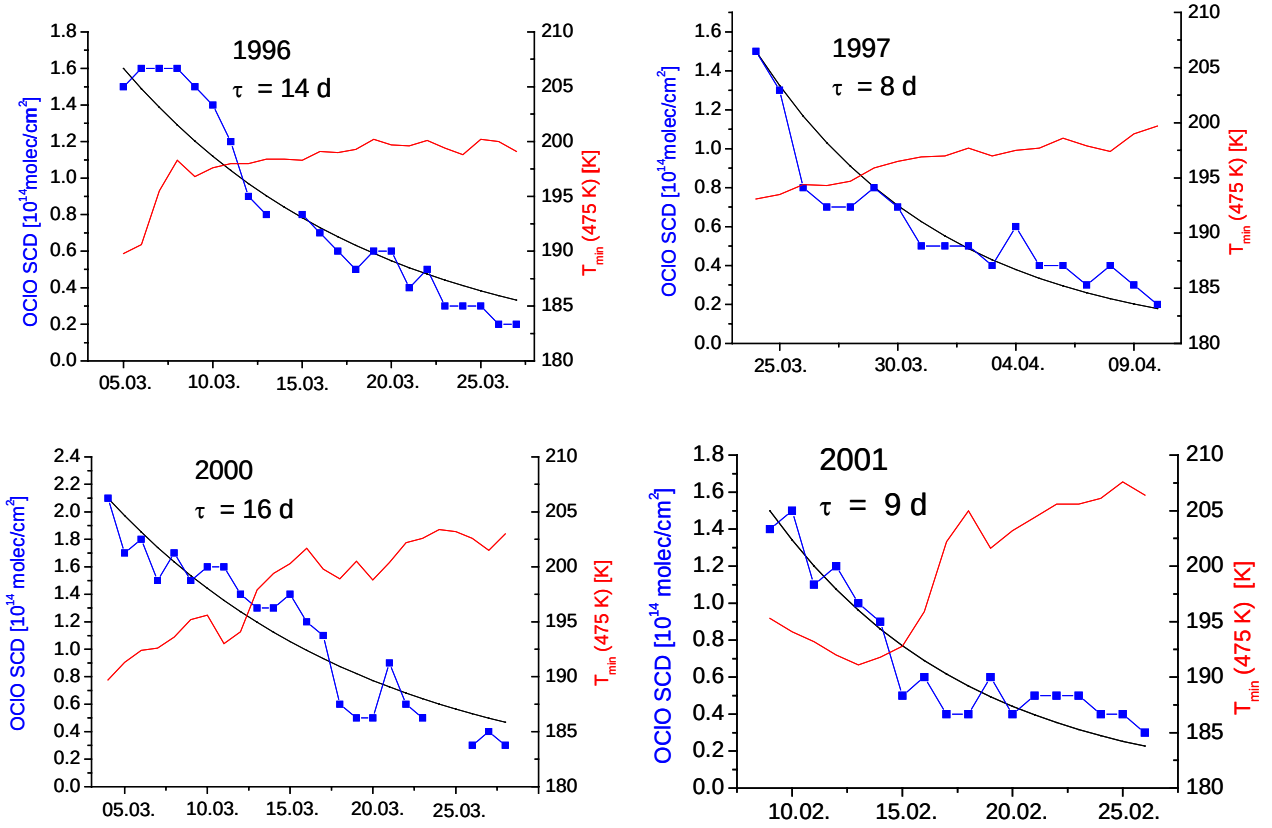

FIGURE 5.25: Daily maximum of the OClO SCDs at an SZA of 90° in four different arctic springs, also shown is the exponential fit to the data and the minimum temperature at the 475 K level. The SCDs of OClO decrease as soon as the minimum temperature at the 475 K level stays above 195 K. A deactivation time of 16 days for the winter 1999/2000, 14 days for 1995/96, 8 days for the winter 1996/97 and 9 days for the winter 2000/01 was found.

The determined time for chlorine deactivation seems to be related to the different degrees of denitrification in the respective Arctic winter, see table 5.1.

Arctic Spring	Time for deactivation (days)	Maximum of average denitrification (%)
1996	14	52 [1)]
1997	8	44 [1)]
2000	16	66 [1)]
2001	9	
Antarctic	18-22	80-100 [2)]

Table 5.1: Chlorine deactivation time derived from the exponential fit to the GOME OClO SCDs in comparison to the degree of denitrification in % determined by model calculation 1): for the Arctic [*Mann et al., 2003*], 2): for the Antarctic [*Schoeberl et al., 1996*].

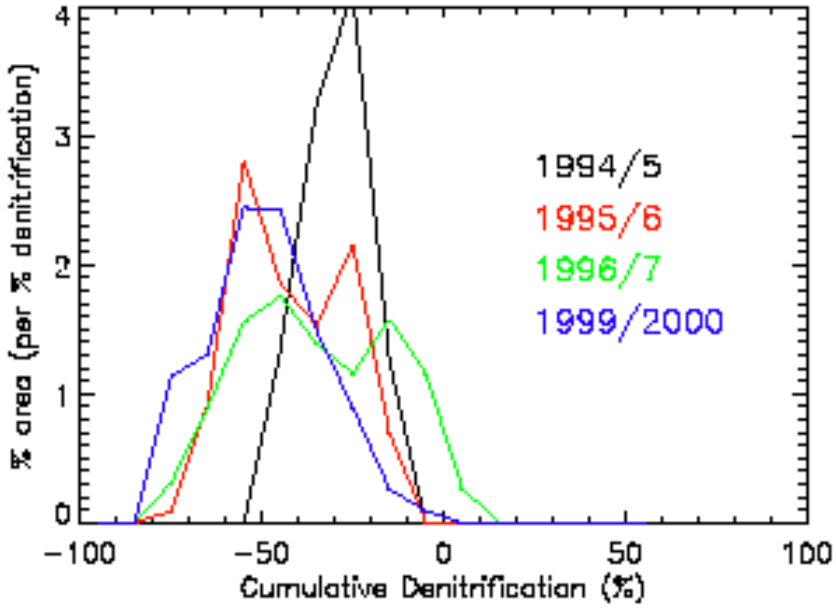

FIGURE 5.26: Histogram of area showing denitrification in % at the 465 K level on the 28th of February for the years 1995, 1996, 1997 and 2000. Adapted from [*Mann et al., 2003*].

For the Antarctic stratosphere, the time needed for deactivation of chlorine shows much less variability. From the exponential fit to the OClO SCDs, it was determined to vary between 18-22 days for the Antarctic winters 1996 to 2001. This is consistent with the meteorological conditions in the southern polar stratosphere that are much less variable than in the Arctic (see Fig. 2.2) and also with the MLS measurements of HNO_3 (see Fig. 5.24). Thus, the amount of NO_2 available in the chlorine deactivation phase (middle of September) is similar for every winter due to same degree of denoxification and denitrification. In addition, chlorine deactivation in the southern hemisphere also largely takes place by formation of HCl (*Douglass et al., 1995; Groos et al., 1997*).

6 SCIAMACHY Results

On 1st of March 2002, ENVISAT was launched. On board it carries the spectrometer SCIAMACHY, which has, in comparison to its predecessor GOME, a few advantages that are also very useful for measurements of OClO.
For the Nadir measurements, the spatial resolution is increased (30*60 km^2 compared to 40*320 km^2), which allows a more detailed study of small scale structures like e.g. chlorine activation at the edge of the polar vortex and by mountain waves. In addition, SCIAMCHY performs measurements also in the limb geometry, which, together with radiative transfer simulations, can be inverted to obtain vertical concentration profiles.
Compared to measurements of column densities, the vertical profiles of stratospheric trace gases like ozone, nitrogen dioxide, bromine oxide and chlorine dioxide significantly enhance the capability of interpreting the observations, and thereby will significantly increase the possibilities for studies on stratospheric chemistry. However, the alternating limb nadir measurements also have disadvantages, in particular regarding the global coverage: While GOME nadir measurements cover the whole globe every three days, SCIAMACHY needs six days.

In this thesis, the OClO retrieval which was successfully applied to GOME spectra, has been adopted to the SCIAMACHY nadir spectra. As well, algorithms for the retrieval of vertical profiles of O_3, NO_2, BrO and OClO have been developed. This chapter describes the spectroscopic retrieval, its optimization, the combination with radiative transfer simulations for inversion to vertical profiles, and also presents first results.

It is structured as follows:

- In section 6.1 first results of the OClO analysis from SCIAMACHY nadir spectra are presented: The OClO SCDs retrieved for different fit parameters are investigated and compared to the ones derived from GOME measurements for corresponding orbits. Then the first results for selected winters are discussed.

- The retrieval of vertical profiles from the SCIAMACHY limb measurements for O_3, NO_2 and BrO is described in detail in section 6.2. Also, the derived profiles are compared to other analysis of SCIAMACHY limb measurements and tested for consistency with the expectations from atmospheric chemistry.

- First results on the retrieval of OClO profiles from SCIAMACHY limb measurements are presented in section 6.3. For selected polar winters, the retrieved profiles are investigated in more detail regarding their seasonal and latitudinal variability.

6.1 SCIAMACHY Measurements of OClO in Nadir mode

6.1.1 First Results

As mentioned in section 3.7, SCIAMACHY spectra are disturbed by polarisation features which are especially strong in the near UV region, thereby causing difficulties for the retrieval of absorbers at these wavelengths. After the first spectra were analysed for OClO and also BrO, it turned out that it is essential to include the Eta and Zeta key data spectra for correction of polarisation features [*M. van Roozendael; A. Richter, personal communication, 2003*]. This is seen very nicely in Fig. 6.1 which shows OClO SCDs for retrievals with and without these spectra for otherwise constant parameters. Only the retrieval including both polarisation correction spectra leads to an acceptable offset of the OClO SCDs.

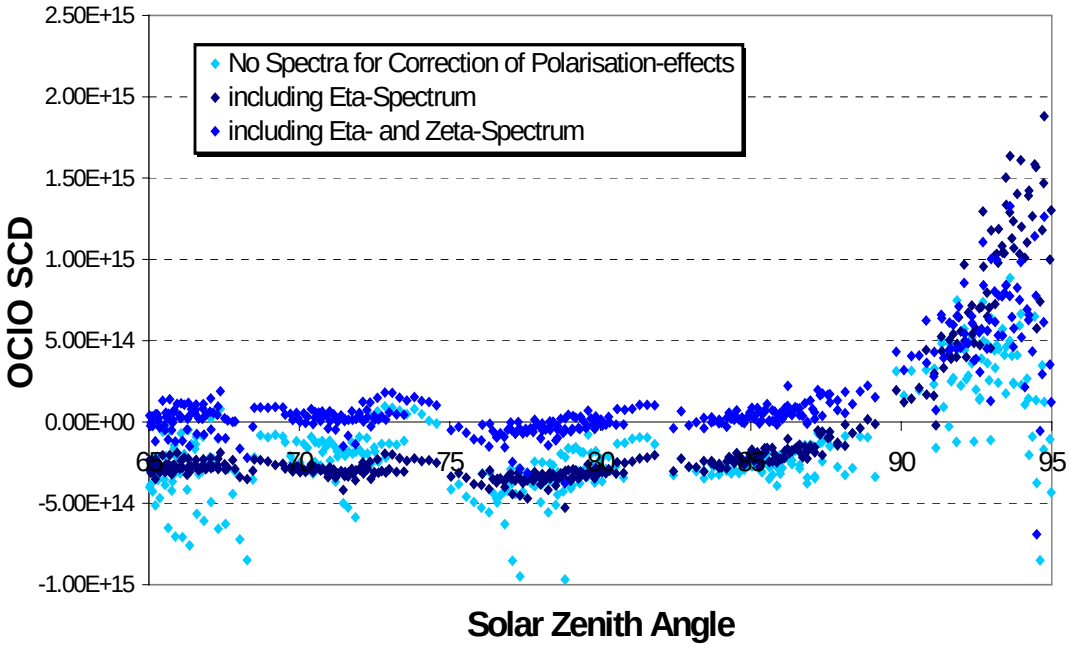

FIGURE 6.1: OClO SCDs as function of the SZA including and excluding the Eta and Zeta spectrum in the DOAS analysis of SCIAMACHY spectra. Shown are results for the orbit 2509 from 23rd of August, 2002. As Fraunhofer reference, the direct sunlight spectrum from the Azimuth scanning mirror (ASM) was used.

Other parameters that have a large impact on the retrieved OClO SCDs are the choice of the Fraunhofer reference and the wavelength interval utilized for the analysis. We compared the OClO SCDs retrieved for the same orbits when using either the ESM-, ASM- or an earth shine spectrum as Fraunhofer reference. While the OClO retrieval is possible for all of these Fraunhofer references, they reveal significant differences.
For the retrieval with the ESM spectrum, the retrieved SCDs show a large scatter and also reveal a strong artificial latitudinal dependence. For the polar regions, the best results (in terms of the magnitude of the OClO SCD) are obtained when using the earth shine spectrum at SZA=70°. However, along the whole orbit, this retrieval shows a considerable scatter and provides unrealistically large OClO SCDs, especially for the equatorial regions. Therefore, the SCIAMACHY OClO results from nadir spectra presented in this thesis are obtained from the retrieval using the ASM-spectrum as Fraunhofer reference. Also this retrieval shows an offset, which is nevertheless very constant along an orbit and also for the whole time series of SCIAMACHY measurements. For the wavelength interval, the best results (in terms of reducing the offset and the scatter of the retrieved SCDs) are obtained when using the range from 363-391 nm.

For the first SCIAMACHY spectra, which were poorly corrected for polarisation effects, the retrieval had to be performed at wavelengths from 363-382 nm, see also section 3.7. Later, a further band at the long wavelength side could be added, thereby using the same fit window as for the GOME OClO analysis. Figs. 6.2 and 6.3 exemplarily show some steps in the optimization process of the OClO retrieval.

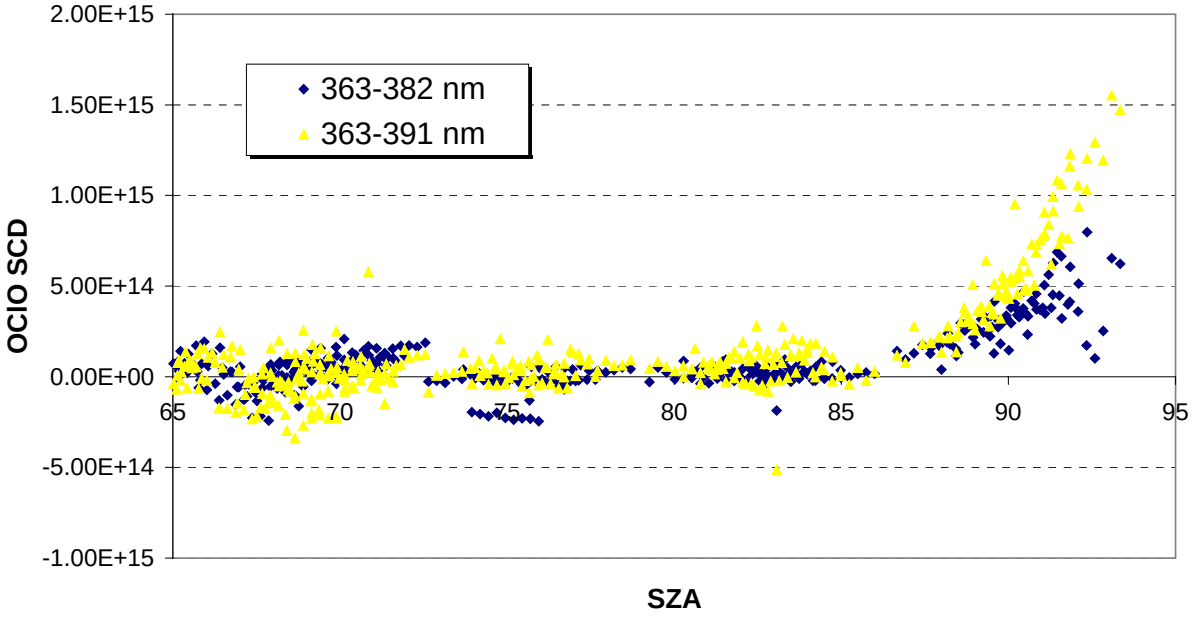

FIGURE 6.2: OClO SCDs as function of the SZA for the orbit 4426 from 4th of January 2003. Results were obtained by the analysis with the ASM spectrum as Fraunhofer reference, using either the wavelength range from 363 to 382 nm (blue dots) or from 363 to 391 nm (yellow dots).

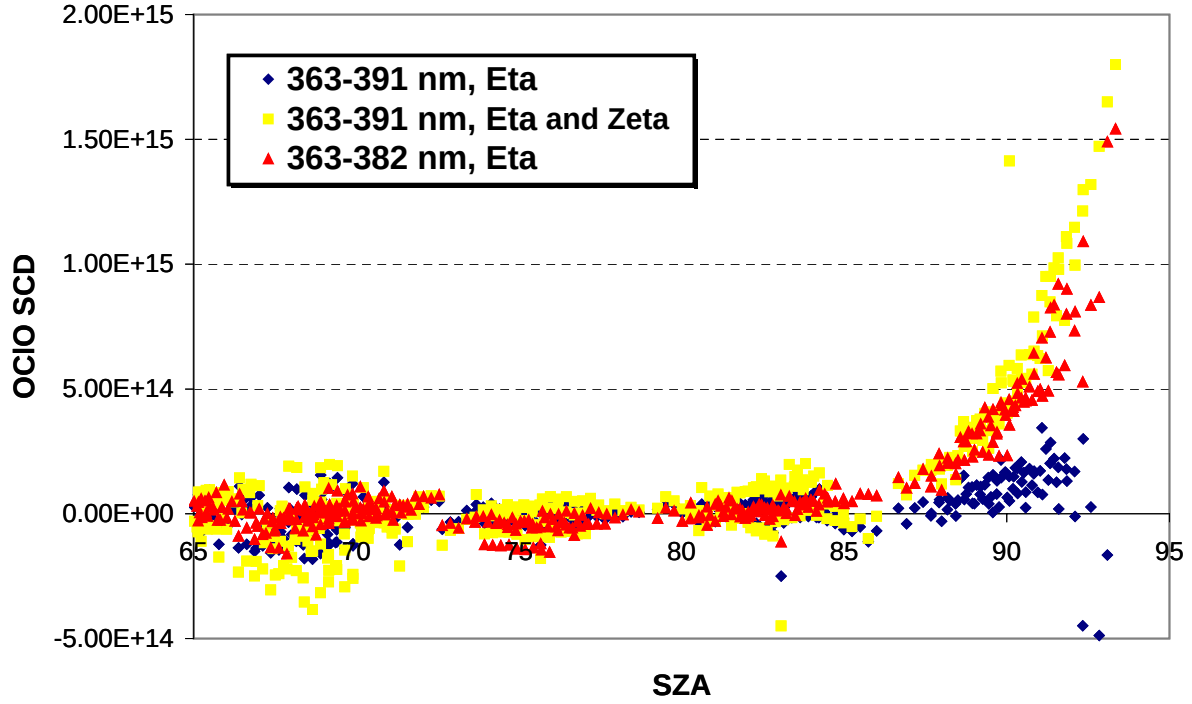

FIGURE 6.3: OClO SCDs as function of the SZA for the orbit 4426 from 4th of January 2003. Results were obtained by the analysis with an Earth shine spectrum (SZA = 70°) as Fraunhofer reference, using two different wavelength ranges and including or excluding the Zeta spectrum.

A further check for consistency is performed by inspecting the retrieved OClO SCDs visualized in terms of a map. Fig. 6.4 shows a global map of OClO SCD for all SCIAMACHY orbits from the 1st of August, 2003 (remember that the gaps result from the alternating limb-nadir measurements).

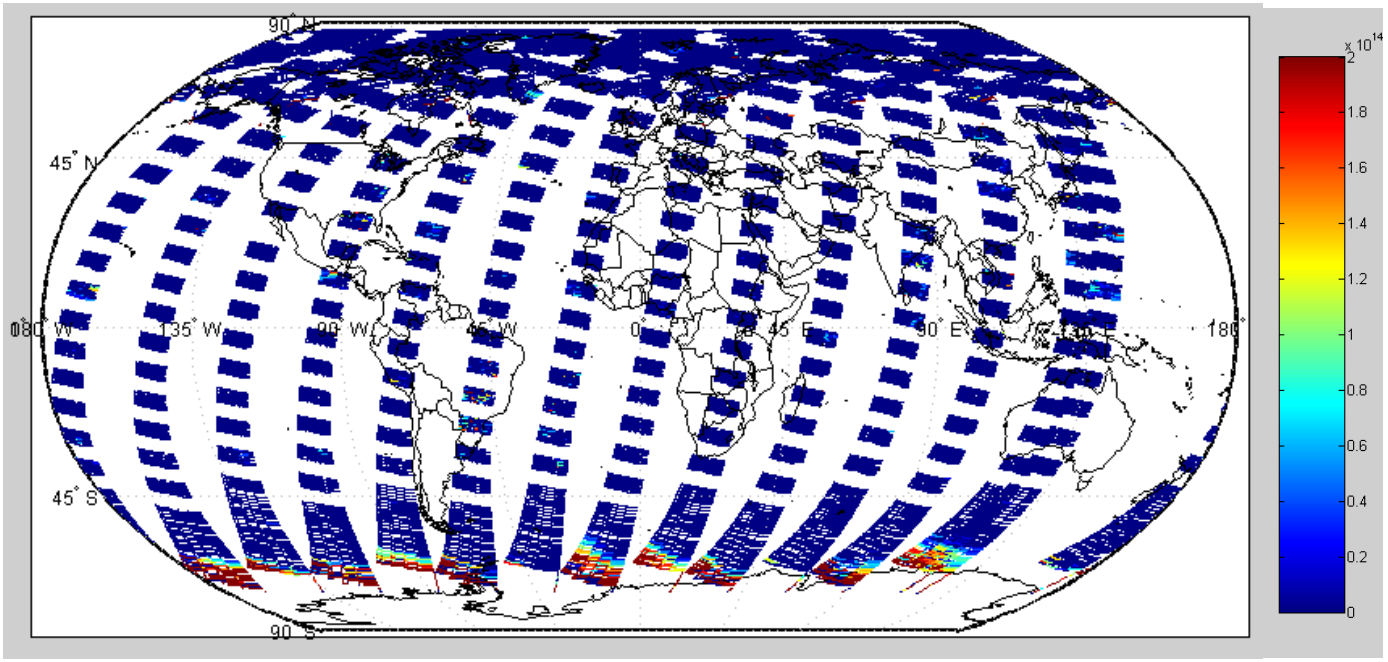

FIGURE 6.4: Global map of SCIAMACHY OClO SCDs for the 1st of August, 2003.

The spatial extension of the chlorine activated air masses is in good agreement with expectations from atmospheric chemistry: Enhanced OClO SCDs are retrieved only in the southern hemisphere close to the winter pole. Also, the magnitude of the OClO SCDs, which is around $2.0*10^{14}$ molec/cm^2 and above for the most southern part of the orbits, is in good agreement with the GOME OClO SCDs measured for other Antarctic winters in August (see Fig. 5.1).
In the following, we investigate in more detail, how well the OClO SCDs derived from SCIAMACHY spectra agree with the GOME measurements, also for corresponding orbits.

6.1.2 Comparison with GOME

When comparing measurements from SCIAMACHY to the ones from GOME one has to consider the difference in the time of the measurement: The difference in the equator crossing of 20 minutes (GOME: 10:30 am, SCIAMACHY: 10:10 am) leads to considerable larger SZAs for the SCIAMACHY measurements. Due to the strong diurnal cycle of OClO, this has a significant effect on the retrieved OClO SCD: The magnitude of the SCD should generally be larger since less OClO is destroyed by photolysis. Further discrepancies may arise because the situation at the location of the measurement changes due to transport or chemical processes. Also, the increased spatial resolution of the SCIAMACHY measurements may result in smaller or larger OClO SCDs for the same location.

Due to the failure of the ERS-2 tape recorder in June 2003, the overlap of SCIAMACHY and GOME measurements is only about one year. Thus it is not possible to compare long time series. Moreover, SCIAMACHY measurements are provided on a regular basis only since beginning of 2003, and periods with significant chlorine activation are confined to the polar winters. This means that for a comparison of retrieved OClO SCDs for a longer time period, only data from January and May 2003 can be used (for February 2003 there was no significant chlorine activation in the Arctic, and for the remainder of the Antarctic winter 2003 there are no more GOME measurements).
However, single orbits for the northern and southern hemisphere in 2002 and 2003 can be compared (for the Arctic, also a few GOME orbits around the Kiruna station are still delivered). In addition, for the southern hemisphere, where meteorological variability is smaller, the magnitude and the temporal evolution of the OClO SCDs during the winter can be compared also for measurements from different years.

Figs. 6.5 and 6.6 show OClO SCDs derived from SCIAMACHY and GOME measurements for corresponding orbits from 23rd of August, 2002.

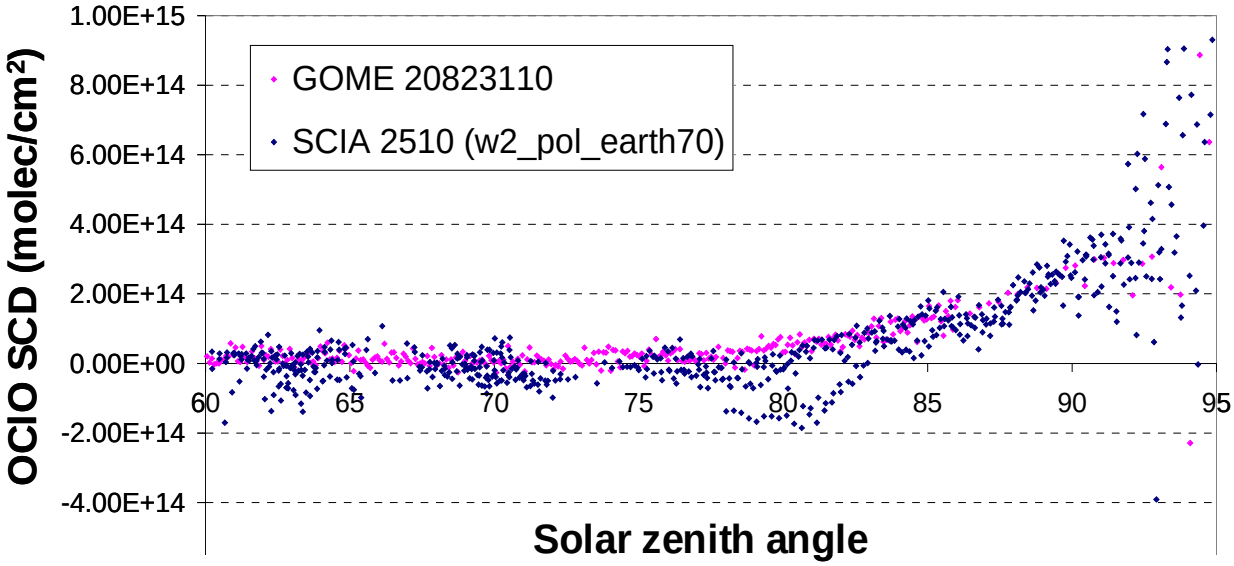

FIGURE 6.5: OClO SCDs from SCIAMACHY and GOME for corresponding orbits as function of the solar zenith angle. For both instruments, the OClO analysis was performed with an earth-shine spectrum as Fraunhofer Reference. Displayed is the orbit 2510 for SCIAMACHY and 20823110 for GOME, both from 23rd August 2002. They reveal high OClO SCDs for latitudes > 60° S (SZA > 80°).

The OCO SCDs derived from SCIAMACHY spectra are in good qualitative and quantitative agreement with the GOME OClO retrieval. Enhanced OClO SCDs are found only for SZAs above 80 degrees, which for this orbit corresponds to regions inside the Antarctic polar vortex. The magnitude of the SCDs at the SZA of 90 degrees is around $3.0*10^{14}$ molec/cm2 which is a typical value for the month of August (see Fig. 5.1). However, the scatter of the retrieved SCDs is much larger for SCIAMACHY. We investigated the possible reasons for this scatter by calculating the ratio spectrum of pixels with large and small OClO SCDs at nearly the same geolocation and the same orbit. It turned out that this ratio spectrum is almost identical to the Eta spectrum for correction of polarisation features (see section 6.1.1). This reveals that also including the Eta and Zeta spectra from keydata does not perfectly correct for the polarisation features of the SCIAMACHY spectra.

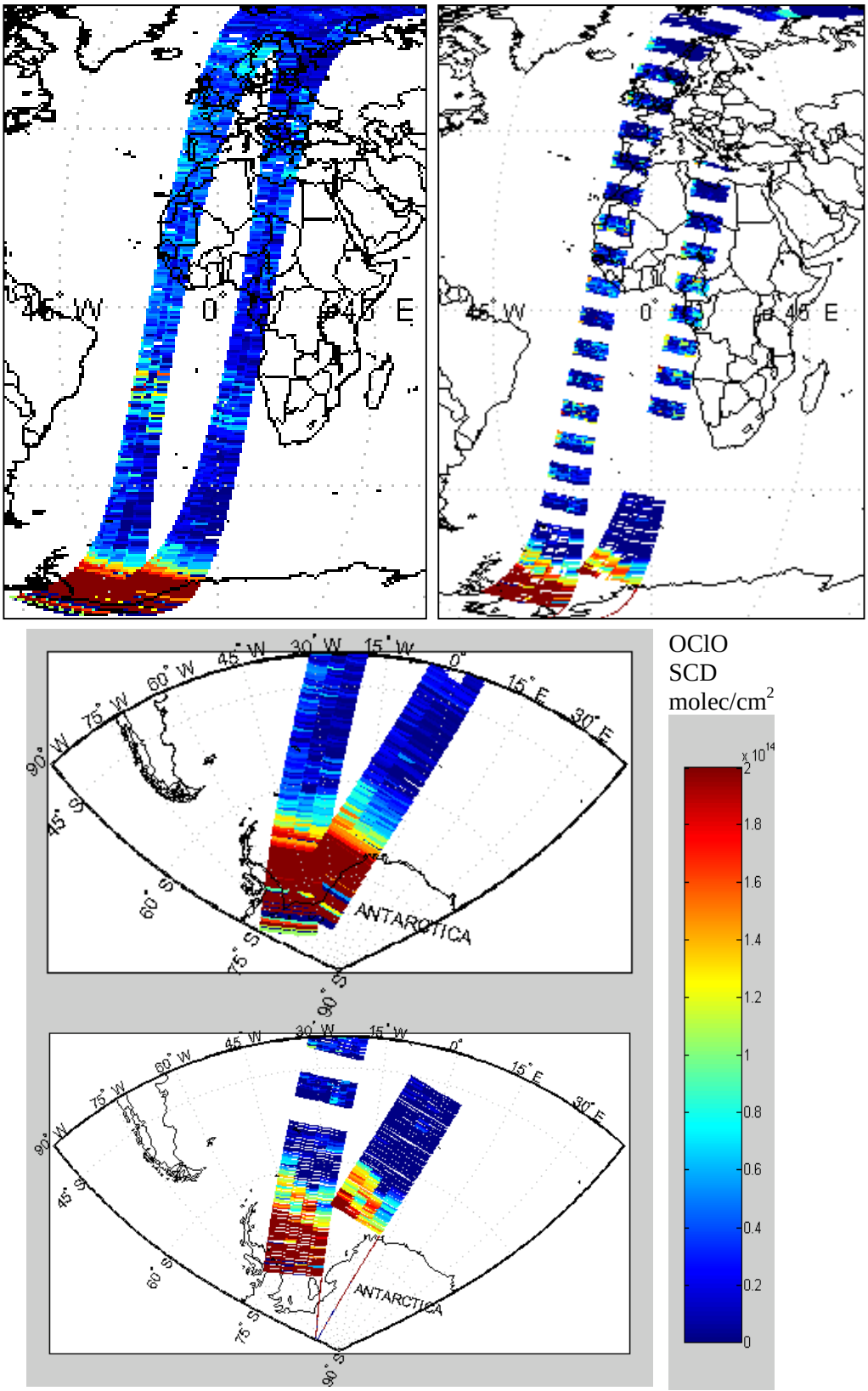

FIGURE 6.6: OClO SCDs measured by GOME and SCIAMACHY on the 23rd of August, 2002. Top: GOME orbits 20823096 and 20823110 and (left) and SCIAMACHY orbits 2509 and 2510 (right). Bottom: same, but in south pole projection (top: GOME, bottom: SCIAMACHY).

While the comparison to the one from simultaneous GOME orbits, it is also interesting, how well the retrievals developed by different groups agree.
Fig. 6.7 shows the OClO SCDs of the Heidelberg analysis in comparison to the one from the Bremen group for the orbit 12986 from 24th of August, 2004. Both evaluations show large OClO SCDs for large latitudes in the southern hemisphere and significantly lower values elsewhere with a similar shape of the whole curve. Also, the scatter is of similar magnitude ($\approx 1.0*10^{14}$ molec/cm^2). The main difference is the magnitude of the SCDs, especially for low and mid latitudes. While the Heidelberg retrieval has a negative offset, the mean value of the SCDs from the Bremen retrieval is close to zero. However, the Bremen analysis shows unrealistically large values for the midlatitudes and the equator. For high latitudes (>70°) in the southern hemisphere, where large OClO abundances are expected, the magnitude of the SCDs is quite similar. The difference in the offset is not essential since it can be easily corrected for. A significant improvement would be a reduced scatter of the OClO SCDs. However, since the scatter likely results from improper correction for polarisation effects (see section 6.1.2), it can probably only be reduced by a better calibration of the SCIAMACHY spectra.

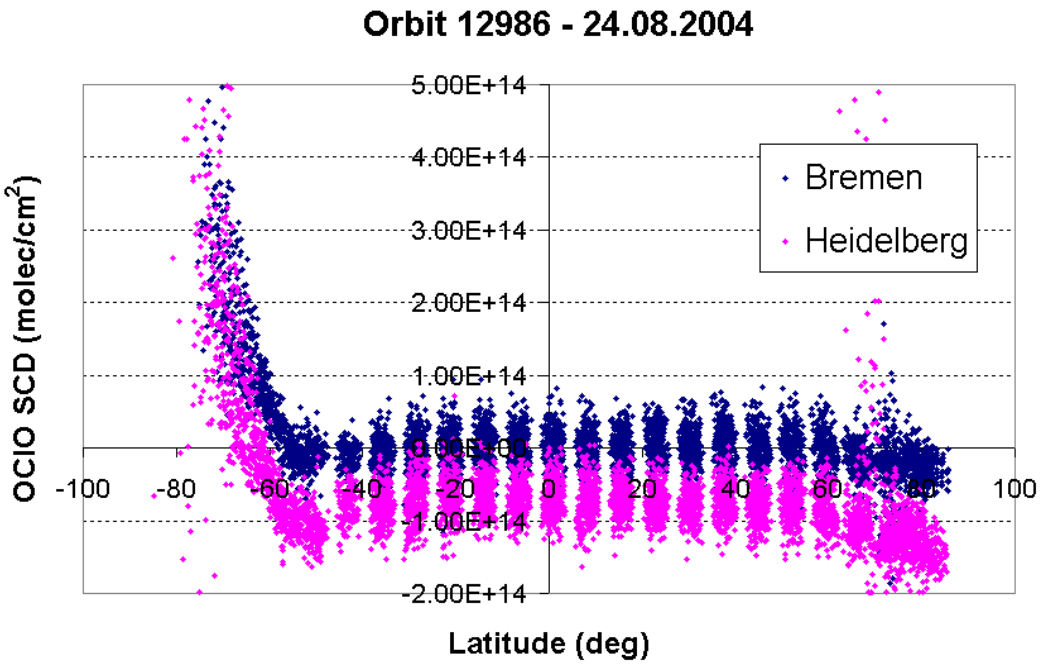

FIGURE 6.7: Typical curve for OClO SCDs as function of latitude for the Heidelberg and Bremen SCIAMACHY OClO analyses. Results are shown for the orbit 12986 from 24th of August, 2004.

6.1.3 The Arctic winter 2004/05

In the following, we present first results of the SCIAMACHY OClO analysis for the latest Arctic winter. This winter featured the coldest stratospheric temperatures of all Arctic winters observed by GOME and SCIAMACHY. Accordingly, formation of PSCs was possible for extended areas, over a wide altitude range and also for a long time period, see Figs 5.5 and 6.8. Fig. 6.9 shows single day OClO maps for selected days in comparison to results for ClO_x from the 4D VAR model BASCOE.

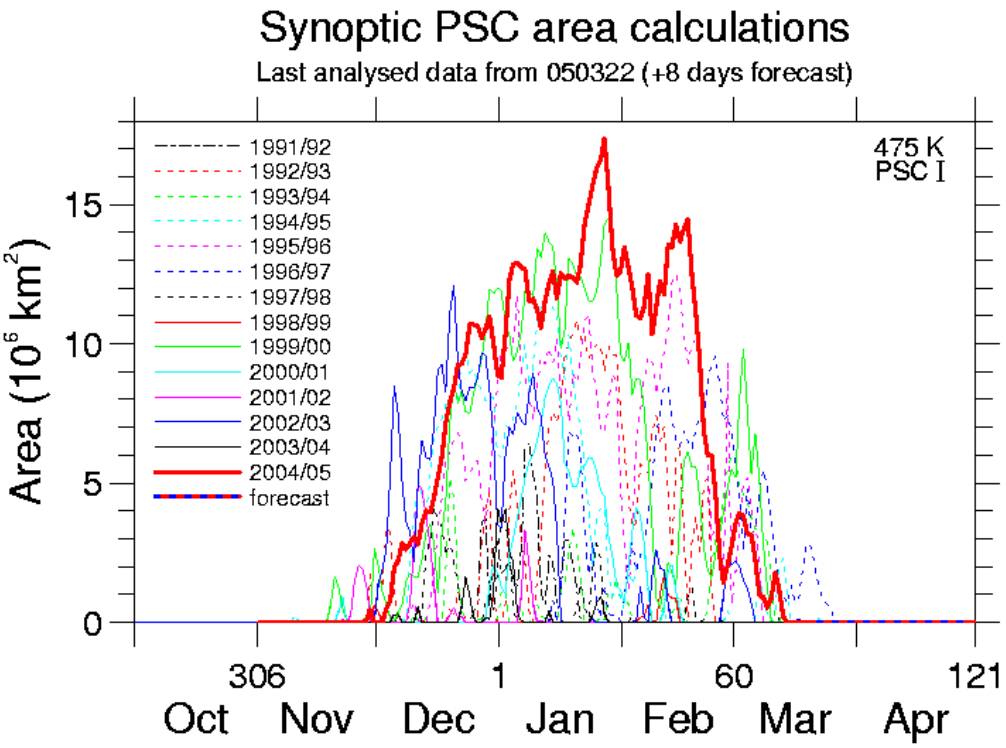

FIGURE 5.5: Daily areas of possible PSC type 1 (NAT) formation at the 475 K level for all Arctic winter since 1991/92, based on ECMWF temperatures and on the NAT existence hypothesis. Threshold temperatures are calculated according to [*Hanson and Mauersberger, 1988*]. Adapted from: http://www.awi-potsdam.de/www-pot/atmo/met/psc1.html

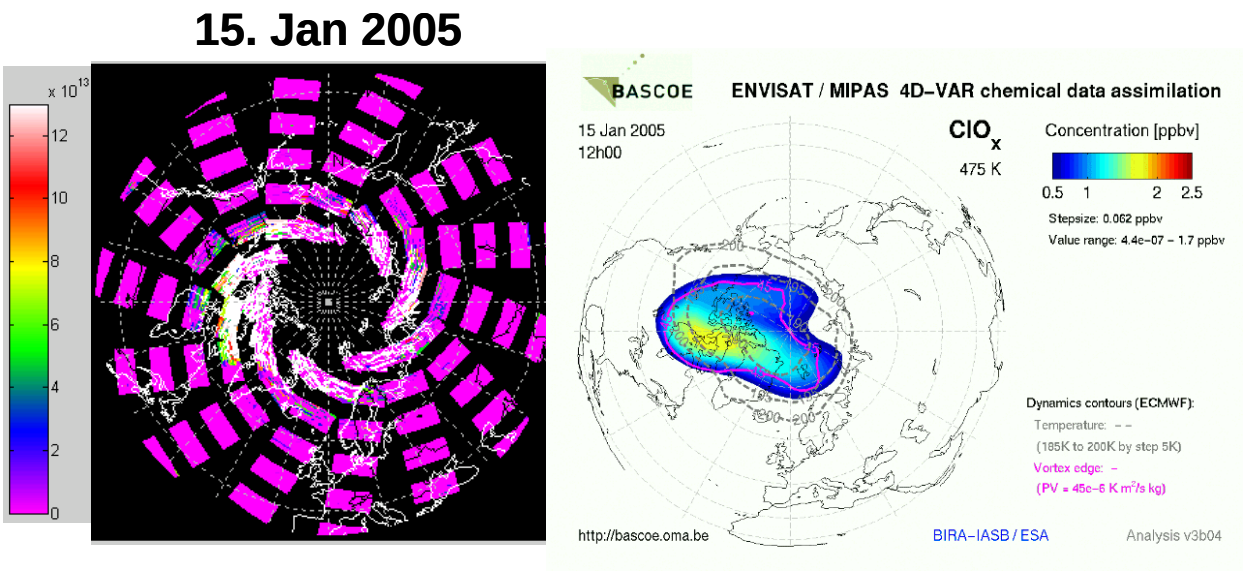

FIGURE 6.9: Single day maps of SCIAMACHY OClO SCDs in comparison to results from the 4D VAR model BASCOE (continued on next page).

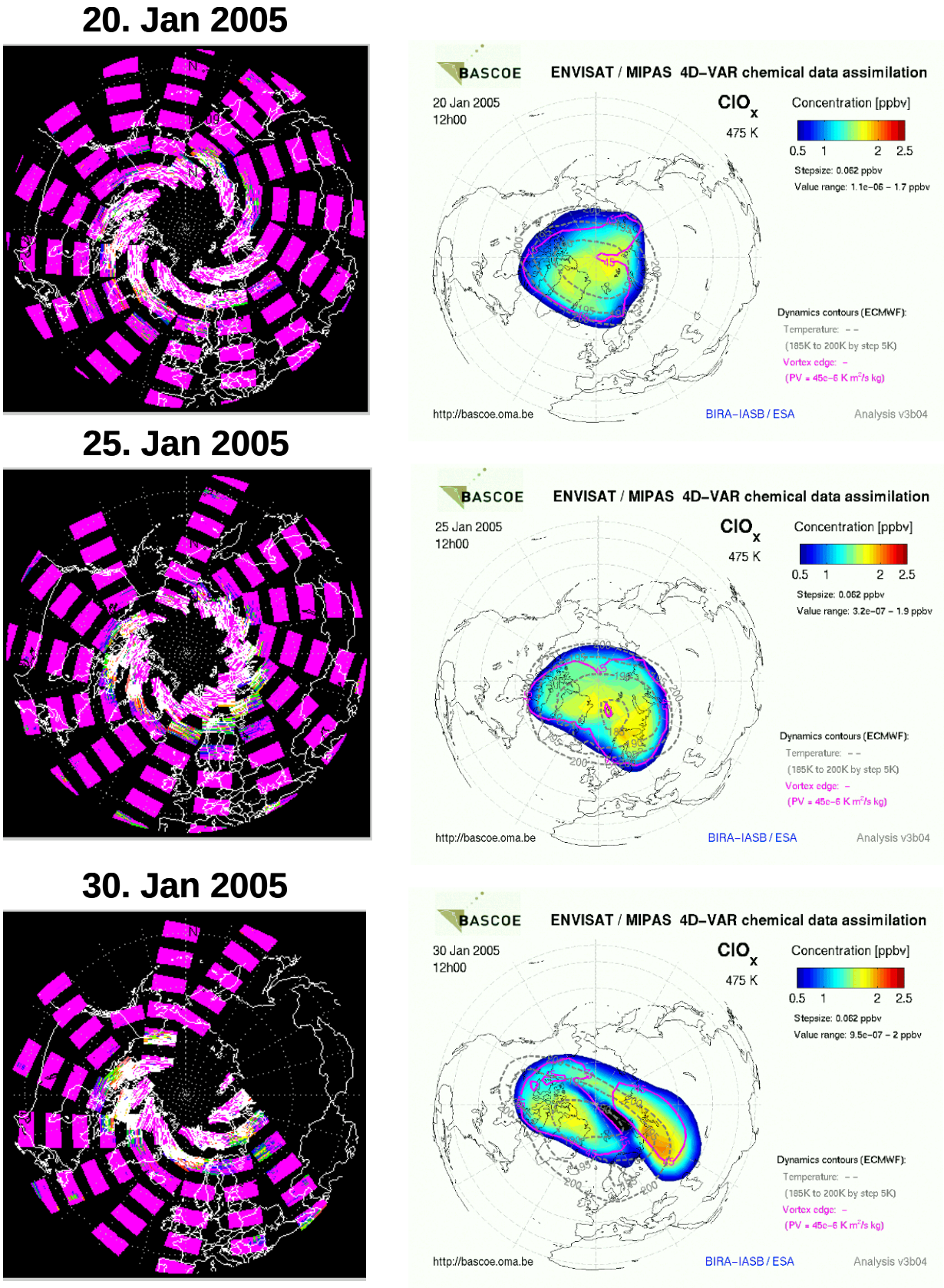

FIGURE 6.9: Single day maps of SCIAMACHY OClO SCDs in comparison to results from the 4D VAR model BASCOE.

6.2 SCIAMACHY Measurements of O_3, NO_2 and BrO in Limb mode

The development of an algorithm for the retrieval of vertical OClO profiles from limb measurements is not a trivial task. The optical density of the OClO absorption is one or two magnitudes smaller than for ozone or NO_2. In addition, large OClO abundances occur only for high latitudes, corresponding to large SZAs, for which the simulation of the radiative transfer is difficult.
It is thus advantageous, to first examine the algorithm with stronger absorbers for which the quality of the spectroscopic retrieval and the proper implementation of the radiative transfer simulations in the inversion process can be easier studied. Therefore, the approach is first tested on the retrieval of vertical profiles of O_3, NO_2 and also BrO. Also, with the retrieved profiles for ozone, which are expected to be derived with relatively high accuracy, it is possible to study the correctness of the radiative transfer calculations. In addition, O_3, NO_2 and BrO are closely related to the chemistry of stratospheric chlorine. Thus the retrieved profiles can also be used to study interconnections between the different trace gases.

As described in section 3.3., the retrieval of vertical trace gas profiles from SCIAMACHY limb spectra is done in two steps: First, the SCDs of the considered atmospheric absorber as function of the tangent height are retrieved by DOAS. Second, the SCDs are inverted by optimal estimation applying the box AMFs calculated by the radiative transfer model TRACY. This two step approach enables us to study separately the impact of spectroscopy and radiative transfer simulation on the retrieved profile.
In the following sections, the two step approach is described in detail for the respective trace gas: First, the SCDs are discussed regarding their consistency with expectations from atmospheric chemistry and radiative transfer. Then, the weighting function for the inversion, the box AMF as function of altitude, relevant for the wavelength interval of the retrieval, are introduced.
Typical averaging kernels for the inversion are shown, revealing the altitude range for which information about the vertical profile can be obtained from the measurement. Then, first results of retrieved vertical profiles are presented. They are compared to other SCIAMACHY limb retrievals and discussed in the context of their application for studying atmospheric chemistry.

6.2.1 Retrieval of vertical O_3 profiles

The ozone analysis of SCIAMACHY limb spectra is performed in the UV region (337 to 358 nm), see section 3.9.
As an example, Figure 6.10 shows the **measured SCDs** for an orbit from the 24th of August, 2004. For each tangent height the retrieved values for the four pixels of the vertical scan are shown.
While the top panel shows the O3 SCDs as function
bottom
The latter reveals that the scatter of the retrieved SCDs results (not only) from the statistical measurement error, but mainly from the latitudinal dependence of the ozone profile: While the ozone SCDs at the equator and at 45° N are of similar magnitude, the ones at 55° S have significantly smaller values, in good agreement with the expectation from atmospheric chemistry for the month of August.
For the same latitude, the scatter of the SCDs retrieved for the four pixels of the vertical scan is smaller than $1.0*10^{19}$ and about $2.0*10^{19}$ (molec/cm^2) for the southern hemisphere. The increase of the scatter for the state close to the south pole may arise from two factors: It may indicate a larger variability in the concentration of O_3 (inside and outside vortex). Also, it possibly indicates a smaller signal to noise ratio for measurements at large SZAs.

Together with the box AMFs, calculated by Janis Pukite with the radiative transfer simulation TRACY, the SCDs are inverted to vertical ozone profiles.

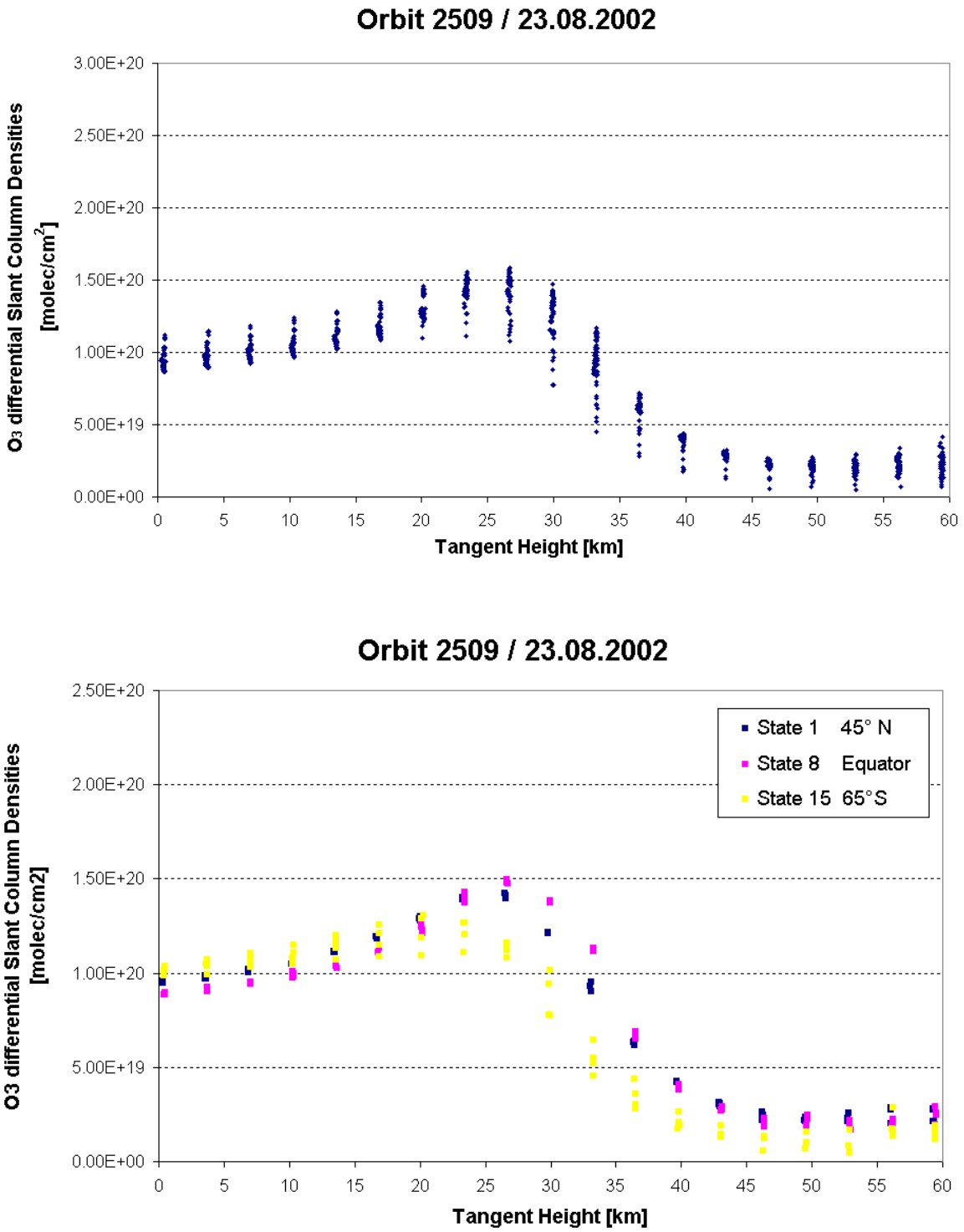

FIGURE 6.10: O_3 SCDs as function of tangent height for orbit 2509 from 23rd of August 2002. Top: for all limb states of that orbit, bottom: for selected states in the northern and southern hemisphere and at the equator.

Fig. 6.11 shows **box air mass factors** for the wavelength of 340 nm, the center of the wavelength interval utilized for the retrieval of ozone SCDs.

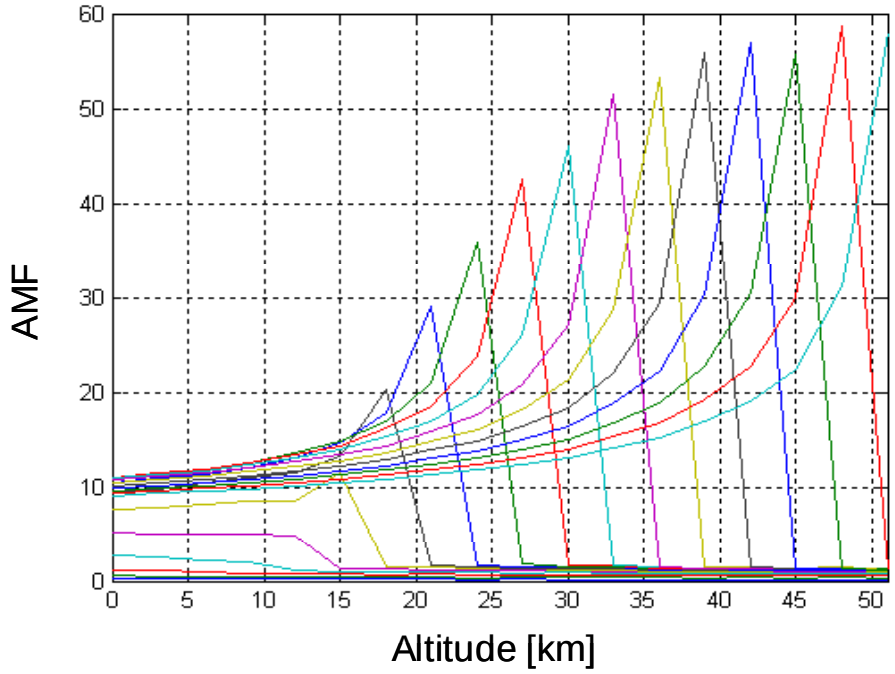

FIGURE 6.11: Box air mass factors as function of altitude calculated by the RTM Tracy for the wavelength of 340 nm. SZA = 40 degrees.

The box AMF are used as weighting functions for the inversion of the SCDs, see section 3.3.As **a priori** we use the climatology of *Lamsal et al.* [2004]. The resulting **Averaging Kernels** for a typical ozone profile retrieval, displayed in Fig. 6.12, demonstrate that ozone profiles can be obtained from SCIAMACHY limb measurements in an altitude range from 15 to 43 km.

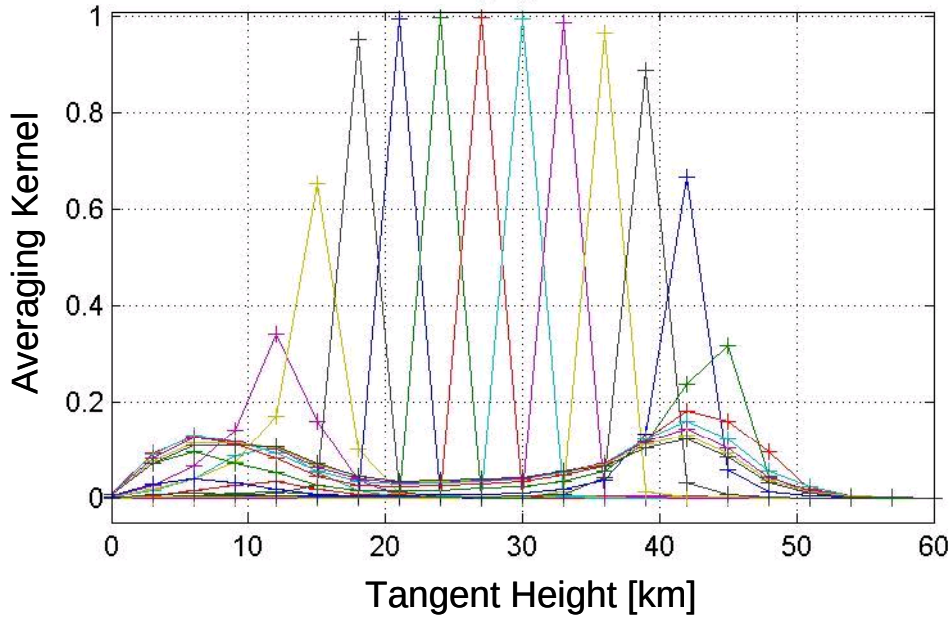

FIGURE 6.12: Typical averaging kernels as function of the tangent height for a retrieved O_3 profile.

In the following, we present first results on the vertical O_3 profiles for selected SCIAMACHY orbits: 2509 from 23rd of August, 2002 and 12984, 12986 and 12990 from 24th of August, 2004. The locations for the respective limb states of these orbits are shown in Fig. 6.13.

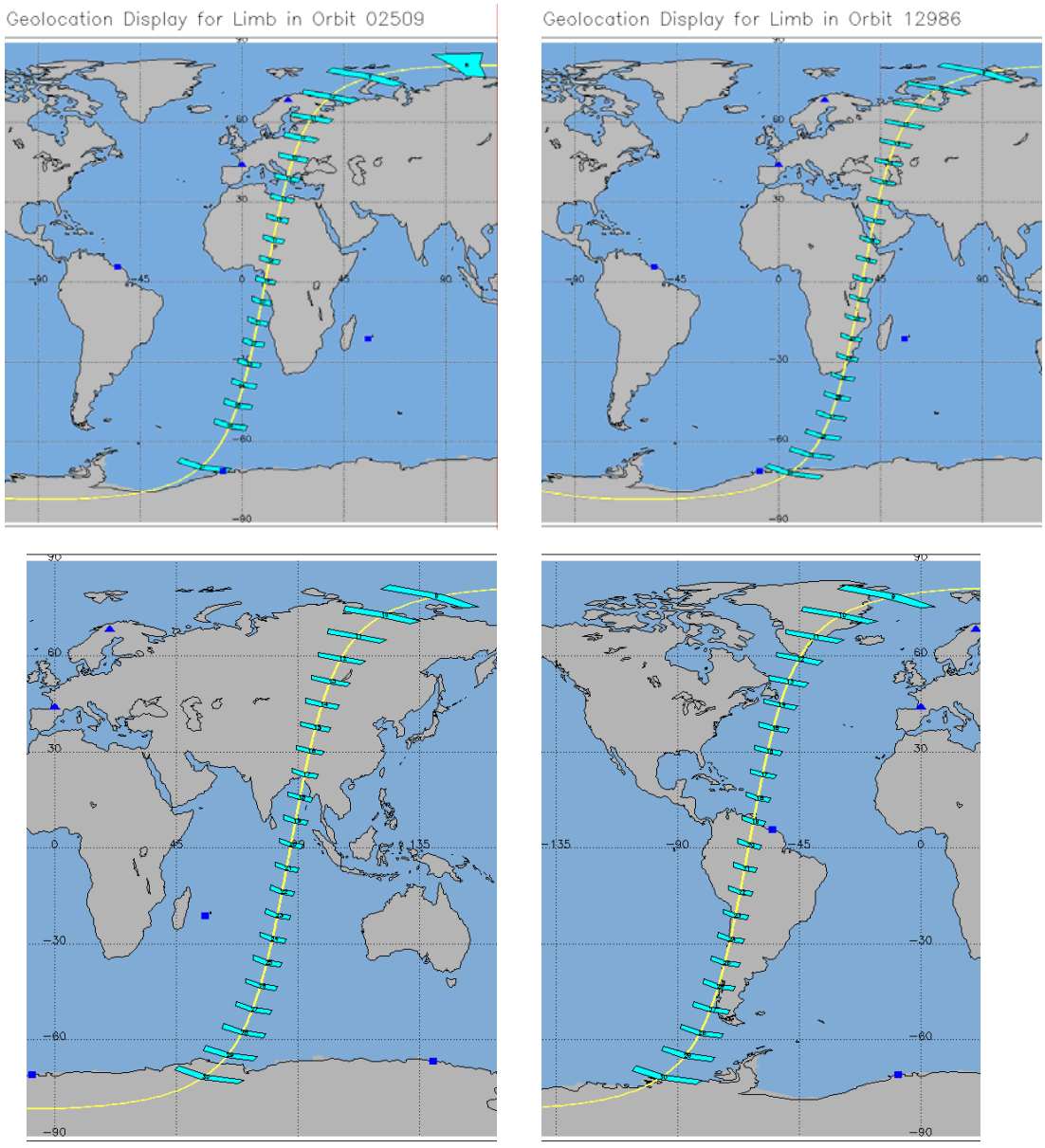

FIGURE 6.13: Geolocation maps for the limb states of orbit 2509 from 23.08.2002 (top, left), orbit 12986 from 24.08.2004 (top, right) and orbit 12984 (bottom, left) and 12990 (bottom, right) from 24.08.2004.

The latitudinal cross section of the ozone profile for the orbit 2509 is compared to the one from the Bremen analysis, see Fig. 6.14. The averaging kernels displayed in Fig. 6.12 show that information about the ozone profile can be retrieved from SCIAMACHY limb measurements between 15 and 43 km. Thus, for altitudes below 15 km, any discrepancies in the O_3 profiles result not from the measurement but from the a priori profile. Therefore, the retrieved profiles should only be compared from 15 to 45 km altitude. The Bremen retrieval of SCIAMACHY O_3 profiles has been intensively validated [*von Savigny et al., 2004; Bracher et al., 2005*]. Thus the good accord of our retrieved profiles with the Bremen results implies that they are accurate.

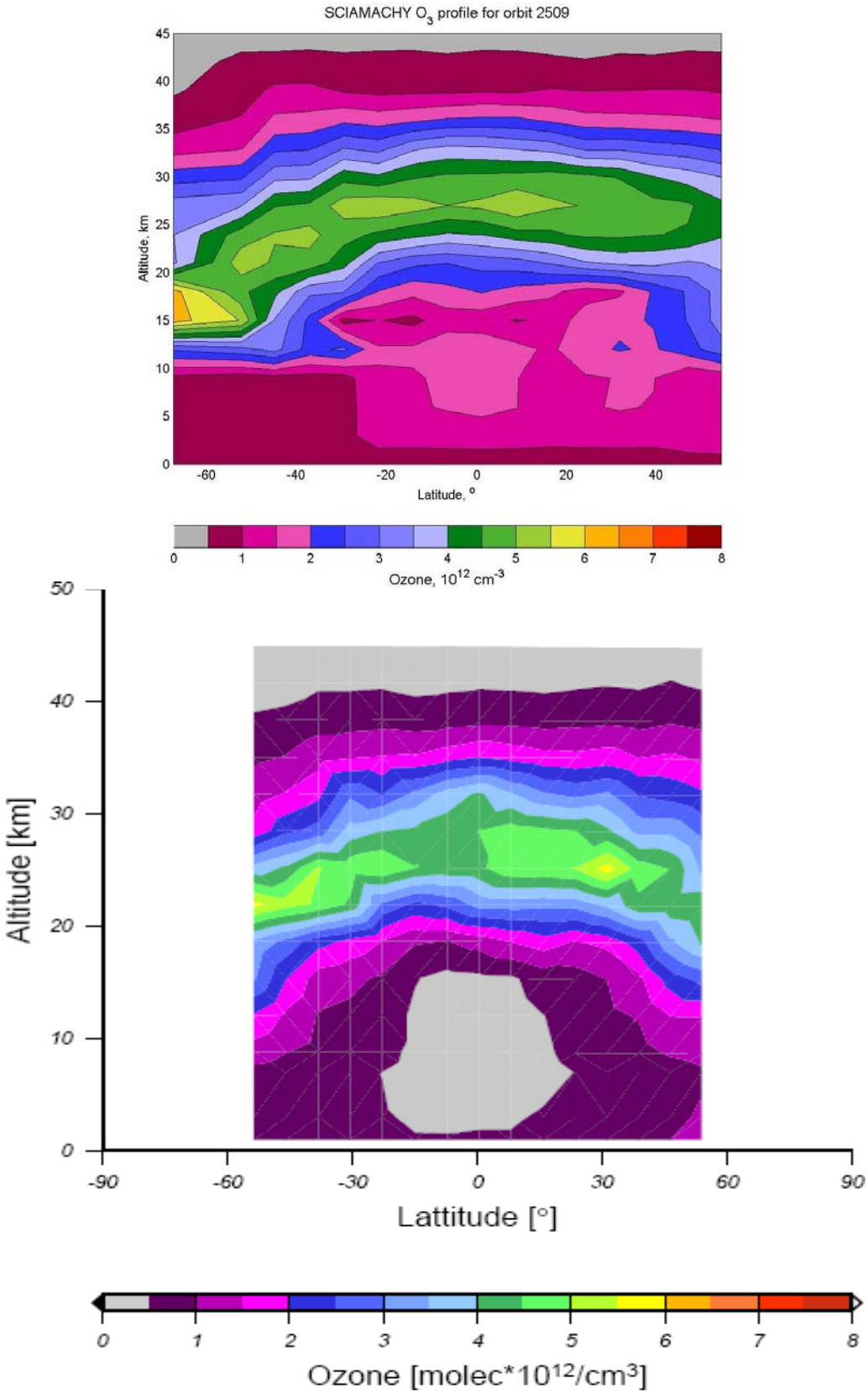

FIGURE 6.14: Latitudinal cross section of the O_3 concentration profile for the orbit 2509 from 23rd of August, 2002. Top: Retrieval developed in this thesis. Bottom: Retrieval by C. v. Savigny, IUP Bremen. Latitude axis different and scaled to match.

A further check for consistency is performed by comparing the ozone profiles derived from the SCIAMACHY limb measurements with the total ozone column from TOMS measurements. Fig. 6.15 shows the TOMS total ozone columns for the 24th of August, 2004.

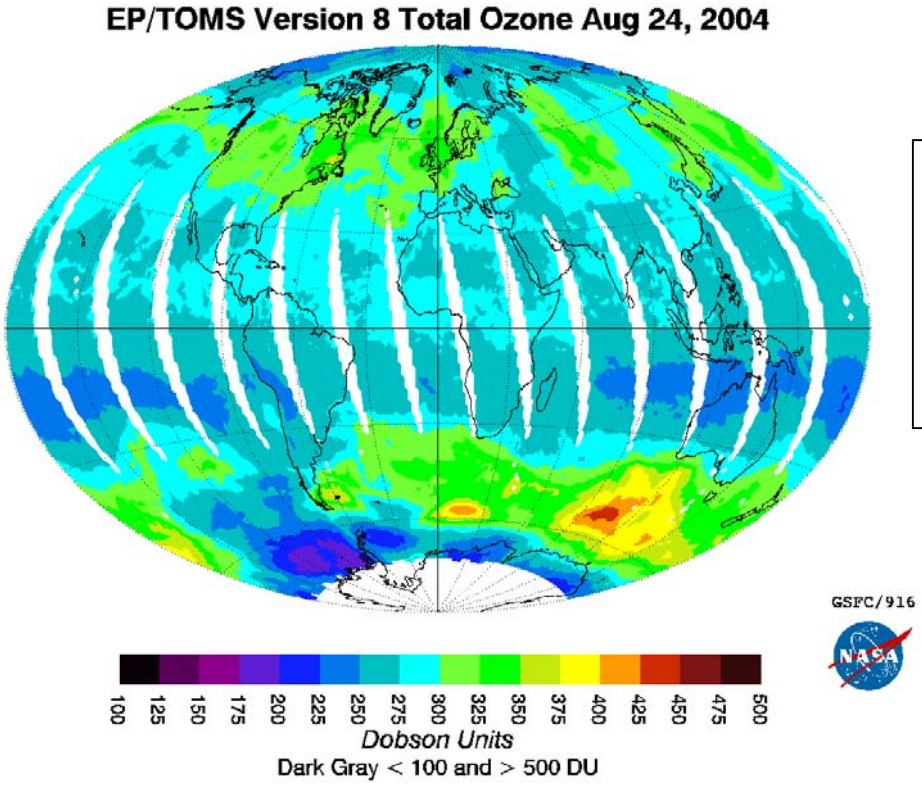

FIGURE 6.15: Global total ozone columns in DU as derived from TOMS measurements for the 24th of August, 2004.

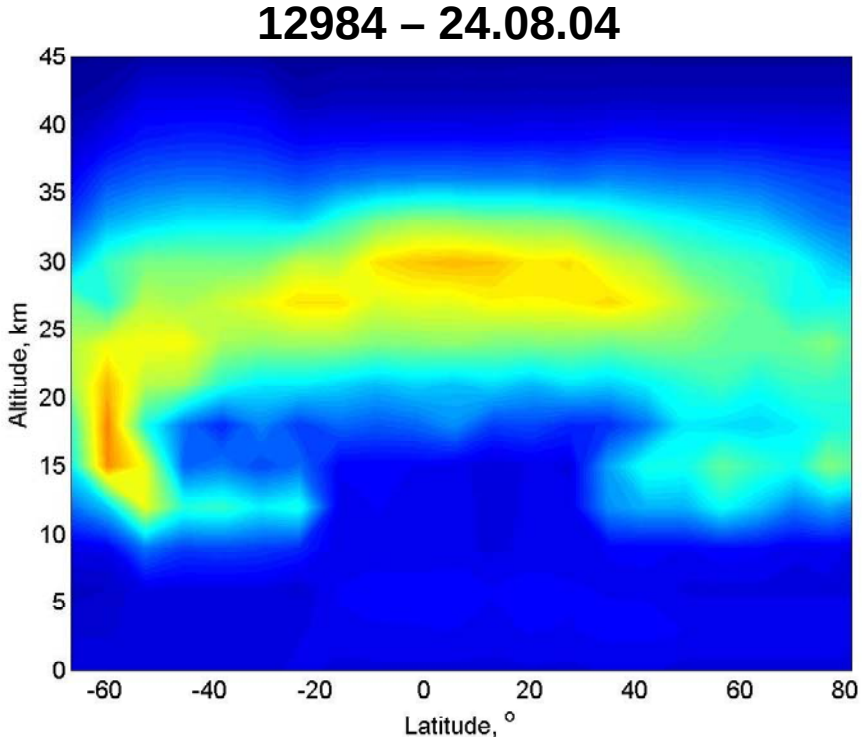

FIGURE 6.16: Ozone number density as function of latitude and altitude for the orbit 12984 (compare Fig. 6.13.)

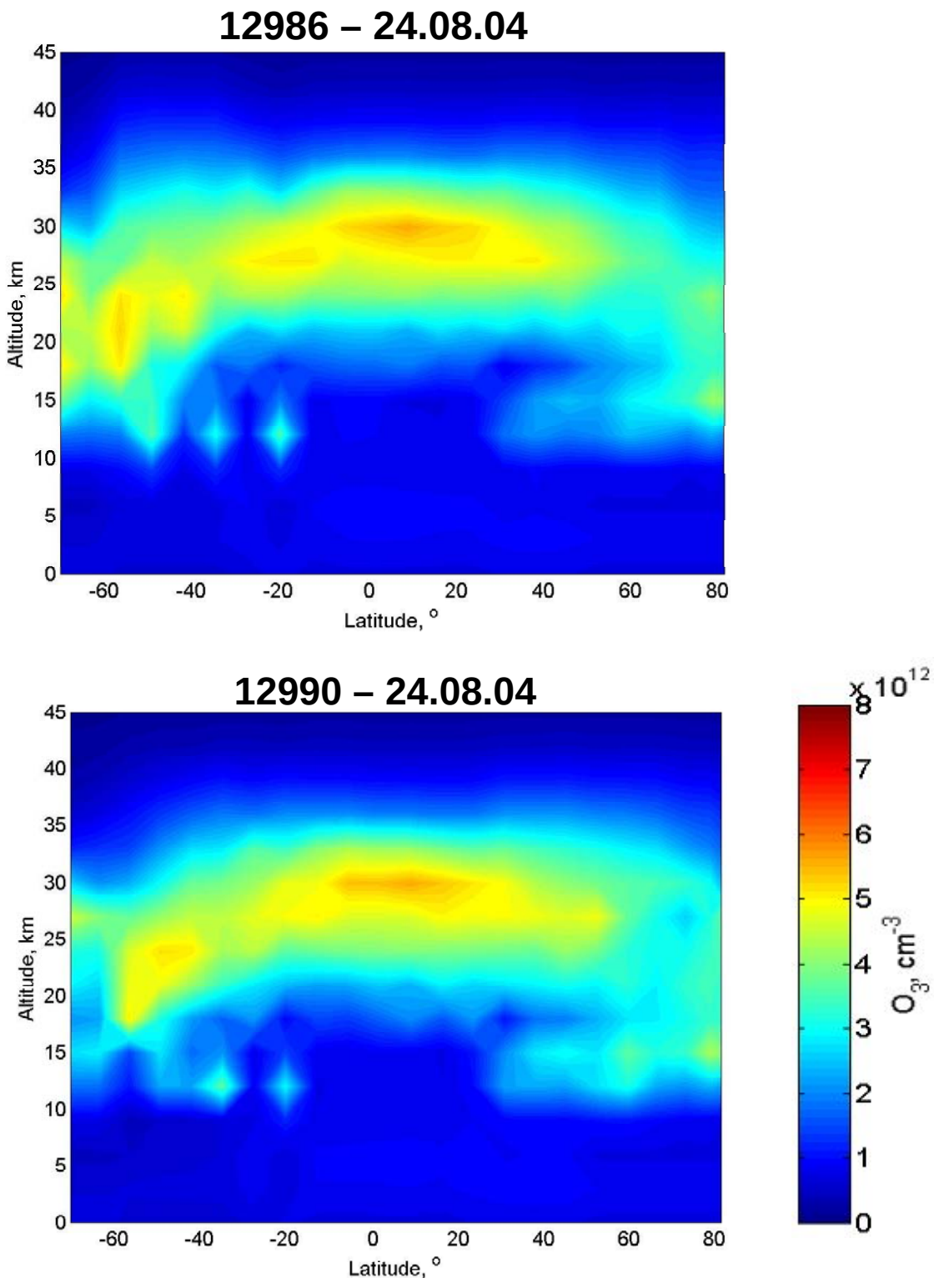

FIGURE 6.17: same as Fig. 6.16, but for the orbits 12986 and 12990. For the geolocations of these orbits see Fig. 6.13.

The cross-sections above show very nicely the zonal variability of the ozone layer, also observed in the TOMS total column for high southern latitudes: While for orbit 12984, there is maximum at 60 °S, orbit 12990 has minimum ozone concentrations for altitudes between 15 and 25 km, and for orbit 12986, values are in between, in good agreement with the TOMS total ozone column for the corresponding locations.

Since the results from the comparison with other ozone profile and total column measurements were quite promising, we decided to investigate also the seasonal variability of the ozone profile by evaluating orbits over a long time series. One very prominent feature is the ozone hole, which occurs every southern hemisphere spring at altitudes between 12 and 20 km, see section 1.51 and Fig. 1.14a.
Fig. 6.18 shows the temporal evolution of ozone profile measured by SCIAMACHY for selected days from end of August till end of September / beginning of October for the latitudes of 65° S and 70° S. The altitude range of the observed ozone depletion and the times when it occurs at the two latitudes is in good agreement with expectations based on previous balloon measurements, etc.

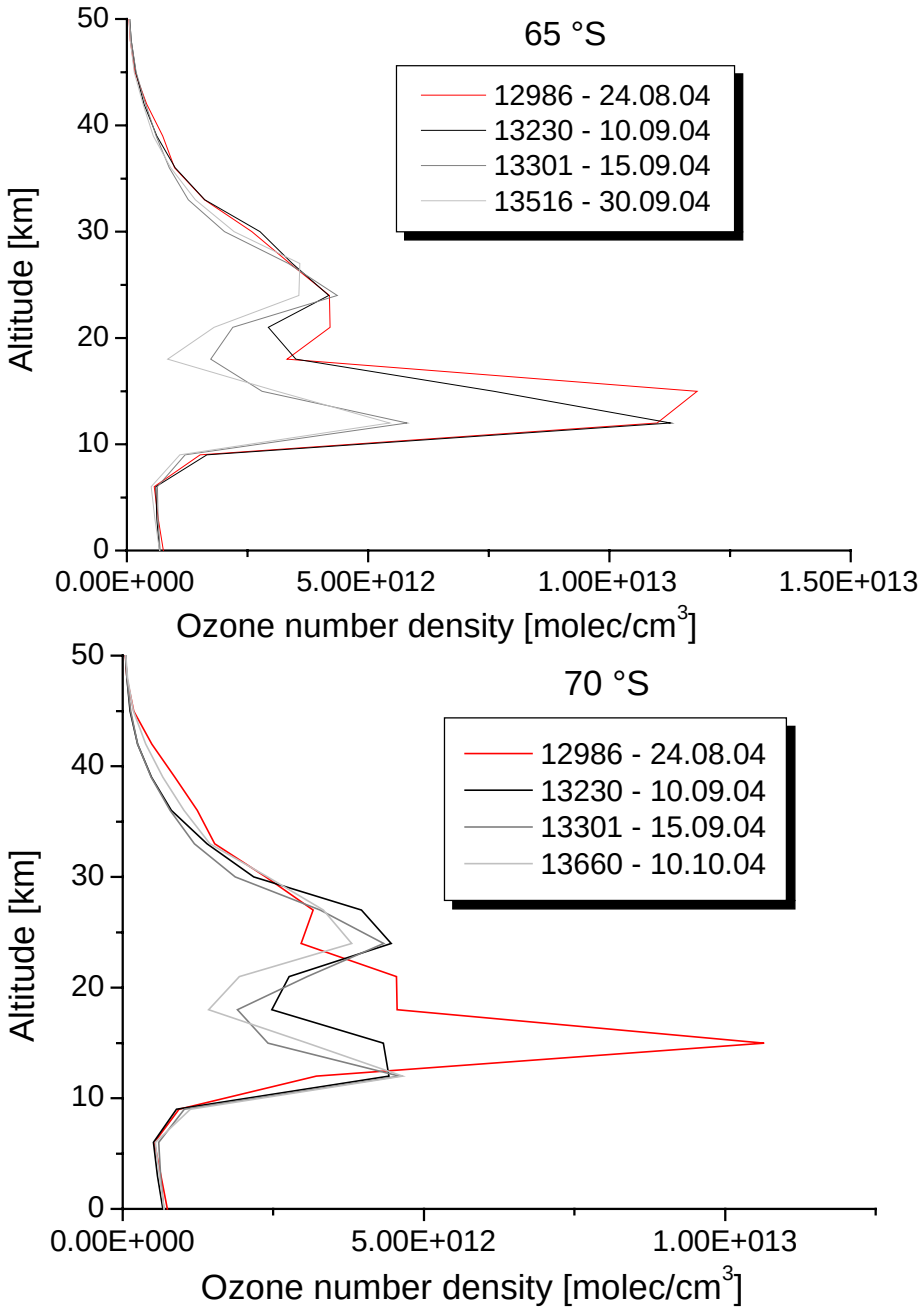

FIGURE 6.18: Temporal evolution of the vertical ozone profile during southern spring 2004. Top: For the latitude of 65° S. Bottom: For the latitude of 70° S.

6.2.2 Retrieval of vertical NO_2 profiles

Measured SCDs

Due to the strong diurnal cycle of NO_2, the SCDs show a large dependency on latitude, see Fig. 6.19.

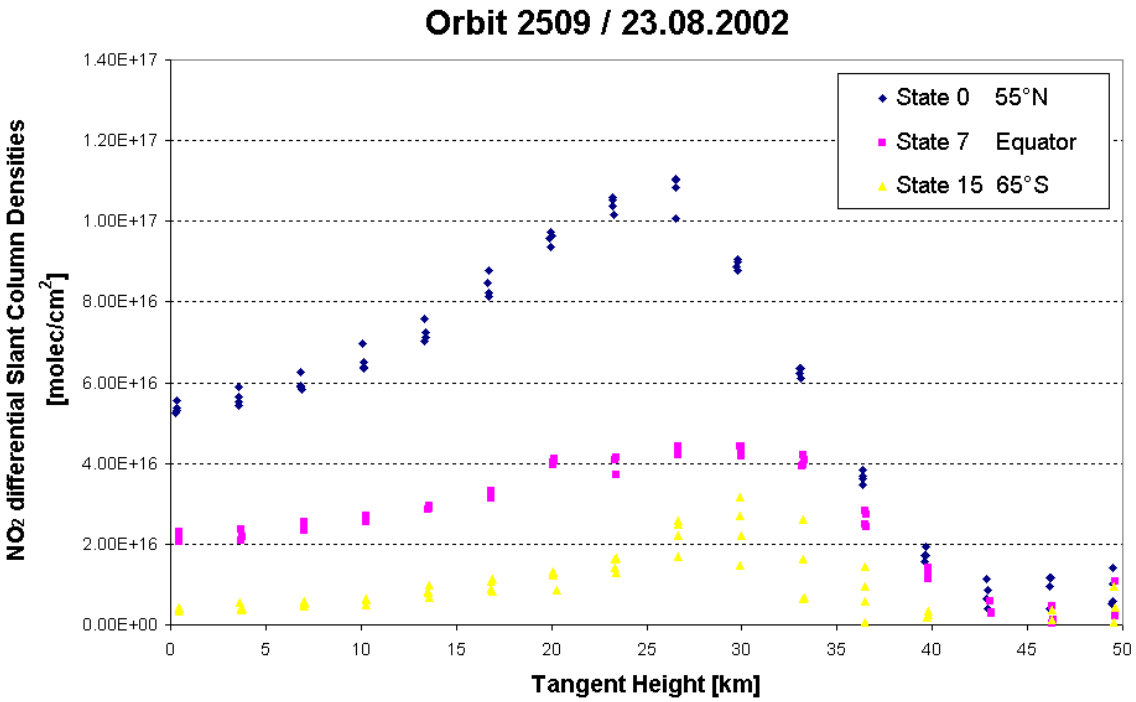

FIGURE 6.19: NO_2 dSCDs as function of tangent height for orbit 2509 from 23rd of August 2002 for selected states in the northern and southern hemisphere and at the equator.

Large NO_2 SCDs are derived for the state close the summertime North pole. The shape of the curve implies that the maximum of the NO_2 profile is located at altitudes between 25 and 30 km. At the state near the equator, NO_2 SCDs are considerably smaller, the height of the maximum seems to be located higher than for the state at 55° N. For the state close to the wintertime South pole (65° S) the smallest NO_2 SCDs are retrieved (in the polar night, the equilibrium between NO_x and NO_y is far on the side of the reservoirs N_2O_5 and HNO_3).
This is in good agreement with expectations from atmospheric chemistry and the observations of stratospheric NO_2 by GOME [*Wenig et al., 2003*]. Thus, the retrieved NO_2 SCDs are realistic and can be used as input for the inversion process. Fig. 6.20 shows the box air mass factors calculated for NO_2 at a wavelength of 440 nm.

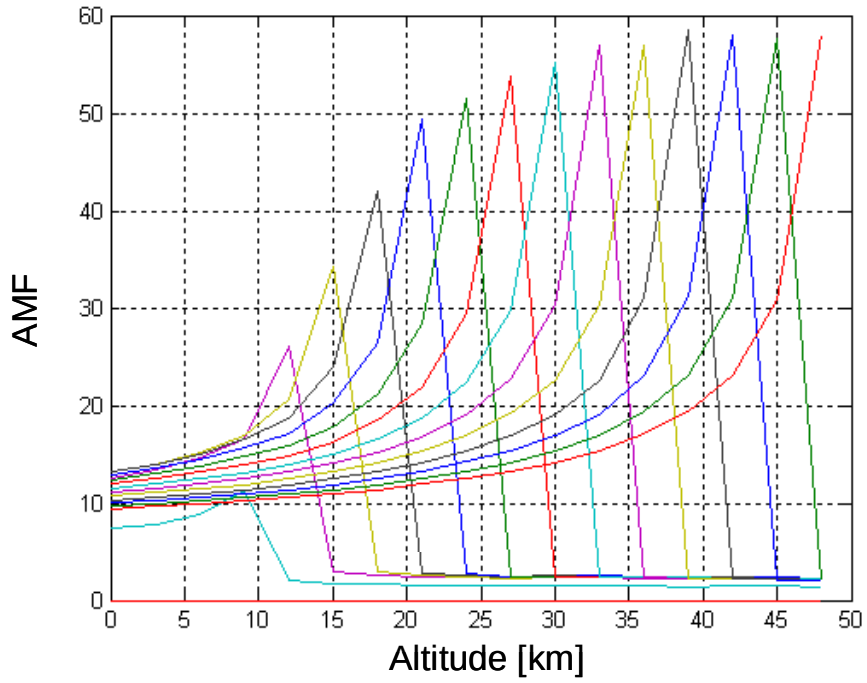

FIGURE 6.20: Box air mass factors as function of altitude calculated by the RTM Tracy for the wavelength of 440 nm.

An example for **averaging kernels** of a typical NO_2 profile retrieval is shown in Fig. 6.21. They reveal that information about the NO_2 concentration can be retrieved for altitudes between 18 to 40 km.

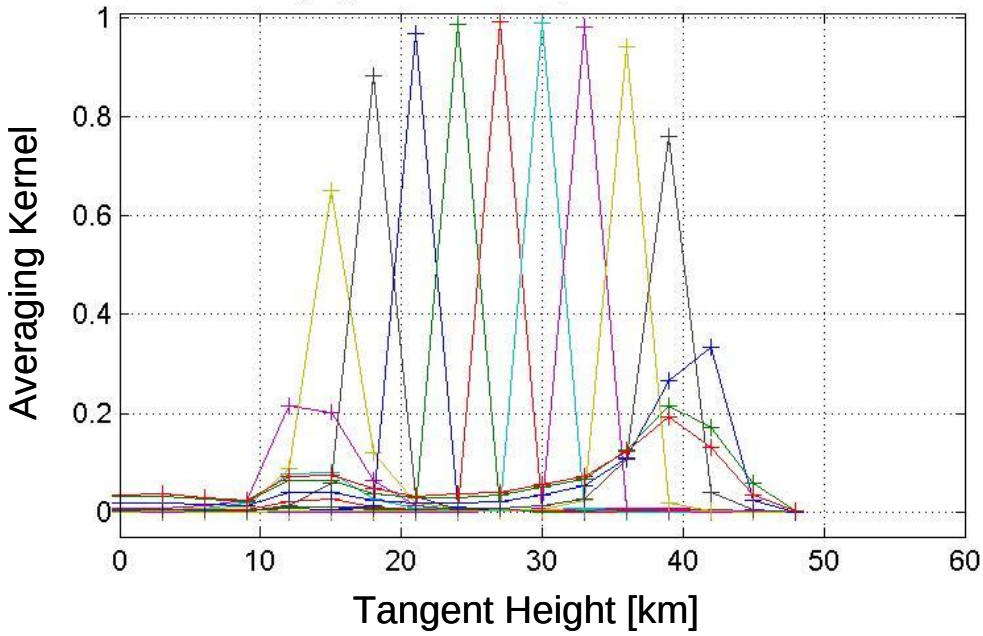

FIGURE 6.21: Averaging kernels as function of tangent height for a typical NO_2 vertical profile retrieval.

Fig. 6.22 shows a cross-section of the NO_2 concentration for an orbit from 10th of September, 2004 in comparison to the results from the Bremen retrieval.

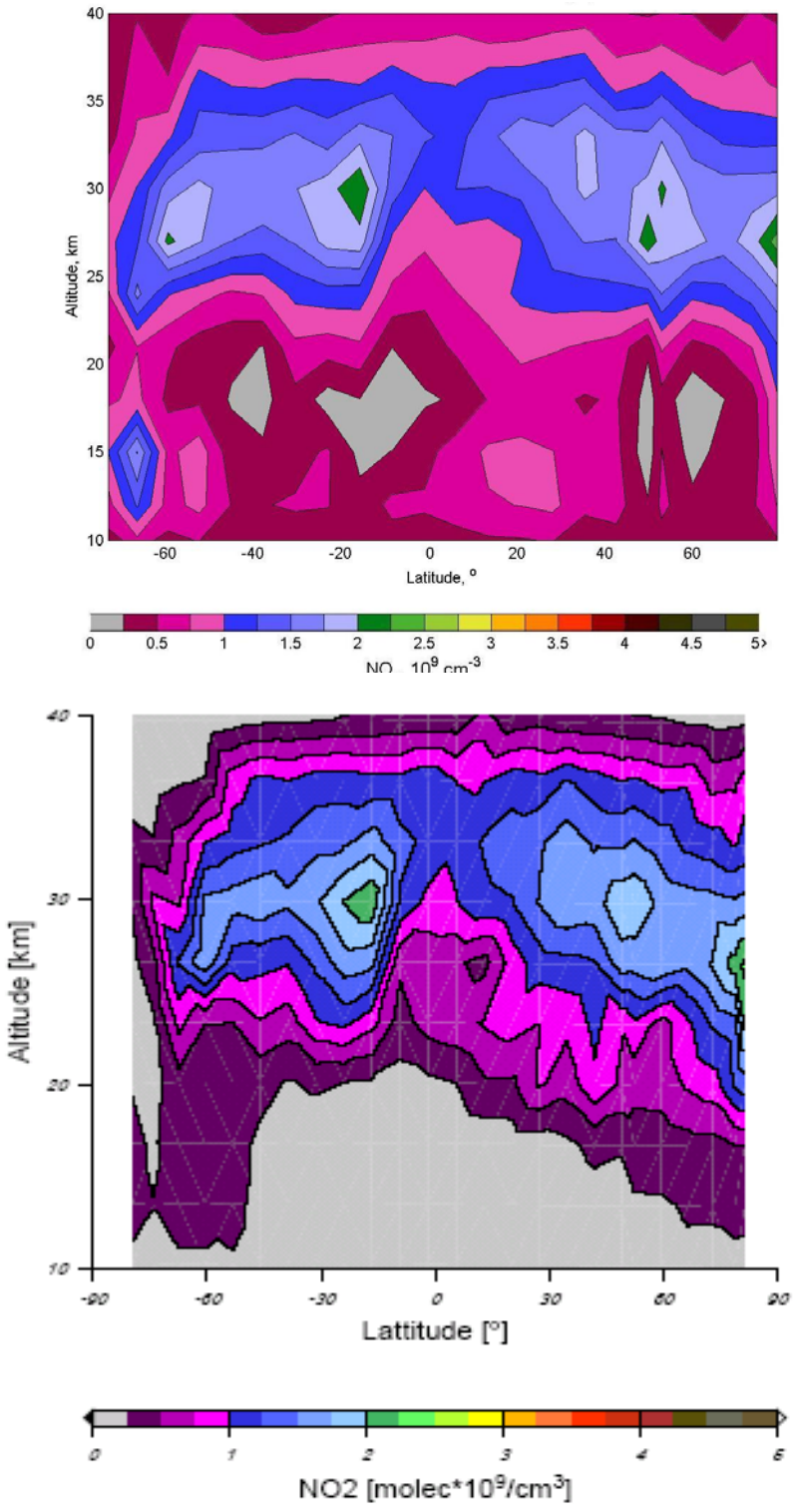

Figure 6.22: Latitudinal cross section of the NO_2 concentration profile for the orbit 13230 from 10th of September, 2004. Top: Retrieval developed in this thesis. Bottom: Retrieval by A. Rozanov, IUP Bremen.

Figs. 6.23 and 6.24 compare the Bremen and Heidelberg NO_2 analysis for single profiles retrieved for selected states of orbit 12986. For the altitude range in which information about the NO_2 profile can be retrieved (see Fig. 6.20) the discrepancy is less than 10%.

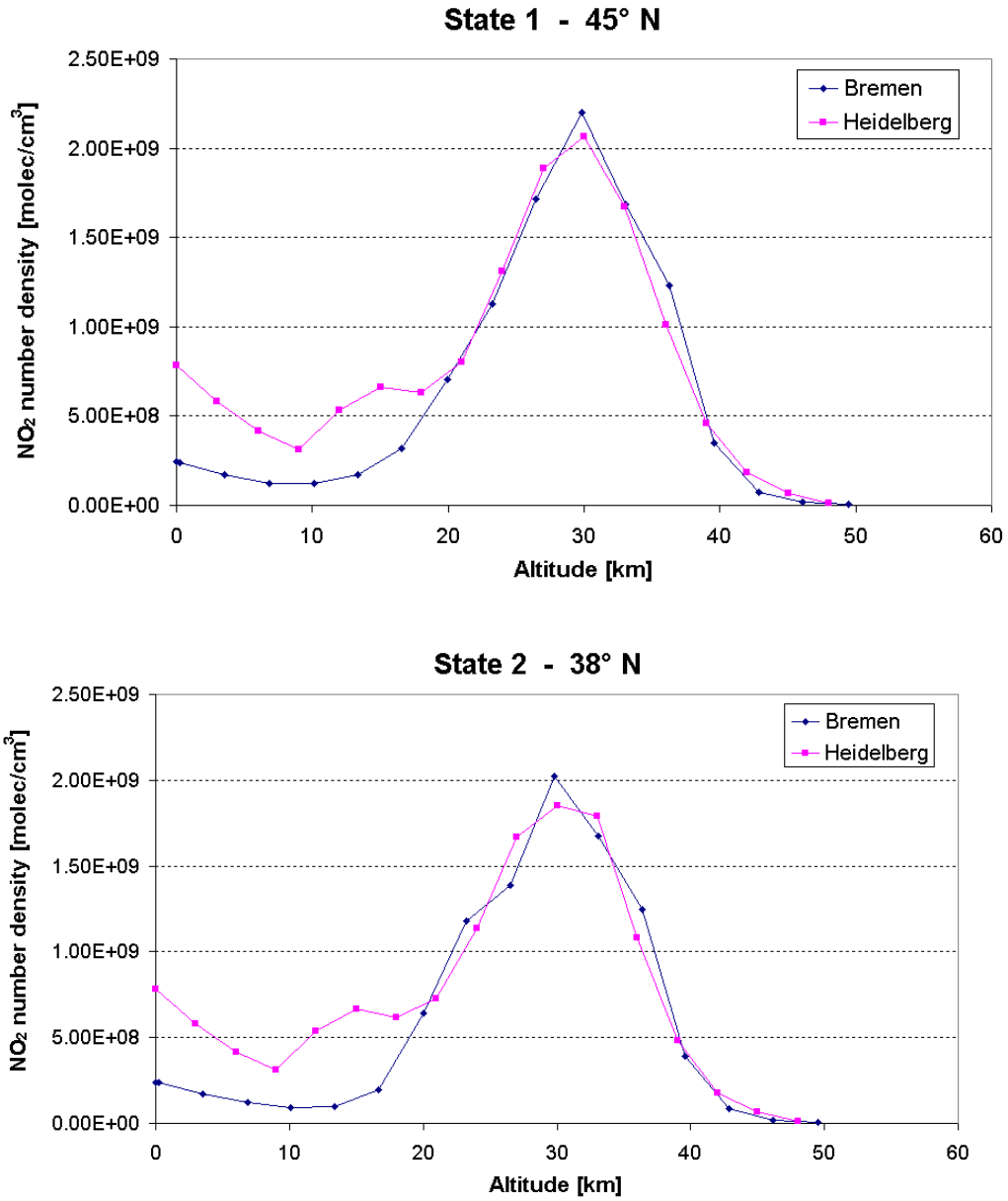

FIGURE 6.23: Comparison of vertical NO_2 profiles retrieved from SCIAMACHY limb spectra by the Bremen and Heidelberg group. Shown is the number density as function of altitude for selected states of the orbit 12986 from 24.08.2004.

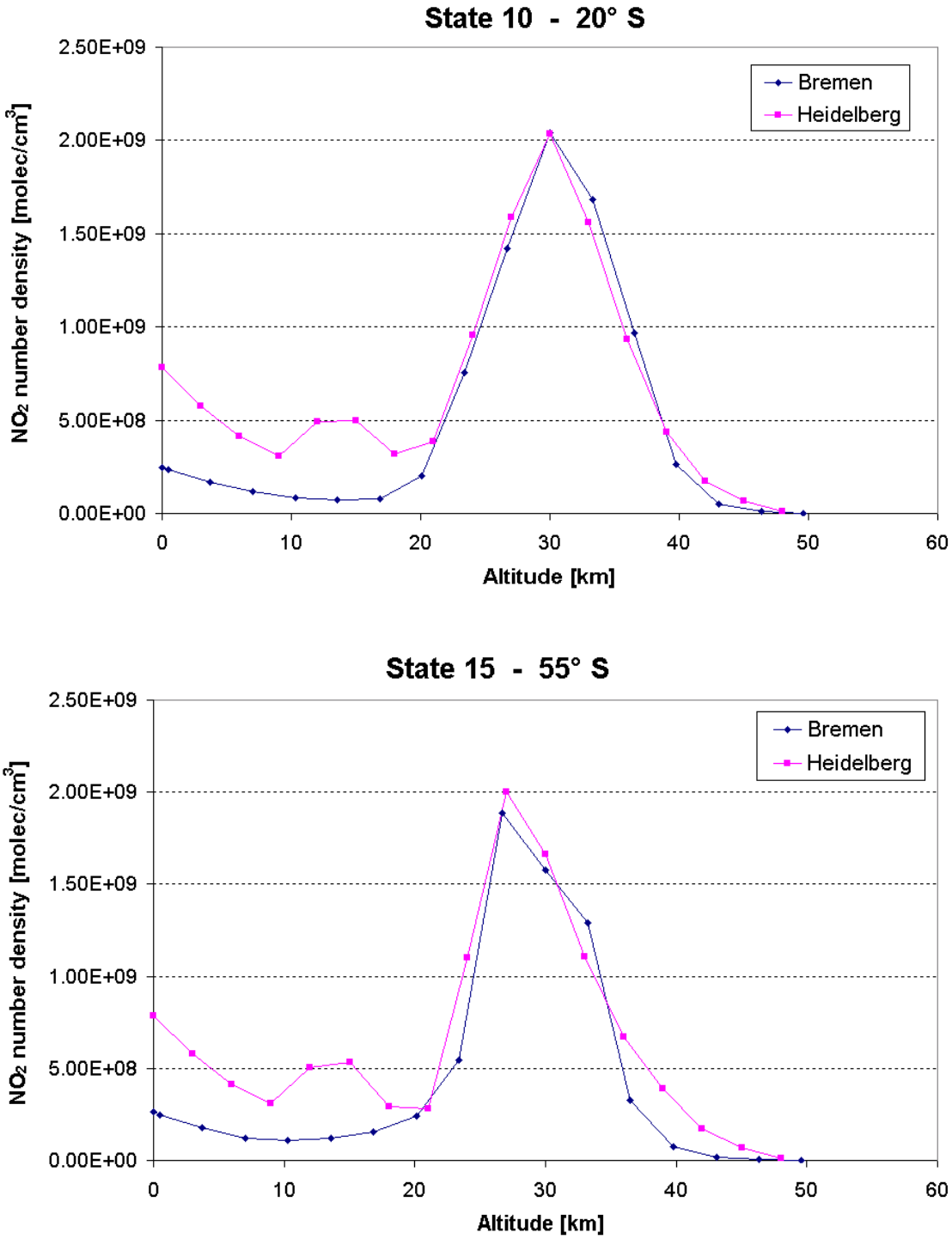

FIGURE 6.24: Same as Fig. 6.23, but for selected states of the southern hemisphere part of orbit 12986.

6.2.3 Retrieval of vertical BrO profiles

The BrO retrieval is performed in the same wavelength range as the one for ozone, therefore the box **air mass factors** are the same as shown in Fig. 6.11.The **measured SCDs** as function of the tangent height are shown for orbit 12986 in Fig. 6.25. The lower panel of the figure reveals very nicely the latitudinal dependence of the BrO SCDs. Large SCDs are retrieved for the two states close to the wintertime South pole.

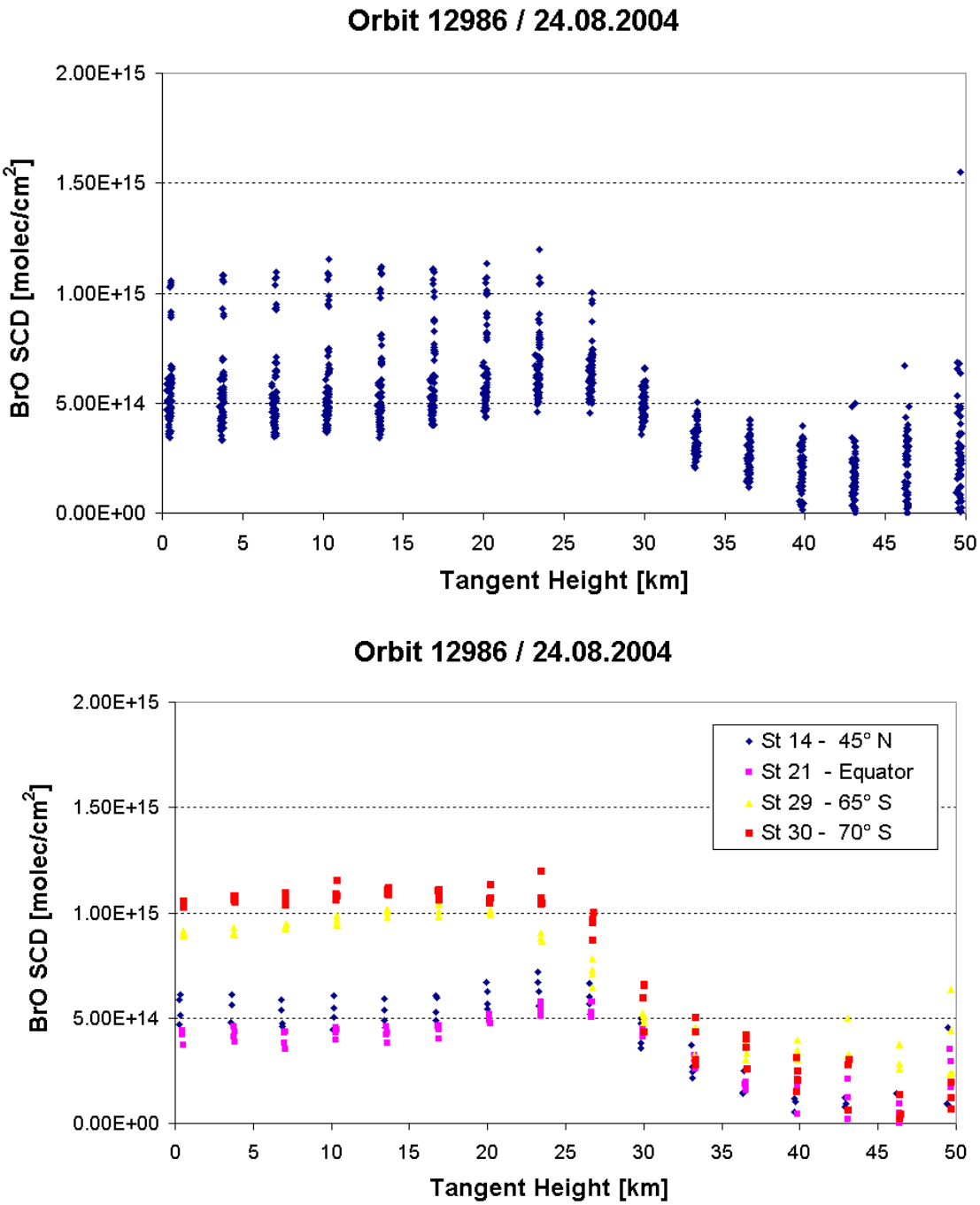

FIGURE 6.25: BrO SCDs for the orbit 12986 from 24th of August 2004. Top: for all limb states. Bottom: for selected states.

Since the BrO SCDs seem realistic, we can use them as input for the inversion. As **a priori** we apply the climatology derived by *McLinden et al.* [2003]. Fig. 6.26 shows the **averaging Kernels** for a typical retrieval of a BrO profile.

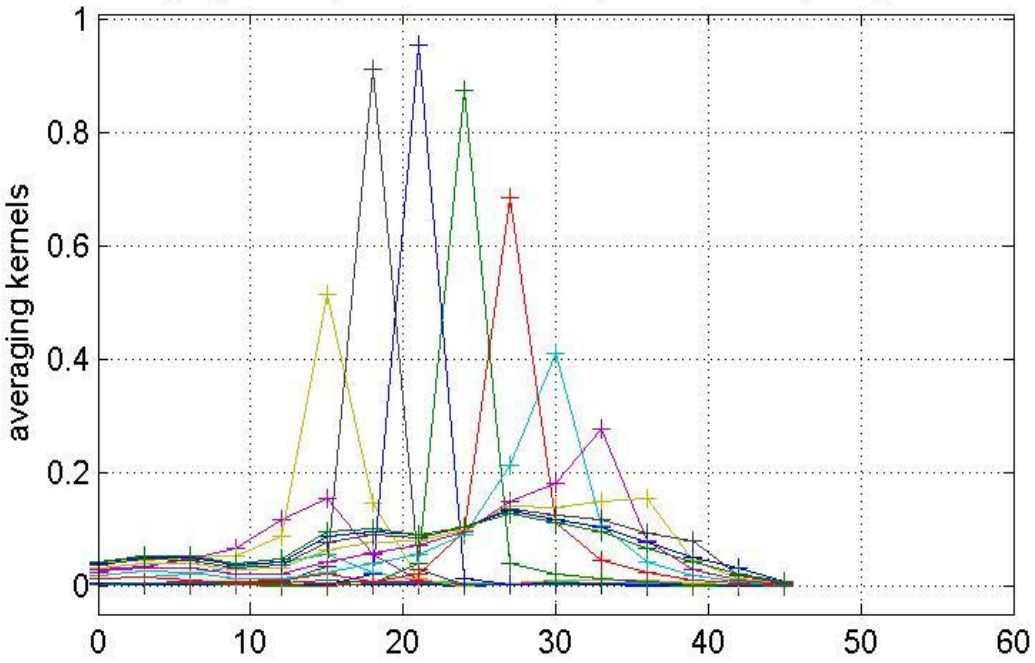

FIGURE 6.26: Averaging kernels as function of tangent height for a typical BrO vertical profile retrieval.

Figs. 6.27 and 6..28 show the latitudinal cross section of the BrO profile for the orbit12986 from 24th of August, 2004 and a difference plot in comparison to the Bremen retrieval.

Along the whole orbit, the BrO number density differs by about –0.5 to +0.25 * 10^7 molec/cm^3, which is a good agreement, considering the accuracy of the BrO profile retrieval, which is estimated to be 0.2*10^7 molec/cm^3 [*A. Rozanov, personal communication, 2005*].
For the south pole region there are large discrepancies, likely arising from the increased uncertainty for the AMF calculation there.

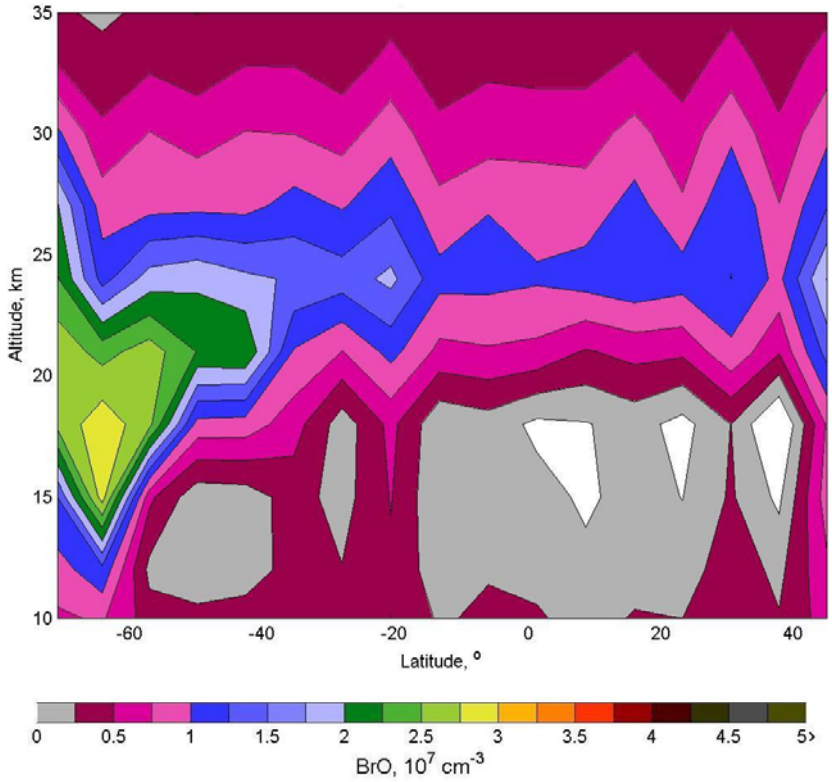

FIGURE 6.27: Latitudinal cross sections of BrO for the orbit 12986 from 24th of August 2004.

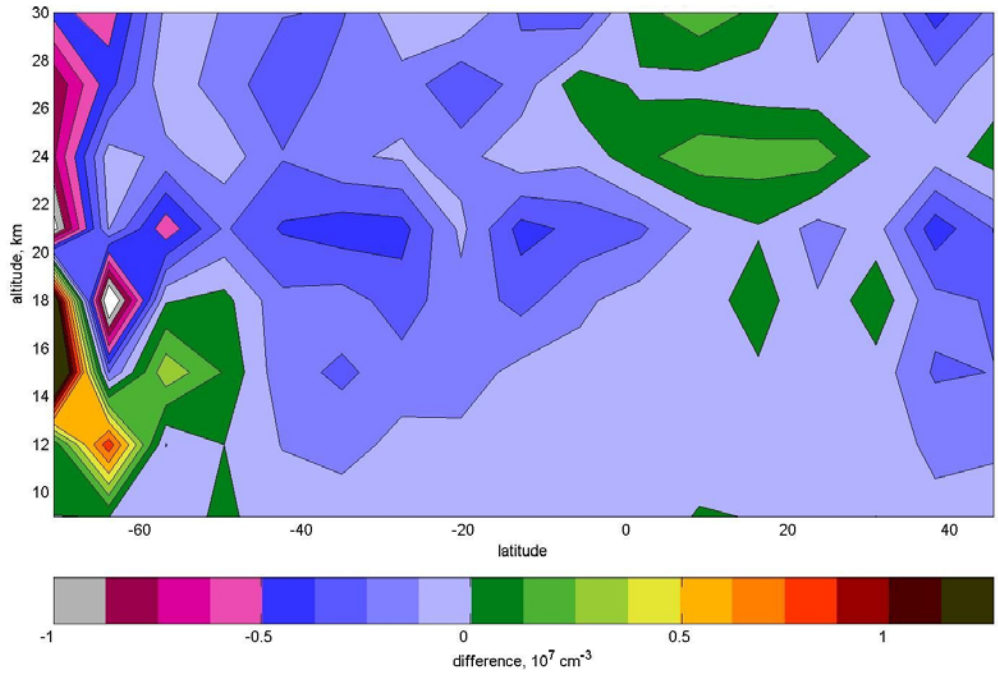

FIGURE 6.28: Difference of the latitudinal cross sections for BrO retrieved by the Bremen and Heidelberg BrO limb analysis for the orbit 12986 from 24th of August 2004.

6.3 SCIAMACHY Measurements of OClO in Limb mode

By the good agreement with other, already established measurements it was demonstrated that with the two step approach vertical profiles of Ozone, NO_2 and BrO can be retrieved accurately. Therefore, we decided to apply the algorithm also for the retrieval of vertical OClO profiles.
However, for OClO the optical depth and thus the signal to noise ratio is smaller, causing larger errors for the retrieved SCDs and thus also for the profile. Also, the latitudinal dependence of the OClO SCDs is expected to be even stronger as for NO_2 or BrO. While enhanced OClO SCDs should be observed inside the polar vortex, the OClO SCDs measured at smaller latitudes and SZAs should be close to zero due to chemistry but also due to rapid photolysis (see section 2 and 4).

Fig. 6.29 shows OClO SCDs for the orbit 12986 from 24th of August, 2004. The retrieved OClO SCDs are in very good agreement with the described expectations: While values for the (summer-) North pole and the equator are close to zero (a negative offset is also visible), large OClO SCDs are observed for the two states close to the south pole, with growing magnitude moving poleward.

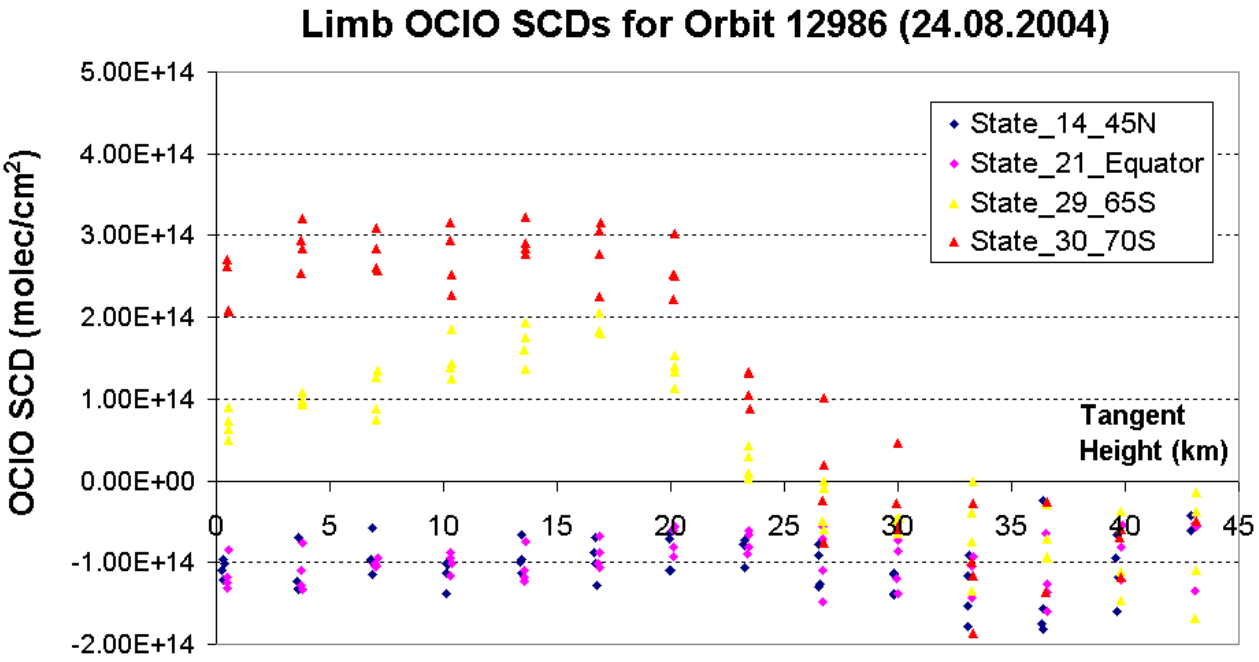

FIGURE 6.29: OClO SCDs as function of tangent height for orbit 12986 from 24th of August 2004 for selected states in the northern and southern hemisphere and at the equator.

The box air mass factors for the inversion of the SCDs are calculated at the wavelength of 368 nm, see Fig. 6.30.

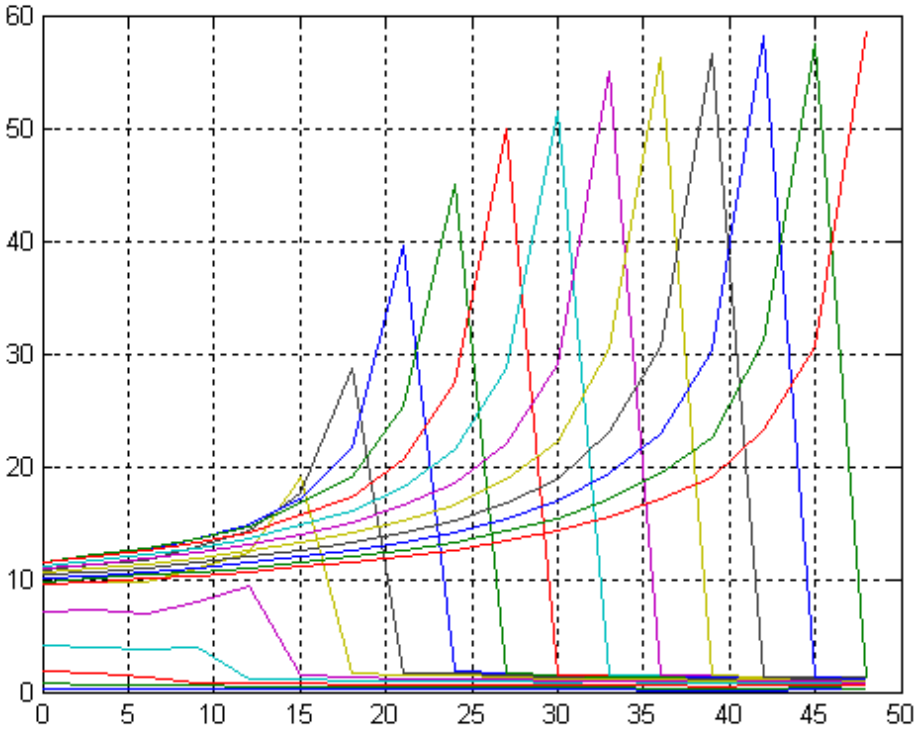

FIGURE 6.30: Box air mass factors as function of tangent height, calculated by TRACY for the wavelength of 368 nm.

The graph reveals that for altitudes below 15 km, the sensitivity of the measurements is significantly reduced because the impact from concentrations at altitudes above gets larger than the one from the concentration at the probed altitude.
Also it can be seen that for the tangent height of 27 km there is practically no influence from altitudes below, where enhanced OClO concentrations are expected for polar winter conditions. Therefore, and because the concentration of OClO at and above 27 km is expected to be close to zero, we utilize the spectrum measured at this tangent height as Fraunhofer reference spectrum.

Figs. 6.31 to 6.33 show the retrieved OClO SCDs, the resulting OClO profile and the averaging kernels for the three southern most states of the orbit 12986. The retrieved OClO concentration decreases for lower latitudes, as is expected from atmospheric chemistry. The absolute magnitude of the OClO concentration for 70° S (Fig. 6.31) and the height of the maximum is in good agreement with balloon measurements [*Pommerau and Piquard, 1994; Fitzenberger, 1998*]. Fig. 6.33 also demonstrates that the magnitude of the retrieved profile is independent of the a priori for altitudes with large averaging kernels (17-24 km).

Figs. 6.34 and 6.35 show latitudinal cross sections of the OClO profile for selected orbits during the Antarctic winter 2004 and Arctic winter 2004/05. They reveal the much stronger chlorine activation in the southern hemisphere polar vortex compared to the northern counterpart, also for the January of the cold Arctic winter 2004/05. In Fig. 6.34, the deactivation of chlorine from 24th of August until 10th of September is seen.

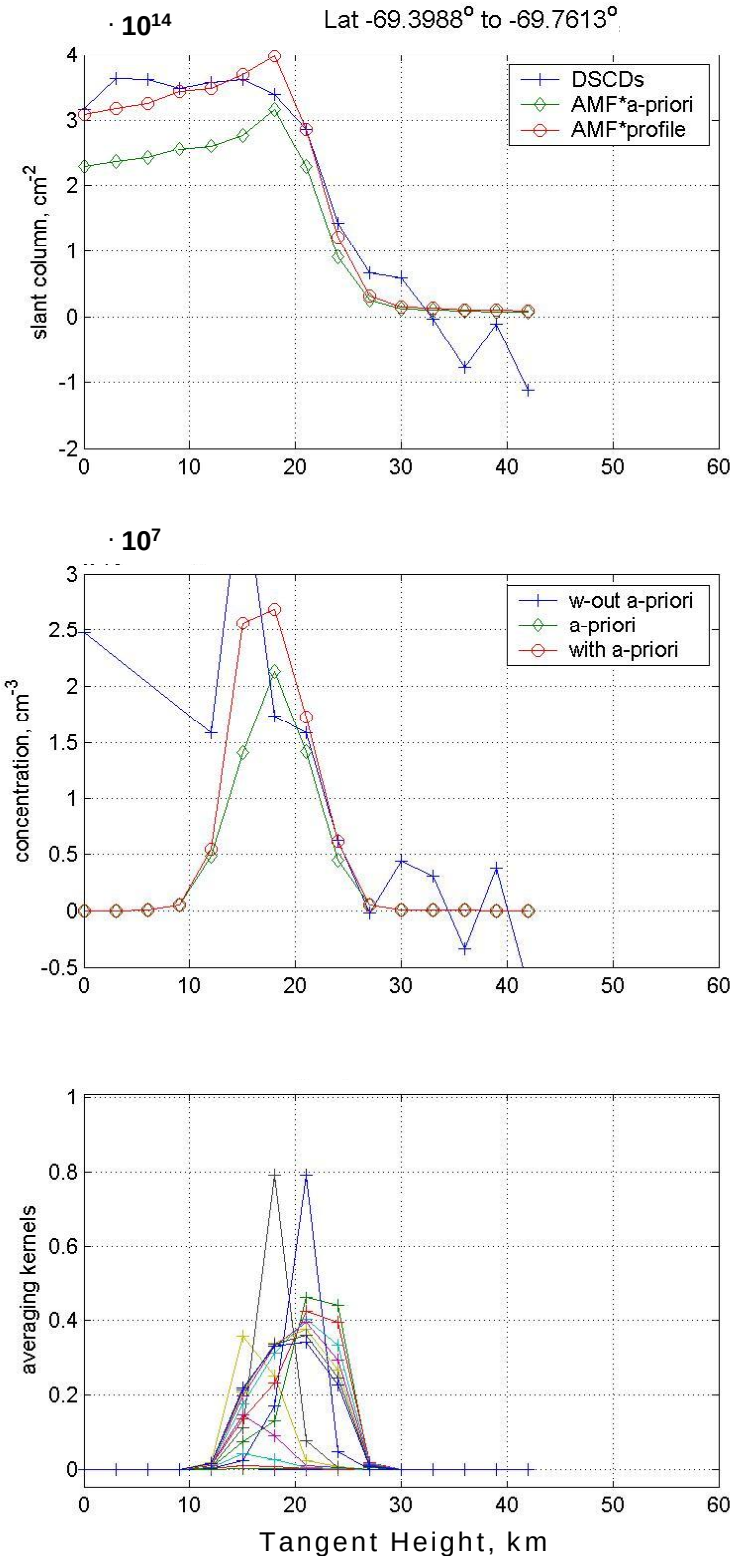

FIGURE 6.31: OClO SCDs (top), retrieved OClO profile (middle) and averaging kernels (bottom) for the state 30 at 70° S from orbit 12986 (24.08.2004). Blue crosses/line: measured OClO SCDs (top) and profile retrieved without using an a priori (middle). Green dots/line: OClO SCDs (top) corresponding to the a priori profile (middle). Red dots/line: OClO SCDs (top) corresponding to the profile retrieved with a priori (middle).

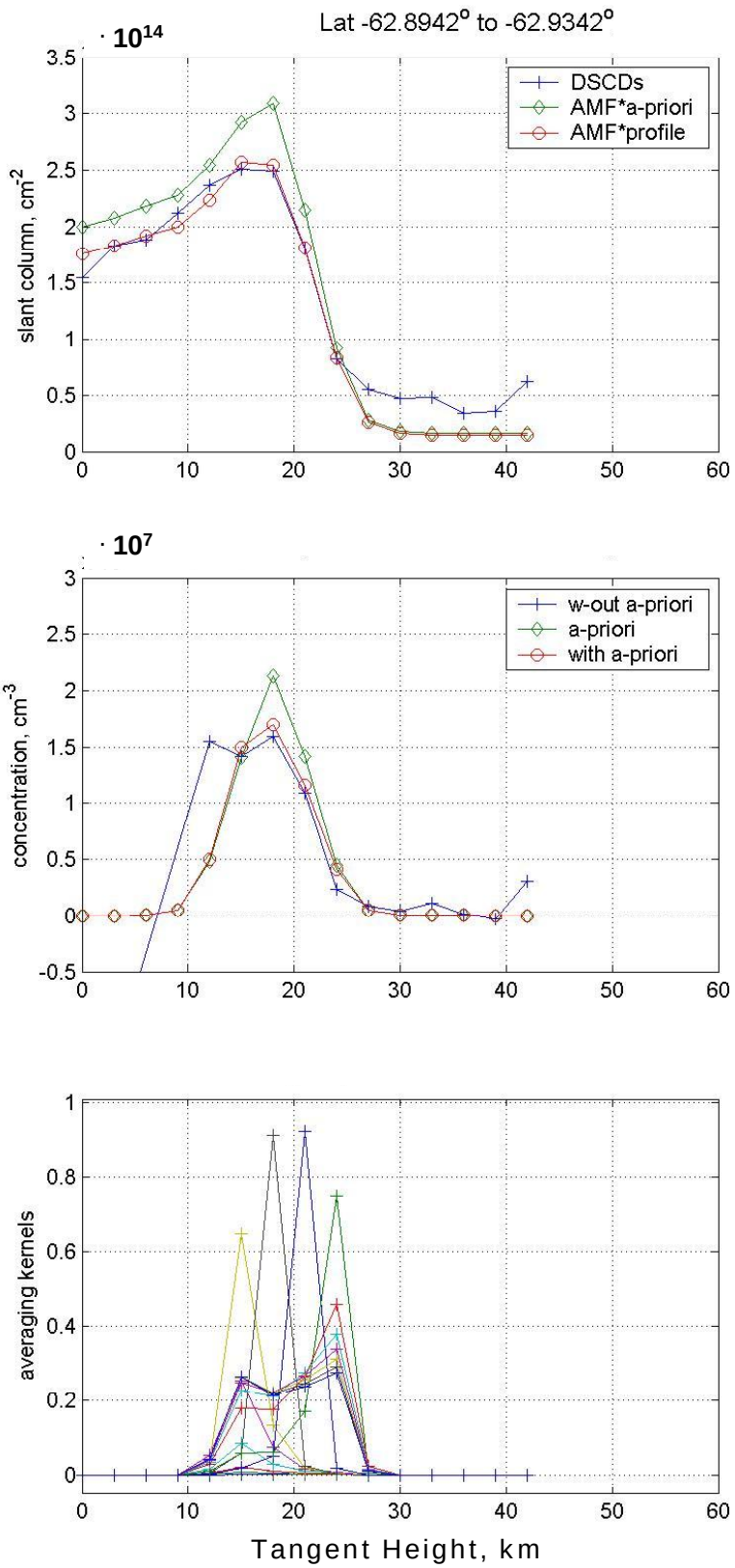

FIGURE 6.32: Same as Fig. 6.31 but for state 29 at 63° S.

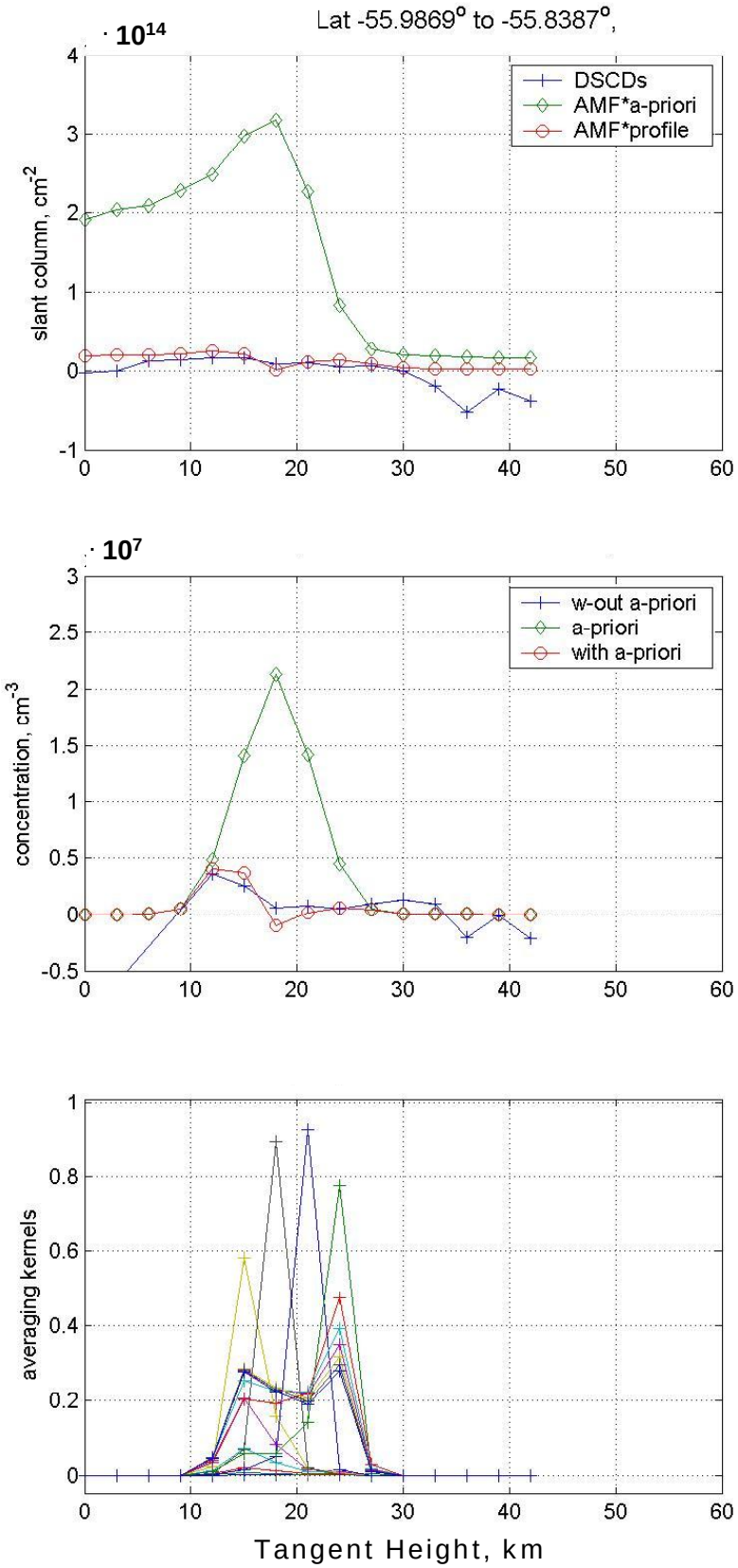

FIGURE 6.33: Same as Fig. 6.31 but for state 28 at 56° S.

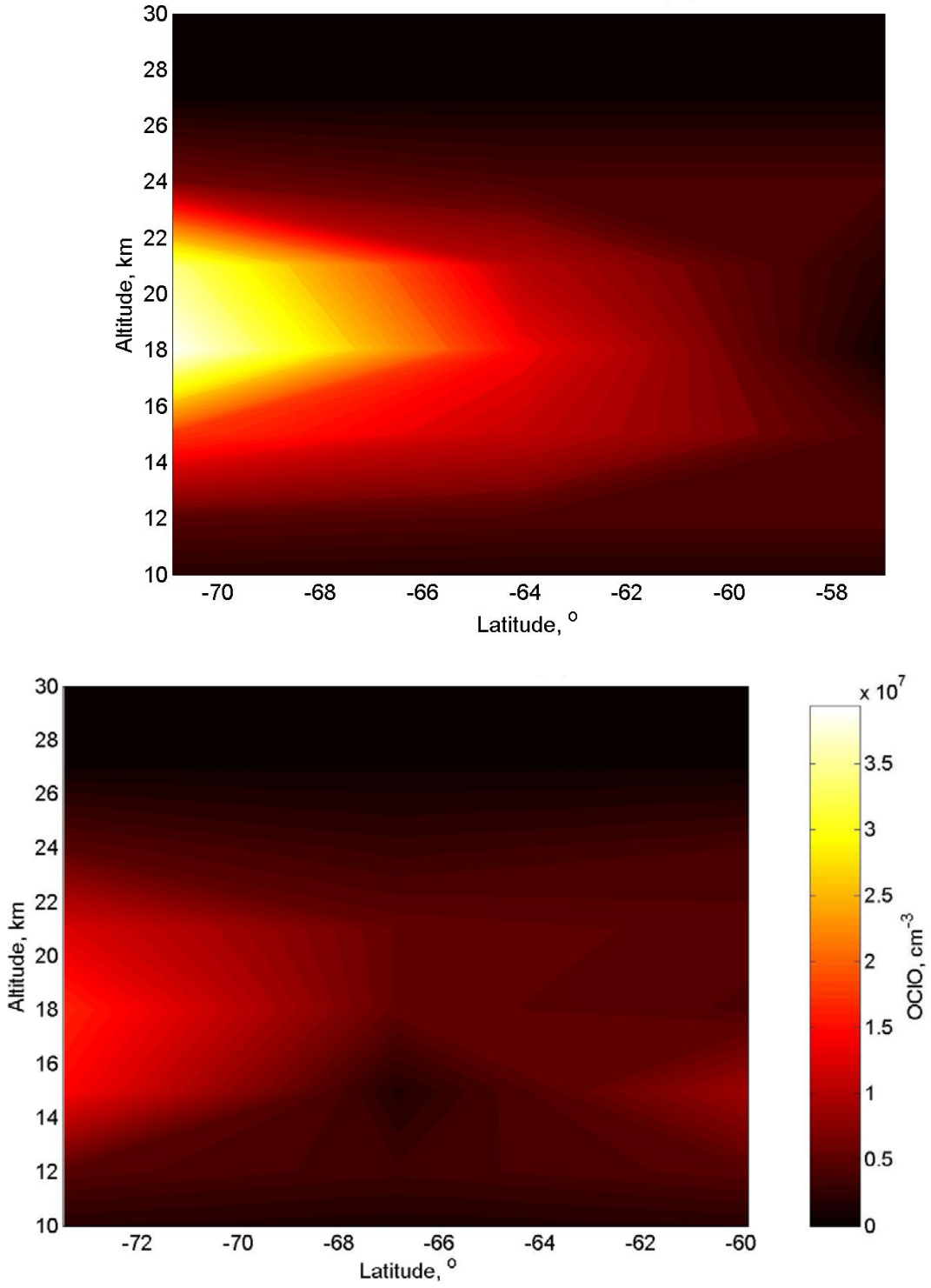

FIGURE 6.34: OClO number density as function of altitude and latitude for the southern part of the orbits 12986 from 24th of August, 2004 (top) and 13230 from 10th of September, 2004 (bottom).

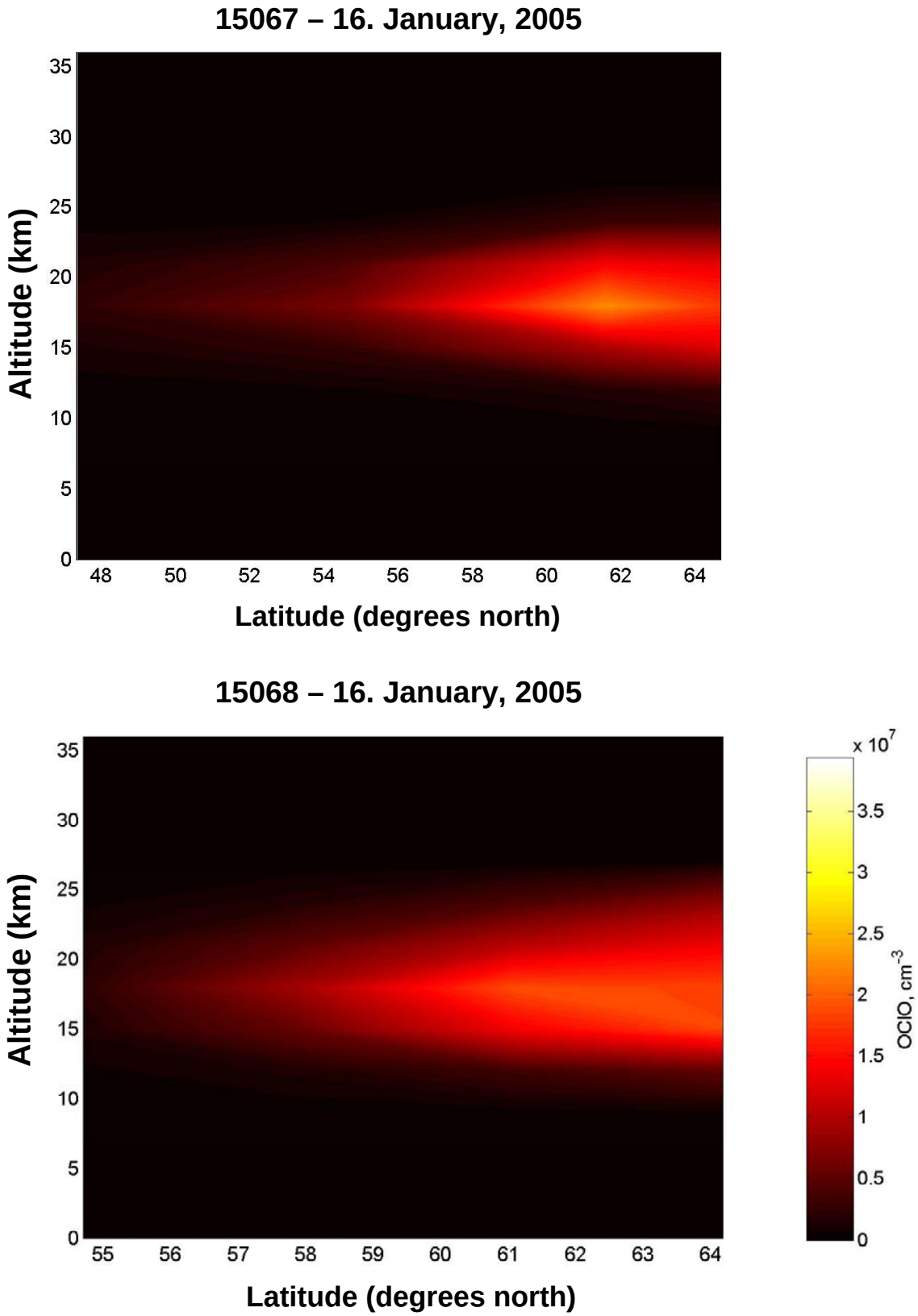

FIGURE 6.35: OClO number density as function of altitude and latitude for the northern part of the orbits 15067 (top) and 15068 (bottom) from 16th of January 2005.

7 Mountain wave-induced chlorine activation

7.1 Mountain Waves

It is well known that winds across topographically barriers lead to vertical displacement of air parcels, which results in internal gravity waves, oscillating about the equilibrium level. In a stable-layered atmosphere, gravity waves which are excited by airflow over mountains can propagate vertically up to stratospheric levels. At that height, the vertical displacements increase up to 1000-2000 m, due to the exponential decrease of pressure with increasing height.
Assuming an adiabatic cooling ($c_p \Delta T = - g \Delta z$), this corresponds to a decrease in temperature of up to 10-20 K. For cold stratospheric temperatures on the synoptic scale, this shift in temperatures has the potential to cause formation of PSCs and thereby enhance chlorine activation.
It has been shown by model simulations from *Carslaw et al.* [1998] that mountain wave-induced PSCs can cause substantial chlorine activation. By theoretical calculations along mesoscale trajectories through mountain wave-induced PSCs with a chemical box model they determined that chlorine activation is significantly enhanced compared to the synoptic scale, leading to additional ozone depletion. Further studies by *Rivière et al.* [2000] and *Dörnbrack et al.* [2001] came to similar conclusions. Although measurements of mountain wave-induced PSCs have been reported [*Deshler et al., 1994; Enell et al., 1999; Wirth et al., 1999; Dörnbrack et al., 1999; Voigt et al., 2000; Voigt et al., 2003*], there are no observations of the corresponding chlorine activation.

FIGURE 7.1.: Pictures of PSCs formed in the lee of the Scandinavian mountain ridge.

Carslaw et al. [1998], found that the favourite regions for this additional chlorine activation are the Scandinavian mountains, the Urals and the East Greenland Coast. They concluded that mountain waves increase activation of chlorine species significantly and therefore lead to an enhanced ozone destruction in the Artic springtime stratosphere.
A detailed study of the meteorological conditions necessary for mountain waves in the lee of the Scandinavian mountain ridge has been given by *Dörnbrack and Leutbecher* [2001]. They found that the activity of mountain waves is largest in the month of January and that the potential for formation of PSC type 2 (Ice) in this region is dominated by mesoscale contributions.

7.2 The event of 20-22 January 1997

Large amplitude mountain wave activity above Northern Scandinavia was reported for 20-22 January, 1997 [*Dörnbrack et al., 1999; Dörnbrack et al., 2001*]. GOME OClO measurements show a substantial increase at the location of the mountain wave activity, see section 7.2.2.
By radiative transfer calculations the measured slant column densities (SCDs) are converted to vertical column densities (VCDs). Combining the satellite observations with mesoscale meteorological model simulations, we give an estimate for the increase in the level of chlorine activation at the respective altitude range by assuming different vertical profiles for the OClO mixing ratio.

7.2.1 Meteorological situation

Figure 7.2a and b show the temperature at the 475 K isentropic surface (corresponding to ≈ 20 km altitude) based on T106 ECMWF operational analyses for 20 and 21 January 1997 at 1200 UT. Although the vortex was shifted off the pole it was only slightly elongated. On 21 January, temperatures were as low as 192 K, i.e. about 3 K below T_{NAT}, the threshold for formation of PSC type I, and about 4 K above the threshold T_{frost} for water ice (PSC type II) formation. For the whole month of January 1997, T106 ECMWF synoptic-scale temperatures never fell below T_{frost} at any altitude level.
On the other hand, strong mountain wave activity above northern Scandinavia was reported for January 1997, especially during the period of 20-22 January [*Dörnbrack et al., 1999*]. Above northern Scandinavia, minimum mesoscale temperatures fell below the frost point at all levels between 100 and 30 hPa on 21 January [*Dörnbrack et al., 2001*]. Figure 7.2c shows simulated temperatures at the 475 K level based on the MM5 mesoscale model calculation. Also in the synoptic scale ECMWF analysis (Fig. 7.2b), the effect of the mountain waves on the stratospheric temperatures can clearly be seen in the lee of the Scandinavian mountain ridge. But, in contrast to the rather homogeneous ECMWF temperature field, the mesoscale field consists of two nearly parallel stratospheric temperature anomalies aligned with the main Scandinavian mountain ridge. Their distance is about 600 km, resulting from the horizontal wavelength of the mountain waves.
Inside the coldest areas, the simulated mesoscale temperature drops by $\Delta T = 11$ K below the ECMWF temperature ($T_{min} = 181$ K) and falls significantly below the threshold for formation of solid ice PSCs of $T_{frost} = 188$ K. These mesoscale simulation results are in accord with ground-based lidar observations of ice PSCs at Esrange, Sweden [*Fricke et al., 1997*] and at Sodankylä, Finland [*Stein et al., 1999*] as well as with other reported observations [*Dörnbrack et al., 1999*] on this particular day. Because synoptic scale temperatures were above T_{frost}, the formation of the ice PSCs must have been induced by mountain waves.

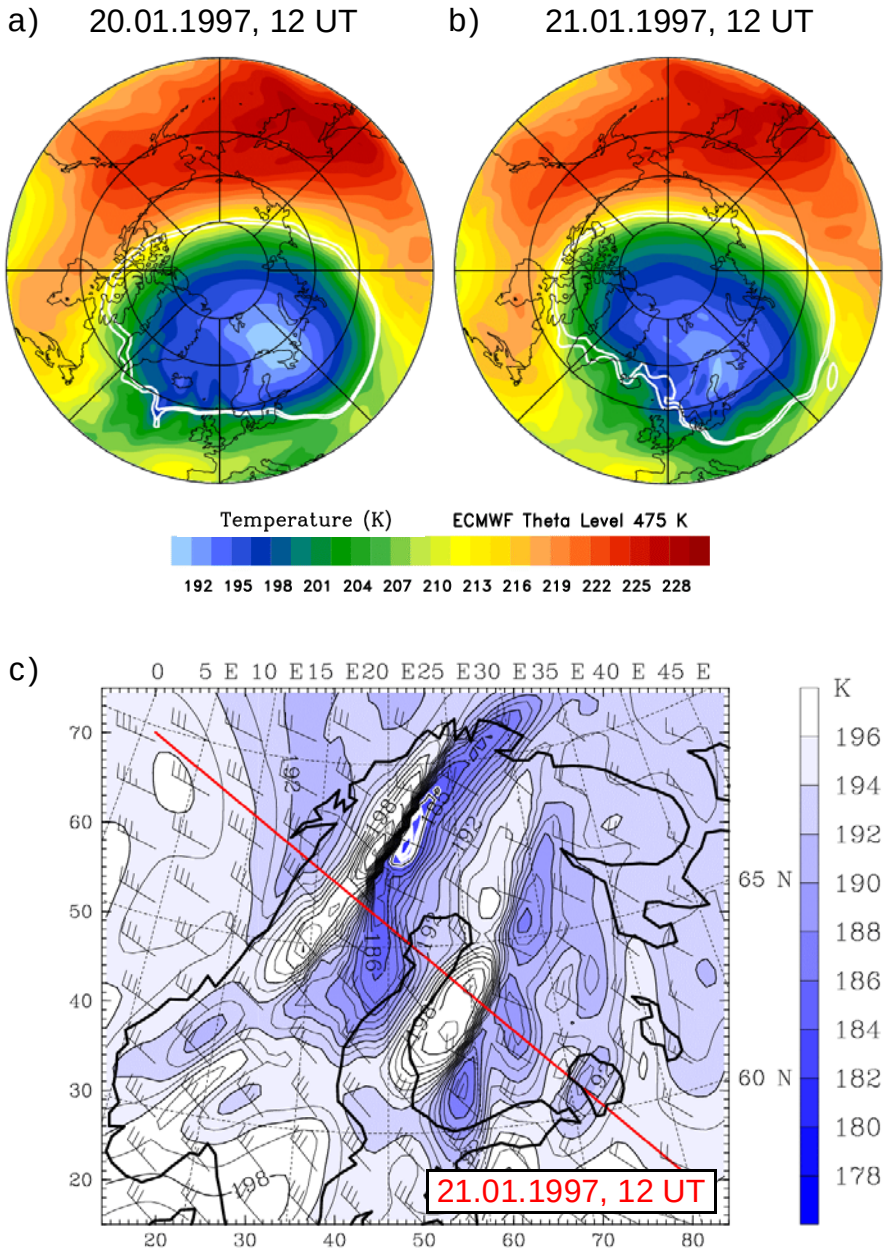

FIGURE 7.2. a) Synoptic-scale temperatures of the 475 K isentropic surface (approx. 20 km height) based on the operational T106 ECMWF analysis for 20 January, 1997, 1200 UT in K, color shaded. The white lines represent the edge of the polar vortex with values of 34 and 36 Potential Vorticity Units (PVU=1×10^{-6} K kg^{-1} m^2 s^{-1}).
b) same as a) for 21 January, 1997.
c) Mesoscale temperatures at the 475 K isentropic surface on 21 January 1997, 1200 UT according to the MM5 analysis (T<196 K, color shaded; K).
Additional fields: Temperature isolines with ΔT=1 K (black lines), horizontal wind vectors (barbs; long: 10 ms^{-1}, short: 5 ms^{-1}).
The red line indicates a path parallel to the wind direction, for which the mesoscale temperature profile is shown in Fig. 7.6.

7.2.2 OClO Measurements

Figure 7.3 shows the GOME measurements of OClO during the mountain wave period. On 20 January, high OClO SCDs (> $1.3*10^{14}$ molec/cm^2) were observed, which coincide with the shape of the polar vortex extending from north-western Greenland via northern Scandinavia to Russia (see Fig. 7.2a). For the SZA of 90° (which at that time corresponds to a latitude of 70° N), maximum OClO SCDs of approx. $1.2*10^{14}$ molec/cm^2 are found, indicating that the vortex air masses were, considering the total column, moderately activated (in the cold Arctic winters 1995/96 and 1999/2000, GOME measured OClO SCDs larger than $2.0*10^{14}$ molec/cm^2 at the same SZA on 20 January, see section 5.1). A comparison with the synoptic scale ECMWF temperatures reveals that temperatures inside the vortex had fallen below the threshold for PSC formation only since the beginning of January [*Coy et al., 1997; Pawson and Naujokat, 1999*], which is rather late compared to other Arctic winters observed by GOME.
On 21 January, a substantial increase in the OClO SCDs from approx. $0.6*10^{14}$ on 20 January to $1.3*10^{14}$ (molec/cm^2) is observed above mid Scandinavia, clearly south of the already activated area inside the vortex core. Such a rapid increase of OClO in a localised area is quite unusual in all GOME measurements, especially at these relatively small solar zenith angles of 75° to 85°. As chlorine activation takes place on PSC particles, an increase in the OClO SCDs is an indication for a decrease in temperatures (or for a transport of already activated air). However, the synoptic scale temperatures in the considered region differ only marginally between 20 and 21 January ([*Dörnbrack et al., 2001*], see also Fig. 7.2a and b), and do not explain the observed increase in chlorine activation.

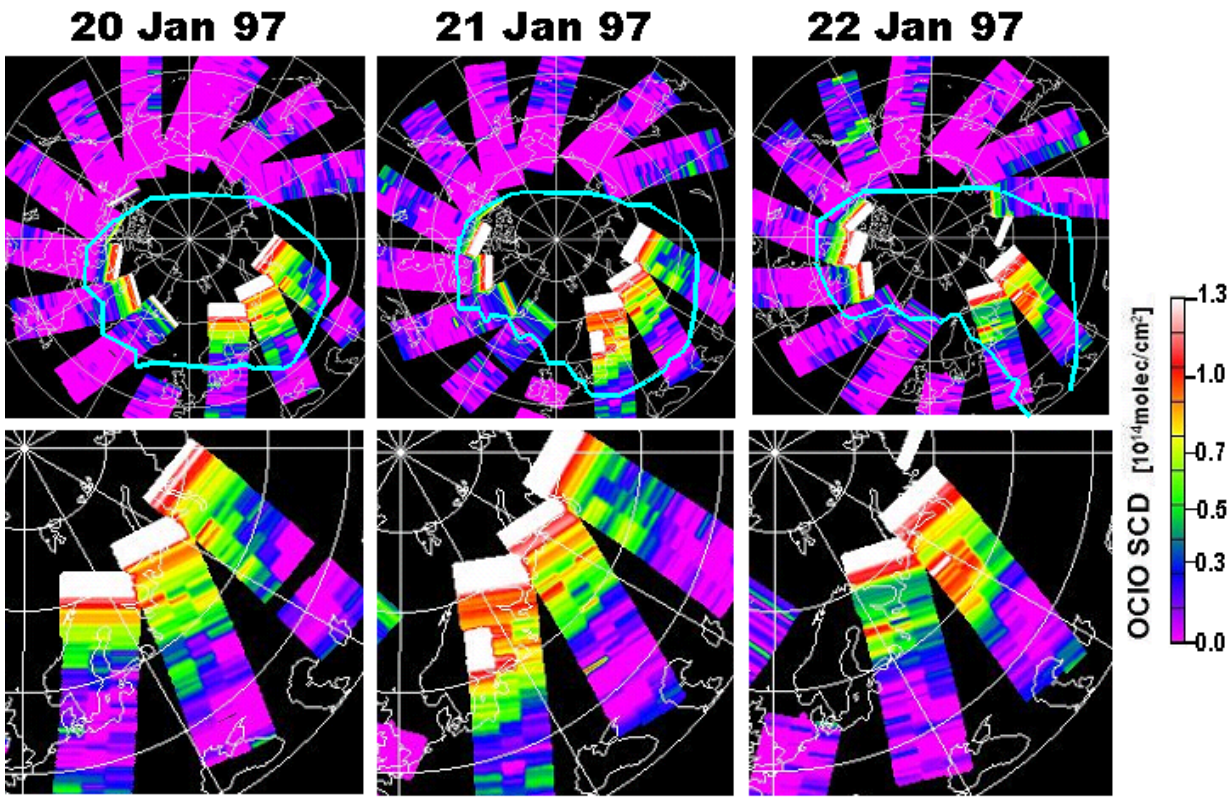

FIGURE 7.3: Maps of OClO Slant Column Densities (SCDs) derived from GOME measurements for 20 to 22 January 1997. North pole at center of the map, all orbits of the GOME measurements are shown. The solar zenith angle (SZA) ranges from 66 to 92 degrees from south to north. Due to the polar night, trace gases can not be observed at SZAs > 95 ° by GOME. There is a gradual decrease of the SCDs from north to south due to the increasing OClO photolysis and decreasing air mass factor (AMF) for lower SZA. On 21 January, a substantial increase in the slant column densities (SCDs) of OClO is seen in the lee of the Scandinavian mountain ridge.

Also, a transport of already activated air masses to the considered region can be excluded as an explanation for the increase of the OClO SCDs. Figure 7.4 shows synoptic-scale trajectory calculations for parcels arriving and starting at the 30 and 50 hPa levels (2.5 days back and forward trajectories) based on the code LAGRANTO [*Wernli and Davis, 1997*] and using 6 hourly ECMWF operational analyses. For parcels at 30 hPa (approx. 22 km altitude) temperatures fall below the PSC threshold (T_{NAT} = 192 K) already on 20 January, indicating that heterogeneous processing probably occurred on the synoptic scale. At the 50 hPa level (approx. 19 km altitude), the air parcels did not encounter temperatures below the PSC threshold (T_{NAT} = 195 K) before passing the Scandinavian mountain ridge.

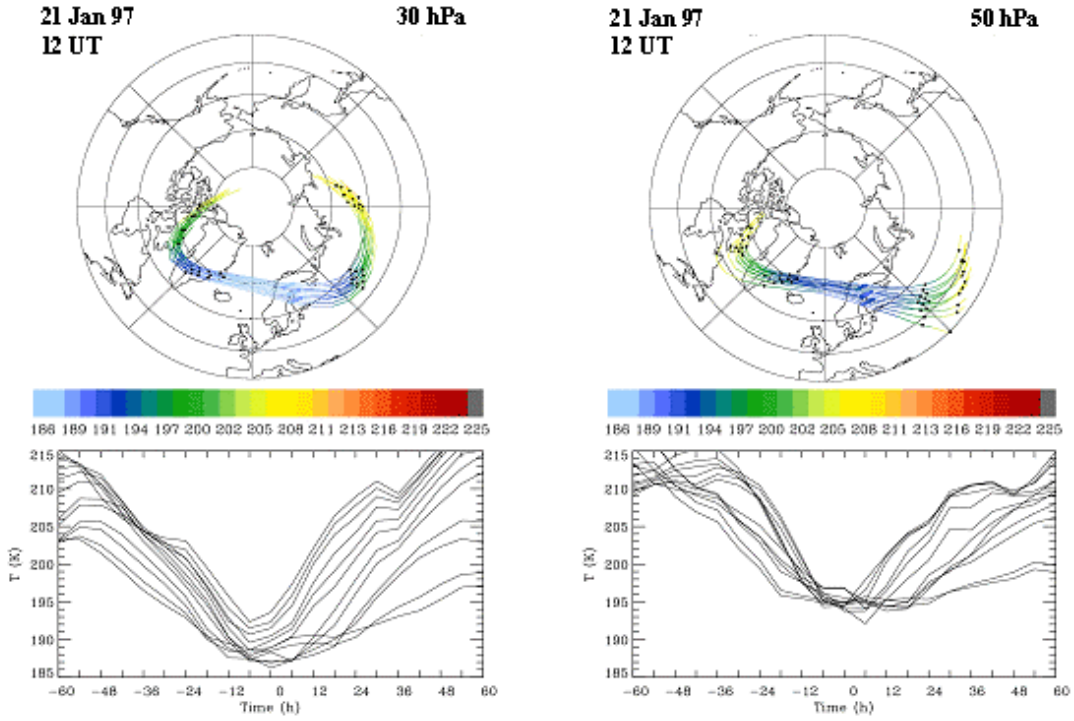

FIGURE 7.4: 2.5 days backward and forward trajectories at the 30 and 50 hPa level for the air parcel for which the rapid increase of the OClO SCDs was observed above the Gulf of Bothnia on 21 January 1997. Also shown is the temporal evolution of the temperature for the respective trajectories.

At any pressure level, temperatures below the threshold for ice formation (PSC type II) are encountered only on the mesoscale (see Fig. 7.2c). Comparing with Figure 7.3 it can be seen that the GOME measurements between northern Scandinavia and the east coast of Greenland, where the air parcels originated on 20 January (based on calculations for the 30, 40 and 50 hPa level), show only weak chlorine activation in the most northern parts of the orbit (the increase of the OClO SCDs and related VCDs as a function of latitude and solar zenith angle is shown in Fig. 7.5 and discussed in detail in section 7.2.3).

Comparing the GOME OClO map of 21 January with the mesoscale temperature field in Figure 7.2c, one finds that the location of the increase in the chlorine activation level agrees very well with the location of the simulated stratospheric temperature anomaly. Due to the spatial and temporal coherence, the abrupt rise in the OClO SCDs on 21 January can be attributed to chlorine activation on PSCs formed by adiabatic cooling in mountain waves, for which the activity was reported to be strongest on that day. This is supported by the fact that similar increases in the GOME OClO observations for the same region are also correlated with strong mountain wave activity (for example 30/31 January, 1996 and 25-27 January, 2000).

One day later, on 22 January, the activated air masses have been advected eastward (see Fig. 7.3) with an apparent speed of approx. 10 m/s, in good agreement with ECMWF forward trajectories starting above the Gulf of Bothnia and arriving over northern Russia (see Fig. 7.4). The air activated by the mesoscale stratospheric temperature anomalies is localised and can be clearly distinguished from activated air masses with different origin further north inside the polar vortex. While the spatial extension of this mountain wave activated air appears to have increased, especially in the west-east direction, maximum values of OClO decreased at the same time (from OClO SCDs above $1.3*10^{14}$ on 21 January to values around $1.0*10^{14}$ on 22 January), indicating that horizontal expansion of the activated air masses took place. However, on both days, the spatial extension of the mesoscale activated air masses is not fully covered by the GOME orbits. Instead, the orbits appear to miss some activation on the western part, which leads to an underestimation of the total area being heterogeneously processed.
Additionally, GOME measured a small spot of enhanced OClO SCDs above Finland east of the Gulf of Bothnia on 22 January. This increase in OClO is in good agreement with PSC observations extending from 20 to 26 km altitude by the ground-based lidar at Sodankylä, during the night of 21 January [*Stein et al. 1999*] and with record low stratospheric temperatures measured by a regular radiosounding at the same location [*Dörnbrack et al., 1999*]. Again, adiabatic cooling in large-amplitude mountain waves determined the local temperature distribution [*Dörnbrack et al., 1999*].
After 23 January, the region of mesoscale activated air is not distinguishable in the GOME OClO maps from usual activation on the synoptic scale. It probably has been mixed with air inside the vortex (see trajectories in Fig. 7.4), or has been partly deactivated by reaction of ClO with NO_2 to $ClONO_2$. Trajectory calculations shown in Fig 7.4. reveal that the air column with enhanced OClO split after 22 January: At the 30 hPa level, the activated air masses move into the polar vortex, while they move further south at the 50 hPa level. This split of the air column also leads to a reduction of the OClO SCDs observed, even if the concentration of OClO at the respective pressure levels remained constant.

7.2.3 Quantifying the increase in chlorine activation

Although there are several model simulations of mountain wave-induced chlorine activation [*Carslaw et al., 1998; Carslaw et al., 1999; Rivière et al., 2000*], no measurements have been reported so far detailing the extent of chlorine activation by mesoscale mountain waves. Since the synoptic-scale temperature remained almost constant [*Dörnbrack et al., 2001*], see also Fig. 7.2, and the relevant air mass showed only little level of activation before, the GOME observations of the OClO increase above northern Scandinavia on 21 January, 1997 constitute an optimal opportunity for quantifying the chlorine activation by mountain wave-induced PSCs.
For that purpose, the GOME OClO measurements are combined with radiative transfer calculations and with mesoscale simulations of the MM5 model: By calculation of air mass factors, the OClO SCDs measured by GOME are converted to VCDs and by employing a mesoscale temperature profile at the location of the measurement, the vertical column is divided into OClO concentrations at the respective altitude levels. Utilizing the JPL 2002 recommendation for the rate constant of the formation reaction for OClO [*Sander et al., 2003*], this leads to an estimation of the vertical ClO mixing ratio profile.

However, the substantial mountain wave induced enhancements in the GOME OClO SCDs discussed in this paper were measured at SZAs significantly lower than 90° ($\theta < 85°$). Therefore, the AMF does not depend strongly on the vertical profile of OClO (see Fig. 4.1) and the GOME SCD measurements can be converted into VCDs, although the actual OClO profile is not known. Likewise, the photolysis rate of OClO for low SZAs can be calculated with little uncertainty and the dependence of the OClO observations on its photochemistry can be accounted for in order to quantify the degree of chlorine activation from our observations. Also, for these relatively low SZAs, the photolysis rate of OClO does not vary that strongly with the solar zenith angle as it does for e.g. $\theta > 90°$ (see Figure 4.3). Therefore, it is not necessary to account for chemical enhancement and to apply a chemical air mass factor (for a solar zenith angle of 83°, the difference between the standard and the chemical AMF is less than 2 %).

Fig. 7.5 shows the SCDs and corresponding VCDs for the orbit above Northern Scandinavia on 21 January, and for the sum of the two orbits above Greenland on 20 January, where the air parcel originated on that day. For comparison, the SCDs and VCDs for the orbit above Northern Scandinavia on 20 January (the same location, where the rapid increase of the OClO SCDs occurs on 21 January) are also shown.
An ideal approach to determine the mountain wave-induced increase in chlorine activation would be to compare the OClO column densities of the same air mass for both days by consulting the related trajectories. GOME measurements cover the place of the origin of the air mass above Greenland (see Figs. 7.4 and 7.3), thereby enabling us to quantify the increase of the OClO VCDs. However, there is the complication that the related trajectories are different for each height level (see Fig. 7.4): For the 50 hPa level (approx. 19 km altitude), the trajectory calculations reveal that the considered air mass emanated from above East Greenland on 20 January. On the other hand, trajectories for the 30 hPa level started above the mid of Greenland. These locations correspond to different GOME orbits (compare Fig. 7.3), which makes it impossible to attribute the observed increase in the VCDs to an increase between a single pair of GOME orbits.

Therefore, we decided to take the sum of the OClO SCDs and VCDs of the two orbits above Greenland on 20 January (Fig. 7.5a). The GOME OClO SCDs for 20 January above Greenland are significantly lower than the ones above Northern Scandinavia (Fig. 7.5b, see also Fig. 7.3), even when the sum of the two Greenland orbits is taken: While the orbits above Greenland show almost no chlorine activation at the location of the air mass origin (OClO SCDs are around $0.3*10^{14}$ molec/cm^2), the orbit above Northern Scandinavia features OClO SCDs around 0.5 to $0.7*10^{14}$ molec/cm^2. This indicates that, due to temperatures below T_{NAT} on the synoptic scale (see Fig 7.1a), air masses above Northern Scandinavia were moderately activated on 20 January.

As already mentioned, the trajectories in Fig. 7.4 reveal that, for the air parcel being heterogeneously processed by the mountain wave event on 21 January, some activation probably occurred already before passing the Scandinavian mountain ridge on the synoptic scale, especially at the low pressure levels (p = 30 hPa). In order to account for this activation on the synoptic scale and not to overestimate the mountain wave induced chlorine activation, the following calculations investigate the increase appearing in the orbits above Northern Scandinavia between 20 and 21 January. For comparison, the increase relative to the sum of the two orbits above Greenland is given in brackets. Both figures may serve as an upper and lower limit for the mountain wave induced increase in chlorine activation in the investigated air mass.

Due to the increase of the AMF, all SCDs for 20 and 21 January in Fig. 7.5 show a gradual increase towards higher SZAs. On 21 January, an unusual rise of the SCDs above Northern Scandinavia is seen at the location of the mountain wave-induced temperature anomaly (see Fig. 7.5c). This rapid increase is seen more clearly in the related VCDs, which do not increase due to the increase of the AMF. A comparison of the OClO VCDs above Northern Scandinavia on 20 January with the ones on 21 January shows a significant enhancement extending from 53° N to 65° N (73°< SZA <85°). The most pronounced increase from approx. 0.7 (0.5) to $1.6*10^{13}$ molec/cm^2 is found for solar zenith angles between 78° and 84° (58° N to 64° N), indicating an increase in chlorine activation by a factor of 2 to 3 for the respective vertical columns. While this represents the increase of the average values for the latitude range stated, some GOME pixels, at an SZA of 83 °, show an increase of the OClO VCDs from 0.8 (0.5) to above $1.9*10^{13}$ molec/cm2, which implies significant activation of chlorine species over a wide altitude range.
In the following section we investigate the increase of the OClO VCDs observed near 64° N / 22° E at an SZA of 83° from 0.8 (0.5)$*10^{13}$ molec/cm^2 on 20 January to $1.8*10^{13}$ molec/cm^2 on 21 January. By applying different vertical OClO and ClO profiles, which are derived from the mesoscale temperature profile collocated with the observed OClO VCD, we give an estimate for the related increase of the mixing ratios of OClO and ClO.

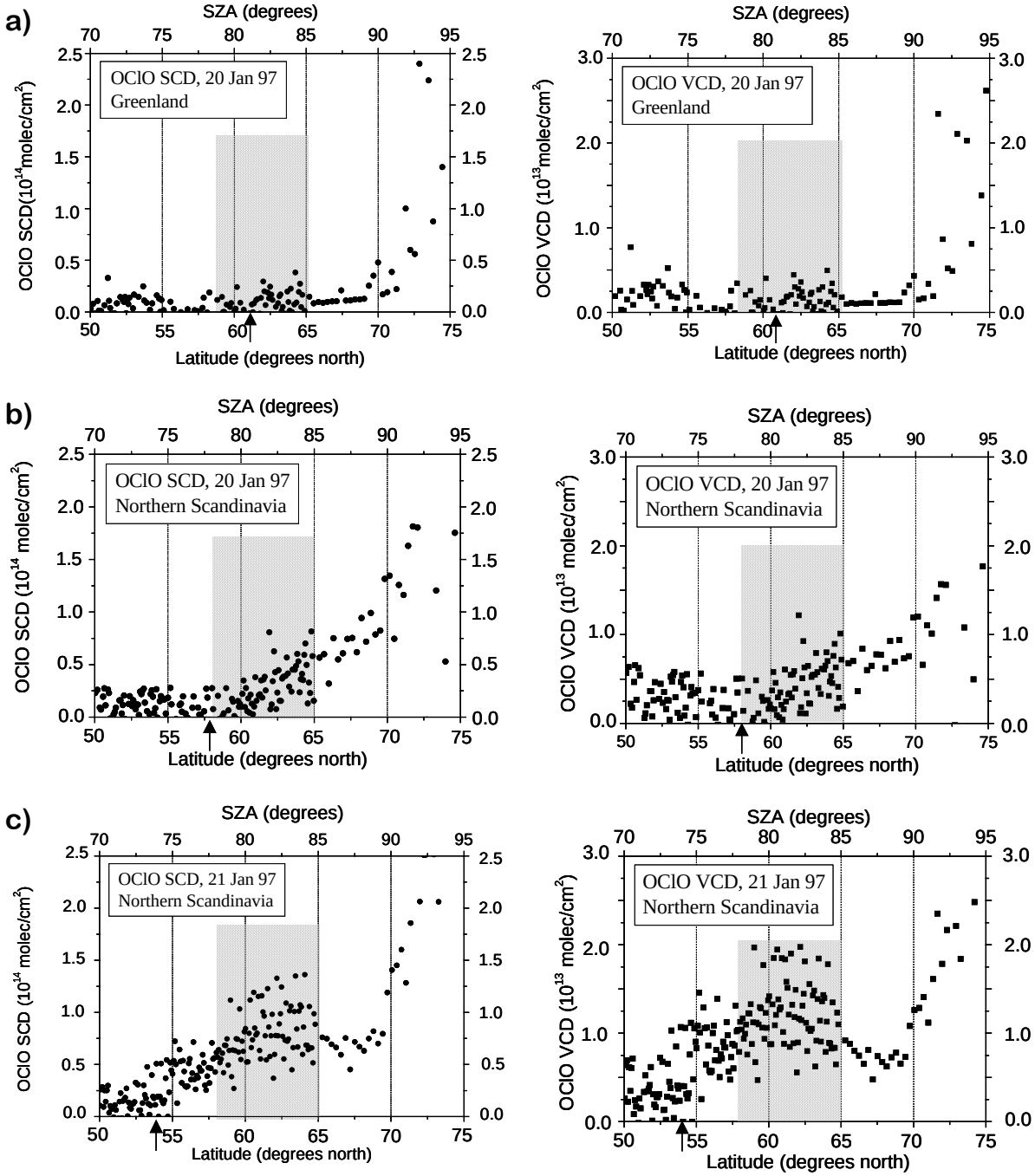

FIGURE 7.5: GOME OClO SCDs and related VCDs as a function of the solar zenith angle (SZA) and latitude. VCDs were derived with the corresponding AMFs calculated by AMFTRAN for a gaussian profile of the OClO mixing ratio, maximum at 19 km, full width half maximum of 8 km. The arrow at the latitude axis indicates the vortex edge at the 475 K level.
a) for the sum of the two orbits above Greenland on 20 January 1997
b) for the orbit above northern Scandinavia on 20 January 1997
c) for the orbit above northern Scandinavia on 21 January 1997.

In this study, we assume various profiles in order to investigate how the observed increase of the OClO VCDs can be attributed to an increase in the mixing ratio of OClO at the different altitude levels. Since, for low SZAs, the steady state assumption (Eq. 4.2) holds, meaning that [OClO] is linear to [ClO], the corresponding mixing ratios of ClO can then be calculated. For all calculations, we apply the temperature and pressure profile derived from the mesoscale calculations for the location of the high OClO SCDs measured by GOME near 64° N / 22° E on 21 January. Furthermore, we assume a constant mixing ratio for BrO of 15 pptv and consider the height-dependence of the photolysis rate of OClO. The rate constant for the formation reaction of OClO (R 4.1) is taken from the JPL 2002 recommendation [*Sander et al., 2003*]. The uncertainties of the calculations and the underlying assumptions as well as the sensitivity of the results on parameters not observed by GOME are discussed in section 7.2.4.

The motivation for the different profile shapes is given by the dependence of chlorine activation on the formation of PSCs, i.e. we assume that high levels of chlorine activation are to be found for altitudes where temperatures drop below the threshold for formation of PSCs. In Figure 7.6, a cross-section of the simulated mesoscale temperatures along a trajectory downstream of the Scandinavian mountain ridge including the location of the OClO VCD of $1.8*10^{13}$ molec/cm^2 on January 21 near 64° N / 22° E is plotted. It can be seen that minimum temperatures of 187 K are found at the 520 K level, which is below T_{NAT}, the threshold for formation of PSC type Ia, already before the air parcels reach the Scandinavian mountain ridge. However, temperatures below T_{frost}, the threshold for formation of PSC type II, are encountered only downstream of this high mountain barrier. In addition, the vertical extension of the altitude for which formation of PSCs and hence chlorine activation is possible, is significantly enhanced by the mountain wave-induced temperature anomaly.

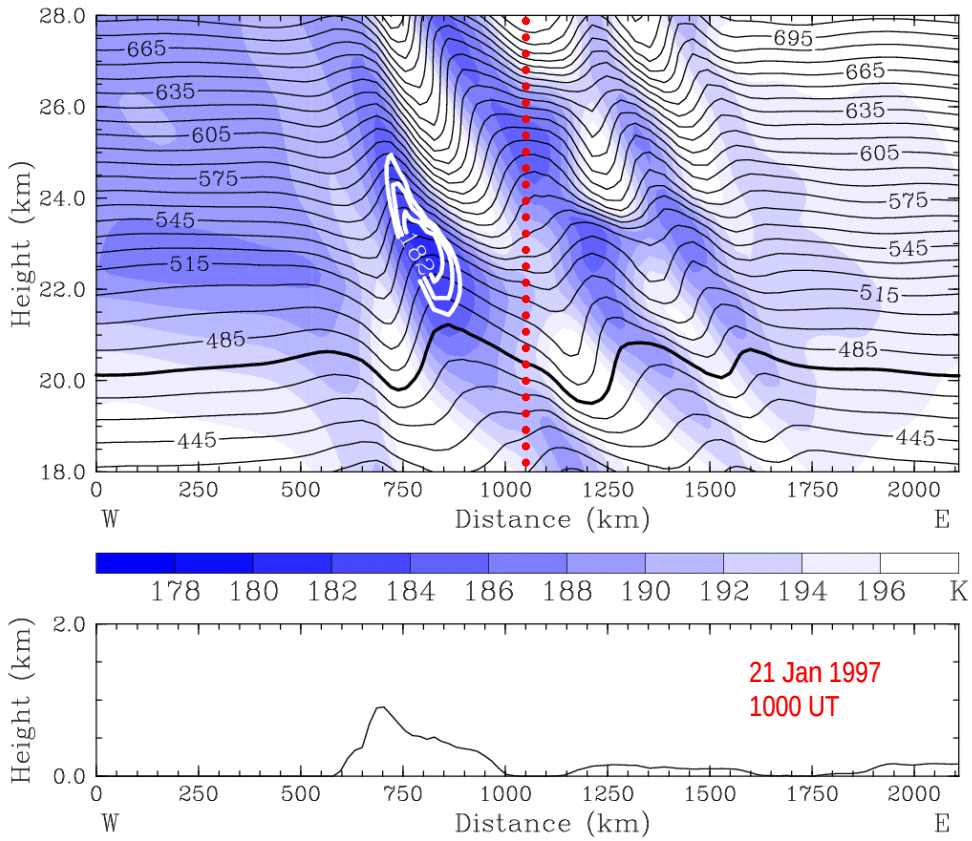

FIGURE 7.6: Temperature T<196 K (color shaded; K) and potential temperature Θ (solid black lines, ΔΘ=10 K) on 21 January 1997 1000 UT (close to the time of the GOME measurement) along the vertical west-east section marked by the red line in Fig. 7.2c. The location of the maximum OClO VCD for which the vertical profile of the chlorine activation is calculated, is indicated by the red dotted line. Temperatures below T_{frost} are indicated by the white shaded contours. The height of the model orography is plotted below the vertical section. Numerical results are from the outer domain of the mesoscale model (Δx=27 km).

The altitude region with possible PSC formation can be seen more easily in Figure 7.7. It shows the range of temperatures that the air masses encountered traveling downstream of the Scandinavian mountain ridge up to the location of the observed maximum VCD of OClO in comparison to the PSC formation threshold temperatures. T_{NAT} and T_{frost} were calculated according to *Hanson and Mauersberger* [1988] with the assumption of constant mixing ratios for nitric acid and water vapour (HNO_3 = 10 ppbv and H_2O = 5 ppmv). According to this estimate, formation of PSC type Ia (NAT) was possible in an altitude range from 15 to 28 km, while temperatures below T_{frost} occur in the range from 21 to 24 km.
These calculations are in good agreement with Lidar measurements above Sodankyla during the nights of 21 and 22 January [*Stein et al. 1999*], where PSCs were observed from 20 to 26 km, and PSCs type II were observed from 21.5 to 22.5 km. In addition, the mesoscale temperature profile calculated by MM5 for the 21 January 1997 has been shown to be in very good agreement with measurements from ozone sondes [*Dörnbrack et al., 1999*].

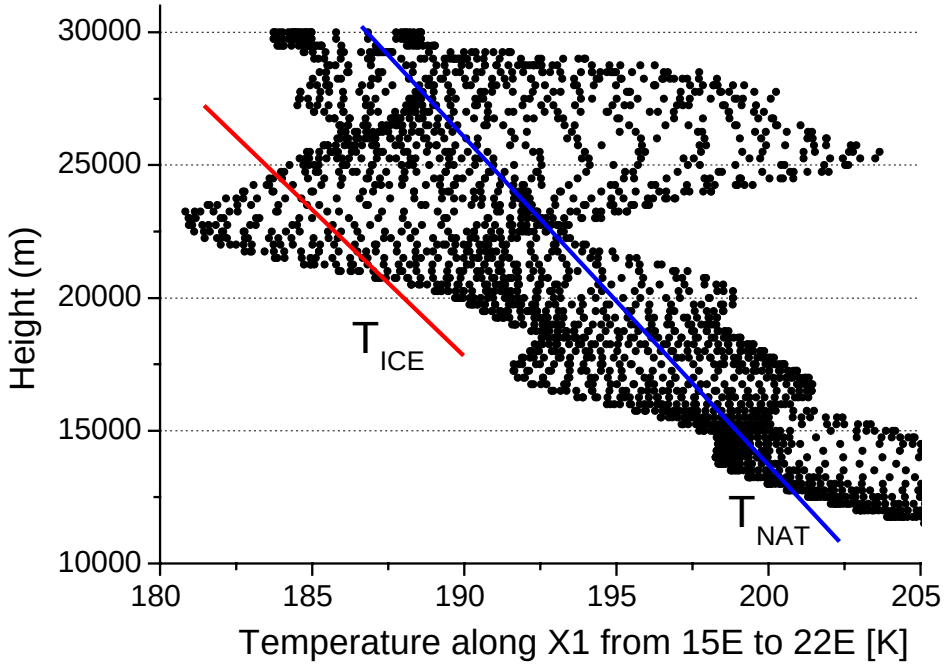

FIGURE 7.7: Range of temperatures encountered by air parcels 400 km upstream of the location of the high OClO VCDs on 21 January, 1000 UT, as calculated by MM5 for the west-east section in Fig. 7.6 (see also the red line in Fig. 7.2c), approx. from 15° E to 22° E (from the mountain ridge to the location of the GOME measurement). In comparison, the threshold temperatures for the formation of PSC type 1 (T_{NAT}, blue line) and PSC type 2 (T_{ICE}, red line) at the respective height levels are shown. The PSC formation temperatures were calculated according to *Hanson and Mauersberger* [1988], assuming 10 ppbv HNO_3 and 5 ppmv H_2O.

In the following we assume three different vertical profile shapes for the ClO mixing ratio, based on the estimate of possible PSC formation derived from the mesoscale temperature profile. First, the altitude range of temperatures below T_{NAT} is considered by assuming a box profile for the ClO mixing ratio.
As the probability of PSC formation increases for lower temperatures, higher ClO and OClO concentrations are to be expected for altitude levels with lower temperatures. A rough approximation to the probability for chlorine activation or formation of PSCs as a function of altitude is given in Figure 7.8. It shows the difference of the simulated temperatures to the PSC type Ia formation temperature (T_{NAT}). This temperature difference profile can be well described by a gaussian function with the maximum at a height of 21 km and a full width at half maximum of 8 km. As second case, we assume this gaussian fit to the temperature profile as the vertical profile for the ClO mixing ratio. In the third case, we assume that the ClO mixing ratio profile has exactly the same shape as the temperature difference profile derived from the simulated mesoscale temperature profile.

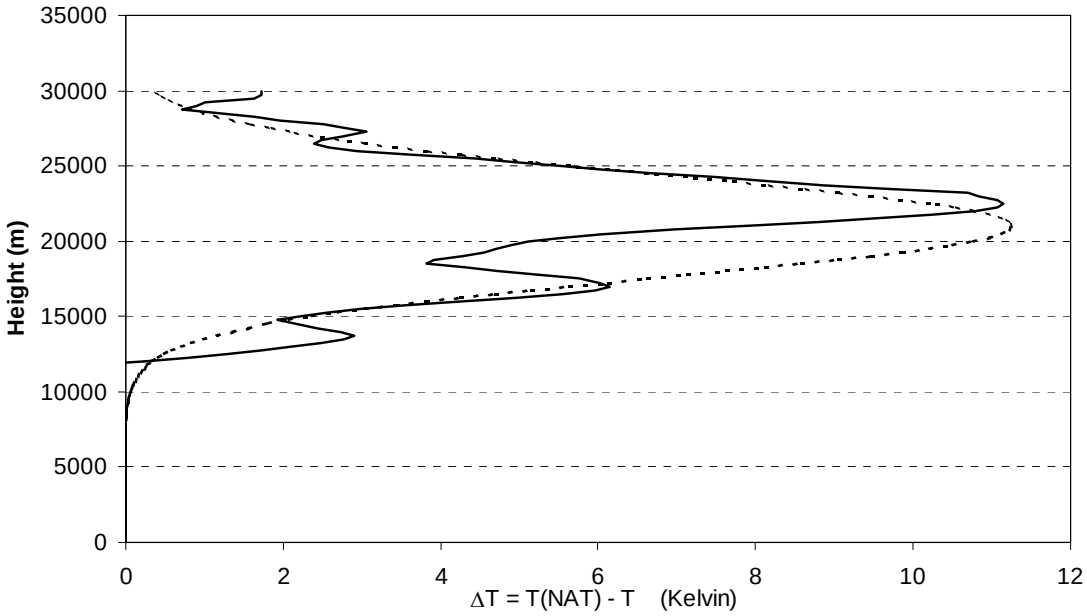

FIGURE 7.8: Temperatures below T_{NAT} encountered by air parcels 400 km upstream of the location of the maximum OClO VCD near 64° N / 22° E on 21 January as an estimate for the probability of chlorine activation. Also shown is a gaussian fit to the curve with the maximum at 21 km and a full width at half maximum of 8 km.

We want to point out here that the OClO and ClO mixing ratio profiles discussed in the following are not measured by GOME but derived from assumptions about the relative profile shape. Since there are no other measurements detailing the extent of mountain wave induced chlorine activation, we want to give a rough estimate of the increase in quantities that are more familiar than OClO column densities. Of course, there are many uncertainties in the necessary calculations and further uncertainties arise due to the assumptions made (see section 7.2.4). However, the result of a rapid increase of the OClO and ClO mixing ratios over a wide altitude range during the mountain wave event is the same for all profiles that can be assumed due to the given meteorological situation.

Box profile for mixing ratio of ClO

This box profile indicates, which ClO mixing ratios are consistent with the observed GOME OClO VCDs, when no specific profile is assumed. At the same time, this profile may represent the threshold character of the processes involved in chlorine activation. We assume that activation of chlorine takes place when temperature drops below the threshold for formation of PSCs and neglect the temperature dependence of the reactions involved. This results in a constant ClO mixing ratio for altitudes where PSC formation was possible on 21 January (15 to 28 km, see Fig. 7.7). Using the steady state assumption (Eq. 4.1), this ClO box-profile can be constrained to the GOME OClO measurements by changing its maximum mixing ratio until the resulting OClO VCD matches the OClO VCD measured by GOME. For 21 January, the OClO VCD of $1.8*10^{13}$ molec/cm^2 measured by GOME corresponds to a constant ClO mixing ratio of 1.3 ppbv. The same box profile applied to the GOME OClO VCD of $0.8\ (0.5)*10^{13}$ molec/cm^2 measured on 20 January, results in a ClO mixing ratio of 0.6 (0.4) ppbv. This implies that for the total column, the level of activation increased by a factor of 2.2 (3.4); the values in brackets indicate the increase relative to the sum of the two orbits above Greenland.

Gaussian profile of ClO mixing ratio, derived from the mesoscale temperature profile

The next two profiles account for the temperature dependence of the heterogeneous chlorine activation reactions by linearly increasing the volume mixing ratio of ClO for altitudes with temperatures below T_{NAT}. First, we adopt the gaussian function to the temperature profile shown in Fig. 7.8 for the vertical profile of the ClO mixing ratio and constrain it to the GOME OClO measurements as described above. In particular, this allows us to calculate the mixing ratios of OClO and ClO at the 30 and 50 hPa level for the air parcel for which the high OClO VCDs were measured by GOME on 21 January. The observed VCD of OClO on 21 January of $1.8*10^{13}$ molec/cm^2 near 64° N / 22° E corresponds to an OClO concentration of $6.3*10^6$ molec/cm^3 at 30 hPa (22.3 km) and $1.7*10^7$ molec/cm^3 at 50 hPa (19.5 km) (mixing ratios: 5.5 and 9.1 pptv respectively). Following the steady state assumption (Eq. 4.1), these OClO concentrations correspond to mixing ratios for ClO of 1.7 ppbv at 30 hPa and 1.6 ppbv at 50 hPa.
For 20 January, we assumed the same gaussian profile for ClO, which is constrained to the GOME OClO measurements in the described way. On that day the OClO VCD measured by GOME at 64° N / 22° E (SZA of 83°) was $0.8*10^{13}$ molec/cm^2, resulting in substantially lower mixing ratios for ClO (0.75 ppbv at 30 hPa and 0.7 ppbv at 50 hPa) and OClO (2.5 pptv at 30 hPa and 4.1 pptv at 50 hPa). The vertical profile for the OClO mixing ratio resulting from the calculation sketched above for 21 January is shown in Fig. 7.9.

Profile of ClO mixing ratio directly scaled to mesoscale temperature profile

The gaussian fit to the simulated mesoscale temperatures overestimates the temperature difference to T_{NAT} below 22 km, where $\Delta T = T_{NAT} - T$ shows a rapid decrease (see Fig. 7.8). This probably leads to an overestimation of the mountain wave-induced chlorine activation at these altitudes. At the same time, the gaussian fit underestimates the temperature-difference to T_{NAT} (and consequently the induced chlorine activation) for heights between 13 and 15 km. Since these altitude levels have higher number densities, possible chlorine activation at these heights will lead to high concentrations of OClO and thus could represent a significant part of the observed OClO VCD, even when the mixing ratio of OClO (or ClO) is lower than for higher altitudes.
The possible chlorine activation in the high pressure regions (low altitudes) is better accounted for, if we adopt the difference of the mesoscale temperatures to the threshold for formation of PSC type Ia (T_{NAT}), shown in Fig. 7.8, for the vertical profile of the ClO mixing ratio. The resulting profile (see Fig. 7.10) shows the same wave-like structure as the mesoscale temperatures, with minima and maxima alternating with a period of approx. 4-5 km. The derived OClO profile depicts three peaks with nearly the same magnitude (see Fig. 10), arising mainly from a weighting of the ClO profile with the height dependent photolysis rate of OClO.
Fig. 7.10 depicts the mixing ratios for ClO and ClO_x (= ClO + ClOOCl x 2), resulting at an SZA of 83° at the respective pressure levels. The ClO mixing ratios were calculated for three different BrO profiles of constant mixing ratio: 12, 15 and 18 pptv. The ClO_x values were calculated for two scenarios: a) according to the JPL 2002 recommendation [*Sander et al.*, 2003], and b) by increasing J(ClOOCl) by a factor of 1.3, as suggested by *Stimpfle et al.* [2004]. Compared to the gaussian fit (see Section 5.3.2), mixing ratios for ClO at the height of 19.5 km (≈ 50 hPa) are significantly reduced (from 1.6 to 0.7 ppbv). However, mixing ratios at the 30 hPa level (≈ 22 km) remain nearly unchanged (0.8 compared to 0.7 ppbv on 20 January, and 1.75 compared to 1.7 ppbv on 21 January). The resulting mixing ratios for ClO_x are below the total Cl_y for all height levels [*Schmidt et al.*, 1994; *Engel at al.*, 2002], but reveal that almost complete activation of chlorine occurred, especially in the mountain wave induced temperature minima.
The shape and magnitude of the derived ClO profile is in good agreement with observations: While ground and space based microwave measurements show a gaussian shape vertical profile with peak mixing ratios around 2 ppbv [*Solomon et al.*, 2002; *Santee et al.*, 2003], high resolution in situ measurements reveal that the ClO mixing ratio profile can consist of multiple peaks [*Pierson et al.*, 1999; *Vogel et al.*, 2003], depending on the temperature profile which enabled the heterogeneous processing of chlorine species in PSCs.

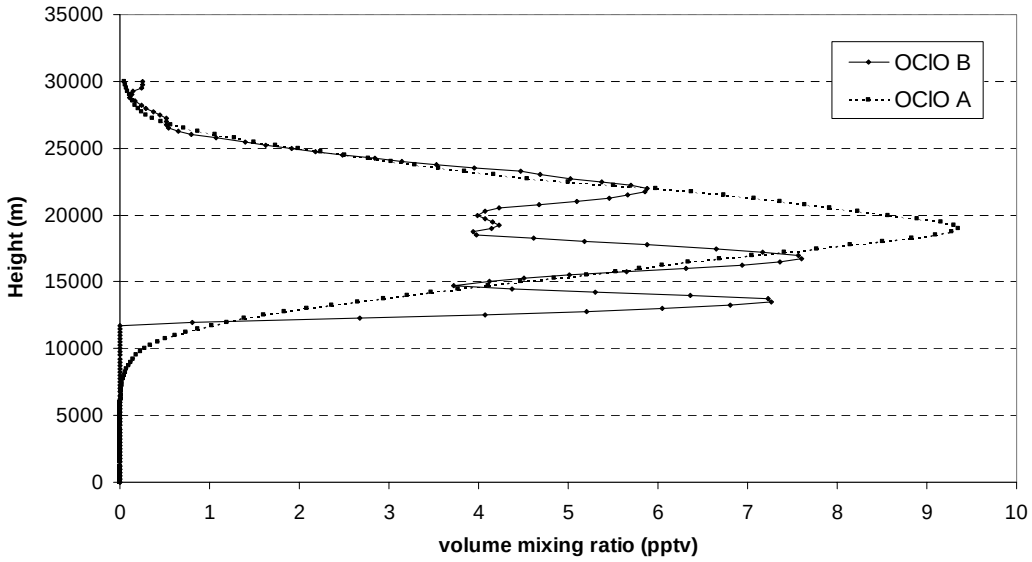

FIGURE 7.9: Vertical profiles of the OClO mixing ratio on 21 January 1997, according to the temperature difference profile obtained from the mesoscale simulations (see Fig. 9) and scaled to the GOME observations of the OClO SCDs. Calculations were performed using the mesoscale temperature and pressure profiles at the location of the GOME measurement and applying the JPL 2002 recommendation [*Sander et al*., 2003] for the rate constant of the formation reaction of OClO (details see text).
'OClO A': for the ClO volume mixing ratio profile scaled by the gaussian fit to the temperature difference profile with maximum at 21 km and full width at half maximum of 8 km
'OClO B': for the ClO volume mixing ratio profile scaled directly by the difference of the simulated mesoscale temperatures to T_{NAT} (see Fig. 7.10).

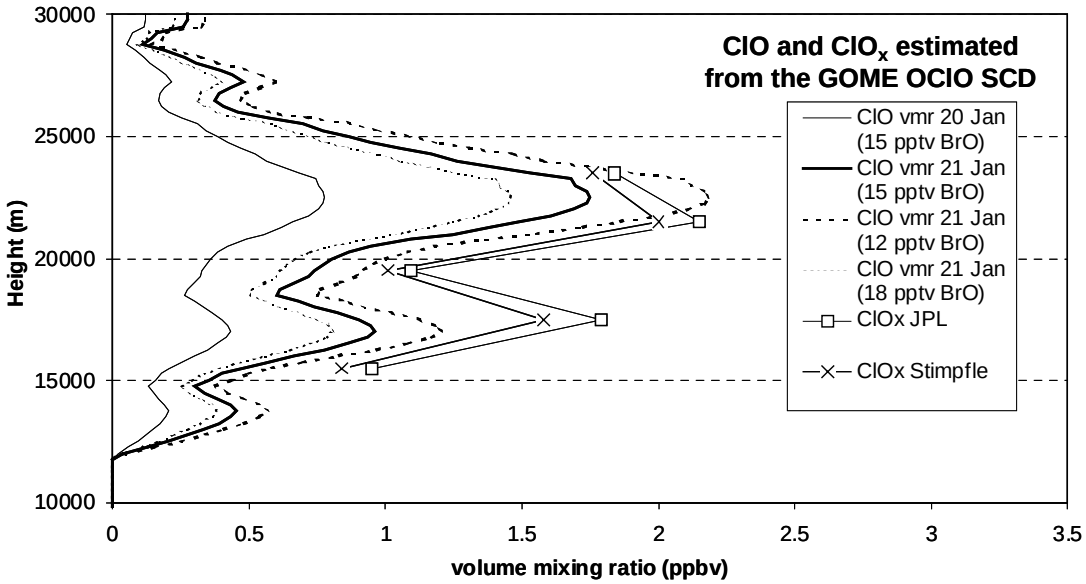

FIGURE 7.10: Vertical profiles of the ClO mixing ratio on 20 and 21 January 1997, estimated from the GOME observations of the OClO SCDs by applying the temperature difference profile ($\Delta T = T_{NAT} - T$) obtained from the mesoscale simulations (see Fig. 7.8). The ClO mixing ratio profile for 21 January is plotted for three different BrO profiles of constant mixing ratio: 12, 15, and 18 pptv; for 20 January only the ClO profile resulting for 15 pptv BrO is plotted. Details of the calculations based on the steady state assumption are described in the text. Also shown is the resulting mixing ratio for ClO_x (= ClO + ClOOCl x 2) for 15 pptv BrO for 21 January, applying either the JPL 2002 recommendation [*Sander et al*., 2003], or increasing J(ClOOCl) by the factor 1.3 as suggested by *Stimpfle et al*. [2004].

7.2.4 Estimation of the measurement errors and uncertainties of the calculations

Uncertainties of the GOME OClO analysis were discussed in detail by *Wagner et al*. [2001]. The precision was estimated to about ± 10 % for large OClO SCDs and the additional systematic errors arising from the absolute calibration of the OClO cross section are less than 8 %. In the same study, the influence of the optical density of PSCs on the AMF for OClO was investigated. In particular, it was shown that PSCs have only a negligible effect on the retrieved OClO SCD.

For the GOME OClO measurements presented in this study, an additional error may arise from the extraordinarily high backscatter ratio of mountain wave PSCs. Since the bulk of the OClO SCD is located below the PSCs, this could lead to an underestimation of the OClO SCD (shield effect). However, the influence of the PSCs on the retrieved OClO SCDs should be of greater importance for higher SZAs around 90° and is expected to be negligible for lower SZAs, for which the increase in chlorine activation was observed in this study. This view is supported by the very high OClO and ClO concentrations resulting from the calculations in Section 5 for 21 January 1997, which indicate that a shielding by PSCs does not occur.

In the conversion of the OClO SCDs to VCDs, further uncertainties arise as it depends on the AMF. As is seen in Fig. 4.1, the calculation of the AMF for the SZAs relevant for this study (75° < SZA < 85°) shows only slight variation for different OClO profiles: For a gaussian profile with maximum at 19 km and a FWHM of 8 km the AMF is 7.1 at an SZA of 83°. For the same SZA and FWHM the AMF is 7.4 when the maximum is at 21 km and 6.9 when the maximum is at 18 km. Comprising, the AMF for OClO at an SZA of 83° can be determined independently of the actual profile with an uncertainty less than 10 % (neglecting profiles that can be excluded due to the meteorological situation).

Likewise, for low SZAs, the calculation of the photolysis rate of OClO (J (OClO)) can be done with relatively low uncertainty (+/- 5 %), leading to a good approximation of the ClO/OClO relation by the steady state assumption (Eq. 4.1).

As the concentration of OClO and the deduced mixing ratio of ClO are calculated from the VCD they depend on the vertical profile of OClO, which has to be assumed or can be estimated from the temperature profile. We investigated this uncertainty by assuming different profile shapes with different vertical extensions. For a profile, which shape was adopted from the profile of the mesoscale temperatures, we derive ClO mixing ratios that indicate almost complete activation of chlorine species. Even for a box profile extending over the whole altitude range for which PSC formation was possible (15-28 km), the ClO mixing ratio amounts to 1.3 ppbv. If, in contrast, the vertical extension is limited to a region between 21 and 24 km (approximately the altitude region where $\Delta T = T_{NAT} - T$ has the highest values), unrealistically high values result for the ClO mixing ratio. Parameters that effect the estimated vertical range of PSC-formation are the mixing ratios of HNO_3 and H_2O. Here, we assumed standard values for the polar stratosphere.

The resulting mixing ratios for ClO are also influenced by the vertical profiles of the BrO mixing ratio and the mesoscale temperature. The simulated mesoscale temperature profile has been shown to match very good with measurements of an ozonesonde at Sodankylä [*Dörnbrack et al*., 1999]. In order to investigate the sensitivity of the ClO mixing ratio on the assumed BrO profile, BrO mixing ratios were increased and decreased from the standard calculation by 20 %, i.e. from 15 pptv to 12 and 18 pptv, representing the range of measured profiles [*McKinney et al*., 1997; *Harder et al*., 1998; *Fitzenberger* 2001] and model calculations [*Sinnhuber et al*., 2002]. Since steady state between OClO and its educts is assumed, the ClO mixing ratios deduced from the observed OClO VCDs are then lowered or increased by 20 % respectively.

There are considerable uncertainties in the kinetics and the partitioning of the reaction between ClO and BrO [*Sander et al*., 2003]. However, this uncertainty would only alter the absolute values of the deduced mixing ratios for ClO, the relative increase of the OClO and ClO mixing ratios as well as of the observed OClO SCDs and VCDs is unaffected.

7.3 The event of 20-27 January 2000

This mountain wave event has been intensively studied by model simulations [*Dörnbrack et al., 2002; Flueglistaler et al., 2002; Larsen et al., 2003*], in situ PSC measurements [*Voigt et al., 2001*] and also satellite remote sensing of PSCs [*Bevilacqua et al., 2002*].
Figs 7.11 and 7.12 illustrate the increase in the GOME OClO SCDs during these days in comparison to the determining stratospheric meteorological parameters potential vorticity, temperature and area of possible PSC formation.

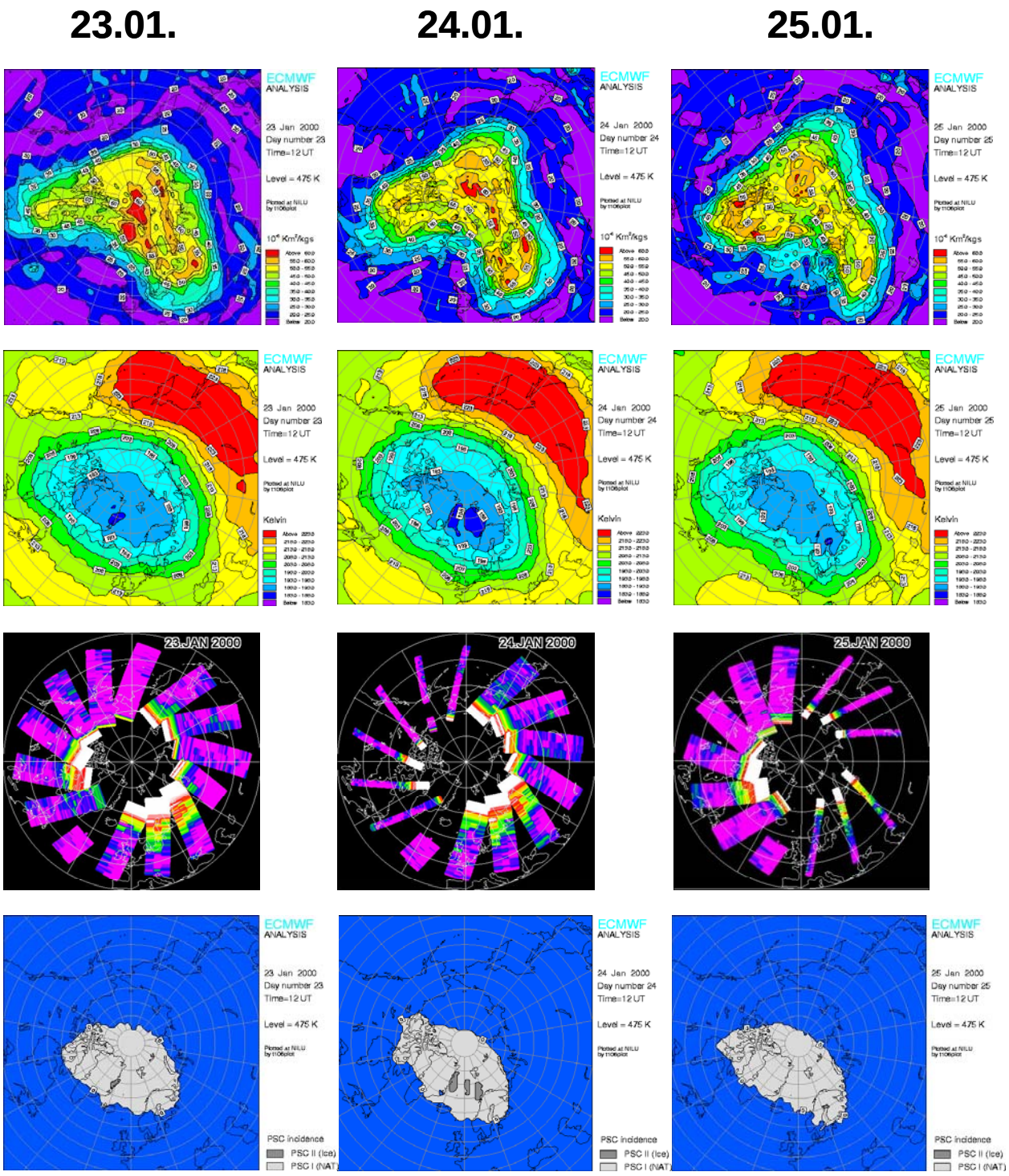

FIGURE 7.11: ECMWF potential vorticity and temperature at the 475 K level (upper two panels), GOME OClO SCDs and PSC existence areas for 23.01- 25.01.2000.

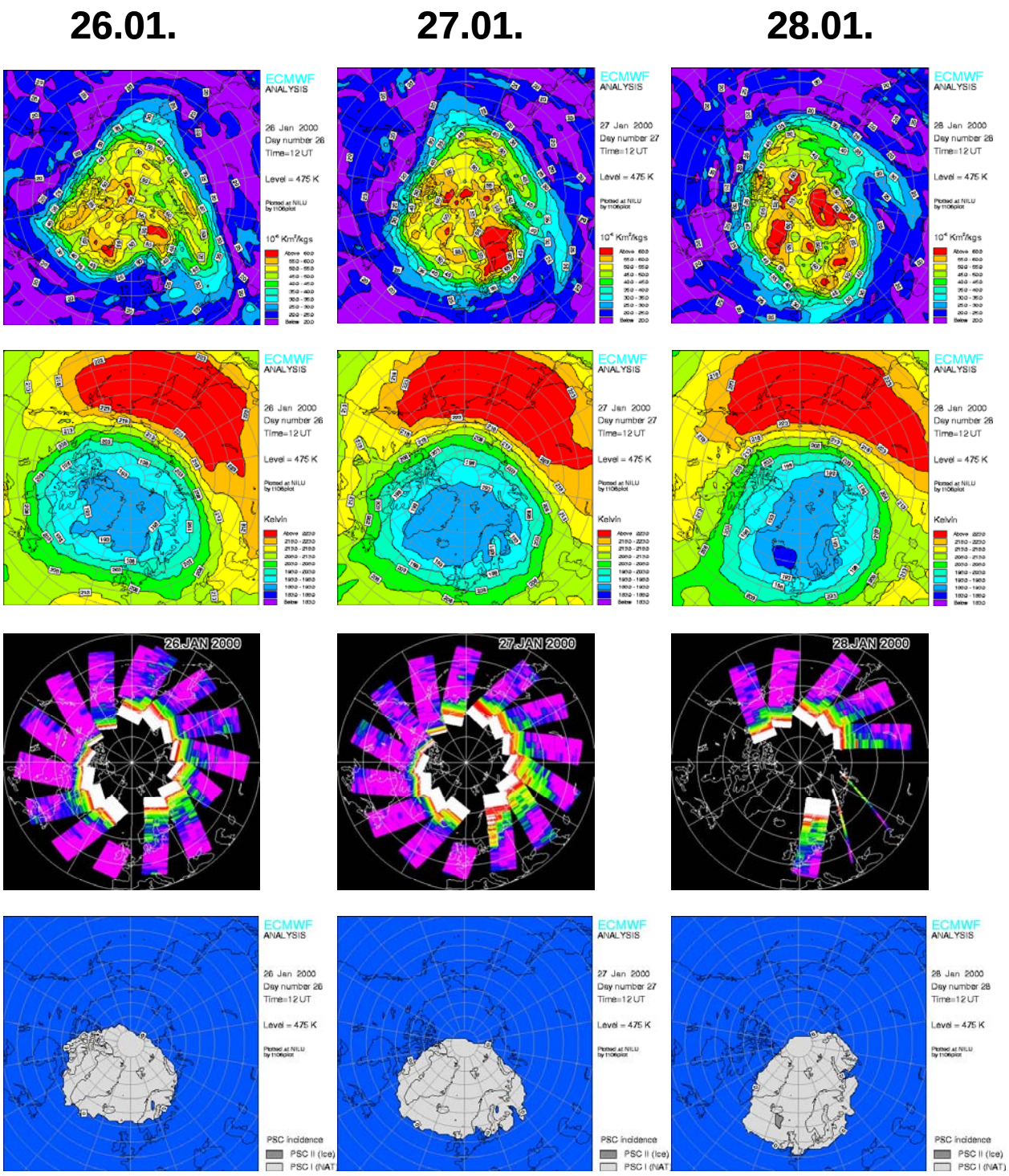

FIGURE 7.12: ECMWF potential vorticity and temperature at the 475 K level (upper two panels), GOME OClO SCDs and PSC existence areas for 26.01- 28.01.2000.

7.4 The event of 18-20 December 2002

A further extremely strong mountain wave event took place in December 2002, which featured extraordinarily cold temperatures in the Arctic stratosphere already on the synoptic scale (compare section 5.1.6).

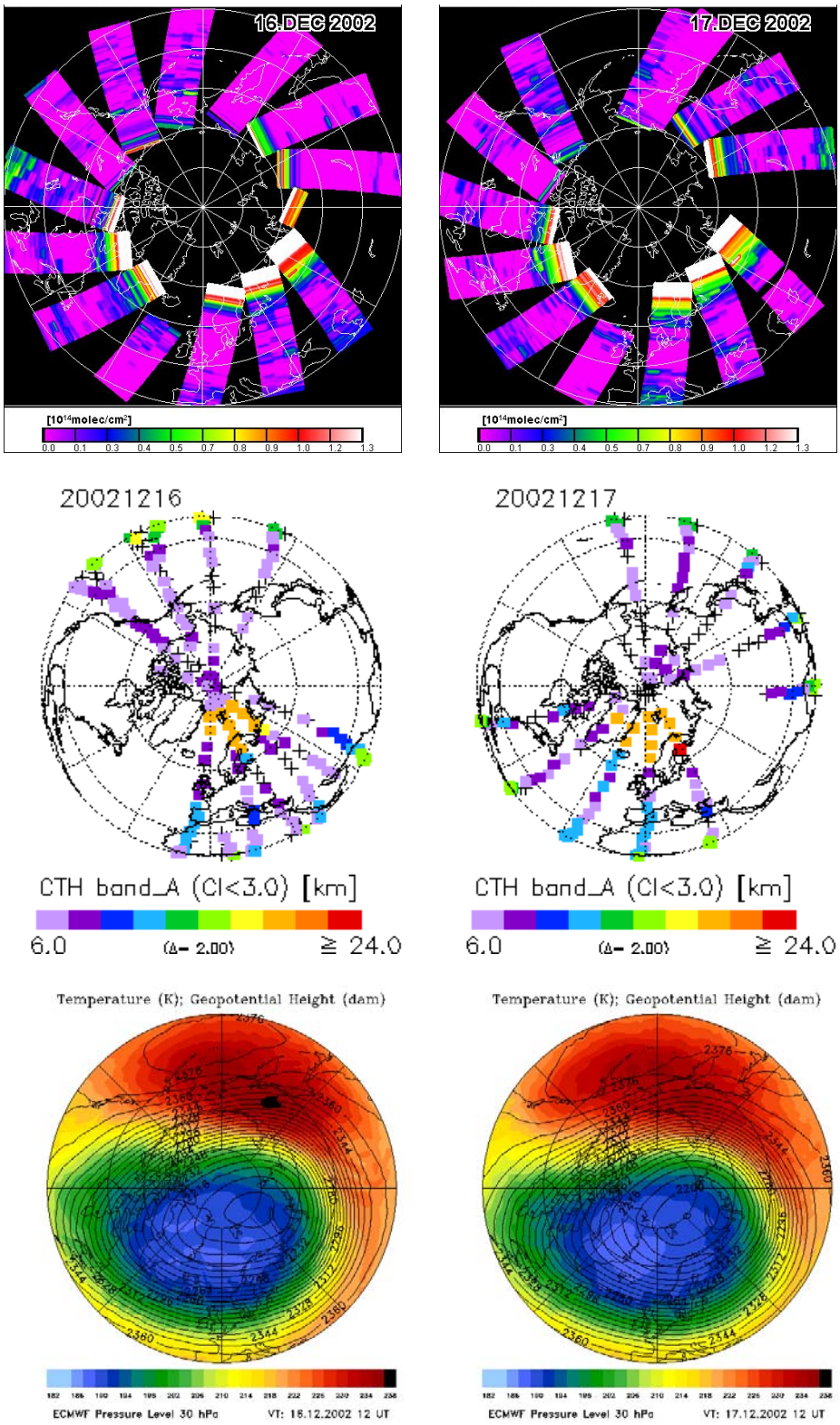

FIGURE 7.13: GOME OClO SCDs, MIPAS PSC observations and ECMWF temperatures at the 30 hPa level for 16th and 17th of December, 2002.

GOME OClO measurements reveal the mountain wave-induced chlorine activation, while MIPAS PSC observations show the formation of PSCs in the local temperature minima, see Figs. 7.13 and 7.14.

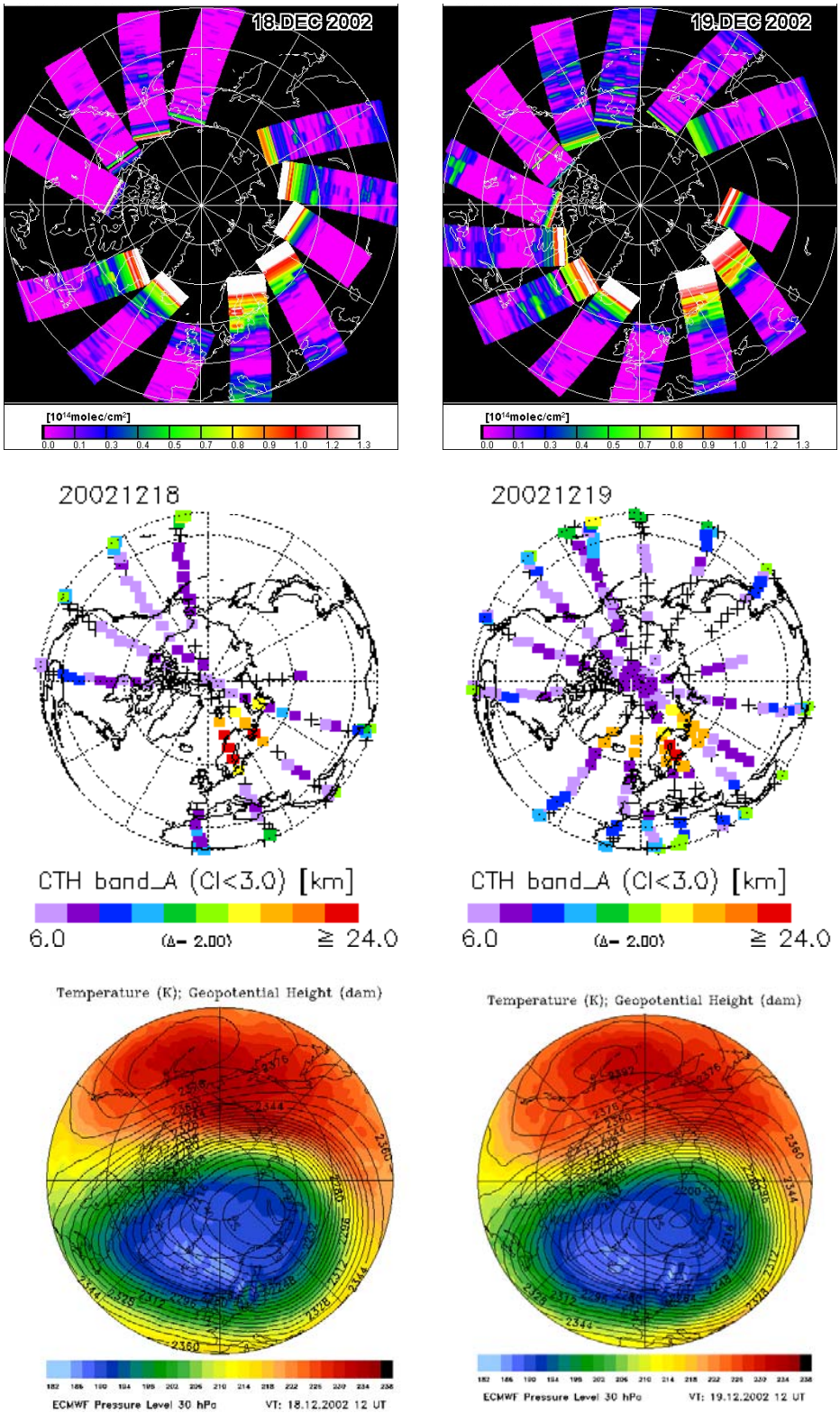

FIGURE 7.14: same as Fig. 7.13 but for 18th and 19th of December, 2002.

7.5 Implications for stratospheric chemistry

Carslaw et al. [1998] have shown that chlorine activation induced by mesoscale mountain wave PSCs leads to additional depletion of ozone. The mountain wave-induced enhancements of OClO, observed by GOME, discussed above take place in sunlit regions (75° < SZA < 85°). Therefore, the activation of chlorine immediately leads to effective ozone depletion by the catalytic cycles. Further destruction of ozone occurs when the activated air mass stays in or returns to areas exposed to sunlight, or if it remains activated until the end of the polar night. However, some of the air masses that are activated by mesoscale mountain wave events might also get activated on the synoptic scale until polar spring. Thus, chemical ozone loss will be increased compared to activation on the synoptic scale. Model studies based on synoptic scale temperature analyses tend to underestimate chlorine activation and ozone loss in the Arctic stratosphere [*Lutman et al.*, 1997; *Hansen et al.*, 1997; *Becker et al.*, 1998; *Woyke et al.*, 1999; *Becker et al.*, 2000]. The GOME OClO observations presented in this study give further reason to suggest that this discrepancy might partly be explained by chlorine activation on mesoscale mountain wave PSCs.

The eight year data set of GOME enables us to assess the frequency of the mountain wave induced rises in chlorine activation and thereby provides the opportunity to estimate their contribution to chlorine activation in the Arctic stratosphere during the time of GOME measurements. It is found that the observed increases in chlorine activation are concentrated in the month of January, when the activity of stratospheric mountain waves peaks [*Dörnbrack and Leutbecher, 2001*]. In most of the cases these rises appear in the lee of the Scandinavian mountain ridge, only few mountain wave induced enhancements of the OClO column densities were found for the East Greenland Coast and the Urals.

Due to the high annual variability of the Arctic stratosphere, the effect of mountain waves on chlorine activation is very different for each Arctic winter. For warm winters, when mountain waves can induce the formation of PSC type 1, the additional activation is localised to areas of 100.000 km^2 and is found to be moderate. In cold winters, when mountain waves lead to the formation of PSC type 2, the region of additional activation is much larger (up to 900.000 km^2) and almost complete activation of the chlorine species takes place.

These observations confirm the importance of mountain waves for chlorine activation that is not accounted for by synoptic temperature analyses [*Carslaw et al.*, 1998]. Model calculations of ozone loss presently do not include these mesoscale processes, which therefore are one possible explanation for the underestimation of chlorine activation and ozone loss in the Arctic stratosphere [*Lutman et al.*, 1997; *Woyke et al*., 1999; *Becker et al*., 2000]. It is remarkable that this discrepancy is highest in the month of January [*Becker et al*., 2000], when the activity of mountain waves has its maximum [*Dörnbrack and Leutbecher*, 2001] and thus increases in chlorine activation will be of the type reported here.

CONCLUSIONS

The satellite instruments GOME and SCIAMACHY made measurements of the spectral intensity of the sunlight, reflected by the Earths atmosphere, during the years 1995-2005.
By Differential Optical Absorption Spectroscopy, these spectra were analysed to derive column densities and vertical profiles of chlorine dioxide, OClO, an important indicator of stratospheric chlorine activation. In addition, also vertical profiles of ozone, nitrogen dioxide and bromine monoxide were derived from the SCIAMACHY measurements.

Utilizing this unique dataset, stratospheric chlorine activation and its relation to ozone chemistry was investigated. The derived abundances of OClO were discussed regarding their relation to meteorological parameters, other trace gases and their relevance for open questions in stratospheric chemistry.
By analysing the slant column densities of OClO during the polar winters 1995-2003, the interhemispheric differences in magnitude, spatial extension and duration of chlorine activation were revealed:
While the magnitude and the temporal evolution of chlorine activation show a large year to year variability in the Arctic stratosphere, they are very similar for every Antarctic winter. Furthermore, in the southern hemisphere the period of chlorine activation lasts approx. 2 months longer into polar spring, thereby substantially increasing the efficiency of the sunlight driven ozone depletion cycles.
The results agree with ground based measurements of OClO in the northern and southern hemisphere, which show the same magnitude and temporal evolution for the investigated winters.
The location of areas with enhanced active chlorine is largely impacted by the shape of the polar vortex, which is concentrically located around the south pole, while the northern counterpart is frequently deformed by planetary wave activity and often located above Northern Scandinavia.
To study the quality of OClO as an indicator of stratospheric chlorine activation, the GOME OClO measurements were compared to other observations of active chlorine species, in particular satellite measurements of ClO. The regions of air masses with enhanced active chlorine are in good accord and also the relative degree of chlorine activation, observed during winter and spring, is analogous. For most of the cases also the magnitude of the measured degree of chlorine activation was well correlated.

Furthermore, we studied the agreement of the satellite observations with model simulations of chlorine activation. The SLIMCAT results for ClO and OClO were compared to the GOME OClO observations for selected Arctic winters.
First, the comparison was performed qualitatively to verify if the onset of active chlorine, its evolution and its deactivation are correctly calculated by the model. Then, the GOME OClO SCDs were converted to VCDs by applying a chemical air mass factor. This enabled us to compare the observed and simulated OClO VCD also in a quantitative manner. While the qualitative comparison shows that the onset and duration of chlorine activation agrees, in particular for lower latitudes, the quantitative comparison reveals also significant differences. Especially for higher latitudes in early winter, the magnitude of the OClO VCD is substantially underestimated by the model.

This reveals the difficulties in calculating the OClO abundances accurately and comparing them to observations. However, the comparison might be a first step in determining the causes for known short-comings of the SLIMCAT simulations – like e.g. underestimation of chlorine activation and ozone loss in Arctic winters, and thereby improving the correct description of stratospheric chemistry and dynamics.

In various case studies we investigated the impact of stratospheric meteorology on the GOME OClO SCDs, the interaction with other trace gases and discussed the relevance for current questions regarding polar stratospheric ozone:

OClO SCDs observed by GOME at a solar zenith angle of 90 degrees for the cold Arctic winters 1996–2003 show significant enhancements only for temperatures below T_{NAT}, the threshold for PSC formation.
Accordingly the volume of possible PSC formation, V_{PSC}, is in good correlation to the sum of the OClO SCDs for the Arctic winters 1996 to 2003.

With the return of sunlight in polar spring, the amount and extent of heterogeneously processed air masses determines the chemical ozone depletion. Thus, the total ozone column in the northern polar regions observed by the GOME spectrometer in March reveals a strong anti-correlation to the sum of the OClO SCDs also observed by GOME in the corresponding polar spring (February to March). The correlation of the OClO SCDs to the chemical ozone loss is weaker, implying that ozone as well as OClO are also significantly impacted by stratospheric dynamics.

By investigating the decline of the OClO SCDs in Arctic spring, the time needed for deactivation of chlorine could be determined. It was found to be 14 and 16 days for the cold winters 1996 and 2000, during which PSC formation was possible over a wide altitude range and for a long time period, thereby enabling the sedimentation of HNO_3 containing particles. In warm winters with only small areas of PSC formation and thus only modest denitrification, the enhanced OClO SCDs disappear within 8 (1997) or 9 (2001) days. These deactivation times correlate to the level of denitrification calculated for the respective winters by model simulations. For the Antarctic stratosphere GOME OClO observations imply a chlorine deactivation time of 18-22 days, which is in accord with the high level of denitrification (80-100 %) occurring there in every winter.

For the strong mountain wave event above Northern Scandinavia during 20-22 January, 1997 the increase of chlorine activation due to mountain wave activity could be observed for the first time: In the centre of the mesoscale temperature anomaly the OClO SCDs increase from 0.5 to $1.8*10^{13}$ molec/cm^2. Combining the GOME OClO measurements with meteorological parameters (temperature, pressure, windspeed and -direction) from a mesoscale simulation, and applying current recommendations for chemical kinetics, the increase of the ClO mixing ratio during the time of the mountain wave activity could be estimated. For the largest observed OClO SCDs, it jumps from 0.8 ppbv on 20 January to 1.7 ppbv on 21 January for the altitude of 22 km. The area of significantly enhanced OClO columns is about 900.000 km^2. These results are in good agreement with previous model studies, where similar increases and additional areas of additional chlorine activation were calculated.

Similar increases of the GOME OClO SCDs, also correlated with strong mountain wave activity, are observed for the 31 January 1996, 20-27 January, 2000 and 18-20 December, 2002. In warmer winters, mountain wave induced activation is more moderate and localized. In the lee of the Scandinavian mountain ridge, enhancements of OClO due to mountain wave activity concentrates in the month of January, which is again in accord with model simulations and PSC sightings. For the East Greenland Coast and the Urals only few mountain wave induced enhancements of the OClO column densities were found.
The GOME OClO observations confirm the importance of stratospheric mountain waves for chlorine activation and subsequent ozone depletion that has been postulated by model studies. Due to their daily coverage of the polar regions they substantially contribute to quantify the impact of mountain wave activity on stratospheric chlorine and ozone chemistry. SCIAMACHY measurements of OClO will increase the information about the degree of chlorine activation due to its increased spatial resolution. In addition, the vertical extent of the chlorine activation and its relation to the mountain wave induced temperature minima and PSC formation can be studied by the vertical OClO profiles.

Thus, to continue the studies summarized above also using SCIAMACHY data, the retrieval of OClO SCDs from the SCIAMACHY nadir measurements has been optimised. As well, algorithms for the retrieval of vertical O_3, NO_2, BrO and OClO profiles from the SCIAMACHY limb measurements were developed.
First results of the retrieved OClO SCDs showed a good agreement with simultaneous GOME observations. For the extremely cold winter 2004/05, SCIAMACHY measurements reveal the strong activation of chlorine, in good agreement with results from the 4d VAR model BASCOE.
The vertical profiles retrieved from the limb measurements are consistent with expectations from atmospheric chemistry. The latitudinal and seasonal variation as well as the height of the maximum of the retrieved profiles are realistic. Selected profiles and latitudinal cross sections illustrating the vertical extent of ozone depletion, chlorine activation and denitrification were presented. Also, the vertical profiles were compared to other SCIAMACHY limb retrievals and showed a good agreement.
With accurate vertical profiles of OClO and related trace gases it is possible to investigate stratospheric chlorine chemistry in much more detail. The onset of chlorine activation can be related to the altitude at which T_{NAT} is reached and PSCs are formed. On the other hand, the deactivation of chlorine can be studied as function of the coinciding NO_2 profile. For the polar spring, the vertical extent of ozone loss can be compared to the altitude range of chlorine activated air masses. Also, it can be studied how well all these relations observed by SCIAMACHY can be described by model simulations, thereby testing the current understanding of stratospheric chlorine chemistry and its relation to ozone.

With the development of the algorithms for the retrieval of vertical profiles, the basis for these studies has been laid, which will probably largely contribute to increase our knowledge of stratospheric chemistry. With the already launched OMI and the scheduled GOME-2 instruments, the monitoring of chlorine activation can be maintained into the phase when total stratospheric chlorine substantially declines and cooling of the stratosphere increases due to the growing greenhouse effect.

References

Aliwell, S.R.et al.(2002), Analysis for BrO in zenith-sky spectra – an intercomparison exercise for analysis improvement, *J. Geophys. Res.*, *107*, doi: 10.1029/2001JD000329.

Anderson, J. G., W. H. Brune, and M. H. Proffitt (1989), Ozone destruction by chlorine radicals within the Antarctic vortex: The spatial and temporal evolution of ClO-O_3 anticorrelation based on *in situ* ER-2 data. *Journal of Geophysical Research* 94 (D): 11,465-79.

Anderson, J.G., D.W. Toohey, and W.H. Brune, Free Radicals within the Antarctic Vortex: The Role of CFCs in Antarctic Ozone Loss, Science 251, 39, 1991

Austin, J., N. Butchart, and K.P Shine (1992), Possibility of an Arctic ozone hole in a doubled-CO_2 climate, *Nature, 360*, 221-225.

Austin, J. et al. (2002), Uncertainties and assessments of chemistry-climate models of the stratosphere, *Atmos. Chem. Phys., Vol.3*, 1-27.

Backus, G.E. and J.F. Gilbert (1970), Uniqueness in the inversion of inaccurate gross earth data, *Phil. Trans. R. Soc. Lond., 266*, 123.

Banwell C.N., Fundamentals of Molecular Spectroscopy, McGraw Hill Book Company, Berkshire, 1994.

Bates, D.R. and Nicolet. M. (1950), The photochemistry of atmospheric water vapor, *J. Geophys. Res.*, 55, 301.

Becker, G., et al. (1998), Ozone loss rates in the Arctic stratosphere in the winter 1991/92: Model calculations compared with Match results, *Geophys. Res. Lett., 25*, 4325–4328.

Becker, G., R. Müller, D.S. Mc Kenna, M. Rex, and K.S. Carslaw (2000), Ozone loss rates in the Arctic stratosphere in the winter 1994/1995: Model simulations underestimate results of the Match analysis, *J. Geophys. Res.,105*, 15175-15184.

Becker, G., J.-U. Grooß, D. S. McKenna, and R. Müller (2000), Stratospheric photolysis frequencies: Impact of an improved numerical solution of the radiative transfer equation, *J. Atm. Chem., 37*, 217-229.

Benson, S.W. and A.E. Axworthy, (1965), Reconsiderations of the rate constants from the thermal decomposition of ozone, *J. Chem. Phys., 42*, 2614.

Bliefert (2002), Umweltchemie, Wiley-VCH, Weinheim.

Bodeker, G.E., J.C. Scott, K. Kreher, and R.L McKenzie (2001), Global ozone trends in potential vorticity coordinates using TOMS and GOME intercompared against the Dobson network: 1978-1998, *J. Geophys. Res.,106*, 23029-23042.

Bogumil, K., J. Orphal und J. P. Burrows (2000), Temperature dependent absorption cross sections of O_3, NO_2, and other atmospheric trace gases measured with the SCIAMACHY spectrometer, Proceedings of the ERS - Envisat - Symposium, Goteborg, Sweden.

Bohren, C. and D.R. Huffman (1983), Absorption and scattering of light by small particles, John Wiley & Sons Inc., New York.

Borrmann, S., S. Solomon, J.E. Dye, and B. Luo (1996), The potential of cirrus clouds for heterogeneous chlorine activation, *Geophys. Res. Lett., 23*, 2133–2136.

Borrmann, S., S. Solomon, J. E. Dye, D. Baumgardner, K. K. Kelly, K. R. Chan (1997), Heterogeneous reactions on stratospheric background aerosols, volcanic sulfuric acid droplets, and type I polar stratospheric clouds: Effects of temperature fluctuations and differences in particle phase, *J. Geophys. Res.,102*, 3639-3648, doi:10.1029/96JD02976.

Bovensmann, H., J.P. Burrows, M. Buchwitz, J. Frerick, S. Noel, V.V. Rozanov, K.V. Chance and A.P.H. Goede (1999), SCIAMACHY: Mission objectives and measurement modes, *J. Atmos. Sci*., 56, 127

Brasseur, G. and S. Solomon. (1984), Aeronomy of the Middle Atmosphere, Reidel, Dordrecht.

Brewer, A.W. (1949), Evidence for a world circulation provided by the measurements of helium and water vapor distribution in the stratosphere, *Q.J.R. Meteorol. Soc., 75*, 351-361.

Brune, W.H., J.G. Anderson, D.W. Toohey, D.W.Fahey, S.R. Kawa, R.L. Jones, D.S. McKenna, and L.R. Poole, The Potential for Ozone Depletion in the Arctic Polar Stratosphere, Science 252, 1260, 1991

Burrows, J. P., A. Dehn, B. Deters, S. Himmelmann, A. Richter, S. Voigt, and J. Orphal (1998), Atmospheric Remote-Sensing Reference Data from GOME: 1. Temperature-Dependent Absorption Cross Sections of NO_2 in the 231-794 nm Range, J*ournal of Quantitative Spectroscopy and Radiative Transfer 60*, 1025-1031.

Burrows, J.P. et al. (1999), The Global Ozone Monitoring Experiment (GOME): Mission Concept and First Scientific Results, *J. Atmos. Sci., 56*, 151-175.

Bussemer, M. (1993), Der Ring-Effekt: Ursachen und Einfluß auf die spektroskopische Messung stratosphärischer Spurenstoffe, Diploma thesis, University of Heidelberg.

Cadle, R.D., P. Crutzen, and D. Ehhalt (1975), Heterogeneous chemical reactions in the stratosphere, *J. Geophys. Res., 80*, 3381-3385.

Canty, T., et al. (2005), Nighttime OClO in the winter Arctic vortex, *J. Geophys. Res., 110*, D01301, doi:10.1029/2004JD005035.

Carslaw, K.S. (1994), Stratospheric aerosol growth and HNO_3 gas phase depletion from coupled HNO_3 and water uptake by liquid particles, *Geophys. Res. Letts*., 21, 2479-2482.

Carslaw, K.S., and T. Peter (1997), Uncertainties in reactive uptake coefficients for solid stratospheric particles – 1. Surface chemistry, *Geophys. Res. Letts*., 24, 1743

Carslaw, K.S. et al. (1998), Increased stratospheric ozone depletion due to mountain-induced atmospheric waves, *Nature, 91,* 675-678.

Carslaw, K.S. et al. (1999a), Widespread solid particle formation by mountain waves in the Arctic stratosphere, *J. Geophys. Res.,104*, 1827-1836.

Carslaw, K.S. et al. (1999b), in: Mesoscale Processes in the Stratosphere – Their effect on stratospheric chemistry and microphysics, Air Pollution Research Report No. 69.

Chapman, S. (1930), A theory of upper atmospheric ozone, *Mem. R. Soc., 3*, 103-125.

Chipperfield, M., Multiannual simulations with a three-dimensional chemical transport model (1999), *J. Geophys. Res*., *104*, 1781-1805.

Chipperfield, M.P and J.A. Pyle (1998), Model sensitivity studies of Arctic ozone depletion, *J. Geophys. Res., 103*, 28389-28403.

Chubachi, S. (1984), Preliminary result of ozone observations at Swoya station from February, 1982 to January, 1983, *Mem. Natl. Inst. Polar Res. Jpn. Spec. Issue, 34*, 13-20.

Coy, L., E.R. Nash and P.A. Newman (1997), Meteorology of the polar vortex: Spring 1997, *Geophys. Res. Lett., 24*, 2693-2696.

Crutzen, P.J. (1970), The influence of nitrogen oxides on the atmospheric ozone content, *Q.J.R. Meteorol. Soc., 96*, 320-325.

Crutzen, P.J. and F. Arnold (1986), Nitric acid cloud formation in the cold Antarctic stratosphere: A major cause for the springtime 'ozone hole', *Nature, 324*, 651-655.

Dameris, M., M. Wirth, W. Renger, and V. Grewe (1995), Definition of the polar vortex edge by lidar data of the stratospheric aerosol: a comparison with values of potential vorticity, *Beitr. Phys. Atmosph., 68*, 113-119.

Daniel, J.S., S. Solomon, R.W. Portmann, R.R. Garcia (1999), Stratospheric ozone destruction: The importance of bromine relative to chlorine, *J. Geophys. Res*., 104, 23871

de Gruijl et al. (2003), Health effects from stratospheric ozone depletion and interactions with climate change, *Photochem. Photobiol. Sci., 2*, 16-28.

Deshler, T., T. Peter, R.Müller and P. Crutzen (1994), The lifetime of leewave-induced particles in the Arctic stratosphere: I. Ballonborne Observations, *Geophys. Res. Lett., 21,* 1327-1330.

Deshler, T., N. Larsen, et al. (2003), Large nitric acid particles at the top of an Arctic stratospheric cloud, *J. Geophys. Res*., 108, 4517, doi:101029/2003JD003479

Dessler et al. (1996), A test of the partitioning between ClO and $ClONO_2$ using simultaneous UARS measurements of ClO, NO2, and $ClONO_2$, *J. Geophys. Res., 101(D7),* 12,515–12,522.

de Zafra et al. (1987), High concentrations of chlorine monoxide at low altitudes in the Antarctic spring stratosphere: Diurnal variation, *Nature, 328*, 408-411.

de Zafra et al. (1989), New observations of a large concentration of ClO in the springtime lower stratosphere over Antarctica and its implications for ozone-depleting chemistry, *J. Geophys. Res., 94*, 11423-11428.

Dobson, G.M.B. (1930), Observations of the amount of ozone in the Earth's atmosphere and its relation to other geophysical conditions, *Proc. R. Soc. London, Ser. A., 129*, 411.

Dörnbrack, A., M. Leutbecher, R. Kivi and E. Kyrö (1999), Mountain-wave induced record low stratospheric temperatures above northern Scandinavia, *Tellus, 51A*, 951-963.

Dörnbrack, A. et al. (2001), Relevance of mountain wave cooling for the formation of polar stratospheric clouds over Scandinavia: Mesoscale dynamics and observations for January 1997, *J. Geophys. Res., 106*, 1569-1581.

Dörnbrack, A. and M. Leutbecher (2001), Relevance of mountain wave cooling for the formation of polar stratospheric clouds over Scandinavia: A 20 year climatology, *J. Geophys. Res., 106*, 1583-1593.

Dörnbrack, A. et al. (2002), Evidence for inertia gravity waves forming polar stratospheric clouds over Scandinavia, *J. Geophys. Res., 107,* 10.1029/2001JD000452.

Douglass et al. (1995), Interhemispheric differences in springtime production of HCl and ClONO2 in the polar vortices, *J. Geophys. Res., 100*,13967-13978.

Drdla, K., and M.R. Schoeberl (2003), Microphysical modeling of the 1999-2000 Arctic winter 2. Chlorine activation and ozone depletion, *J. Geophys. Res., 108*, 10.1029/2001JD001159.

Dudhia, J. (1993), A non-hydrostatic version of the Penn State—NCAR Mesoscale Model: Validation tests and simulation of an Atlantic cyclone and cold front. *Mon. Weather Rev., 121*, 1493-1513.

Dudhia, J., D. Gill, Y.-R. Guo, K. Manning, and W. Wang (2001), *PSU/NCAR Mesoscale Modeling System Tutorial Class Notes and User Guide: MM5 Modeling System Version 3*. Also http://www.mmm.ucar.edu/mm5/doc.html.

Enell, C., A. Steen, T. Wagner, U. Frieß, K. Pfeilsticker, U. Platt and K.-H. Fricke (1999), Occurrence of polar stratospheric clouds at Kiruna, *Ann. Geophys., 17*, 1457-1462.

Engel, A., M. Strunk, M. Müller, H.-P. Haase, C. Poss, I. Levin, U. Schmidt (2002), Temporal development of total chlorine in the high-latitude stratosphere based on reference distributions of mean age derived from CO_2 and SF_6, *J. Geophys. Res., 107*, 4136, 10.1029/2001JD000584.

European Centre for Medium-Range Weather Forecasts (ECMWF) (2000), Temperature and potential vorticity analyses, Dan. Meteorol. Inst., Copenhagen.

Evans, W.F.J., C.T. McElroy, and I.E. Galbally (1985), The Conversion of N_2O_5 to HNO_3 at High Latitudes in Winter, *Geophys. Res. Lett., 12*, 825, 1985.

Farman, J.C., B.G. Gardiner, and J.D. Shanklin (1985), Large losses of total ozone in Antarctica reveal seasonal ClO_x/NO_x interaction, *Nature, 315*, 207-210.

Fioletov et al. (2002), The global ozone and zonal total ozone variations estimated from ground-based and satellite measurements: 1964-2000, *J. Geophys. Res., 107,* D22, 4647, doi.:10.1029/2001JD001350.

Fish, D.J. (1994), Measurements of stratospheric composition using ultraviolet and visible spectroscopy, PhD thesis, University of Cambridge.

Fish, D.J., and R.L. Jones (1995), Rotational Raman scattering and the Ring effect in zenith-sky spectra, *Geophys. Res. Lett., 22*, 811-814.

Fitzenberger, R. (2001), Investigation of the Stratospheric Inorganic Bromine Budget for 1996-2000: Balloon-Borne Measurements and Model Comparisons, Ph.D.-Thesis, University of Heidelberg, Heidelberg, Germany.

Flentje, H. et al. (2002), Denitrification inside the Stratospheric Vortex in the Winter 1999/2000 by Sedimentation of large Nitric Acid Trihydrate Particles, *J. Geophys. Res., 107*, D16, doi.:10.1029/2001JD001015.

Fricke, K.-H., K.P. Müller, G. Baumgarten and J. Siebert (1997), Presentation at the 7th Statusseminar des Ozonforschungsprogramm, July 1997, Bonn.

Goody R.M. and Y.L. Yung (1991), Atmospheric radiation, Oxford University Press, Oxford.

Grainger, J.F., and J. Ring (1962), Anomalous Fraunhofer line profiles, *Nature, 193*, 762.

Greenblatt G. D., J.J. Orlando, J.B. Burkholder, and A.R. Ravishankara (1990), Absorption measurements of oxygen between 330 and 1140 nm, *J. Geophys. Res., 95*, 18577-18582.

Grooß, J.-U., R. B. Pierce, P. J. Crutzen, W. L. Grose, and I. Russell, J. M., Re-formation of chlorine reservoirs in southern hemisphere polar spring, *J. Geophys. Res., 102*, 13141-13152, 1997.

Hansen, G., T. Svenoe, M.P. Chipperfield, A. Dahlback and U.-P. Hoppe (1997), Evidence for substantial ozone depletion in winter 1995/96 over northern Norway, *Geophys. Res. Lett., 24*, 799-802.

Hanson, D. and K. Mauersberger (1988), Laboratory studies of the nitric acid trihydrate: implications for the south polar stratosphere, *Geophys. Res. Lett., 15*, 855-858.

Harder, H., C. Camy-Peyret, F. Ferlemann, R. Fitzenberger, T. Hawat, H. Osterkamp, M. Schneider, D. Perner, U. Platt, P. Vradelis, K. Pfeilsticker (1998), Stratospheric BrO profiles measured at different latitudes and seasons: Atmospheric observations, *Geophys. Res. Lett., 25*, 3843-3846, doi:10.1029/1998GL900026.

Hare, S. H. E., L. J. Gray, W. A. Lahoz, A. O'Neill, and L. Steenman-Clark (2004), Can stratospheric temperature trends be attributed to ozone depletion ?, *J. Geophys. Res., 109*, D05111, doi:10.1029/2003JD003897.

Hönninger, G. (2002), Halogen Oxide Studies in the Boundary Layer by Multi Axis Differential Optical Absorption Spectroscopy and Active Longpath-DOAS, PhD thesis, University of Heidelberg.

Hofmann, D.J., J.W. Harder and J.M. Rosen (1989), Ozone Profile Measurements at McMurdo Station, Antarctica, During the Spring of 1987, *J. Geophys. Res*., 94, 16527.

Hitchman, M. H.; M. L. Buker, G.J. Tripoli, E. V. Browell, W. B. Grant, T. J. McGee, J. F. Burris (2003), Nonorographic generation of Arctic polar stratospheric clouds during December 1999, *J. Geophys. Res., 108*, doi:10.1029/2001JD001034.

Huppert, R. (2000), Theoretische und experimentelle Untersuchungen zum solaren I_0-Effekt, Diploma thesis, Institut für Umweltphysik, Universität Heidelberg.

Jacobson, M.Z.: Fundamentals of atmospheric modelling, Cambridge University Press, Cambridge, 1999.

Johnston, H.S. (1971), Reduction of stratospheric ozone by nitrogen oxide catalysts from supersonic transport exhaust, Science, 173, 517-522.

Koop, T., K.S. Carslaw, and T. Peter (1997), Thermodynamic stability and phase transitions of PSC particles, *Geophys. Res. Lett., 24*, 2199-2202.

Kraus, H. (2001): Die Atmosphäre der Erde, Springer, Berlin.

Kraus, S. (2004), Entwicklung eines flexiblen Softwaresystems zur Auswertung spektroskopischer Satelliten-Bildsequenzen, PhD thesis, Technische Informatik, Universität Mannheim.

Kühl, S., T. Wagner, W. Wilms-Grabe, et al. and U. Platt (2002), Stratospheric Chlorine Activation derived from GOME OClO Measurements - Case Studies and Comparison to SLIMCAT model results, *Air pollution research report 79*, Proceedings of the Sixth European Symposium on Stratospheric Ozone, Göteborg, Sweden, 2002, available under: http://www.ozone-sec.ch.cam.ac.uk/EORCU/goteborg.html

Kühl, S., W. Wilms-Grabe, S. Beirle, C. Frankenberg, M. Grzegorski, J. Hollwedel, F. Khokhar, S. Kraus, U. Platt, S. Sanghavi, C. von Friedeburg and T. Wagner (2004), Stratospheric Chlorine Activation in the Arctic winters 1995/96 to 2001/02 derived from GOME OClO Measurements, *Adv. Space Res., 34*, 798-803.

Kühl, S., A. Dörnbrack, W. Wilms-Grabe, B.-M. Sinnhuber, U. Platt, and T. Wagner (2004), Observational evidence of rapid chlorine activation by mountain waves above northern Scandinavia, *J. Geophys. Res., 109*, D22309, doi:10.1029/2004JD004797.

Labitzke, K. (1999), Die Stratosphäre, Springer, Berlin.

Larsen, N. (2000), Polar Stratospheric Clouds – Microphysical and optical models, Danish Meteorological Institute Scientific Report 00-06, Copenhagen.

Lary, D.J., and J.A. Pyle (1991), Diffusive radiation, twilight and photochemistry, *J. Atmos. Chem., 13*, 373-392.

Lee, A.M., R.L. Jones, I. Kilbane-Dawe, and J.A. Pyle (2002), Diagnosing ozone loss in the extratropical lower stratosphere, *J. Geophys. Res*., 107, 4110, doi: 10.1029/2001JD000538

Lefèvre, F., F. Figarol, K.S. Carslaw, T. Peter (1998), The 1997 Arctic ozone depletion quantified from three-dimensional model simulations, *Geophys. Res. Lett., 25*, 2425-2428.

Leue, C. (1999), Globale Bilanzierung der NOx-Emissionen aus GOME Satelliten-Bildfolgen, PhD thesis, University of Heidelberg.

Leutbecher, M. and H. Volkert (1996), Stratospheric temperature anomalies and mountain waves: A three-dimensional simulation using a multi-scale weather prediction model, *Geophys. Res. Lett., 27*, 3329-3332.

Leutbecher, M. and H. Volkert (2000), The propagation of mountain waves into the stratosphere: quantitative evaluation of three-dimensional simulations, *J. Atmos. Sci., 57*, 3090-3108.

Levenberg, K. (1944), A method for the solution of certain non-linear problems in least squares, *Quart. Appl., Math., 2*, 164-168.

Logan, J. A., et al. (1999), Trends in the vertical distribution of ozone: A comparison of two analyses of ozonesonde data, *J. Geophys. Res., 104(D21)*, 26,373–26,400.

Lutman, E.R. et al. (1997), Three-dimensional studies of the 1991/1992 northern hemisphere winter using domain-filling trajectories with chemistry, *J. Geophys. Res., 102*, 1479-1488.

Mann, G.W., S. Davies, K. S. Carslaw, and M. P. Chipperfield (2003), Factors controlling Arctic denitrification in cold winters of the 1990s, Atmos. Chem. Phys., 3, 403–416.

Mann, G. W., K. S. Carslaw, M. P. Chipperfield, S. Davies, and S. D. Eckermann (2005), Large nitric acid trihydrate particles and denitrification caused by mountain waves in the Arctic stratosphere, *J. Geophys. Res., 110*, D08202, doi:10.1029/2004JD005271.

Manney, G.L., L. Froidevaux, M.L. Santee, R.W. Zurek, and J.W. Waters (1997), MLS observations of Arctic ozone loss in 1996-97, *Geophys. Res. Lett., 24*, 2697-2700.

Marquardt, D.W. (1963), An algorithm for least-squares estimation of nonlinear parameters, *J. Soc. Indust. Math., 11*, 431-441.

Marquard, L.C. (1998), Modellierung des Strahlungstransports in der Erdatmosphäre für absorptionsspektroskopische Messungen im ultravioletten und sichtbaren Spektralbereich, PhD thesis, University of Heidelberg.

Marquard, L.C., T. Wagner and U. Platt (2000), Improved air mass factor concepts for scattered radiation differential optical absorption spectroscopy of atmospheric species, *J. Geophys. Res., 105*, 1315-1327.

Martin, R. V., et al. (2002), An improved retrieval of tropospheric nitrogen dioxide from GOME, *J. Geophys. Res., 107(D20)*, 4437, doi:10.1029/2001JD001027.

McCormick, M.P. et al. (1982), Polar stratospheric cloud sightings by SAM II, *J. Atm. Sci., 39*, 1387-1397.

Mc Elroy, M.B., R.J. Salawitch, S.C. Wofsy and J.A. Logan (1986), Reductions of Antarctic ozone due to synergistic interactions of chlorine and bromine, *Nature, 321*, 759-762.

McKinney, K.A., J.M. Pierson, and D.W. Toohey (1997), A wintertime in situ profile of BrO between 17 and 27 km in the Arctic vortex, *Geophys. Res. Lett., 24*, 853-856.

Menke (1999), Geophysical data analysis: discrete inverse theory, Academic Press.

Michelsen, H.A., et al. (1996), Stratospheric chlorine partitioning: Constraints from shuttle-borne measurements of HCl, $ClNO_3$ and ClO, *Geophys. Res. Lett., 23*, 2361-2364.

Millard, G. A., A. M. Lee, and J. A. Pyle (2002), A model study of the connection between polar and midlatitude ozone loss in the Northern Hemisphere lower stratosphere, *J. Geophys. Res., 108(D5)*, 8323, doi:10.1029/2001JD000899.

Molina, M.J and F.S. Rowland (1974), Stratospheric sink for chloroflouromethanes: chlorine-atom catalysed destruction of ozone, *Nature, 249*, 810-812.

Molina, L.T. and M.J. Molina (1987), Production of Cl_2O_2 from the self reaction of the ClO radical, *J. Chem. Phys., 91*, 433-436.

Montzka et al. (1996), Decline in the tropospheric abundance of halogen from halocarbons: Implications for stratospheric ozone depletion, *Science, 272*, 1318-1322.

Müller, R., J.-U. Grooß, D.S. McKenna, P.J. Crutzen, C. Brühl, J.M. Russel III, A. F. Tuck, HALOE observations of the vertical structure of chemical ozone depletion in the Arctic vortex during winter and early spring 1996-1997, *Geophys. Res. Lett., 24*, 2717-2720.

Newman, P.A., J.F. Gleason, R.D. McPeters and R.S. Stolarski (1997), Anomalously low ozone over the Arctic, *Geophys. Res. Lett., 24*, 2689-2692.

Noël, S., H. et al. (2002), Nadir, limb, and occultation measurements with SCIAMACHY, *Adv. Space Res., 29, (11)*, 1819-1824.

Ottoy, J., and G. Vansteenkiste (1981), A computer algorithm for non-linear curve fitting, *Adv. Eng. Software, 3*, 55-61.

Pagan, K. L., A. Tabazadeh, K. Drdla, M. E. Hervig, S. D. Eckermann, E. V. Browell, M. J. Legg, and P. G. Foschi (2004), Observational evidence against mountain-wave generation of ice nuclei as a prerequisite for the formation of three solid nitric acid polar stratospheric clouds observed in the Arctic in early December 1999, *J. Geophys. Res., 109*, D04312, doi:10.1029/2003JD003846.

Pawson, S. et al. (1995), On the polar stratospheric cloud formation potential of the northern stratosphere, *J. Geophys. Res., 100*, 23,215-23,225.

Pawson, S., B. Naujokat (1999), The cold winters of the middle 1990s in the northern lower stratosphere, *J. Geophys. Res., 104*, 12,209-12,222.

Peter, T. (1997), Microphysics and heterogeneous chemistry of polar stratospheric clouds, *Annu. Rev. Phys. Chem., 48*, 785-822.

Pierson, J. M. et al. (1999), An Investigation of ClO Photochemistry in the Chemically Perturbed Arctic Vortex, *J. Atm. Chem., 32*, 61-81.

Platt, U., D. Perner und H. Pätz (1979), Simultaneous measurements of atmospheric CH_2O, O_3 and NO_2 by differential optical absorption. *J. Geophys.Res., 84*, 6329-6335.

Platt, U. (1994), Differential Optical Absorption Spectroscopy (DOAS), in *Air Monitoring by Spectroscopic Techniques*, edited by M. W. Sigrist, Chemical Analysis Series Vol. 127, John Wiley, New York.

Platt, U., L. Marquard, T. Wagner and D. Perner (1997), Corrections for zenith scattered light DOAS, *Geophys. Res. Lett., 24*, 1759-1762.

Platt, U., J. Stutz (2005), Differential Optical Absorption Spectroscopy. Principles and applications, Springer, Berlin.

Pommerau, J.-P. and J. Piquard (1994), Observations of the vertical distribution of stratospheric OClO, *Geophys. Res. Lett., 21*, 1231-1234.

Poole, L.R. and M.P. McCormick (1988), Polar stratospheric clouds and the Antarctic ozone hole, *J. Geophys. Res., 93*, 8,423-8,430.

Portmann, R.W. et al. (1996), Role of aerosol variations in anthropogenic ozone depletion in polar regions, *J. Geophys. Res., 101*, 22,991-23,006.

Randel, W.J. and F.J. Wu (1999), Cooling of the Arctic and Antarctic polar stratospheres due to ozone depletion, J. Climate, 12, 1467.

Ravishankara, A.R. and D.R. Hanson (1996), Differences in the reactivity of type 1 PSCs depending on their phase, *J. Geophys. Res., 101*, 3,885-3,890.

Rex, M. et al. (2003), On the unexplained stratospheric ozone losses during cold Arctic Januaries, *Geophys. Res. Lett., 30* (1), 1008, doi:10.1029/2002GL016008.

Rex, M., R. J. Salawitch, P. von der Gathen, N. R. P. Harris, M. P. Chipperfield, and B. Naujokat (2004), Arctic ozone loss and climate change, *Geophys. Res. Lett., 31*, L04116, doi:10.1029/2003GL018844.

Richter, A. et al. (1999), Validation of GOME O3, NO2, BrO and OClO Measurements in Southern High Latitudes, *Fifth European Workshop on Stratospheric Ozone*, St. Jean de Luz, France. Available under http://www.ozone-sec.ch.cam.ac.uk/EORCU/Workshops/Fifthproc.html

Richter, A., F. Wittrock, M. Weber, S. Beirle, S. Kühl, U. Platt, T. Wagner, W. Wilms- Grabe and J.P. Burrows (2004), GOME observations of stratospheric trace gas distributions during the splitting vortex event in the Antarctic winter 2002 Part I: Measurements, *J. Atm. Sci., 62*, 778-785.

Rivière et al. (2000), Role of lee waves in the formation of polar stratospheric clouds: Case Studies from February 1997, *J. Geophys. Res., 105*, 6845-6853.

Rodgers, C.D. (2000), Inverse methods for atmospheric sounding. Theory and practice, World Scientific Publishing Co. Ltd., Singapore.

Roedel, W.: Physik unserer Umwelt: Die Atmosphäre, Springer, Berlin, 2002

Russel, J.M. III et al. (1996), Satellite confirmation of the dominance of chlorofluorocarbons in the global stratospheric chlorine budget, *Nature, 379*, 526-529.

Sander, S.P. and R.R. Friedl (1989), Kinetics and Product Studies of the Reaction ClO + BrO Using Flash Photolysis-Ultraviolet Absorption, *J. Phys. Chem., 93*, 4764-4771.

DeMore, Sander, S.P. et al. (1997) Chemical kinetics and photochemical data for use in stratospheric modeling, evaluation 12, *JPL Publ.97-4.*

Salawitch, R. J., D. K. Weisenstein, L. J. Kovalenko, C. E. Sioris, P. O. Wennberg, K. Chance, M. K. W. Ko, and C. A. McLinden (2005), Sensitivity of ozone to bromine in the lower stratosphere, Geophys. Res. Lett., 32, L05811, doi:10.1029/2004GL021504.

Sander, S.P. et al. (2000), Chemical kinetics and photochemical data for use in stratospheric modeling, evaluation 14, *JPL Publ. 02-25.*

Sander, S.P. et al. (2003), Chemical kinetics and photochemical data for use in stratospheric modeling, evaluation 14, *JPL Publ. 02-25.*

Santee, M.L., W.G. Read, J.W. Waters, L. Froidevaux, G.L. Manney, D.A. Flower, R.F. Jarnot, R.S. Harwood, and G.E. Peckham (1995), Interhemispheric differences in polar stratospheric HNO_3, H_2O, ClO, and O_3, Science, 267, 849-852

Santee, M.L., G.L. Manney, L. Froidevaux, R.W. Zurek, and J.W. Waters (1997), MLS observations of ClO and HNO_3 in the 1996-97 Arctic polar vortex, *Geophys. Res. Lett., 24*, 2713-2716.

Santee, M.L., G.L. Manney, J.W. Waters and N.J. Livesey (2003), Variations and climatology of ClO in the polar lower stratosphere from UARS Microwave Limb Sounder measurements, *J. Geophys. Res*., *108*, 4454, doi:10.1029/2002JD003335

Schiller, C. (1990), Spektroskopische Beobachtungen der Gesamtsäulendichte stratosphärischer Spurengase, Dissertation, Forschungszentrum Jülich.

Schiller, C. and A. Wahner (1996), Comment on 'Stratospheric OClO Measurements as a poor quantitative indicator of chlorine activation' by J. Sessler, M.P. Chipperfield, J.A. Pyle and R. Toumi, *Geophys. Res. Lett., 23*, 1053-1054.

Schmidt, U., R. Bauer, A. Engel, R. Borchers, J.Lee (1994), The variation of available chlorine, Cl_y, in the Arctic polar vortex during EASOE, *Geophys. Res. Letts., 21*, 1215-1218.

Schoeberl, M.R. et al. (1996), Development of the Antarctic ozone hole, *J. Geophys. Res., 101*, 20909-20924.

Schreiner, J. et al. (2003), Chemical, microphysical and optical properties of polar stratospheric clouds, *J. Geophys. Res., 108*(D5), 8313, doi:10.1029/2001JD000825.

Seinfeld J.H. and Pandis, S.N., Atmospheric Chemistry and Physics, John Wiley, Chichester, 1998

Sessler, J., M.P. Chipperfield, J.A. Pyle and R. Toumi (1995), Stratospheric OClO Measurements as a poor quantitative indicator of chlorine activation, *Geophys. Res. Lett., 22*, 687-690.

Sessler, J., M.P. Chipperfield, J.A. Pyle and R. Toumi (1996), Reply to Schiller, C. and A. Wahner (1996), *Geophys. Res. Lett., 23*, 1055.

Sierk, B., A. Richter, A. Rozanov, Ch. von Savigny, A.M. Schmoltner, M. Buchwitz, H. Bovensmann, and J.P. Burrows (2004), Retrieval and Monitoring of atmospheric trace gas concentrations in nadir and limb geometry using the space-borne SCIAMACHY instrument, presented at the "5th International Symposium on Advanced Environmental Monitoring", submitted to "Environmental Monitoring and Assessment".

Sinnhuber, B.-M., et al. (2002), Comparison of measurements and model calculations of stratospheric bromine monoxide, *J. Geophys. Res., 107*(D19), 4398, doi:10.1029/2001JD000940.

Solomon, S., R.R. Garcia, F.S. Rowland, D.J. Wuebbles (1986), On the depletion of Antarctic ozone, *Nature*, 321, 755-758

Solomon, S., G.H. Mount, R.W. Sanders and A.L. Schmeltekopf (1987a), Visible Spectroscopy at McMurdo Station, Antarctica 2. Observations of OClO, *J. Geophys. Res., 92,* 8329-8338.

Solomon, S., A.L. Schmeltekopf and R.W. Sanders (1987b), On the interpretation of zenith sky absorption measurements, *J. Geophys. Res., 92,* 8311-8319.

Solomon, S., R.W. Sanders and H.L. Miller (1990), Visible and Near-Ultraviolet Spectroscopy at McMurdo Station, Antarctica 7. OClO Photochemistry and Ozone destruction, *J. Geophys. Res., 95,* 13807-13817.

Solomon, S., R. W. Portmann, R. R. Garcia, L. W. Thomason, L. R. Poole, and M. P. McCormick (1996), The role of aerosol variations in anthropogenic ozone depletion at northern midlatitudes, *J. Geophys. Res., 101(D3),* 6713–6728.

Solomon, S., S. Bormann, R. R. Garcia, R. Portmann, L. Thomason, L. R. Poole, D. Winker, and M. P. McCormick (1997), Heterogeneous chlorine chemistry in the tropopause region, *J. Geophys. Res., 102(D17),* 21,411–21,430.

Solomon, S. (1999), Stratospheric Ozone Depletion: A Review of Concepts and History, *Reviews of Geophysics, 37*(3), 275-316.

Solomon, P., B. Connor, J. Barrett, T. Mooney, A. Lee, and A. Parrish (2002), Measurements of stratospheric ClO over Antarctica in 1996-2000 and implications for ClO dimer chemistry, *Geophys. Res. Lett., 29*(15), 10.1029/2002GL015232.

Stein, B. et al. (1999), Optical classification, existence temperatures, and coexistence of different polar stratospheric cloud types, *J. Geophys. Res., 104,* 23983 – 23993.

Stimpfle, R.M. et al. (1999), The coupling of $ClONO_2$, ClO, and NO_2 in the lower stratosphere from in situ observations using the NASA ER-2 aircraft, *J. Geophys. Res. 104,* 16,649-16663.

Stimpfle, R. M., D. M. Wilmouth, R. J. Salawitch, and J. G. Anderson (2004), First measurements of ClOOCl in the stratosphere: The coupling of ClOOCl and ClO in the Arctic polar vortex, *J. Geophys. Res., 109,* D03301, doi:10.1029/2003JD003811.

Stolarski, R.S. and Cicerone, R.J. (1974), Stratospheric chlorine: A possible sink for ozone, *Canad. J. Chem.*, 52, 1610-1615.

Stolarski, R.S. et al. (1986), Nimbus 7 Satellite measurements of the springtime Antarctic ozone decrease, *Nature, 322,* 808-811.

Stutz, J., and U. Platt (1996), Numerical analysis and error estimation of Differential Optical Absorption Spectroscopy measurements least-squares methods, *Appl. Opt., 35,* 6041-6053.

Tabazadeh et al. (1994), A study of Type I polar stratospheric cloud formation, *Geophys. Res. Letts*., 21, 1619-1622.

Terao, Y., Y. Sasano, H. Nakajima, H.L. Tanaka, T. Yasunari (2002), Stratospheric ozone loss in the 1996/1997 Arctic winter: Evaluation based on multiple trajectory analysis for double-sounded air parcels by ILAS *J. Geophys. Res., 107,* 8210, doi:10.1029/2001JD000615.

Tilmes, S., R. Müller, J.-U. Grooß, D.S. McKenna, J.M. Russel III, Yasuhiro Sasano (2003), Calculation of chemical ozone loss in the Arctic winter 1996–1997 using ozone-tracer correlations: Comparison of Improved Limb Atmospheric Spectrometer (ILAS) and Halogen Occultation Experiment (HALOE) results, *J. Geophys. Res.*, *108*, 4045, doi:10.1029/2002JD002213.

Toon, O.B. and M.A. Tolbert (1995), Spectroscopic evidence against nitric acid trihydrate in polar stratospheric clouds, Nature, 375, 218-221.

Toon, O.B. and R.P Turco (1991), Polar stratospheric clouds and ozone depletion, *Scientific American*, June, 68-74.

Toon, O.B. et al. (1986), Condensation of HNO_3 and HCl in the winter polar stratosphere, *Geophys. Res. Lett.,13,* 1284-1287.

Tornkvist, K.K., D.W. Arlander and B.-M. Sinnhuber (2002), Ground-Based UV Measurements of BrO and OClO over Ny-Alesund during Winter 1996 and 1997 and Andoya during Winter 1998/99, *J. Atm. Chem., 43,* 75-106.

Toumi, R. (1994), Reaction of ClO with NO_3: OClO formation and night-time O_3 loss, *Geophys. Res. Lett., 21*(13), 1487-1490.

Urban, J., N. Lautie et al. (2004), The northern hemisphere stratospheric vortex during the 2002-03 winter: Subsidence, chlorine activation and ozone loss observed by the Odin Sub-Millimetre Radiometer, *Geophys. Res. Letts., 31*, doi: 10.1029/2003GL019089.

Van der Leun, J.C. (1998), Environmental Effects of Ozone Depletion, United Nations Environmental Programme.

Vogel, B. et al. (2003), Vertical profiles of activated ClO and ozone loss in the Arctic vortex in January and March 2000: In situ observations and model simulations, J. Geophys. Res., 108(D22), 8334, doi:10.1029/2002JD002564.

Voigt, C. et al. (2000), Non-equilibrium compositions of liquid polar stratospheric clouds in gravity waves, *Geophys. Res. Lett*., *27*(23), 3873-3876.

Voigt, C. et al. (2003), In situ mountain-wave polar stratospheric cloud measurements: Implications for nitric acid trihydrate formation, *J. Geophys. Res., 108*(D5), 8331, doi:10.1029/2001JD001185.

Vountas, M., V.V. Rozanov, and J.P. Burrows (1998), Ring Effect: Impact of rotational Raman scattering on radiative transfer in Earth's Atmosphere, *JQSRT, Vol. 60, No. 6*, 943-961.

Wagner, T. (1999), Satellite observations of Atmospheric Halogen oxides, PhD thesis, University of Heidelberg.

Wagner, T., C. Leue, K. Pfeilsticker and U. Platt (2001), Monitoring of the stratospheric chlorine activation by Global Ozone Monitoring Experiment (GOME) OClO measurements in the austral and boreal winters 1995 through 1999, *J. Geophys. Res., 106*, 4971-4986.

Wagner, T. (2001b), Correction of the Ring effect and I_0-effect for DOAS observations of scattered sunlight, *Proc. of the 1st DOAS Workshop*, Heidelberg, 13., 14. Sept., Heidelberg, Germany.

Wagner, T., F.Wittrock, A. Richter, M.Wenig, J.P. Burrows, and U. Platt (2002a), Continuous monitoring of the high and persistent chlorine activation during the Arctic winter 1999/2000 by the GOME instrument on ERS-2, *J. Geophys. Res., 107*(D20), 8267, doi : 10.1029/2001JD000466.

Wagner, T., S. Beirle, C. v.Friedeburg, J. Hollwedel, S. Kraus, M. Wenig, W. Wilms-Grabe, S. Kühl, U. Platt (2002b), Monitoring of trace gas emissions from space: tropospheric abundances of BrO, NO_2, H2CO, SO_2, H_2O, O_2, and O_4 as measured by GOME, *Air Pollution 2002*, WIT Press, *10*, 463-472.

Wahner A., G. Tyndall, and A. Ravishankara (1987), Absorption cross sections for OClO as a function of temperature in the wavelength range from 240-490 nm, *J. Phys. Chem., 91*, 2735-2738.

Waibel et al. (1999), Arctic ozone loss due to denitrification, *Science, 283*, 2064-2069.

Wang, H. J., D. M. Cunnold, L. W. Thomason, J. M. Zawodny, and G. E. Bodeker (2002), Assessment of SAGE version 6.1 ozone data quality, *J. Geophys. Res., 107(D23)*, 4691, doi:10.1029/2002JD002418.

Wayne, R.P. (2002), Chemistry of Atmospheres, Oxford University Press, New York.

Weber, M., S. Dhomse, F. Wittrock, A. Richter, B.-M. Sinnhuber and J.P. Burrows (2003), Dynamical control of NH and SH winter/spring total ozone from GOME observations in 1995-2002, *Geophys. Res. Lett., 30*(1), doi: 10.1029/2002GL016008.

Webster, C.R. et al. (1993), Chlorine chemistry on polar stratospheric cloud particles in the Arctic winter, *Science, 261*, 1130-1133.

Webster, C.R. et al. (1994), Balloon profiles of stratospheric NO_2 and HNO_3 for testing the heterogeneous hydrolysis of N_2O_5 on sulfate aerosols, *Geophys. Res. Lett., 21*, 53-56.

Wenig, M., S. Kühl, S. Beirle, E. Bucsela, B. Jähne, U. Platt, J. Gleason, and T. Wagner (2004), Retrieval and analysis of stratospheric NO2 from the Global Ozone Monitoring Experiment, *J. Geophys. Res., 109*, D04315, doi:10.1029/2003JD003652.

Wernli, H., and H.C. Davis (1997), A Lagrangian-based analysis of extratropical cyclones. I: The method and some applications, *Q.J.R. Meteorol. Soc., 123*, 467-489.

Wilms-Grabe, W. et al. (2002), Monitoring of Stratospheric Chlorine Activation with GOME OClO Measurements, *Air pollution research report 79*, Proceedings of the Sixth European symposium on stratospheric ozone, Gothenburg, Sweden. Available under: http://www.ozone-sec.ch.cam.ac.uk/EORCU/goteborg.html

Wirth, M. et al. (1999), Model-guided Lagrangian observation and simulation of mountain polar stratospheric clouds, *J. Geophys. Res.*, *104*, 23971- 23981.

Wittrock, F., A. Richter, J.P. Burrows (1999), Validation of GOME BrO and OClO observations in the northern hemisphere, Proceedings of the European Symposium on Atmospheric Measurements from Space (ESAMS 99), Noordwijk, Netherlands, WPP-161, pp. 735-738.

Wofsy, S.C., M.B. McElroy, Y.C. Yung (1975), The chemistry of atmospheric bromine, *Geophys. Res. Lett*., *2*, 215-218.

WMO, World Meteorological Organization (1982), Scientific Assessment of Ozone Depletion: 1982, Geneva.

WMO, World Meteorological Organization (1999), Scientific Assessment of Ozone Depletion: 1998, Geneva.

WMO, World Meteorological Organization (2003), Scientific Assessment of Ozone Depletion: 2002, Geneva.

Woyke, T., R. Müller, F. Stroh, D. S. McKenna, A. Engel, J. J. Margitan, M. Rex, K. S. Carslaw (1999), A test of our understanding of the ozone chemistry in the Arctic polar vortex based on in situ measurements of ClO, BrO, and O_3 in the 1994/1995 winter, *J. Geophys. Res.*, *104*(D15), 18755-18768, doi :10.1029/1999JD900287.

Zängl, G. (2002), Stratified flow over a mountain with a gap: Linear theory and numerical simulations, *Q. J. R. Meteorol. Soc.*, *128*, 927-949.

Danksagung

Diese Arbeit entstand in der Atmosphären-Chemie Gruppe des Instituts für Umweltphysik der Universität Heidelberg. Die Arbeit dort hat mir sehr viel Freude bereitet sowie mein Wissen und meinen Horizont deutlich erweitert. Insbesondere möchte ich mich bedanken bei:

Herrn Prof. Ulrich Platt für die freundliche Aufnahme in seine Arbeitsgruppe, die Themenstellung dieser Arbeit, sowie die kompetenten Anregungen.

Herrn Prof. Bernd Jähne für die interessierte Begutachtung dieser Arbeit.

Herrn Priv. Doz. Thomas Wagner für die zahlreichen Anregungen und Vorschläge über den gesamten Zeitraum, die freundschaftliche, humorvolle und anspornende Atmosphäre, sowie das umfangreiche Korrekturlesen dieser Arbeit.

Frau Dr. Walburga Wilms-Grabe für die stets angenehme Zusammenarbeit, die umfassende Beantwortung meteorologischer Fragen und das Korrekturlesen dieser Arbeit.
Herrn Dipl. Phys. Janis Pukite für die tatkräftige und ideenreiche Unterstützung bei der Auswertung und Visualisierung der SCIAMACHY Limb-Messungen.

Herrn Dr. Andreas Dörnbrack für die MM5 Simulationen bezüglich des Mountain Wave events vom 21. Januar 1997 sowie zahlreiche erhellende Diskussionen betreffend die Meteorologie der polaren Stratosphäre und die fruchtvolle und angenehme Zusammenarbeit.
Prof. Martyn Chipperfield, University of Leeds, for providing the SLIMCAT MPC 320 dataset and fruitful discussions regarding various aspects of polar stratospheric chemistry.

Herrn Dr. Björn-Martin Sinnhuber für die Berechnung der Photolysefrequenzen von OClO und die fruchtvolle und angenehme Zusammenarbeit.
Herrn Dr. Francois Hendrick für die Berechnung der chemischen Airmass-Faktoren für OClO.

Dr. Michel van Roozendael und Dr. Andreas Richter für die fruchtvollen Diskussionen bezüglich der OClO Auswertung sowie die freundliche Bereitstellung ihrer Ergebnisse.

Herrn Dr. Geir Braathen und Dr. Markus Rex für die Daten bezüglich des chemischen Ozonabbaus und die umfangreiche Beantwortung der Fragen zur polaren Ozonchemie.

Dr. Alexei Rozanov und Dr. Christian von Savigny, Universität Bremen für die Ergebnisse ihrer SCIAMACHY Limb-Auswertungen bezüglich OClO, O_3, BrO und NO_2 sowie die fruchtvollen Diskussionen.

Herrn Dipl. Phys. Frank Weidner für die Unterstützung bei der Entwicklung des Algorithmus zur Inversion der SCIAMACHY Limb-Messungen.

Allen Satellities für die angenehme „Arbeits“-Atmosphäre und die stetige Hilfsbereitschaft.